Electro-optic frequency combs and their applications in high-precision metrology and high-speed communications

Zur Erlangung des akademischen Grades eines

DOKTOR-INGENIEURS

von der KIT-Fakultät für
Elektrotechnik und Informationstechnik
des Karlsruher Instituts für Technologie (KIT)

genehmigte

DISSERTATION

von

Dipl.-Phys. Claudius Weimann
geb. in Backnang, Deutschland

Tag der mündlichen Prüfung: 19.06.2020

Hauptreferent: Prof. Dr.-Ing. Christian Koos
Korreferenten: Prof. Dr.-Ing. habil. Dr. h. c. Wolfgang Freude
Prof. Dr. rer. nat. habil. Andreas Heinrich

Abstract (German)

Optische Frequenzkämme haben sich in den letzten Jahren zu einem vielseitigen Werkzeug im Bereich der Optik und Photonik entwickelt. Sie ermöglichen den Zugang zu einer Vielzahl von schmalbandigen Spektrallinien, die einen breiten Spektralbereich abdecken und gleichzeitig hochgenau definierte Frequenzen aufweisen. Dadurch wurden Experimente in vielfältigen Anwendungsgebieten ermöglicht, zum Beispiel in den Bereichen optischer Atomuhren, der Präzisionsspektroskopie, der Frequenzmesstechnik, der Distanzmesstechnik und der optischen Telekommunikation. Allerdings umfassen übliche Frequenzkammquellen und die jeweiligen Laboraufbauten typischerweise komplexe opto-elektronische und opto-mechanische Anordnungen, welche aufgrund von Baugröße und fehlender Robustheit gegenüber Umwelteinflüssen wie Temperatur bislang kaum Einzug in breitere industrielle Anwendungen gefunden haben. Diese Arbeit legt deshalb ein besonderes Augenmerk auf die praktische Nutzbarkeit von frequenzkamm-basierten Systemen in industriellen Anwendungen. Im Fokus stehen dabei Robustheit, Kompaktheit und flexible Anpassungsmöglichkeiten an die jeweilige Anwendung. Das bezieht sich sowohl auf die Frequenzkammquellen selbst, als auch auf die zugehörigen anwendungsspezifischen optischen Systeme, in welchen die Frequenzkämme genutzt werden.

In der vorliegenden Arbeit wird das Potential elektro-optischer Frequenzkämme in der optischen Messtechnik sowie der optischen Kommunikationstechnik anhand ausgewählter experimenteller Demonstrationen untersucht. Als Mittel zur Realisierung miniaturisierter optischer Systeme mit einem Flächenbedarf von wenigen Quadratmillimetern wird die photonische Integration in Silizium verfolgt. Ein integriertes System zur Frequenzkamm-basierten Distanzmessung sowie integriert-optische Frequenzkammquellen werden demonstriert.

Die Erzeugung von Frequenzkämmen durch Dauerstrichlaser in Kombination mit elektro-optischen Modulatoren ist dabei ein besonders vielversprechender Ansatz. Zwar werden dabei üblicherweise kleinere optische Bandbreiten

erzielt als bei der weitverbreiteten Frequenzkammerzeugung durch modengekoppelte Ultrakurzpulslaser oder durch Kerr-Nichtlinearitäten, aber es bieten sich andere wertvolle Vorteile an. So erlaubt die elektro-optische Kammerzeugung beispielsweise eine nahezu freie Wahl der Mittenfrequenz durch Auswahl oder Einstellung des Dauerstrichlasers. Durch den Einsatz verschiedener Laser können sogar gleichzeitig mehrere Frequenzkämme unterschiedlicher Mittenfrequenz erzeugt werden, was sich in verschiedenen Anwendungen vorteilhaft ausnutzen lässt. Dies wird in dieser Arbeit anhand zweier Beispiele aus der optischen Messtechnik demonstriert, siehe Kapitel 3 und Kapitel 5. Der Kammlinienabstand ist bei elektro-optisch erzeugten Kämmen definiert durch die elektronisch erzeugte Modulationsfrequenz. Das bietet mehrere Vorteile: Der Linienabstand ist frei einstellbar, sehr stabil, und einfach rückführbar auf einen Frequenzstandard. Der Verzicht auf einen optischen Resonator macht die Kammquelle robust gegenüber Umwelteinflüssen wie z.B. Vibration. Zudem machen Fortschritte bei der Entwicklung von hochintegrierten optischen Modulatoren auf Silizium eine Umsetzung der Frequenzkammquellen in Siliziumphotonik möglich. Die erste derartige Komponente und deren Anwendung in der optischen Telekommunikation wird in Kapitel 6 vorgestellt. Photonische Integration in Silizium bietet außerdem das Potential, miniaturisierte optische Systeme mit vielfältiger Funktionalität zu realisieren. Solche Systeme zeichnen sich durch extrem kleinen Platzbedarf, Kompatibilität mit hochentwickelten und massentauglichen Fertigungstechniken aus der CMOS-(Complementary Metal-Oxide-Semiconductor)-Mikroelektronik und durch die Möglichkeit zur Kointegration elektronischer Schaltungen auf demselben Chip aus. Die hohe Integrationsdichte eröffnet die Perspektive, optische Systeme z.B. für Sensorik tief in industriellen Maschinen zu integrieren.

Kapitel 1 gibt eine kurze Einführung in optische Frequenzkämme und deren vielfältige Anwendungen in Wissenschaft und Technik. Der Stand der Technik zu unterschiedlichen Ansätzen zur Frequenzkammerzeugung und deren jeweiligen Eigenschaften werden diskutiert, und es werden die Vorzüge der in dieser Arbeit verwendeten elektro-optischen Frequenzkämme erläutert. Des Weiteren wird die Integration photonischer Systeme und Bauelemente auf Silizium vorgestellt. Schließlich werden die sich ergebenden Vorteile bei der Anwendung in optischer Messtechnik und optischer Telekommunikation diskutiert.

Kapitel 2 fasst die physikalischen Grundlagen der Arbeit zusammen. Die Funktionsprinzipien elektro-optischer Modulatoren werden beschrieben sowie de-

ren Anwendung zur Erzeugung von Frequenzkämmen. Zusätzlich wird das Konzept sogenannter synthetischer Wellenlängen eingeführt, welches in der optischen Distanzmesstechnik Anwendung findet.

Kapitel 3 beschreibt ein Prinzip zur Distanzmessung mittels zweier elektro-optischer Frequenzkämme zur kontaktlosen Vermessung technischer Objekte. Die Leistungsfähigkeit des Ansatzes wird durch eine Erfassung von ausgedehnten Oberflächenprofilen in Form von Punktwolken demonstriert, wobei eine verhältnismäßig kurze Messzeit von 9.1 µs pro Punkt ausreichend ist. Dabei wird der faseroptisch angebundene Sensorkopf von einer Koordinatenmessmaschine über die Oberfläche bewegt. Durch Temperaturschwankungen im faser-optischen Aufbau ausgelöste Messabweichungen werden durch die Messung mit Lasern unterschiedlicher Emissionsfrequenz kompensiert.

Kapitel 4 beschreibt ein integriert-optisches System auf Silizium zur frequenzkammbasierten Distanzmessung. Das System beinhaltet das zum Heterodynempfang genutzte Interferometer inklusive eines einstellbaren Leistungsteilers sowie der Photodetektoren. Der Platzbedarf aller Komponenten auf dem Siliziumchip beträgt 0.25 mm^2. Der Chip wird in dem in Kapitel 3 eingeführten Messverfahren eingesetzt, wobei Distanzmessungen mit Root-mean-square-Fehlern von 3.2 µm und 14 µs Erfassungszeit demonstriert werden.

Kapitel 5 stellt ein Distanzmesssystem vor, bei welchem eine grobauflösende Phasenlaufzeitmessung mit großem Eindeutigkeitsbereich mit einer interferometrischen Distanzmessung mit synthetischen Wellenlängen zur Verfeinerung der Messgenauigkeit kombiniert wird. Die durch vier Laser erzeugten synthetischen Wellenlängen bzw. die Frequenzabstände der Laser werden zeitgleich zur Distanzmessung mittels eines auf elektro-optischer Modulation basierenden Verfahrens vermessen. Durch diese Referenzierung wird der Einsatz freilaufender Laser ohne Wellenlängenstabilisierung ermöglicht. Es werden Messraten von 300 Hz und Genauigkeiten im Mikrometerbereich erreicht.

Kapitel 6 beschreibt die weltweit erste Demonstration elektro-optischer Frequenzkammquellen auf Silizium und die hierzu genutzte hybride Materialplattform aus Silizium und organischen Materialien (Silicon-Organic Hybrid, SOH). Spektral flache Frequenzkämme mit 7 Linien innerhalb von 2 dB und Linienabständen von 25 GHz und 40 GHz werden erzeugt. Die praktische Anwendbarkeit solcher Frequenzkämme wird durch eine Reihe von Datenübertragungexperimenten demonstriert. Die einzelnen Kammlinien dienen als Träger

für Daten in einem Wellenlängenmultiplex-System, womit eine spektral effiziente Datenübertragung mit Datenraten von über 1 Tbit/s über Distanzen von bis zu 300 km demonstriert wird.

Kapitel 7 fasst die Ergebnisse der vorliegenden Arbeit zusammen und gibt einen Ausblick auf die Möglichkeiten, die sich durch weiterentwickelte Kammquellen und fortschreitende Möglichkeiten in der photonischen Integration ergeben.

Preface

In recent years, optical frequency combs have evolved into a versatile tool in the field of optics and photonics. Offering a multitude of highly coherent narrowband optical tones that cover a broad spectral range, frequency combs have unlocked a wide range of applications in the fields of optical high-precision time-keeping and frequency metrology, precision spectroscopy, distance metrology and optical telecommunications. However, conventional frequency comb sources and the associated laboratory set-ups typically comprise rather complex opto-electronic and opto-mechanical arrangements which, due to their size and sensitivity to environmental influences such as temperature and vibrations, have not yet found their way into broader industrial applications. This work therefore focuses on the practical usability of comb-based optical systems in industrial applications, where robustness, form factor and flexible adaptability to application-specific requirements are key. This applies both to the frequency comb sources themselves and to the respective application-specific optical systems in which the combs are used.

In this work, the potential of electro-optic frequency combs in optical metrology and optical communications is explored through selected experimental demonstrations. Photonic integration on silicon is being pursued as a means of realizing miniaturized optical systems with a footprint of only a few square millimetres. An integrated system for comb-based distance metrology and integrated frequency comb sources are demonstrated.

In this context, the generation of frequency combs by electro-optic modulation of continuous-wave laser tones is a particularly promising approach. Although this approach usually leads to smaller optical bandwidths than widely-used frequency comb generation techniques that rely on mode-locked lasers or Kerr-nonlinear devices, there are other valuable advantages. As an example, electro-optic comb generation offers a nearly free choice of the center frequency by selection or adjustment of the emission frequency of the continuous-wave laser. Furthermore, multiple frequency combs exhibiting different center frequencies

can be generated simultaneously within a single electro-optic modulator. This property can be used advantageously in different applications as demonstrated in this work with two examples in the field of optical metrology, see Chapter 3 and Chapter 5. Moreover, the comb-line spacing for electro-optically generated combs is defined by the electronically generated modulation frequency. This provides several advantages: The line spacing is freely adjustable, very stable and easily traceable to a frequency standard. The absence of an optical cavity makes the comb source robust against environmental influences such as vibration. In addition, progress in the development of integrated electro-optic modulators on silicon makes it possible to realize such frequency comb sources on silicon photonic platforms. The first demonstration of an integrated frequency comb generator on silicon and its application in optical telecommunications is presented in Chapter 6. Photonic integration on silicon also offers the possibility to realize sophisticated optical systems with a wide range of functionality on an extremely small footprint, systems that are compatible with advanced production processes from the complementary-metal-oxide-semiconductor (CMOS) microelectronics industry, and that offer the ability to co-integrate electronic and photonic circuits on the same chip. The high robustness and compactness of photonic integrated systems offer the potential to integrate them deeply into industrial machines.

Chapter 1 gives a brief introduction to optical frequency combs and their various applications in science and technology. The state of the art regarding different approaches to frequency comb generation and their respective properties are discussed. The focus on electro-optic frequency combs is motivated as well as the accompanying topic of integration on silicon. Finally, the specific advantages for applications in optical metrology and optical telecommunications are summarized.

Chapter 2 gives a compact introduction into the fundamentals needed for understanding the following chapters. The basics of electro-optic modulators and their application to comb generation are described. In addition, the concept of so-called synthetic wavelengths is introduced, which is used in optical distance metrology.

Chapter 3 describes the concept and the demonstration of a novel distance measurement technique that relies on two electro-optic frequency combs for non-contact measurement of technical objects. The quick digitization of entire surface profiles as point clouds is made possible by a short acquisition time of

9.1 µs, and by connecting the fiber optic sensor head to a coordinate measuring machine. Measurement errors caused by temperature fluctuations in the fiber-optical system are avoided by a scheme with two lasers at different emission frequencies.

Chapter 4 describes a silicon photonic receiver system for comb-based distance metrology. The optical system includes the interferometer used for heterodyne reception including an adjustable power divider and photodetectors. The space requirement of all components on the silicon chip is 0.25 mm^2. The chip is used for the measurement method introduced in Chapter 3, and distance measurements with root-mean-square errors of 3.2 µm and 14 µs acquisition time are demonstrated.

Chapter 5 introduces a distance measurement system in which a coarse-resolution time-of-flight measurement with a wide unambiguity range is combined with an interferometric distance measurement with synthetic wavelengths to refine the measurement accuracy. The synthetic wavelengths generated by four continuous-wave laser tones are measured simultaneously with the distance via a method based on electro-optic modulation. This reference measurement makes the use of free-running lasers without wavelength stabilization possible. Measurement rates of 300 Hz and micrometer accuracy are obtained.

Chapter 6 describes the first demonstration of electro-optic frequency comb generation on a silicon photonic chip along with the underlying hybrid integration concept that combines silicon waveguides and organic materials (silicon-organic hybrid, SOH). Spectrally flat frequency combs offering 7 lines with a spectral flatness of 2 dB and comb line spacings of 25 GHz and 40 GHz are generated. The practical applicability of such frequency combs is demonstrated by a series of data transmission experiments. The individual comb lines serve as carriers of information in a wavelength-division multiplexing system, and spectrally efficient data transmission at data rates of more than 1 Tbit/s over distances of up to 300 km is demonstrated.

Chapter 7 summarizes the results of the presented work and gives an outlook on further developments related to frequency comb sources and advanced capabilities in photonic integration.

Achievements of the present work

In this thesis, novel approaches in optical metrology and optical communications making use of electro-optic frequency combs are investigated. The potential for realizing miniaturized photonic systems is shown by demonstrating a monolithically integrated silicon photonic optical receiver system for comb-based distance measurements. Furthermore, electro-optic frequency comb generators realized through a hybrid combination of nanophotonic silicon waveguides and highly efficient organic eletro-optic materials are demonstrated for the first time.

In the following, a short overview of the main achievements presented in this thesis is given.

Development of a fiber-based, robust, fast and precise distance measurement system based on electro-optic frequency combs
A distance measurement system based on electro-optic frequency combs has been developed, see Chapter 3 and references [C4, C6, C34, J1, J6]. Measurement standard deviations below 2 µm for an acquisition time of 9.1 µs are demonstrated. The approach relies on robust, off-the-shelf components, the achieved performance can well compete with other comb-based distance metrology demonstrations, and the accuracy can be maintained even under industrial operating conditions.

Compensation of temperature-induced measurement fluctuations
A novel approach for continuous compensation of temperature-induced distance measurement fluctuations based on dual-color electro-optic frequency combs is demonstrated, see Chapter 3 and references [C6, J1]. The compensation scheme enables accurate measurements through 7 m of optical fiber in environments without temperature control. No detrimental dead-zones occur in the measurement range due to the novel dual-color approach. The effec-

tiveness of the scheme is demonstrated by conducting accurate measurements while rapidly heating the fiber with a heat gun.

Integration of the distance measurement system with a coordinate measuring machine
A fiber-coupled sensor head mounted to a coordinate measuring machine is used to measure the distances to naturally scattering surfaces while being moved, thereby accurately digitizing extended surfaces of technical objects, see Chapter 3 and references [C6,J1]. A real-time measurement rate of 3.3 kHz is achieved by signal processing on a field-programmable gate array (FPGA), allowing fast acquisition of point clouds of up to 5 million data points during continuous movement of the sensor head.

Realization of a silicon photonic receiver system for dual-comb distance metrology
A receiver system for comb-based distance measurements is integrated on a silicon photonic chip with a footprint of approximately 1 mm × 1 mm, see Chapter 4 and references [C5, C34, J11]. The chip realizes a heterodyne interferometer with photodetection, comprising couplers, waveguides, photodiodes and variable power splitters for distributing the power between reference and measurement signals as an added functionality. Standard deviations below 5 µm for an acquisition time of 14 µs are demonstrated. To the best of our knowledge, our experiments represent the first demonstration a comb-based distance measurement scheme relying on a silicon photonic chip.

Development of a referencing module capable of measuring laser frequency differences of multiple lasers
A referencing module capable of measuring laser frequency differences of multiple lasers simultaneously was developed, see Chapter 5 and references [1, C1, J4]. The laser frequency differences are tracked continuously in order to calibrate the synthetic wavelengths used for distance measurement in an interferometric system during operation. High-precision measurements with free-running lasers are made possible by the referencing module, and standard deviations between 3 µm and 15 µm are achieved for a measurement rate of 300 Hz when measuring a machined aluminum target at a stand-off distance of 1 m.

First demonstration of electro-optic frequency comb generation on silicon
Electro-optic frequency comb generators integrated on silicon photonic chips are demonstrated by making use of the silicon-organic hybrid (SOH) approach, see Chapter 6 and references [C2,C3,J5]. Frequency combs comprising 7 lines with a spacing of 40 GHz and a spectral flatness of 2 dB are generated. To the best of our knowledge, our experiments represent the first demonstration of electro-optic frequency comb generation on silicon.

Demonstration of terabit/s data transmission using chip-scale silicon-organic hybrid (SOH) frequency comb generators
The viability of the chip-scale SOH comb generators is demonstrated in data transmission experiments, see Chapter 6 and references [C2,C3,J5]. The comb lines are generated from a single continuous wave laser and serve as carriers for a wavelength division multiplexing data transmission. Transmission at data rates of more than 1 Tbit/s over distances of up to 300 km are demonstrated.

Table of Contents

1 Introduction

This chapter starts with a brief introduction of optical frequency combs and their diverse applications in science and technology. As different applications lead to different requirements regarding the properties of frequency comb sources, a brief overview of key parameters of different comb sources is given. In this work, electro-optic comb generation is used for applications in the fields of optical metrology and optical communications. So-called electro-optic frequency combs have the advantage of a tunable, electronically defined line spacing, free choice of the central frequency, and robustness against environmental influences due to the absence of a cavity. Furthermore, the scheme is compatible with silicon photonic integration. Silicon photonic integration provides huge benefits for the realization of the compact optical systems and for the miniaturized electro-optic comb generators demonstrated in this thesis. Finally, the application of frequency combs and photonic integration in distance metrology and optical communication is motivated.

1.1 Optical frequency combs: Precise tools for high frequencies

Optical frequency combs (FC) comprise a multitude of discrete spectral lines, which are regularly spaced in the frequency domain [2]. Typically, they cover a relatively large optical bandwidth, and their frequencies are very precisely defined – two properties which make frequency combs particularly useful. As illustrated in Fig. 1.1, the absolute optical frequency f_m of each comb line with line index m is determined by the offset frequency f_off and the line spacing f_r, $f_\mathrm{m} = mf_\mathrm{r} + f_\mathrm{off}$. If both parameters are precisely known, a frequency comb is said to be fully referenced, providing precise absolute measurements at optical frequencies. To fully reference a frequency comb, an attractive approach is to generate a very broadband comb with a bandwidth exceeding one octave, to

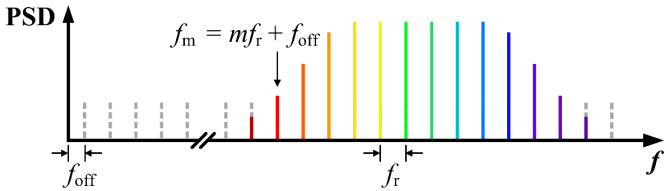

Fig. 1.1: Sketch of the power spectral density (PSD) of a frequency comb. A multitude of discrete spectral lines, regularly spaced in frequency domain by a line spacing f_r are characteristic of frequency combs. With the offset frequency f_{off}, the frequency of the mth comb line can be expressed as $f_m = mf_r + f_{off}$.

enable self-referencing with an interferometric f–$2f$ scheme [3–5]. However, for many purposes relative measurements are adequate and control of only f_r provides a precise and broadband frequency ruler.

Many applications in science and technology benefit greatly from access to the broadband spectrum of coherent radiation with precisely defined frequencies provided by frequency combs [6]. Examples are spectroscopy [7–16], optical atomic clocks [17–19], waveform generation in both the optical and the microwave regime [20, 21], optical coherence tomography [22, 23], generation of terahertz radiation [24–27], optical signal processing [28–30], frequency calibration [31–33], optical distance measurements [34–37, J1, J4], and optical communications [38, 39, J2, J3, J5]. The variety of these research fields testifies the versatility of optical frequency combs as scientific and technical tools. However, the various applications pose different requirements on the attributes of the frequency comb, and not all are served equally well by the same kind of comb source. This is visualized qualitatively for a number of applications in Fig. 1.2. The relative importance of comb properties for a particular application is denoted by the overhead arrows in Fig. 1.2. Important properties are bandwidth, precision, accuracy, metrological accessibility of the comb lines, robustness, and simplicity. Some applications only use few comb lines but require them to be defined with highest precision, e.g., in optical clocks for precise measurements of narrow atomic transitions. Here, ultranarrow atomic transitions are measured with optical frequency standards provided by frequency combs with relative frequency uncertainties of 10^{-19} [19]. This low uncertainty is needed, e.g., for the search of possible time variations of fundamental constants [40, 41], and highly elaborate setups can be utilized

because the application is confined to laboratories with tightly controlled conditions. Other applications such as optical data transmission typically use all comb lines, e.g., as carriers for wavelength-division multiplexing (WDM), with relaxed frequency precision, however with the need for a high robustness and simplicity due to their intended use in industrial products. In many use cases in applied science, the robustness and simplicity of the comb source becomes increasingly important, especially when considering the implementation in future products. Luckily, this is often accompanied by somewhat relaxed requirements in terms of absolute accuracy and bandwidth. The application fields treated within this thesis are marked by bold fonts in Fig. 1.2. In general terms, the applications in comb-calibration of lasers [C1, J4], optical data transmission [C2, C3, J5] and optical distance measurements [C4–C6, J6] have a higher emphasis on the robustness and the simplicity of the comb sources and relatively modest bandwidths are sufficient. These general requirements have thus to be considered when choosing a frequency comb source for a certain application. Different comb generation schemes and their properties will be introduced in the following paragraphs to provide an overview.

Several methods exist to generate frequency combs: Combs can be formed by pulse trains from mode-locked lasers, they can be generated by electro-optic modulation of a continuous-wave (CW) laser, or by nonlinear parametric processes, e.g., cascaded four-wave mixing and/or self-phase modulation in nonlinear devices.

1.1.1 Mode-locked lasers

Distinct comb-shaped optical spectra have been observed since 1964 with the introduction of the actively mode-locked laser (MLL) [42]; however the term “frequency comb” was introduced several years later [43]. The train of equidistantly spaced, short pulses emitted by mode-locked lasers is represented in the frequency domain by a frequency comb, where the comb line spacing is determined by the pulse repetition rate and where the bandwidth of the spectral envelope is determined by the pulse duration [44, 45]. One very early application of frequency combs was the use of the spectrum of a synchronously pumped actively mode-locked picosecond dye laser for measurements of the fine and hyperfine structure of spectral lines in atomic sodium in 1978 [43]. An important milestone was the introduction of octave-spanning frequency

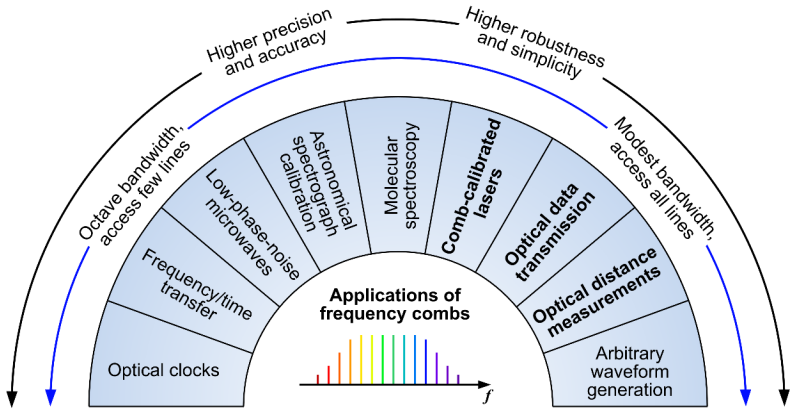

Fig. 1.2: Some applications of optical frequency combs with associated requirements, adapted from [6]. Application fields treated within this thesis are marked by bold letters. The relative importance of comb properties for a particular application is denoted by the overhead arrows. Important properties are bandwidth, precision, accuracy, metrological accessibility of the comb lines, robustness and simplicity. Some applications only use few comb lines but require them to be defined with highest precision, e.g., in optical clocks for precise measurements of narrow atomic transitions. Highly elaborate setups can be utilized due to the application being confined to laboratories with tightly controlled conditions. Other applications such as optical data transmission typically use all comb lines, e.g., as carriers for WDM, with relaxed frequency precision, however with the need for a high robustness and simplicity due to their intended use in industrial products.

combs in 1999, making ultra-precise measurements of optical frequencies possible [4, 32, 46]. The importance of this technique was recognized by the Nobel Prize for physics, which was awarded to John L. Hall and Theodor W. Hänsch in 2005. MLL as comb generators have since then been further developed, and remarkable progress has been made in terms of increased optical bandwidth, improved stability of repetition rate, higher repetition rates, and decreased sensitivity to environmental influences [3, 47–54]. However, many applications require, e.g., a large line spacing in the order of tens of gigahertz, robustness, and independent tuning of center frequency and line spacing. Despite all progress, these properties are difficult to obtain with MLL. For example, the line spacing of a MLL is dictated by the cavity size which cannot be decreased arbitrarily, as enough gain needs to be available to compensate the losses of the optical resonator. Furthermore, the line spacing is difficult to tune and might be sensitive to environmental influences.

1.1.2 Parametric frequency combs

Parametric frequency combs are generated by cascaded third-order nonlinear processes such as four-wave mixing, self-phase modulation and cross-phase modulation, which are induced by the interaction of strong pump lasers with a Kerr-nonlinear medium [55, 56]. Parametric comb sources can be realized with resonant structures such as whispering-gallery-mode resonators [57, 58] or planar microring resonators [59, 60]. Other approaches use non-resonant waveguides such as highly nonlinear fibers (HNLF) [61–64] or nanowire waveguides [65–68]. Typically, these techniques allow generation of very broadband combs. However, high-power pump lasers or resonators with a high quality factor are needed. While demonstrations using high-Q resonators have shown comb generation with just a few milliwatts of pump power [69–71], the conversion efficiency is limited [72], leading to powers per comb line in the microwatt-regime – too low for many applications. Furthermore, the flexibility regarding line spacing and center frequency is impaired either due to dispersion effects or the free spectral range of the resonator cavity.

1.1.3 Electro-optic comb generation

A different method for comb generation was first introduced in 1972, where a narrowband CW laser beam was phase-modulated by an electro-optical modulator [73]. Although the term “frequency comb” is not mentioned in the paper, the spectrum clearly displays the comb-like shape of equidistant optical lines. In this scheme, the frequency comb is formed by the modulation sidebands generated by phase modulation. The spectral bandwidth of the comb envelope is determined by the modulation depth, where a strong phase modulation results in a large bandwidth. The line spacing is determined by the electrical modulation frequency, making the method easy to use, and especially well-suited for large line spacings in the range of several tens of gigahertz, which are not easily reachable by MLL. An early application of this electro-optic comb generation scheme was the accurate measurement of laser frequency differences in 1992 [74]. Today’s wide availability of low-noise high-frequency electronic oscillators and telecommunication-grade electro-optic modulators with low half-wave voltages, high bandwidth, and high power handling makes this approach increasingly popular [21]. Several schemes using electro-optic mod-

ulation have been developed to generate broadband combs. Some approaches rely on phase modulation inside an optical cavity to increase the modulation efficiency [73–76]. However, in such schemes the radio-frequency (RF) driving signal has to be matched precisely to the free-spectral range of the cavity, and the input CW laser has to be tuned to one of the optical resonances. Additionally, the cavity must be stabilized to compensate environmental influences such as temperature change or mechanical vibrations. Other approaches without optical cavities use combinations of phase modulators and/or amplitude modulators to generate frequency combs with spectrally flat envelopes [77–85]. This allows electrical tuning of the line spacing by tuning the driving frequency, free choice of the central frequency, and robustness against environmental influences. Even though the bandwidth of electro-optic combs is low when compared to other schemes, the combination of the aforementioned properties makes the principle of cavity-less electro-optic modulation very flexible.

Along with properties such as robustness, precision, simplicity and flexibility, bandwidth and line spacing are key comb parameters for most applications. Experimentally obtained values from literature are plotted in Fig. 1.3. The basic physical concept behind the respective comb generation technique is color-coded, with black/grey for mode-locked lasers, orange/red for electro-optic modulation, and dark green/bright green for parametric comb generation. The data further distinguishes between different kinds of MLL, direct electro-optic modulation vs. cavity-enhanced modulation, and between microring resonators and HNLF. Demonstrations of tunability are included as lines between the lowest and highest values. If the bandwidth of an initial frequency comb is further broadenend by a nonlinear stage, the data points are depicted as open symbols. It can be seen in Fig. 1.3 that the values for bandwidth and line spacing are clustered in distinct regions for each of the three different comb generation principles. Electro-optic comb generators occupy a technically very interesting region with line spacings of tens of gigahertz and up to terahertz-scale bandwidths, while at the same time tunability of the line spacing is relatively easy to realize, as demonstrated in some of the publications.

Weighing the attributes of the different comb generation techniques against each other, the choice within this thesis is for cavity-less electro-optic comb generation. The benefits of electro-optic combs are advantageously exploited, e.g., by using a second center wavelength for temperature compensation in distance metrology, Chapter 3, or by adapting the channel spacing in a WDM

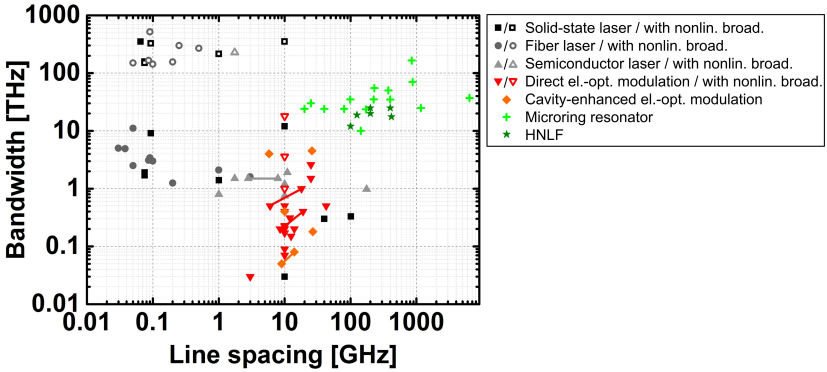

Fig. 1.3: Bandwidth vs. line spacing for different categories of frequency comb sources found in the literature. Comb spectra obtained by nonlinear broadening of ultrashort laser pulses are denoted by open symbols. For comb sources with tunable line spacing, the tuning range is denoted by lines. The data used to compile this graph are listed in Appendix C.

transmission setup to realize a high spectral efficiency, Chapter 6. In Chapter 5, the frequencies of four independent lasers used for synthetic-wavelength interferometry are referenced with respect to each other by exploiting electro-optic comb generation from each of the lasers. Furthermore, electro-optic modulators can be realized efficiently on silicon photonic integrated circuits (PIC) using the so-called silicon-organic hybrid (SOH) approach [86–91, J13]. Combined with the concept of modulator-based comb generation, this made the first demonstration of an electro-optic comb source on a silicon-on-insulator (SOI) substrate possible, see references [C2, C3, J5], and Chapter 6.

1.2 Silicon photonic integration

Silicon photonics has become a mature technology platform for realization of sophisticated photonic integrated circuits (PIC) [92–94]. Complex optical systems with a large number of optical components can be integrated on a single chip, providing unprecedented functionality within a very small footprint [95, 96]. While several material systems for photonic integration exist, e.g., polymers [97], glass [98], or III-V semiconductors [99, 100], the silicon-on-insulator (SOI) material system commonly used in silicon photonics has

some crucial advantages. Silicon is transparent in the near-infrared, starting from wavelengths of approximately 1.1 µm up to mid-infrared wavelengths of almost 10 µm. The material properties of SOI are also very suited for photonic integration: With a high refractive index of 3.476 at the widely used telecommunication wavelength of 1550 nm, nanometer-size SOI waveguides with tight bend radii are possible. Optical systems with many functional building blocks thus can be realized within a very small footprint. Silicon oxide with a low refractive index of 1.45 at 1550 nm can not only be used as a buried oxide layer, but also as a readily available cladding material. In addition, silicon exhibits a large thermal conductivity. Probably its largest advantage is the compatibility with established fabrication processes of the microelectronics industry. Decades of development related to the production of complementary metal-oxide-semiconductor (CMOS) integrated electric circuits have led to highly sophisticated, high-yield processes, that may also be used for low-cost mass production of photonic integrated circuits (PIC). Furthermore, a dense co-integration of PIC with microelectronic circuits makes fully integrated opto-electronic systems possible [101, 102]. The combination of these attributes make silicon photonics a prime candidate for photonic integration with huge potential for many applications.

The main drivers behind silicon photonics are applications in optical interconnects, where the critical tasks are a massive parallelization of optical links, reduction of costs and reduction of consumed power per transmitted bit [93], making scalability of the technology a necessity. However, the potential of silicon photonic integration is not limited to the field of optical telecommunication. Many other applications can be realized by exploiting the rich device portfolio available in silicon photonics, with huge potential benefits in scalability, footprint (size, weight and power), robustness and added functionality. Emerging examples are in medical diagnostics [103], spectroscopy [104], optical metrology [105, 106, C5, J10], optical coherence tomography [107, J7], and beam steering [108].

1.3 Scope of this thesis

1.3.1 Overview

In this thesis, electro-optic frequency combs are employed for experiments in optical distance metrology and optical communications. In addition, silicon photonic integration as a technology to realize miniaturized optical systems is investigated in the context of optical metrology.

In a first set of experiments, the frequency combs are used to directly measure distances using a dual-comb measurement scheme that relies on the concept of synthetic-wavelength interferometry. A fiber-optical system is implemented and used to acquire surface profiles of various technical samples with a remote measurement head mounted on a coordinate measuring machine. Thermal drift is mitigated by a dead-zone free temperature compensation scheme, Chapter 3. The potential of silicon photonic integration for applications in distance metrology is explored by realizing a silicon PIC comprising a heterodyne receiver with tunable power splitters and on-chip photodetectors. The PIC with an on-chip footprint of well below $1\,\mathrm{mm}^2$ is used to demonstrate fast and precise distance measurements in combination with the dual-comb measurement scheme, Chapter 4.

In another set of experiments, electro-optic comb generators are used to calibrate the relative frequency differences between four lasers used for synthetic-wavelength interferometry. The frequency referencing scheme allows to use free-running lasers, greatly simplifying the technical effort required for synthetic-wavelength interferometry, Chapter 5.

Silicon photonic integration of electro-optic comb generators is explored in Chapter 6. Making use of the so-called silicon-organic hybrid (SOH) approach [86–88, J13], the first realization of an electro-optic comb source on a silicon-on-insulator (SOI) substrate is demonstrated. The feasibility of the comb source is shown by using the generated comb lines as carriers for optical data transmission with terabit/s data rates.

1.3.2 Frequency combs and photonic integration for optical distance metrology

Distance metrology is a field of great importance, serving a wide range of applications in science and technology such as non-destructive testing of mechanical parts, inline inspection during manufacturing, reverse engineering, precise referencing of translation axes in industrial machinery and 3D scanning [109–112, J6]. Metrology systems for such applications are typically required to be accurate, fast, and robust, while being compatible with deep integration into the respective machinery. Non-contact optical measurement methods are especially attractive with respect to the requirements regarding accuracy and speed. While many different optical measurement methods for dimensional metrology have been developed in the past, see [113] for an overview, rapid progress in the field of optics and photonics has opened paths towards new technical approaches. Among these approaches, concepts based on optical frequency combs stand out due to the exceptional performance. As an example, comb-based distance measurement techniques allow to overcome the problem of measurement ambiguity. Many laser-ranging techniques determine distance from the phase shift of a signal after propagation. In conventional single-wavelength interferometry, the phase shift of a single optical carrier is used, leading to sub-wavelength resolution. However, only very small relative displacement can be reliably measured, as the unambiguity range of such methods is limited to half an optical wavelength and thus very small. On the other hand, ranging techniques based on the time of flight of a pulse or a modulated waveform provide a large unambiguity range, but suffer from a poorer resolution. A combination of adequately long unambiguity range and high resolution is attempted with synthetic-wavelength interferometry, where the phase of light with multiple wavelengths is simultaneously evaluated to extend the unambiguity range. However, to achieve high precision, carriers distributed over a wide spectral range with precisely defined frequencies are required. In this respect, optical frequency combs offer unique advantages. The combs are used either directly for distance measurements [34, 35, 37, 114–129, J8] or as a means to calibrate the lasers used for synthetic-wavelength interferometry (SWI) [130, 131, J4] or frequency-modulated continuous-wave (FMCW) laser ranging [132, 133]. So far, experimental demonstrations have mostly relied on femtosecond mode-locked lasers (MLL), parametric combs generated in HNLF, or cavity-enhanced electro-optic combs, with their associated advan-

tages and disadvantages as discussed in Section 1.1. While important results have been obtained with these sources, their most severe drawbacks are lack of robustness, high experimental complexity, incompatibility with silicon photonic integration, and missing flexibility concerning center wavelength and line spacing.

In contrast to these approaches, this work makes use of a relatively simple cavity-less electro-optic modulation scheme to generate frequency combs [134], mitigating the aforementioned drawbacks. In a first set of experiments, pairs of frequency combs with slightly detuned line spacings are generated for a dual-comb distance measurement scheme. The line spacings are electronically defined by the corresponding modulation frequency, making them precise, stable and easy to tune. The achieved measurement precision and speed compares well with the state of the art in comb-based distance measurements, see Chapter 3 and the corresponding discussion. The system comprises fiber optical components, which are robust against dirt and make easy integration in industrial machinery possible, as demonstrated by attaching a remote sensor head to a coordinate measuring machine. However, fiber-based systems are extremely sensitive to temperature changes, either severely limiting the measurement accuracy, or requiring tight control of environmental conditions, which is not feasible in an industrial setting. To solve this issue, a compensation measurement is conducted simultaneously to the distance measurement to mitigate the effect of temperature-induced optical path length fluctuations. To this end, two continuous-wave lasers with different center frequency are jointly fed into the electro-optic comb generators. The generated frequency combs are transmitted via a single optical fiber to a remote sensor head. In the sensor head, the frequency combs at different center frequencies are separated by a dichroic beamsplitter. One of the combs is used to measure a reference distance to a fixed retroreflector to reveal the path-length fluctuations in the optical fiber.

The footprint of the setup used for the distance measurement scheme can be significantly reduced by photonic integration. To this end, the silicon-on-insulator platform is used. Silicon photonic integration of the optical interferometric setup for distribution of light and detection is realized with an on-chip footprint of $0.25\,\mathrm{mm}^2$. The PIC is employed for distance measurements with performance characteristics comparable to the macroscopic fiber-based setup. Additionally, the first realization of an electro-optic comb

source on a silicon-on-insulator (SOI) substrate is demonstrated with another PIC, yielding experimental proof of the compatibility of the comb generation principle with the SOH material platform. This paves the way towards mass-producible, miniaturized sensor chips, which can be tightly integrated into industrial machinery and which are much more robust against mechanical vibrations than fiber-based optical setups.

The inherent tunability of the line spacing and the flexibility concerning the center wavelengths offered by electro-optic comb generators is also exploited in another set of experiments. Synthetic-wavelength interferometry is a common technique to extend the unambiguity range of conventional optical interferometry by employing two or more CW lasers with different wavelengths [135, 136]. However, the measurement accuracy is limited by the relative wavelength stability of the laser sources [137, 138]. Typically, this problem is overcome by locking the laser frequencies to a frequency reference provided by an additional frequency comb [131, 132, 139]. However, feedback loops for frequency locking and an additional comb are required, increasing the setup complexity. In contrast to the state of the art, free-running CW lasers without locking electronics are demonstrated in this thesis [J4]. The differences in emission frequencies are not tightly controlled, but merely monitored simultaneously to the measurement. The effect of relative frequency drifts of the lasers can thus be corrected in a post-processing step. To this end, parts of the light from the four CW laser employed for synthetic-wavelength interferometry are coupled to electro-optic comb generators, and frequency combs are created from the same lasers. The line spacings are chosen such that relative frequency referencing of the four lasers is possible by detecting a beat signal of the modulation sidebands with low-frequency electronics. This greatly simplifies the technical effort for high-precision synthetic-wavelength interferometry.

1.3.3 Integrated electro-optic frequency combs for optical data transmission

The driving force behind the field of optical communications is the increasing demand for data transmission capacity, induced by a growing number of mobile devices, new cloud-based services, connected devices in the context of internet of things, and an increasing consumption of traffic-heavy multimedia data such as high-definition video. A whitepaper by Cisco forecasts an increase of the

annual global data center traffic from 6 zettabytes in 2016 to 20.6 zettabytes in 2021 at a compound annual growth rate of 25% [140]. Data center operators such as Google, Amazon, or Facebook have to keep up with this increasing consumer demand and provide a network infrastructure which can support the increase in bandwidth at lowest possible cost and energy consumption. Thus, there is high pressure for novel solutions with greatly improved efficiency. A key technology for next-generation high-speed medium-reach connections such as data-center interconnects or links within metropolitan-area networks is coherent optical transmission with advanced modulation formats, in conjunction with wavelength division multiplexing (WDM). Increasing the number of parallel channels by using several carriers with different wavelengths makes good use of the bandwidth supported by optical fibers and avoids the problems associated with further increasing single-carrier data rates [141, 142].

Instead of using individually controlled lasers for each carrier, frequency combs lend themselves to be used in WDM data transmission. Combs exhibit a number of carriers with precisely defined frequency spacings, allowing tight channel spacing for an efficient use of the available spectrum [39, J3]. Additionally, only two parameters need to be controlled to precisely define the wavelengths of all comb tones: The comb line spacing and the center frequency. This overcomes the need for control electronics for a large number of individual lasers.

Silicon photonic integration has the potential to realize the required optical systems on multi-transceiver chip modules in a cost-effective way, with small form factor, and high-volume production. While many of the needed optical components such as modulators [87, 143], arrayed-waveguide gratings [144], photodiodes [145, 146], and lasers [147–149] have already been realized, either directly on silicon or via heterogeneous integration, a frequency comb generator has not been available in the platform portfolio. The principle of electro-optic comb generation has a high potential to generate the carriers needed in WDM systems: The tunable line spacing allows easy adaption of carrier spacing in order to maximize spectral efficiency, the phase-noise properties of the lines are derived from the input CW laser, enabling generation of high-quality carriers, and electro-optic modulators are in principle available on the silicon platform. However, all-silicon modulators based on the plasma dispersion effect have a very limited applicability for electro-optic generation of broadband frequency combs. Either they have a very limited

bandwidth, or the efficiency of the phase modulation is too low to realize the high modulation depth needed for frequency comb generation. The alternative approach used in this work overcomes these limitations. Silicon slot waveguides are combined with organic materials [150–153], which are tailored to exhibit high electro-optic coefficients [89, 154–156]. With this so-called silicon-organic hybrid (SOH) approach, modulators exhibiting high bandwidth and highly efficient phase modulation with a small device footprint can be realized [86–88, 90, 91, 157, 158]. This opens up a path towards SOH electro-optic frequency comb generators, which are demonstrated in this thesis and employed in a WDM data transmission experiment achieving terabit/s data rates.

2 Fundamentals

This chapter summarizes the methodical and technical background for the remainder of the thesis in a condensed form.

2.1 Electro-magnetic waves

This section introduces the conventions for wave propagation used for the remainder of the thesis. Electro-magnetic waves are governed by the Maxwell equations, which are treated in more depth in standard textbooks [56, 159]. For a homogeneous, linear, nonmagnetic medium without charges or currents, the electric field vector $\mathbf{E}$ and the magnetic field vector $\mathbf{H}$ fulfill the standard wave equations,

$$\nabla^2\mathbf{E}(\mathbf{r},t) - \frac{\varepsilon_r}{c_0^2}\frac{\partial^2\mathbf{E}(\mathbf{r},t)}{\partial t^2} = 0, \qquad \nabla^2\mathbf{H}(\mathbf{r},t) - \frac{\varepsilon_r}{c_0^2}\frac{\partial^2\mathbf{H}(\mathbf{r},t)}{\partial t^2} = 0, \tag{2.1}$$

where ε_r denotes the relative electric permittivity, $c_0 = 299\,792\,458\,\mathrm{m\,s^{-1}}$ denotes the speed of light in vacuum, and the vector $\mathbf{r} = (x, y, z)^{\mathrm{T}}$ defines a point in three-dimensional space. Simple solutions of Eq. (2.1) are wave functions which are harmonic with respect to time. For a homogeneous medium, plane waves form a complete basis of solutions to Eq. (2.1). The fields of a plane wave solution can be written in complex notation with the analytical signal, or complex wave function, $\underline{\mathbf{E}}(\mathbf{r},t)$ and the complex electric field amplitudes $\hat{\underline{\mathbf{E}}}(\mathbf{r},\omega)$ and $\hat{\underline{\mathbf{E}}}_0$,

$$\mathbf{E}(\mathbf{r},t) = \Re\left\{\underline{\mathbf{E}}(\mathbf{r},t)\right\} = \Re\left\{\hat{\underline{\mathbf{E}}}(\mathbf{r},\omega)\,\mathrm{e}^{\mathrm{j}(\omega t)}\right\} = \Re\left\{\hat{\underline{\mathbf{E}}}_0\mathrm{e}^{\mathrm{j}(\omega t - \mathbf{k}\cdot\mathbf{r})}\right\}. \tag{2.2}$$

The time dependency of a phasor used to describe wave propagation is defined as $\mathrm{e}^{+\mathrm{j}\omega t}$ in accordance to the commonly used notation in electrical engineering.

The imaginary unit is denoted as j. The quantity ω is the angular frequency and related to the frequency f by $\omega = 2\pi f$, and the vector $\mathbf{k}$ is called wave vector. To fulfil the wave equation Eq. (2.1), $\mathbf{k}$ depends on ω via the dispersion relation

$$|\mathbf{k}|^2 = \frac{\omega^2}{c_0^2}\varepsilon_r. \tag{2.3}$$

With the refractive index n,

$$n = \sqrt{\varepsilon_r}, \tag{2.4}$$

and the wave vector in vacuum, $\mathbf{k}_0$, Eq. (2.3) can also be written as

$$|\mathbf{k}| = \frac{\omega}{c_0} n = |\mathbf{k}_0|\, n. \tag{2.5}$$

2.2 Optical distance measurement

Numerous methods for optical distance measurement have been reported in the scientific literature. A broad overview is given, e.g., in [160] and [113]. The sections below give a short summary of the methods relevant within the scope of this thesis: Phase-shift time-of-flight (TOF) distance measurement, frequency-modulated continuous-wave (FMCW) distance measurement, and synthetic-wavelength interferometry.

2.2.1 Phase-shift time-of-flight (TOF) distance measurement

Phase-shift time-of-flight (TOF) distance measurement relies on evaluating the phase difference between a sent and a received time-harmonic signal modulated onto an optical carrier. One commonly employed scheme is sinusoidal intensity modulation. The basic principle is illustrated in Fig. 2.1. A laser is intensity-modulated with a frequency f_{mod}. The modulated laser light is sent by the transmitter unit (TX) towards a target located at a distance z_{TOF}. A part of the backscattered light is collected by the receiver unit (RX) and detected with a photodiode. The intensity-modulated light generates an electrical signal with a frequency f_{mod}. The measured distance is calculated by evaluating the phase

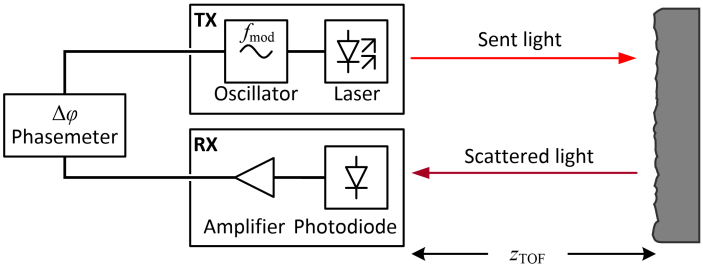

Fig. 2.1: Block diagram of a simple phase-shift TOF distance measurement scheme, comprising a transmitter (TX) and receiver (RX) unit. A laser is intensity-modulated with a frequency f_{mod}. The modulated light is sent towards a target located at a distance z_{TOF}. The backscattered signal is detected with a photodiode, and the phase difference $\Delta\varphi$ between sent and received light is calculated.

difference $\Delta\varphi$ between the received signal and the reference provided by the oscillator. With the time of flight τ_{TOF} of the signal, the phase difference $\Delta\varphi$ is given by

$$\Delta\varphi = 2\pi f_{mod}\tau_{TOF}. \tag{2.6}$$

As the time of flight τ_{TOF} includes the propagation back and forth between the TX/RX unit and the target, the distance z_{TOF} is given by

$$z_{TOF} = \frac{1}{2}c\tau_{TOF} = \frac{c\Delta\varphi}{4\pi f_{mod}}, \tag{2.7}$$

where c is the speed of light. Considering that the phase is only defined in a $[0, 2\pi]$ range, the range where measurements can be made unambiguously, i.e., the so-called unambiguity range Δz_{ua}, amounts to

$$\Delta z_{ua} = \frac{1}{2}\frac{c}{f_{mod}}. \tag{2.8}$$

Thus, the choice of a small modulation frequency f_{mod} would yield a large unambiguity range. However, for a given phase measurement accuracy, the accuracy of the distance measurement increases for larger modulation frequencies. This is due to the linear relationship in Eq. (2.7): Uncertainties of the measured phase value have a linear dependency to uncertainties of the distance value with f_{mod} in the denominator of the proportionality factor. While the

trade-off between unambiguity range and accuracy can be overcome by using multiple modulation frequencies at the same time, achieving an overall high measurement accuracy remains challenging in practice with this method. This is caused by the fact that the bandwidth of the photodetector and of the associated electronics needs to be at least as high as the highest utilized modulation frequency. In practice, frequencies as high as 40 GHz were needed to demonstrate sub-micrometer accuracy, requiring expensive high-frequency detectors and electronics [115].

2.2.2 Frequency-modulated continuous-wave (FMCW) distance measurement

Frequency-modulated continuous-wave (FMCW) distance measurement relies on detecting a frequency difference between sent and received light from a periodically frequency-shifted laser. In practice, this method can be realized by a saw-tooth frequency sweep, where the frequency of a laser is periodically shifted by Δf_{sweep} as shown in Fig. 2.2. The measured intermediate frequency f_{if} corresponds to the frequency difference between a reference signal and the signal which propagated forth and back to a target located at a distance z_{FMCW} before being received, with a round-trip propagation time of $\tau_{\text{FMCW}} = 2z_{\text{FMCW}}/c$. With the frequency sweep period t_{sweep}, the intermediate frequency is given as

$$f_{\text{if}} = \frac{\Delta f_{\text{sweep}}}{t_{\text{sweep}}} \tau_{\text{FMCW}} = \frac{2\Delta f_{\text{sweep}} z_{\text{FMCW}}}{c t_{\text{sweep}}}. \tag{2.9}$$

Rearranging Eq. (2.9) yields the target distance z_{FMCW}:

$$z_{\text{FMCW}} = \frac{c}{2} \frac{t_{\text{sweep}}}{\Delta f_{\text{sweep}}} f_{\text{if}}. \tag{2.10}$$

For a given measurement accuracy of f_{if}, the uncertainty of the distance measurement scales with the factor $t_{\text{sweep}}/\Delta f_{\text{sweep}}$. Since in principle this factor can be chosen arbitrarily, high distance resolution in the micrometer regime can be realized without the need for high-speed electronics [133]. However, the method relies on a precisely defined linear frequency sweep, as deviations from an ideal linear sweep manifest themselves in variation of the intermediate frequency f_{if}. A precise linear sweep of the optical frequency of a laser is not

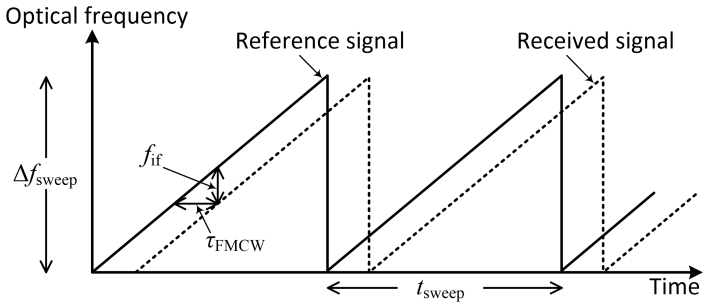

Fig. 2.2: Optical frequency versus time for a saw-tooth frequency sweep. The frequency difference f_{if} between a reference signal and a signal received back from a target is evaluated to measure the round-trip delay time τ_{FMCW} in a FMCW distance measurement system.

straightforward to implement in practice. Various schemes to linearize the optical frequency sweep exist, but they all involve added complexity, experimental effort, and increased hardware costs [101, 133, 133].

2.2.3 Synthetic-wavelength interferometry

In optical interferometry, the phase difference between the fields in a reference arm and a target arm can be evaluated. Using a monochromatic laser as a light source, this approach provides a high distance resolution of a fraction of the wavelength $\lambda = 2\pi/|\mathbf{k}|$. However, the range which can be measured unambiguously is limited to $\lambda/2$ due to the 2π-periodicity of the phase. This allows measurements of small displacements, but no absolute distance measurements. Also, the laser wavelength has to be known with very high precision, as it is utilized as a ruler against which the distance is measured. This represents considerable technical effort – commercially available laser sources used for interferometric displacement measurements are equipped with actively controlled cavity lengths [161]. However, for many practical applications absolute distance measurements in a millimeter to meter range are necessary, and nanometer resolution is not required. This measurement tasks can be solved with so-called synthetic-wavelength interferometry. In this section, its general principle is described.

In synthetic-wavelength interferometry, multiple wavelengths λ_m with $m = 1 \ldots N, \quad N \geq 2$ are used for distance measurement instead of just a single one,

$$\lambda_m = 2\pi / |\mathbf{k}_m| \,. \tag{2.11}$$

The electrical field of the propagating light is approximated as a number of plane waves, propagation parallel to the z-axis is assumed, $|\mathbf{k}_m| = k_{z,m} = n\omega_m / c_0$, and n is assumed to be a constant over the limited frequency range of interest. Using Eq. (2.2), the complex wave function after a back-and-forth propagation over a distance z can be written as

$$\underline{\mathbf{E}}\,(\mathbf{r}, t) = \sum_m \underline{\hat{\mathbf{E}}}_m \exp\left[\mathrm{j}\left(\omega_m t - n\frac{\omega_m}{c_0} \cdot 2z\right)\right]. \tag{2.12}$$

The phases φ_m of the propagators $\exp(-\mathrm{j}n2z\omega_m/c_0)$ in Eq. (2.12) are proportional to the angular frequency ω_m, and the path length $2z$ is contained in the proportionality factor

$$\varphi_m = -\frac{2zn}{c_0}\omega_m. \tag{2.13}$$

The angular frequencies can be expressed with their frequency differences $\Delta\omega_m$ relative to ω_1,

$$\omega_m = \omega_1 + \Delta\omega_m. \tag{2.14}$$

Inserting Eq. (2.14) in Eq. (2.13) results in

$$\varphi_m = -\frac{2zn}{c_0}\Delta\omega_m - \frac{2zn}{c_0}\omega_1. \tag{2.15}$$

Thus, when φ_m and $\Delta\omega_m$ can be accurately determined, the path length $2z$ can be evaluated from the slope of the linear relationship $\varphi_m(\Delta\omega_m)$ without knowing the absolute optical frequencies. Optical frequency combs can be used to provide an accurate determination of $\Delta\omega_m$. In this sense, optical frequency combs can be utilized as rulers in the frequency domain. In this thesis, two ways are demonstrated how this property can be combined advantageously with synthetic-wavelength interferometry. Multiple tones provided by an optical frequency comb are used directly for distance measurement in Chapter 3. In Chapter 5, optical frequency combs are used to calibrate the relative frequency differences between four free-running lasers used for synthetic-wavelength interferometry.

A widespread expression for the synthetic wavelength Λ formed by two optical wavelengths [137,162,163] can be obtained by setting $N = 2$, thus considering only one pair for optical frequencies, which, without loss of generality, we denote as ω_1 and ω_2 in the following. The synthetic wavelength Λ is defined as

$$\Lambda = \frac{2\pi c}{\omega_2 - \omega_1} = \frac{\lambda_1 \lambda_2}{\lambda_1 - \lambda_2}. \tag{2.16}$$

Using this expression in Eq. (2.15), the phase difference $\varphi_2 - \varphi_1$ can be expressed as

$$\varphi_2 - \varphi_1 = -2zn\frac{2\pi}{\Lambda}. \tag{2.17}$$

Eq. (2.17) shows the relation to classical interferometry with a single optical wavelength λ, where the phase φ of the propagator after propagation over the optical path length $2zn$ is given as $\varphi = -2zn\frac{2\pi}{\lambda}$.

The unambiguity range can also be determined by using Eq. (2.17). The maximum phase difference $\varphi_2 - \varphi_1$ which can be uniquely measured is 2π. Therefore, the maximum optical path length $2z_{\mathrm{ua}}n$ that can be measured unambiguously is

$$2z_{\mathrm{ua}}n = \Lambda = \frac{2\pi c}{\omega_2 - \omega_1}. \tag{2.18}$$

Synthetic-wavelength interferometry greatly enhances the range, in which unambiguous measurements are possible. At the same time, the measurement accuracy is reduced, as $\Lambda \gg \lambda$. However, this reduction of accuracy can partly be compensated by using multiple synthetic wavelengths generated by multiple optical lines with frequencies ω_m, spanning a broad spectral range. A linear regression to the relationship Eq. (2.15) then allows to determine the optical pathlength. Thus, accurate measurements with a relatively large unambiguity range can be obtained.

2.3 Linear electro-optic effect

The linear electro-optic effect is exploited to realize the modulator-based comb generation technique used in this thesis. This section summarizes the technical background in a condensed form, while more details can be found, e.g., in [56, 164]. The complex time-domain amplitude of the electric displacement

$\underline{\hat{\mathbf{D}}}(\mathbf{r},\omega)$ in a linear anisotropic medium is linked to the complex time-domain amplitude of the electric field $\underline{\hat{\mathbf{E}}}(\mathbf{r},\omega)$ by the linear permeability tensor $\underline{\boldsymbol{\epsilon}}_r$,

$$\underline{\hat{\mathbf{D}}}(\mathbf{r},\omega) = \epsilon_0 \underline{\boldsymbol{\epsilon}}_r \underline{\hat{\mathbf{E}}}(\mathbf{r},\omega), \tag{2.19}$$

where $\epsilon_0 = 8.85412 \times 10^{-12}\,\mathrm{A\,s/(V\,m)}$ denotes the vacuum permittivity. It is also possible to consider the so-called dielectric impermeability tensor $\underline{\boldsymbol{\eta}} = \underline{\boldsymbol{\epsilon}}_r^{-}1$,

$$\underline{\hat{\mathbf{E}}} = \frac{1}{\epsilon_0}\underline{\boldsymbol{\eta}}\,\underline{\hat{\mathbf{D}}}. \tag{2.20}$$

The optical properties of an anisotropic medium can be described by the so-called index ellipsoid, which can be expressed as

$$\sum_{i,j} \eta_{ij} X_i X_j = 1 \tag{2.21}$$

with $i, j \in 1, 2, 3$ and X_1, X_2, and X_3 denoting the directions x, y, and z of a coordinate system. If the medium is lossless and optically inactive, all elements of the impermeability tensor $\underline{\boldsymbol{\eta}}$ are real and symmetric, $\eta_{ij} = \eta_{ji}$. In the case of electro-optic materials, the index ellipsoid can be changed via a nonlinear interaction by applying a static or low-frequency electric field $\mathbf{E}(t)$, and can be written in a general form as

$$\begin{aligned}&\left(\frac{1}{n^2}\right)_1 X_1^2 + \left(\frac{1}{n^2}\right)_2 X_2^2 + \left(\frac{1}{n^2}\right)_3 X_3^2 \\ &+ 2\left(\frac{1}{n^2}\right)_4 X_2 X_3 + 2\left(\frac{1}{n^2}\right)_5 X_1 X_3 + 2\left(\frac{1}{n^2}\right)_6 X_1 X_2 = 1,\end{aligned} \tag{2.22}$$

where the elements of $\boldsymbol{\eta}$ are denoted as $\eta_{ij} = \left(1/n^2\right)_h$ with the convention

$$\begin{array}{cccccccc} ij & 11 & 22 & 33 & 23,\,32 & 13,\,31 & 12,\,21 \\ h & 1 & 2 & 3 & 4 & 5 & 6 \end{array}. \tag{2.23}$$

To describe the impermeability tensor as a function of the applied electric field, the elements η_{ij} can be expressed by an expansion in terms of the modulating low-frequency electric field components $E_k(t)$,

$$\eta_{ij} = \eta_{ij}^{(0)} + \sum_k r_{ijk} E_k + \sum_{k,l} s_{ijkl} E_k E_l + \ldots \tag{2.24}$$

with the tensor r_{ijk} as the coefficient of the linear electro-optic effect (Pockels effect), and s_{ijkl} as the coefficient of the so-called quadratic electro-optic effect.

As the components η_{ij} are real and symmetric for lossless media, the electro-optic tensor r_{ijk} is also symmetric in its indizes i and j. The number of coefficients is thus reduced, and r_{ijk} can be expressed as a matrix r_{hk} with 18 coefficients using the same contracted notation as defined in Eq. (2.23). Neglecting the second- and higher order terms in Eq. (2.24), the field-induced change $\Delta\left(1/n^2\right)_h = \eta_{ij} - \eta_{ij}^{(0)}$ of the impermeability tensor elements is given as

$$\begin{pmatrix} \Delta\left(1/n^2\right)_1 \\ \Delta\left(1/n^2\right)_2 \\ \Delta\left(1/n^2\right)_3 \\ \Delta\left(1/n^2\right)_4 \\ \Delta\left(1/n^2\right)_5 \\ \Delta\left(1/n^2\right)_6 \end{pmatrix} = \begin{pmatrix} r_{11} & r_{12} & r_{13} \\ r_{21} & r_{22} & r_{23} \\ r_{31} & r_{32} & r_{33} \\ r_{41} & r_{42} & r_{43} \\ r_{51} & r_{52} & r_{53} \\ r_{61} & r_{62} & r_{63} \end{pmatrix} \begin{pmatrix} E_1 \\ E_2 \\ E_3 \end{pmatrix}. \tag{2.25}$$

When the coordinate system is chosen such that X_1, X_2, and X_3 represent the principal axes of the material, the index ellipsoid in the absence of an electric field is simplified to

$$\frac{X_1^2}{n_x^2} + \frac{X_2^2}{n_y^2} + \frac{X_3^2}{n_z^2} = 1, \tag{2.26}$$

with the principal indices of refraction n_x, n_y, and n_z. Applying an electric field and only considering the terms concerned with the linear electro-optic effect, the index ellipsoid is then expressed as

$$\left(\frac{1}{n_x^2}+\sum_k r_{1k}E_k\right)X_1^2+\left(\frac{1}{n_y^2}+\sum_k r_{2k}E_k\right)X_2^2+\left(\frac{1}{n_z^2}+\sum_k r_{3k}E_k\right)X_3^2$$
$$+2\left(\sum_k r_{4k}E_k\right)X_2X_3+2\left(\sum_k r_{5k}E_k\right)X_1X_3+2\left(\sum_k r_{6k}E_k\right)X_1X_2=1, \tag{2.27}$$

where E_k are electric field components along the principal axes. The form of the electro-optic tensor r_{hk} is restricted by material symmetry, which is treated in detail, e.g. in [165] or [164]. As an example, the point group 3m is considered, as, e.g., lithium niobate ($LiNbO_3$), a commonly used material for electro-optic modulators, belongs to this group. The electro-optic tensor for such a material is given as

$$\mathbf{r}=\begin{pmatrix}0 & -r_{22} & r_{13}\\ 0 & r_{22} & r_{13}\\ 0 & 0 & r_{33}\\ 0 & r_{42} & 0\\ r_{42} & 0 & 0\\ -r_{22} & 0 & 0\end{pmatrix}. \tag{2.28}$$

In many practical cases, one wants to avoid coupling of the modulation between different polarization components, and one component of $\mathbf{r}$ dominates (e.g., r_{33}). Thus, the input fields are typically polarized accordingly. With the electro-optic tensor described in Eq. (2.28) and a modulating field $E_{\mathrm{mod}}=(0\ 0\ E_3)^{\mathsf{T}}$, the index ellipsoid becomes

$$\left(\frac{1}{n_x^2}+r_{13}E_3\right)X_1^2+\left(\frac{1}{n_y^2}+r_{13}E_3\right)X_2^2+\left(\frac{1}{n_z^2}+r_{33}E_3\right)X_3^2=1. \tag{2.29}$$

An optical mode with its electric field oriented along the X_3-direction will be influenced by the new principal index $n_{z'}$,

$$\frac{1}{n_{z'}^2} = \frac{1}{n_z^2} + r_{33}E_3. \tag{2.30}$$

Rearranging $\mathrm{d}(n_z^{-2})/\mathrm{d}n_z = -2n_z^{-3}$ one obtains $\mathrm{d}n_z = -\frac{1}{2}n_z^3\mathrm{d}(1/n_z^2)$. With the assumption that $r_{33}E_3 \ll n_z^{-2}$, we have $\mathrm{d}n_z = n_{z'} - n_z$ and $\mathrm{d}(1/n_z^2) = ((1/n_{z'}^2) - (1/n_z^2)) = r_{33}E_3$. Now the induced change Δn of the refractive index is given as

$$n_{z'} - n_z = \Delta n = -\frac{1}{2}n_z^3 r_{33}E_3. \tag{2.31}$$

The relation between the electro-optic coefficient r_{hk} and the second-order susceptibility $\chi_{hk}^{(2)}$ is given by [166, 167]:

$$r_{hk} = -\frac{2\chi_{hk}^{(2)}}{n^4}. \tag{2.32}$$

2.4 Optical frequency comb generation by electro-optic modulation

The electro-optically induced change of the refractive index introduced in the previous section can be utilized to manipulate the phase of the light propagating through the medium. This section describes the use of periodic phase modulation for generation of optical frequency combs from monochromatic light.

2.4.1 Phase modulation of monochromatic light

This section describes frequency comb generation by sinusoidal phase modulation of monochromatic light from a CW laser. Phase-only modulation can be realized in electro-optic modulators exploiting the linear electro-optic effect (Pockels effect). Applying an external electric field $E_{\mathrm{mod}}(t)$ to crystals without inversion symmetry such as lithium niobate or certain noncentrosymmetric

polymer materials leads to a change in refractive index seen by a certain component of the optical field, see Section 2.3. Assuming two plates of a capacitor charged with a voltage $U_{\mathrm{mod}}(t)$ and placed on both sides of the electro-optic material with a spacing d, $E_{\mathrm{mod}}(t)$ can be approximated as $E_{\mathrm{mod}}(t) = U_{\mathrm{mod}}(t)/d$. The change in the optical phase $\Delta\varphi$ of light with a free-space wavenumber $k_0 = |\mathbf{k}_0|$ propagating through a length L of such a medium with a linear electro-optic coefficient r_{33} and a refractive index n, assuming that both input light and electric field are polarized along axis 3, is then given as:

$$\Delta\varphi(t) = \frac{1}{2} n^3 r_{33} \frac{U_{\mathrm{mod}}(t)}{d} k_0 L. \tag{2.33}$$

The voltage needed for a phase shift of π is denoted by U_π,

$$U_\pi = \frac{2\pi d}{n^3 r_{33} k_0 L}. \tag{2.34}$$

With this device-specific parameter for a given wavenumber, Eq. (2.33) can be simplified to

$$\Delta\varphi(t) = \frac{U_{\mathrm{mod}}(t)}{U_\pi}\pi. \tag{2.35}$$

The incident monochromatic light has an angular frequency $\omega_0 = c_0 k_0$. Its time-domain electric field is described by the analytical signal $\underline{E}_{\mathrm{in}}(\mathrm{t})$, with the real part of the analytical signal representing the physically relevant field, $E_{\mathrm{in}}(\mathrm{t}) = \Re\left\{\underline{E}_{\mathrm{in}}(\mathrm{t})\right\}$,

$$\underline{E}_{\mathrm{in}}(t) = \hat{\underline{E}}_0 \exp(\mathrm{j}\omega_0 t). \tag{2.36}$$

A sinusoidal driving signal $U_{\mathrm{mod}}(t) = \hat{U}_{\mathrm{mod}} \sin(\omega_{\mathrm{mod}} t)$ is applied for phase modulation, and the output electric field can be described as

$$\underline{E}_{\mathrm{out}}(t) = \hat{\underline{E}}_0 \exp(\mathrm{j}\omega_0 t) \exp\left(\mathrm{j}\pi \frac{\hat{U}_{\mathrm{mod}}}{U_\pi} \sin(\omega_{\mathrm{mod}} t)\right), \tag{2.37}$$

omitting terms with constant phase due to the spatial propagation.

With the Jacobi-Anger expansion [168] using the Bessel functions of the first kind $\mathrm{J}_m(a)$,

$$\mathrm{e}^{\mathrm{j}a\sin(\theta)} = \sum_{m=-\infty}^{\infty} \mathrm{e}^{\mathrm{j}m\theta} \mathrm{J}_m(a), \tag{2.38}$$

Eq. (2.37) can be expressed as

$$\underline{E}_{\mathrm{out}}(t) = \hat{\underline{E}}_0 \exp(\mathrm{j}\omega_0 t) \sum_{m=-\infty}^{\infty} \exp(\mathrm{j}m\omega_{\mathrm{mod}} t)\, \mathrm{J}_m\left(\pi \frac{\hat{U}_{\mathrm{mod}}}{U_\pi}\right). \tag{2.39}$$

Introducing the modulation depth $A = \pi\hat{U}_{\mathrm{mod}}/U_\pi$, and neglecting a constant phase term, the real output electric field E_{out}(t) is given by:

$$E_{\mathrm{out}}(t) = |\hat{\underline{E}}_0| \sum_{m=-\infty}^{\infty} \mathrm{J}_m(A) \cos((\omega_0 + m\omega_{\mathrm{mod}})\, t). \tag{2.40}$$

The Fourier transform of Eq. (2.40), as defined in Eq. (A.1), reads

$$\begin{aligned} \tilde{E}_{\mathrm{out}}(\omega) &= \int_{-\infty}^{\infty} E_{\mathrm{out}}(t)\, \mathrm{e}^{-\mathrm{j}\omega t}\, \mathrm{d}t \\ &= \pi|\hat{\underline{E}}_0| \sum_{m=-\infty}^{\infty} \mathrm{J}_m(A) \left[\delta(\omega - (\omega_0 + m\omega_{\mathrm{mod}})) \right. \\ &\qquad \left. + \delta(\omega + (\omega_0 + m\omega_{\mathrm{mod}}))\right], \end{aligned} \tag{2.41}$$

where $\delta(\omega)$ denotes the Dirac delta function. The name "frequency comb" becomes evident from Eq. (2.41): The spectrum comprises discrete lines with equidistant spacing of ω_{mod} around a center frequency ω_0. However, the magnitude of the comb lines is governed by the Bessel functions J_m, yielding a non-flat spectral envelope. As spectrally flat combs are beneficial for many applications, a single sinusoidal phase modulation is not sufficient, and more complicated modulation schemes are needed, see Section 2.4.2.

2.4.2 Generation of flat optical frequency combs with Mach-Zehnder modulators

In principle, monochromatic input light can be transformed into an optical frequency comb by using a sinusoidal phase modulation with a single frequency as described in Section 2.4.1. However, to generate spectrally flat frequency combs more elaborated setups are needed. Several methods have been proposed in the literature, making use of specific arrangements of modulators

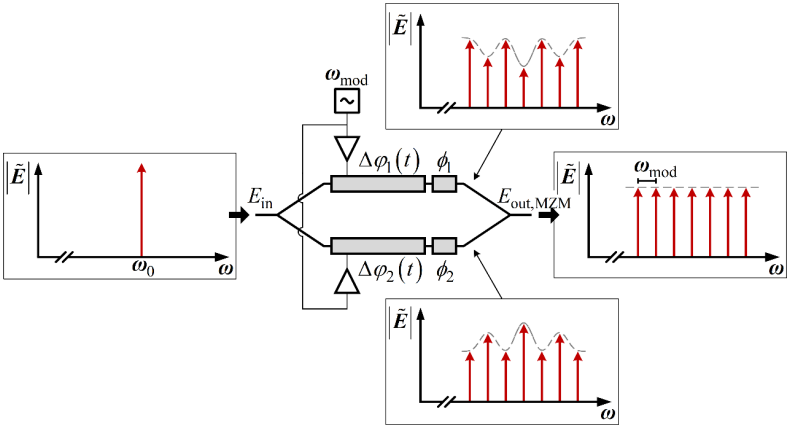

Fig. 2.3: Schematic of a Mach-Zehnder modulator used for generation of spectrally flat frequency combs. Insets depict optical spectra at the indicated positions in the setup. Input light is split and fed into two phase modulators, each generating a non-flat comb, with comb line magnitudes governed by the Bessel functions. The modulation depths and the constant optical phase shifts ϕ_1 and ϕ_2 are chosen such, that the superposition of the light from both arms at the output of the MZM yields a flat frequency comb.

and/or specific modulation waveforms. The method of choice for this thesis and a short overview of related work is presented in the following paragraphs.

A relatively simple way to introduce more degrees of freedom for electro-optic frequency comb generation is the arrangement of two phase modulators in a Mach-Zehnder configuration, forming a Mach-Zehnder modulator (MZM). The setup is sketched in Fig. 2.3: Input light is split into two arms, each containing a phase modulator. In each arm the phase modulation depth is chosen individually, and the modulated light from both arms is superimposed at the output. By a proper choice of the modulation depth and the constant optical phase offset in each of the arms, a spectrally flat frequency comb can be generated. The necessary conditions for a flat comb have been theoretically derived in [134] with an experimental demonstration in [83] and are summarized in the following paragraphs.

The phase modulation $\Delta\varphi_i(t)$ in each arm i of the MZM is described as

$$\Delta\varphi_1(t) = A_1 \sin(\omega_{\mathrm{mod}} t), \qquad \Delta\varphi_2(t) = A_2 \sin(\omega_{\mathrm{mod}} t). \tag{2.42}$$

With Eq. (2.39) and considering the constant optical phase shifts ϕ_i in the two arms, the optical field at the output of the MZM is given by

$$\begin{aligned}\underline{E}_{\text{out,MZM}}(t) = \frac{1}{2}\underline{E}_{\text{in}}(t) \sum_{m=-\infty}^{\infty} &\left[\mathrm{J}_m(A_1)\exp\left(\mathrm{j}\left(m\omega_{\text{mod}}t + \phi_1\right)\right)\right. \\ &\left.+\mathrm{J}_m(A_2)\exp\left(\mathrm{j}\left(m\omega_{\text{mod}}t + \phi_2\right)\right)\right].\end{aligned} \tag{2.43}$$

For large modulation depths A_i and low orders $|m|$, the Bessel functions can be approximated [169], yielding the following expression:

$$\mathrm{J}_m(A_i) \approx \sqrt{\frac{2}{\pi}} A_i^{-\frac{1}{2}} \cos\left(A_i - \frac{(2m+1)\pi}{4}\right). \tag{2.44}$$

Using Eq. (2.44), the power conversion efficiency η_m from input light $\underline{E}_{\text{in}}$ to the mth comb line $\underline{E}_{\text{out},m}$ can be approximated as [134]

$$\begin{aligned}\eta_m &= \frac{\left|\underline{E}_{\text{out},m}\right|^2}{\left|\underline{E}_{\text{in}}\right|^2} \\ &\approx \frac{1}{2\pi\overline{A}}\left[1 + \cos(2\Delta\phi)\cos(2\Delta A)\right. \\ &\left.+ \left\{\cos(2\Delta\phi) + \cos(2\Delta A)\right\}\cos\left(2\overline{A} - \frac{(2m+1)\pi}{2}\right)\right], \\ \overline{A} &= (A_1 + A_2)/2, \quad \Delta A = (A_1 - A_2)/2, \quad \Delta\phi = (\phi_1 - \phi_2)/2.\end{aligned} \tag{2.45}$$

A flat comb is generated, if the power conversion efficiency described in Eq. (2.45) becomes independent of m. This requirement is met for the condition

$$\Delta A \pm \Delta\phi = \frac{\pi}{2}, \tag{2.46}$$

setting the curly brackets in Eq. (2.45) to zero. Substituting Eq. (2.46) in Eq. (2.45) results in

$$\eta_m = \frac{1 - \cos(4\Delta\phi)}{4\pi\overline{A}}, \tag{2.47}$$

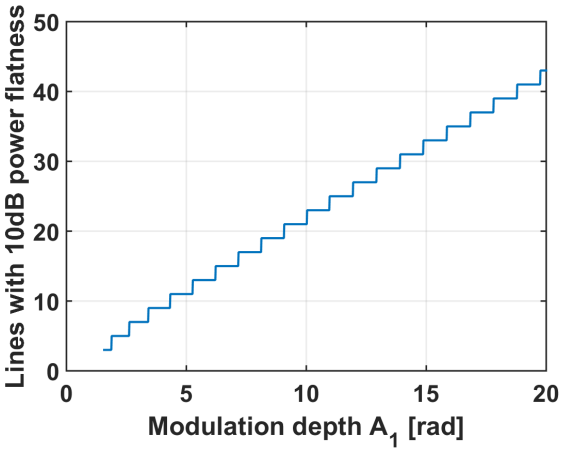

Fig. 2.4: Numerically calculated number of generated comb lines with a maximum difference in power of 10 dB between the weakest line and the strongest line vs. modulation depth A_1, using the driving conditions according to Eq. (2.48). The comb bandwidth can be calculated by multiplying the number of lines with the modulation frequency ω_{mod}, which defines the line spacing. A high modulation depth is essential for generating broadband frequency combs.

yielding a maximum conversion of input light into a flat frequency comb when the condition

$$\Delta A = \Delta\phi = \frac{\pi}{4} \tag{2.48}$$

is fulfilled.

Evaluating Eq. (2.43) numerically with the condition derived above, Eq. (2.48), yields insight into the requirements for the modulation depth. The number of consecutive comb lines with a maximum difference in power of 10 dB between the weakest line and the strongest line is calculated for varying modulation depths A_1. The result is plotted in Fig. 2.4. Due to the characteristics of the Bessel functions, a high modulation depth is needed for generating combs with many lines. The bandwidth of the comb can directly be calculated by multiplying the number of lines with the modulation frequency ω_{mod}, which defines the line spacing, see Eq. (2.41). Thus, electro-optic generation of broadband frequency combs requires both high modulation depth and high modulation frequency.

2.4.3 State of the art in electro-optic comb generation

Using the approach described in Section 2.4.2, a frequency comb with a line spacing of 10 GHz and 11 lines with a power flatness of 1.1 dB has been generated with a conventional lithium niobate MZM [83]. Another application of this approach is demonstrated in this thesis, using a silicon-organic hybrid (SOH) MZM integrated on a silicon-on-insulator (SOI) chip to generate a frequency comb with 40 GHz line spacing and 7 lines with a power flatness of 2 dB, see Section 6.

Other related approaches in literature use different setups to generate optical frequency combs (OFC) electro-optically:

In [80], dual-parallel MZM (a so-called IQ modulator) are used to generate 9 comb lines with 10 GHz line spacing and a power flatness of 2 dB. Also using dual-parallel MZM, in [170] several combs with line spacings from 10 GHz to 60 GHz are demonstrated, while the number of generated comb lines ranges from 7 to 2. Another approach with dual-parallel MZM is presented in [171], demonstrating generation of a FC exhibiting 7 comb lines with 1 dB power flatness at a line spacing of 25 GHz.

Cascading several modulators is another approach to generate broadband combs. By cascading two intensity modulators and a phase modulator, and by driving them with tailored waveforms, the generation of 38 comb lines with a line spacing of 25 GHz and 1 dB power flatness is demonstrated [84]. Another work uses an intensity modulator followed by two phase modulators [172]. With this setup, the authors realize 29 comb lines spaced by 10 GHz with a power flatness of 1.5 dB. Using tailored, multi-harmonic electrical driving signals and 3 cascaded MZM, in [173] the generation of 36 comb lines spaced by 10 GHz with a power flatness of 1.1 dB was demonstrated.

While some of these approaches demonstrate flatter and more broadband combs than it would be achievable with a simple MZM, they do so at the cost of more complicated setups with higher hardware effort. For many applications however, the practicability of the approach is enhanced by the use of simpler setups with less (costly) hardware. This is especially true for cases, where two frequency combs with different comb spacings are desired, effectively doubling the hardware expenses for comb generation. Thus, this thesis makes use of relatively simple comb generators with a single RF oscillator and a

MZM, providing a good trade-off between comb generation performance and technical simplicity.

3 Distance measurements for surface digitization using electro-optic frequency combs

This chapter describes a fiber-based system for distance measurements with electro-optic frequency combs. A summary of the state of the art is given in Section 3.1, and a detailed explanation of the measurement principle along with a description of the experimental setup and a discussion of the measurement results can be found in Section 3.2. Results from an application demonstration are shown, where a fiber-based sensor head mounted to a coordinate measuring machine was used to accurately digitize the surface geometry of technical objects.

3.1 State of the art in comb-based distance measurements

This section provides a summary of the state of the art in distance measurement with optical frequency combs. The approaches can be divided into three categories, according to the basic measurement scheme:

- Time-of-flight (TOF) measurements using beat signals generated by direct detection of a single frequency comb [35, 121, 127]
- Evaluation of interference patterns formed by a single frequency comb in a Michelson interferometer [117, 119, 126, 174, 175]
- Dual-comb schemes using a pair of frequency combs with slightly detuned line spacings for simultaneous heterodyne detection of many comb lines (multi-heterodyne detection) [34, 37, 116, 118, 176].

Additionally, some demonstrations combine two or more measurement schemes, e.g., to enhance the unambiguous measurement range or to increase the measurement precision [34, 119, 175]. An overview of experimentally realized precision and the corresponding acquisition times for FC-based distance measurements is compiled in Fig. 3.8.

3.1.1 TOF measurements using beat signals generated by direct detection of a single FC as modulation

Direct detection of a frequency comb on a photodiode exhibits the beat signals between the various comb lines. These inter-mode beat signals have frequencies corresponding to integer multiples of the comb line spacing and thus form a radio-frequency (RF) comb spectrum. All publications considered in this category measure and evaluate the phase shifts of one or several inter-mode beat signals to obtain a distance measurement. Typically, signals with frequencies ranging from tens of megahertz to several tens of gigahertz are evaluated. The former provide a long unambiguity range, while the latter provide high precision due to their small associated synthetic wavelengths. The broadband nature of a typical frequency comb would allow for frequencies in the terahertz regime, but the highest evaluated frequency is eventually dictated by the bandwidth of the photodiodes and the subsequent electronic circuits.

The first use of optical frequency combs for distance measurements was demonstrated in [35]. A femtosecond mode-locked laser was used to generate a comb with a line spacing of around 50 MHz, and the phase shifts of the 1^{st} and the 19^{th} harmonic (945.3 MHz) of the fundamental beat signal were evaluated to measure the distance, leading to measurements with a standard deviation of 50 µm for an measurement time of 10 ms. To increase the precision, subsequent experiments using higher frequencies were conducted. In [127], inter-mode beats with frequencies of 3.5 GHz and 10 GHz were used, leading to measurements with a standard deviation of 1.6 µm with 10 s measurement time. Using a frequency comb with 100 MHz line spacing, in [121] inter-mode beat frequencies of 100 MHz and 11.4 GHz are exploited, yielding a standard deviation of 9.5 µm for total measurement times of 6 s, including the time needed for calibration measurements to compensate for temperature-induced drift of the measured distance using a fixed reference distance and mechanical shutters.

Directly using inter-mode beats of a single frequency comb for TOF ranging is hence a viable approach as demonstrated by previous experiments. The broad optical bandwidth provided by frequency combs allows for higher precisions by using higher beat frequencies. However, this comes at the price of a need for high-frequency photodiodes and electronics, limiting the scalability to the bandwidth ranges addressable by electronic components, i.e., several tens of gigahertz.

3.1.2 Interference patterns in Michelson interferometers

Another approach to measure an optical path length is the evaluation of interference patterns in Michelson interferometers. To this end, a frequency comb is split, e.g., by a semi-transparent mirror. One part propagates to a reference mirror, the other part to the measurement mirror. After reflection, both parts are superimposed on a detector to form an interference pattern. Spectrally-resolved evaluation of the pattern is achieved by either including a dispersive element at the detector or by scanning the optical path length to the reference mirror and applying a Fourier transform to the recorded pattern [117, 175].

In [117], a mode-locked Ti-Sapphire laser generating a frequency comb with a line spacing of 1 GHz is used. The interferogram formed by the Michelson interferometer is spectrally resolved using a diffraction grating. The intensity as a function of optical frequency hence exhibits a periodic modulation that depends on the path length difference between reference and measurement path. As the interference pattern can only form when the pulses overlap in space, this scheme can only measure displacements around optical path length differences corresponding to multiples of the pulse-to-pulse distance. When the overlap between pulses reflected from the reference and pulses reflected from the measurement detector gets smaller, the modulation depth of the interferogram diminishes. A standard deviation of 1 µm is demonstrated when measuring displacement around multiples of the pulse-to-pulse distance.

In [174], a different approach is used. The frequency comb is generated electro-optically from a CW laser using a Mach-Zehnder modulator (MZM). The MZM is driven by a direct digital synthesizer (DDS) with a linear frequency ramp, generating a comb with a line spacing swept between 14.0 GHz and 14.5 GHz. In the time domain, this frequency sweep leads to varying pulse-

pulse distances. Thus, every time the optical path length difference in the Michelson interferometer is an integer multiple of the instantaneous pulse-pulse distance, an interferogram is observed. The distance can be calculated from the known frequency sweep. Measurements with a standard deviation of 10 µm and a measurement time of 0.1 s are obtained.

In [175], a femtosecond mode-locked laser with 100 MHz repetition rate is used. The Michelson interferometer contains a mechanically scanned reference mirror, referenced to a fringe-counting interferometer. Interference fringes formed by superimposed pulses of the mode-locked laser are detected for different positions of the reference delays. The fringe patterns are evaluated using a Fourier transformation. A spatial resolution of only 21 cm is realized (no standard deviation for repeated measurements is stated), but also an extension of the unambiguity range to 190.5 m is demonstrated. The unambiguity range is extended by combining the spectrally resolved interferometry with a TOF ranging based on modulation with a pseudo-random binary sequence (PRBS).

A displacement measurement method is demonstrated in [126]. A mode-locked laser with adjustable repetition rate is used, generating combs with 100 MHz ± 200 kHz line spacing. The pulses reflected from the reference mirror and the measurement mirror are overlapped in a nonlinear crystal (periodically poled $KTiOPO_4$, short PPKTP), generating a second-harmonic signal when the relative time delay is zero. This signal is used for a feedback loop, which adjusts the line spacing of the comb accordingly, when the measurement mirror is displaced. The displacement can be calculated from the current line spacing. A standard deviation of 117 nm for a measurement time of 5 ms is obtained.

In [119], a femtosecond frequency comb with a line spacing of 1 GHz, stabilized to a cesium atomic clock is used as an optical source. The output of a Michelson interferometer is spectrally resolved by a spectrometer, that is able to separate individual comb tones. To uniquely identify the different comb tones, high-precision calibration of the spectrometer is needed. This is accomplished by an optical parametric oscillator in conjunction with a wavelength meter, which are used to calibrate the spectrometer. The absolute comb line frequency is used to refine the measurement. The coarse measurement is obtained from the slope of the phase as function of the optical frequency, the fine measurement is obtained by evaluating the phases at single optical fre-

quencies. The substantial experimental effort finally allows for measurements with a 28 nm standard deviation for a 100 ms acquisition time.

Note that evaluation of interference patterns formed by a frequency comb in a Michelson interferometer does not require any high-frequency electronics. However, the pulses reflected by the reference mirror and the measurement mirror need to overlap on the detector to interfere. This limits the range where measurements can be conducted to rather small intervals around integer multiples of the pulse–pulse distance. With this approach, disadvantageous dead zones are introduced in the measurement range, where no measurements are possible. Additional measures have to be taken to minimize these blind spots. As reported in the literature, one way is scanning of the delay of the reference arm mechanically [119, 175]. However, this method comes at the disadvantage of having a potentially slow mechanical scan and a more complex setup. Another way is a sweep of the pulse-pulse distance by changing the repetition rate, as done electronically in [174]. While this paper utilizes the flexibility of electro-optic frequency combs in an elegant manner, a fast DDS providing a linear frequency ramp as driving signal is required.

3.1.3 Dual-comb schemes with multi-heterodyne detection

Instead of using a single frequency comb, dual-comb schemes employ two frequency combs with slightly detuned line spacing. Typically, one of the combs is employed as a signal, probing the distance to the measurement target, and the other comb is employed as a local oscillator (LO) for heterodyne detection. A multitude of intermediate frequencies (IF) is generated due to the detuned line spacing. The IF are used to evaluate phase and amplitude information of each individual comb line. As the detuning of the line spacing can be kept relatively small (e.g., in the kilohertz to megahertz regime) compared to the actual line spacing, a broad optical bandwidth can be sampled with low-frequency electronics.

In [34], a fairly sophisticated setup is used, with two erbium-fiber frequency combs with line spacings around 100 MHz, each phase-locked to two CW reference lasers. The distance measurements presented in this section are a combination of synthetic-wavelength interferometry and optical interferometry at the wavelengths of the individual comb lines. A standard deviation of

3 µm for a measurement time of 0.2 ms is obtained when employing only the synthetic-wavelength approach. Combining it with an interferometric evaluation at the absolute comb line frequency, the standard deviation improves to 5 nm for a measurement time of 60 ms. Extension of the unambiguity range to 30 km is demonstrated by switching the roles of signal comb and LO comb, effectively creating a large synthetic wavelength defined by the small 5 kHz detuning of the two combs.

In [37], the setup is simplified, employing two free-running Er-doped mode-locked fiber lasers with repetition rates around 207 MHz. As the lasers are free-running and the absolute frequency of the comb lines is not known, only the synthetic wavelengths derived from multiples of the comb line spacing are evaluated. A standard deviation of 2 µm with a measurement time of 140 µs is demonstrated.

In [118] two free-running femtosecond fiber laser generate frequency combs with a line spacing around 100 MHz. By evaluating the synthetic wavelengths, a standard deviation of 15.2 µm at a measurement time of 200 µs is obtained. Additionally, extension of the unambiguity range of the measurement to 1.26 km is demonstrated by tuning the line spacing of the signal comb.

In [116], frequency combs are generated via parametric nonlinear processes in highly nonlinear fibers. Each comb generator comprises a phase modulator, two injection-locked laser diodes, wavelength-division multiplexing splitters and combiners, two high-power fiber amplifiers, and multiple nonlinear and linear fiber sections. The frequency combs exhibit a line spacing around 100 GHz, yielding broadband combs with high optical power in each line. With these relatively complex sources, a measurement standard deviation of 1.5 µm with a measurement time of 0.5 µs is achieved.

In [176], phase modulators inside cavities, which are stabilized with piezoelectric actuators, are used to generate electro-optic frequency combs from CW lasers. Standard deviations of 11 µm are obtained for distance measurements. The acquisition times are not stated in the paper. The combination of electro-optic modulators and feedback-stabilized optical cavities increases the experimental effort and makes the scheme less robust against environmental influences such as vibrations, as the authors also state in their paper.

In [J8], two broadband Kerr combs and high-frequency detection electronics are utilized to achieve standard deviations of 5 nm for a measurement time of 100 µs, when employing a high-pass filter to the measured values to compensate the effect of drift induced by temperature fluctuations. However, the generation of two Kerr comb involves complicated setups with high power optical amplifiers and the utilized high-frequency detection electronics are prohibitively expensive for many industrial applications.

Hardware complexity concerning the optical part of a setup is increased in dual-comb approaches, as a second comb source with defined detuning in line spacing is required. However, the complexity of the detection electronics is greatly reduced, compared to measuring inter-mode beats with direct detection. Specifically, information from high optical bandwidths can potentially be evaluated with relatively low frequency electronics due to the multi-heterodyne detection. Another benefit is the possibility to detect weak signals by heterodyne detection with a strong LO, making measurements of scattering surfaces possible, see Section 3.2 for more details. In comparison to approaches using Michelson interferometers, no moving parts or dispersive elements are required for dual-comb approaches, and dead zones within the measurement range can easily be avoided. Due to these benefits, the dual-comb approach is also chosen for the work reported in the next section of this thesis. In contrast to many other demonstrations in the field, electro-optic comb generation using fixed-frequency sinusoidal modulation in MZM is employed. A defined detuning in line spacing is easily achieved, as the line spacing is electronically defined by the driving frequencies. The approach is also particularly well suited for photonic integration, with the potential to minimize the hardware effort typically associated with dual-comb schemes, see Chapter 4 for details on integrated optical receiver circuits and Chapter 6 for an experimental demonstration of an integrated silicon-organic hybrid (SOH) frequency comb generator.

3.2 Distance measurements for surface digitization using electro-optic dual-color frequency combs

The contents of the following section is taken from a publication in Optics Express [J1]. The structure and the layout of this document was slightly adapted to fit the format of this thesis.

[*Start of paper* [J1]]

Fast high-precision distance metrology using a pair of modulator-generated dual-color frequency combs

Optics Express; Volume 26; Issue 26; pp. 34305-34335; December 2018
DOI: 10.1364/OE.26.034305

C. Weimann,[1,2,3] A. Messner,[1] T. Baumgartner,[1] S. Wolf,[1] F. Hoeller,[3] W. Freude,[1,2] and C. Koos[1,2]

[1]*Institute of Photonics and Quantum Electronics (IPQ), Karlsruhe Institute of Technology (KIT), 76131 Karlsruhe, Germany*

[2]*Institute of Microstructure Technology (IMT), KIT, 76344 Eggenstein-Leopoldshafen, Germany*

[3]*Corporate Research and Technology, Carl Zeiss AG, Oberkochen, Germany*

We demonstrate fast high-precision non-contact distance measurements to technical surfaces using a pair of dual-color electro-optic frequency combs for synthetic-wavelength interferometry (SWI). The dual-color combs are generated from continuous-wave (CW) lasers at 1300 nm and 1550 nm, which are jointly fed to a pair of high-speed dual-drive Mach-Zehnder modulators. The dual-color approach is used for continuous and dead-zone-free compensation of temperature-induced fiber drift. We achieve standard deviations below 2 µm at an acquisition time of 9.1 µs for measurements through 7 m of single-mode fiber. Despite the technical simplicity of our scheme, our concept can well compete with other comb-based distance metrology approaches, and it can maintain its accuracy even under industrial operating conditions. The viability of the concept is demonstrated by attaching the fiber-coupled sensor head to an industrial coordinate measuring machine for acquisition of surface profiles of

various technical samples. Exploiting real-time signal processing along with continuous fiber drift compensation, we demonstrate the acquisition of point clouds of up to 5 million data points during continuous movement of the sensor head.

3.2.1 Introduction

Optical distance metrology is at the heart of a wide variety of applications in science and industry, such as quality control, wear inspection, reverse engineering, forensics, and 3D scanning. Important requirements are high measurement precision, fast acquisition, and the ability to cope with natural technical surfaces characterized by roughness and strongly varying backscattered power levels. In the context of fast and precise distance metrology, optical frequency combs have emerged as valuable tools, either as light sources for the distance measurement itself [34, 35, 37, 116–129, J8], or as a means for calibrating lasers, e.g., for synthetic-wavelength interferometry (SWI) [130, 131, J4] or for frequency-modulated continuous-wave (FMCW) laser ranging [132, 133]. However, all these demonstrations rely on rather complex and sensitive setups that cannot cope with the stringent requirements that are associated with industrial applications. As an example, the majority of these demonstrations relies on free-space or fiber-based mode-locked lasers (MLL), which, despite considerable progress towards ruggedized implementations [48], are still characterized by considerable technical complexity, especially when it comes to operation in an uncontrolled industrial environment. Additional challenges arise in the context of dual-comb approaches, which generally require adjustment of both line spacing and center frequency along with stable operation without drift. Parametric comb generators [116] have that capability but rely on complex arrangements of phase modulators, injection-locked laser diodes, wavelength-division multiplexing splitters and combiners, high-power fiber amplifiers, as well as multiple nonlinear and linear fiber sections. Moreover, the majority of comb-based distance metrology experiments are limited to laboratory demonstrations of the measurement system itself, using the fundamentally achievable precision as a benchmark. Recently, a system using dual frequency combs generated by electro-optic modulators has been demonstrated for measurements over baselines of up to 1.2 km [177]. However, only measurements to retro-reflectors are carried out with relatively long averaging

times of 1 s for a single measurement, making the approach incompatible with the requirements associated with fast and dense digitization of technical surfaces. With a few exceptions [34, 37], these demonstrations do not consider detrimental effects such as length drift of optical fibers and other thermal and mechanical influences that are unavoidable in real-world applications. It has been demonstrated that such effects can be compensated by using the partial end facet reflex of an optical fiber or a dedicated free-space reflector for a reference measurement [34, 37], but this approach leads to dead spots in the measurement range when target and reference pulses overlap. Hence, despite the tremendous potential of many of the previously demonstrated comb-based distance measurement concepts, none of these approaches has demonstrated its applicability to industrial high-precision metrology.

In this section, we demonstrate a robust, technically straightforward, and yet precise comb-based distance measurement concept that can maintain its precision even under realistic industrial boundary conditions. The concept relies on synthetic-wavelength interferometry (SWI) using a pair of dual-color frequency combs that are generated by a robust fiber-based system of commercially available off-the-shelf components such as continuous-wave (CW) lasers at 1300 nm and 1550 nm and standard telecom-grade dual-drive Mach-Zehnder modulators (MZM). The MZM are operated by fixed-frequency sinusoidal electrical signals, generating a pair of frequency combs for each wavelength. The pair of 1550 nm frequency combs is used for measuring the distance to the target, while the pair of 1300 nm combs is used solely for continuous dead-zone free detection and compensation of temperature-induced optical drift of the fiber that connects the comb measurement unit to a remote passive sensor head. To the best of our knowledge, our experiments represent the first demonstration of dead-zone-free drift compensation for comb-based distance measurements through optical fibers. The accuracy of the distance measurements relies on the line spacing of the respective frequency combs, which can be freely adjusted with high precision using electronic frequency references that are inherently traceable to widely available time standards. The ability to compensate fiber drift enables flexible installations of the passive sensor head on industrial kinematics such as a coordinate measuring machine (CMM) without impeding the measurement accuracy. In our experiments, we demonstrate standard deviations of 2 µm at an acquisition time of 9.1 µs for measurements through 7 m of standard single-mode fiber. Considering the accuracy in relation to the measurement time, our concept outperforms

the majority of competing comb-based distance metrology demonstrations, despite its technical simplicity. Compared to time-of-flight based methods using sinusoidal intensity modulation or pulsed laser sources [35, 160, 178], where the accuracy is tightly linked to the bandwidth of the employed detection electronics, the chosen synthetic wavelength approach decouples the achievable accuracy from the detector bandwidth. This allows using detection electronics with relatively moderate bandwidth under 2 GHz while achieving accuracy in the micrometer regime. For demonstrating operation under industrial conditions, we implement dedicated signal-processing algorithms on a field-programmable gate array (FPGA), achieving a real-time measurement rate of 3.3 kHz, which is only limited by the signal processing speed. The combination of continuous fiber-drift compensation and real-time signal processing allows for fast and dense digitization of three-dimensional surface profiles of technical samples featuring a wide range of rough naturally scattering surfaces. This is demonstrated by the acquisition of point clouds of up to 5 million data points, obtained from a sensor head that is continuously moved by an industrial coordinate measuring machine.

The section is structured as follows: Subsection 3.2.2 provides details on the experimental setup and the comb-based distance measurement principle. Subsection 3.2.3 is dedicated to an in-depth characterization of the system performance and to a comparison with competing concepts. In Subsection 3.2.4, we give a detailed description of our experimental demonstrations. The Appendices A-F give mathematical details of the multi-heterodyne detection scheme and of the impact of noise on the measurement accuracy.

3.2.2 Experimental setup and measurement principle

3.2.2.1 Experimental setup of measurement system

A schematic of the measurement system is depicted in Fig. 3.1. The optical setup is entirely based on fiber-coupled, commercially available telecom-grade equipment. The light from two CW lasers with wavelengths of $\lambda_{\mathrm{cal}} = 1300\,\mathrm{nm}$ and $\lambda_{\mathrm{obj}} = 1550\,\mathrm{nm}$ and power levels of 15 dBm and 18 dBm respectively is split and combined by fiber couplers, feeding two Mach-Zehnder modulators (MZM1 and MZM2) for frequency comb generation. The light entering MZM2 is additionally frequency-shifted by a pair of acousto-optical modula-

tors (AOM). The carrier at wavelength λ_{cal} is shifted by 80 MHz, the carrier at λ_{obj} by 55 MHz. The lithium niobate MZM are driven by sinusoidal electrical signals with frequencies of 39.957 GHz for MZM1 and 40.000 GHz for MZM2. Both signal generators are referenced to a common clock signal (not depicted). The phase-modulated light shows broadband frequency comb spectra with line spacings that are precisely defined by the respective driving frequencies. By adjusting the bias voltage, the relative phase and the amplitudes of the driving signals between both arms of the modulator, spectrally flat frequency combs can be obtained [83,134]. The measured spectra are depicted in Fig. 3.1, insets (1) and (2). The two frequency combs with a 39.957 GHz line spacing are referred to as signal combs, whereas the two frequency combs with a 40.000 GHz line spacing are named local oscillator (LO) combs. The superimposed signal combs are split by coupler CPL1 to propagate along a measurement path and along a reference path towards the optical receivers. In the same manner, the superimposed LO combs are split by coupler CPL2 and propagate towards the optical receivers. Each of the balanced receivers Rx_{meas} and Rx_{ref}, which terminate the measurement paths and the reference paths, comprise a directional coupler followed by a pair of balanced photodiodes. Signal and LO combs are superimposed for heterodyne detection. Photomixing of the signal comb lines with their LO counterparts with detuned line spacing leads to a superposition of sinusoidal photocurrents at distinct intermediate frequencies (IF).

The polarization states of the signal combs are adjusted once at each start-up of the set-up via polarization controllers in order to maximize the amplitude of the generated IF signals. Long-time polarization fluctuations, which could lead to polarization-induced fading of IF signal levels, are ignored in this proof-of-principle experiment and could in principle be compensated for by using a polarization diversity receiver structure [179]. The photocurrent spectrum is evaluated to find the relative distance to the surface of the measurement object and to simultaneously locate the position of the calibration mirror. The relative distances are calculated from the phase differences of the signals received by Rx_{meas} with respect to the signals received at Rx_{ref}. Object and calibration information are discriminated by the respective carrier frequency shifts of 80 MHz and 55 MHz, which act as a label.

The signal combs are guided to a sensor head mounted on a coordinate measuring machine (CMM) via 7 m of standard single-mode fiber. In the sensor head, the signal combs exit the fiber and are separated by a dichroic beam

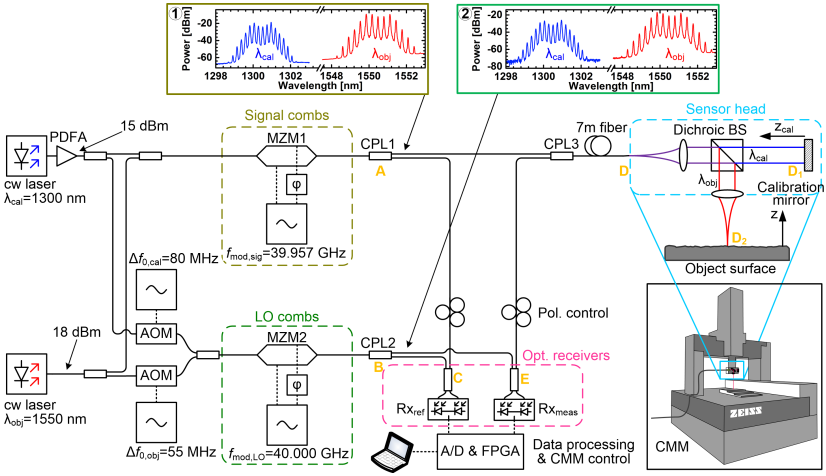

Fig. 3.1: Experimental setup. Light from two continuous-wave (CW) lasers with wavelengths of λ_{cal} = 1300 nm and λ_{obj} = 1550 nm and power levels of 15 dBm and 18 dBm respectively is split and fed to two Mach-Zehnder modulators (MZM1, MZM2). Light guided to MZM2 is additionally frequency-shifted with acousto-optical modulators (AOM) by 80 MHz and 55 MHz, respectively. The MZM are driven with strong sinusoidal signals (peak voltage 6.3 V) at frequencies of 39.957 GHz and 40.000 GHz, respectively. Proper adjustment of phase and amplitude of the driving signal in one arm of a MZM leads to broadband frequency comb generation. In the following, optical paths are described in terms of the points A ... E depicted in the setup sketch (bold, orange letters). The signal combs (Inset 1) are split in fiber coupler CPL1. One part is incident on the balanced photodetector (BD) Rx_{ref} after propagation over the internal optical path AC. The other part is guided through CPL3 to a sensor head via path AD. A dichroic beam splitter (BS) in the sensore head separates λ_{cal} and λ_{obj}. The calibration comb centered at λ_{cal} is reflected from a fixed calibration mirror, the object comb centered at λ_{obj} is scattered back from the object surface. The reflected light is coupled back into the fiber and guided to Rx_{meas} via path ADD_1DE and ADD_2DE, respectively. On both receivers, the signal combs are superimposed with the frequency-shifted local oscillator (LO) combs featuring detuned line spacing (Inset 2) for heterodyne detection. Polarization controllers (Pol. control) are adjusted once at each start-up of the setup. The generated photocurrents are acquired by an analog-to-digital (A/D) converter, and a Fourier transformation is used to isolate the discrete beat notes of the signal and LO combs lines. Digital signal processing is implemented on a field-programmable gate array (FPGA) and a personal computer. The optical path lengths D_2D and D_1D are denoted as z (object height) and z_{cal}. PDFA: Praseodymium-doped fiber amplifier. CMM: Coordinate measuring machine.

splitter cube (BS) upon collimation of the beam. The BS is transparent for the frequency comb around the center wavelength λ_{cal}. This comb then propagates to a fixed calibration mirror, is reflected and coupled back via the fiber and coupler CPL3 to the receiver $\mathrm{Rx}_{\mathrm{meas}}$. The frequency comb with center wavelength λ_{obj} is reflected by the BS and focused onto the object surface by a lens with a focal length of 30 mm and a diameter larger than the diameter 3.4 mm of the collimated beam. The resulting numerical aperture amounts to 0.057. Assuming a Gaussian beam, the beam illuminating the object surface exhibits a beam waist diameter of 17.4 µm, which defines the lateral resolution. The scattered light collected by the lens is coupled back into the fiber and guided to the receiver $\mathrm{Rx}_{\mathrm{meas}}$ as well.

The applied heterodyne reception technique enables sensitive detection of signals with low power [C4]. The IF signals are analog-to-digital converted with 1.8 GSa/s and 12 bit resolution, and a discrete Fourier transform (DFT) is performed. The DFT operates on $2^{14} = 16384$ samples and is implemented on a field-programmable gate array (FPGA). The DFT results are then fed to a personal computer (PC) for further processing. While the recording of the samples takes only 9.1 µs, the complete real-time measurement rate is currently limited to 3.3 kHz by the processing time required for the DFT. As presently only two Fourier transforms are calculated in parallel, future implementation could realize higher real-time measurement rates by a deeper parallelization. The chosen acquisition time and associated DFT length represents a trade-off between measurement rate and precision and allows us to achieve micrometer precision while still maintaining the ability for fast and dense sample digitization. The PC controls the CMM via Ethernet and reads the position of the sensor head with reference to the coordinate system of the CMM. By moving the sensor head across the object surface while optically measuring the height z, surface profiles can be recorded. The CMM is also used for tactile height measurements, which serve as "true" reference data for comparison with the optically obtained results.

3.2.2.2 Measurement principle and data processing

The measurement principle is based on synthetic-wavelength interferometry, evaluating the phase difference of the propagators $\exp\left(-\mathrm{j}\omega_{l,\mathrm{sig}} 2z/c\right)$ of the reflected signal comb lines l with (angular) frequency $\omega_{l,\mathrm{sig}} = 2\pi f_{l,\mathrm{sig}}$ and c

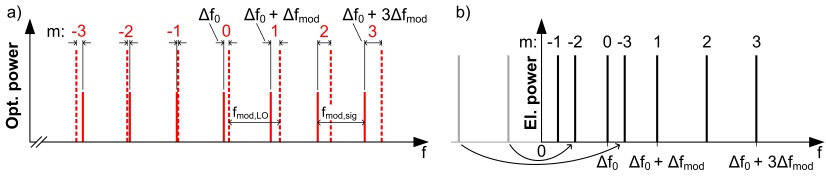

Fig. 3.2: Detection principle. (a) Schematic optical spectra of signal comb (continuous lines) and LO comb (dashed lines). The line spacings of signal and LO comb are slightly detuned by $\Delta f_{\mathrm{mod}} = |f_{\mathrm{mod,LO}} - f_{\mathrm{mod,sig}}|$, and the center frequencies are offset by Δf_0. (b) Schematic one-sided power spectrum of the photocurrent. Quadratic detection of signal and LO comb by a photodiode leads to a multitude of sinusoidal IF signals with frequencies $|\Delta f_0 + m\Delta f_{\mathrm{mod}}|$ in the photocurrent. Negative frequencies of the corresponding two-sided spectrum are drawn in gray and mirrored to positive frequencies of the one-sided spectrum. The phases of the IF signals are directly linked to the phase shifts accumulated by the lines of the FC during propagation.

as the vacuum speed of light [34, 124, 180]. Using two signal combs with different center wavelengths λ_{cal} and λ_{obj} and a calibration mirror in a fixed calibration distance z_{calib}, two independent distance measurements are made simultaneously for compensating the temperature drift of the fibers.

The measurement principle is first explained for only one set of signal comb and LO comb. The signal comb lines are numbered by the integer l and have discrete optical frequencies $f_{l,\mathrm{sig}} = f_{0,\mathrm{sig}} + l f_{\mathrm{mod,sig}}$, where $f_{0,\mathrm{sig}} = c/\lambda_{0,\mathrm{sig}}$ is defined by the input CW laser, and where $f_{\mathrm{mod,sig}}$ is the driving frequency for the MZM. The LO comb's center frequency is shifted with an AOM by Δf_0, and its line spacing is detuned by the difference in MZM driving frequencies Δf_{mod}. The integer m denotes the order of the LO comb lines with optical frequencies $f_{m,\mathrm{LO}} = f_{0,\mathrm{LO}} + m f_{\mathrm{mod,LO}} = \left(f_{0,\mathrm{sig}} + \Delta f_0\right) + m\left(f_{\mathrm{mod,sig}} + \Delta f_{\mathrm{mod}}\right)$. The comb lines of signal comb and LO comb are superimposed on the receivers Rx in Fig. 3.1. The superposition of signal and LO comb spectra is illustrated in Fig. 3.2(a) with 7 comb lines for each comb, $l, m = -3, \ldots, 0, \ldots, 3$. Quadratic detection leads to a multitude of sinusoidal photocurrents at distinct intermediate frequencies (IF) in the baseband. With an integer m denoting the order of the comb lines, the photocurrent shows N spectral lines at frequencies $|\Delta f_0 + m\Delta f_{\mathrm{mod}}|$, as depicted schematically in Fig. 3.2(b). A rigorous mathematical description of the measurement scheme can be found in Appendix A.

In the following, optical paths are described in terms of the points A ... E depicted in the setup sketch of Fig. 3.1. The optical path lengths are denoted as z for path D_2D, $D_{\mathrm{sig,meas}}$ for path ADE, $D_{\mathrm{LO,meas}}$ for path BE, $D_{\mathrm{sig,ref}}$ for path AC, and $D_{\mathrm{LO,ref}}$ for path BC. The phases $\varphi_m\left(2z + D_{\mathrm{sig,meas}}, D_{\mathrm{LO,meas}}\right)$ of the IF signal received by $\mathrm{Rx_{meas}}$ for variable object positions z are compared to the reference phases $\varphi_m\left(D_{\mathrm{sig,ref}}, D_{\mathrm{LO,ref}}\right)$ of IF signal received by $\mathrm{Rx_{ref}}$. The optical path length difference between the measurement and the reference path can be extracted from the phase differences $\Delta\varphi_m(z) = \varphi_m\left(2z + D_{\mathrm{sig,meas}}, D_{\mathrm{LO,meas}}\right) - \varphi_m\left(D_{\mathrm{sig,ref}}, D_{\mathrm{LO,ref}}\right)$, see Appendix A, Eq. (3.36).

The optical path lengths $D_{\mathrm{sig,meas}}(t), D_{\mathrm{sig,ref}}(t), D_{\mathrm{LO,meas}}(t)$ and $D_{\mathrm{LO,ref}}(t)$ inside fibers are subject to variations as a function of time t due to temperature changes [181–183]. The quantities $L_{\mathrm{sig,meas}}(t)$, $L_{\mathrm{sig,ref}}(t)$, $L_{\mathrm{LO,meas}}(t)$ and $L_{\mathrm{LO,ref}}(t)$ denote the actual geometric path lengths for the signal comb and the LO comb at a given time t. Note that these path lengths already consider the fact that the light may propagate back and forth through the same physical section of a path. In detail, $L_{\mathrm{sig,meas}}$, $L_{\mathrm{LO,meas}}$, $L_{\mathrm{sig,ref}}$, $L_{\mathrm{LO,ref}}$ represent the geometrical lengths of paths ADE, BE, AC, and BC, respectively. We further denote n as the group refractive index, $\mathrm{d}n/\mathrm{d}T$ as the thermo-optic coefficient, $\alpha_L = (\mathrm{d}L/\mathrm{d}T)/L$ as the thermal expansion coefficient. Moreover, we use the length-averaged temporal temperature differences with respect to a reference time t_0 of the various fiber paths. For path ADE (length $L_{\mathrm{sig,meas}}$), these temperature differences are denoted as $\Delta T_{\mathrm{sig,meas}} = T_{\mathrm{sig,meas}}(t) - T_{\mathrm{sig,meas}}(t_0)$, and the temperature differences for the other paths are obtained by replacing the subscript 'sig' by 'LO' and/or 'meas' by 'ref'. The optical path length $D_{\mathrm{sig,meas}} = nL_{\mathrm{sig,meas}}$ varies with temperature according to $\mathrm{d}D_{\mathrm{sig,meas}} = \left(n\mathrm{d}\left(L_{\mathrm{sig,meas}}\right)/\mathrm{d}T + L_{\mathrm{sig,meas}}\mathrm{d}(n)/\mathrm{d}T\right)\mathrm{d}T$. Using the previous definitions, this leads to temporal optical path length variations

$$\Delta D_{\mathrm{sig,meas}}(t) = \left(n\alpha_L + \frac{\mathrm{d}n}{\mathrm{d}T}\right) L_{\mathrm{sig,meas}} \Delta T_{\mathrm{sig,meas}}(t)\,. \tag{3.1}$$

The temporal optical path length variations for the other paths are obtained by replacing the subscript 'sig' by 'LO' and/or 'meas' by 'ref'. The considerably smaller temperature-dependent path length changes of the free-space

segment z can be neglected. As a consequence, the phase differences between measurement and reference path $\Delta\varphi_m(z,t)$ now depend also on time,

$$\begin{aligned}\Delta\varphi_m(z,t) = &\frac{m\omega_{\mathrm{mod,sig}}}{c} \\ &\left[2z + D_{\mathrm{sig,meas}}(t) - D_{\mathrm{LO,meas}}(t) - \left(D_{\mathrm{sig,ref}}(t) - D_{\mathrm{LO,ref}}(t)\right)\right] \\ &+ g(z,t) - \left(D_{\mathrm{LO,meas}}(t) - D_{\mathrm{LO,ref}}(t)\right) m\Delta\omega_{\mathrm{mod}}/c.\end{aligned} \tag{3.2}$$

The function $g(z,t)$ depends on time, but not on m,

$$\begin{aligned}g(z,t) = &\left(2z + D_{\mathrm{sig,meas}}(t) - D_{\mathrm{LO,meas}}(t) - \left(D_{\mathrm{sig,ref}}(t) - D_{\mathrm{LO,ref}}(t)\right)\right)\omega_{0,\mathrm{sig}}/c \\ &- \left(D_{\mathrm{LO,meas}}(t) - D_{\mathrm{LO,ref}}(t)\right)\Delta\omega_0/c,\end{aligned} \tag{3.3}$$

see Appendix A, Eq. (3.36). The object height z is extracted by fitting a straight line to the 2π-unwrapped data points $\Delta\varphi_m(z,t)$ and by evaluating its slope with respect to a zero measurement at $z_0 = 0, t_0 = 0$, see Appendix A, Eq. (3.38),

$$\begin{aligned}&\frac{\mathrm{d}\Delta\varphi_m(z,t)}{\mathrm{d}m} - \frac{\mathrm{d}\Delta\varphi_m(z_0=0,t_0=0)}{\mathrm{d}m} \\ &\cong \frac{\omega_{\mathrm{mod,sig}}}{c}\left(2z + \Delta D_{\mathrm{sig,meas}}(t) - \Delta D_{\mathrm{LO,meas}}(t) - \left(\Delta D_{\mathrm{sig,ref}}(t) - \Delta D_{\mathrm{LO,ref}}(t)\right)\right).\end{aligned} \tag{3.4}$$

Obviously, the thermally induced variations of optical path lengths $\Delta D_{\mathrm{sig,meas}}(t)$, $\Delta D_{\mathrm{LO,meas}}(t)$, $\Delta D_{\mathrm{sig,ref}}(t)$ and $\Delta D_{\mathrm{LO,ref}}(t)$ lead to an error when extracting the distance z from the slope of the phases as a function of comb line index m. We estimate the magnitude of this error by using published data. In a single-mode fiber with $n = 1.4679$ [184], $\alpha_L \approx 0.5\times10^{-6}\mathrm{K}^{-1}$ [182, 185, 186], $\mathrm{d}n/\mathrm{d}T \approx 10\times10^{-6}\mathrm{K}^{-1}$ [181, 182, 185–187], the temperature-induced relative optical path length change can be quantified as (dropping the subscripts)

$$(\Delta D/\Delta T)/L = 10.7\,\mu\mathrm{m}/(\mathrm{K\,m}). \tag{3.5}$$

In practically relevant systems, typical fiber lengths are in the meter range (say, 10 m) and temperature changes of a few Kelvin (say, 10 K) are to be expected in a normal industrial environment. As a consequence, accuracies better than 1 mm require a calibration technique, which allows to indepen-

dently determine the temperature-induced variations of the various fiber paths. To this end, we perform a second measurement with frequency combs at a different center wavelength $\lambda_{\mathrm{cal}} = 1300\,\mathrm{nm}$ using a fixed calibration mirror at position D_1, Fig. 3.1. The 1300 nm-combs along with the previous combs at $\lambda_{\mathrm{obj}} = 1550\,\mathrm{nm}$ are generated from two CW lasers by identical modulators, propagate through the same fiber and are separated only in the sensor head by the dichroic beam splitter. Calibration and object measurements are separately evaluated by heterodyne down-conversion to different intermediate frequencies – a measurement of a typical electrical power spectrum of the photocurrent is depicted in Fig. 3.3(a). The IF signals for λ_{obj} and λ_{cal} are centered around different offset frequencies $\Delta f_{0,\mathrm{obj}}$ and $\Delta f_{0,\mathrm{cal}}$ as defined by the two AOM. The associated lines can hence be extracted from the photocurrent spectrum, and the associated optical path lengths can be evaluated separately. In the following, the optical calibration path length is denoted as z_{cal}, which refers to path $\mathrm{D}_1\mathrm{D}$, see Fig. 3.1. We apply Eq. (3.4) for the object and the calibration comb, introduce the effective optical path lengths $D_{\mathrm{obj}}(t)$ and $D_{\mathrm{cal}}(t)$ for the object wavelength λ_{obj} and the calibration wavelength λ_{cal}, with corresponding refractive indices $n_{\lambda_{\mathrm{obj}}}$ and $n_{\lambda_{\mathrm{cal}}}$, and find for the difference

$$\frac{\mathrm{d}\left(\Delta\varphi_{m,\mathrm{obj}}(z,t)\right)}{\mathrm{d}m} - \frac{\mathrm{d}\left(\Delta\varphi_{m,\mathrm{cal}}(z,t)\right)}{\mathrm{d}m} = \frac{\omega_{\mathrm{mod,sig}}}{c}\left[2\left(z - z_{\mathrm{cal}}\right) + D_{\mathrm{obj}}(t) - D_{\mathrm{cal}}(t)\right],$$

$$\begin{aligned} D_{\mathrm{obj}}(t) &= n_{\lambda_{\mathrm{obj}}}(t)\,L_{\mathrm{sig,meas}}(t) - n_{\lambda_{\mathrm{obj}}}(t)\,L_{\mathrm{LO,meas}}(t) \\ &\quad - n_{\lambda_{\mathrm{obj}}}(t)\,L_{\mathrm{sig,ref}}(t) + n_{\lambda_{\mathrm{obj}}}(t)\,L_{\mathrm{LO,ref}}(t), \\ D_{\mathrm{cal}}(t) &= n_{\lambda_{\mathrm{cal}}}(t)\,L_{\mathrm{sig,meas}}(t) - n_{\lambda_{\mathrm{cal}}}(t)\,L_{\mathrm{LO,meas}}(t) \\ &\quad - n_{\lambda_{\mathrm{cal}}}(t)\,L_{\mathrm{sig,ref}}(t) + n_{\lambda_{\mathrm{cal}}}(t)\,L_{\mathrm{LO,ref}}(t). \end{aligned} \tag{3.6}$$

If the group refractive index and the thermo-optic coefficient for the measurement and the calibration combs were identical, we had $D_{\mathrm{obj}}(t) = D_{\mathrm{cal}}(t)$, and the temperature fluctuations would compensate exactly, see Eq. (3.1). However, there is an actual wavelength dependency of n and $\mathrm{d}n/\mathrm{d}T$ [182, 184], and this leads to a remaining differential temperature drift of the individual optical path lengths of (dropping again all individual subscripts)

$$\left(\left(\Delta D_{\mathrm{obj}}/\Delta T\right) - \left(\Delta D_{\mathrm{cal}}/\Delta T\right)\right)/L = 32\,\mathrm{nm/(K\,m)}. \tag{3.7}$$

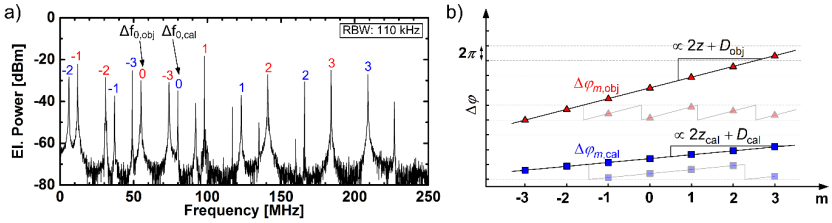

Fig. 3.3: Detection principle and data processing. (a) Measured one-sided spectrum of the photocurrent in a resolution bandwidth (RBW) of 110 kHz. The spectral lines of the photocurrent are indexed by m as in Fig. 3.2. For the object comb (red) $m = 0$ refers to the spectral line at the offset frequency $\Delta f_{0,\mathrm{obj}} = 55\,\mathrm{MHz}$, and for the calibration comb (blue) to the line at offset frequency $\Delta f_{0,\mathrm{cal}} = 80\,\mathrm{MHz}$. The appearance of negative frequencies (m < −1 in the present configuration) in the one-sided electrical spectrum is explained in Fig. 3.2. (b) Differences of the IF phases $\Delta\varphi_{m,\mathrm{obj}}$ and $\Delta\varphi_{m,\mathrm{cal}}$ as measured between the reference and the measurement receiver for object and calibration comb as a function of the line index m. Phase values before unwrapping (sawtooth-like shapes) are depicted in light colors, illustrating the 2π-periodicity. The unwrapped phase values follow a linear relationship. The slopes of the fitted straight lines are proportional to the respective optical length differences between reference and measurement paths. Triangles mark the phase slopes according to Eq. (3.4), where $D_{\mathrm{obj}}(t)$ and $D_{\mathrm{cal}}(t)$ are defined in Eq. (3.6).

Comparing this result to Eq. (3.5), we find that the calibration measurement reduces the temperature influence by three orders of magnitude.

The slopes $\mathrm{d}\left(\Delta\varphi_{m,\mathrm{obj}}(z,t)\right)/\mathrm{d}m$ and $\mathrm{d}\left(\Delta\varphi_{m,\mathrm{cal}}(z,t)\right)/\mathrm{d}m$ used in Eq. (3.6) are determined by a linear regression, as illustrated in Fig. 3.3(b). Note that the measurement does only permit to determine the phase values up to an integer multiple of λ-periodic, and that the measured phases have to be unwrapped before extracting the slope. This determines the unambiguity range Δz_{ua} of the approach: In Eq. (3.4), the quantities D can be assumed to be constant. The maximum change $\Delta\left(\Delta\varphi_m(z,t)\right)$ which can be uniquely measured is $D_{2\times 7\mathrm{m}}$. The associated maximum unambiguously detectable change of Δz_{ua} hence corresponds to a phase shift of 2π between neighboring comb lines ($\Delta m = 1$) and can be expressed as

$$\Delta z_{\mathrm{ua}} = \frac{2\pi c}{2\omega_{\mathrm{mod,sig}}} = \frac{1}{2}\Lambda_1, \quad \Lambda_m = \frac{c}{m\, f_{\mathrm{mod,sig}}}. \tag{3.8}$$

The quantity Λ_1 corresponds to the biggest synthetic wavelength [137] used in the measurement, see Appendix A Eq. (3.34). For our system

we have $f_{\mathrm{mod,sig}} = 39.957\,\mathrm{GHz}$, leading to an unambiguity range of $\Delta z_{\mathrm{ua}} = c/\left(2 f_{\mathrm{mod,sig}}\right) = 3.7\,\mathrm{mm}$. This range could be extended by, e. g., subsequent measurements with different comb line spacings $f_{\mathrm{mod,sig}}$ [34, 125], by a combination with longer-range time-of-flight measurement schemes [J4], or by using special schemes in which the LO comb also propagates to the measurement target [188].

3.2.3 System characterization

In the following we demonstrate the efficiency of our path length drift compensation scheme when the system is exposed to deterministic and stochastic changes of the ambient temperature. If environmental changes are compensated, the limiting measurement accuracy is determined by the system's signal-to-noise power ratio.

3.2.3.1 Deterministic time-dependent system uncertainties due to thermal path length changes

The experimental results can be seen in Fig. 3.4(a) for a qualitative demonstration. A 5 m long fiber leading to the sensor head is heated for a few seconds with a heat gun, while continuously measuring the distance to a fixed spot on an static object. The individual measurement results for the true heights z and z_{cal} are named $\hat{z} = z + 0.5 D_{\mathrm{obj}}(t)$ and $\hat{z}_{\mathrm{cal}} = z + 0.5 D_{\mathrm{cal}}(t)$ and are displayed as red and blue curves in Fig. 3.4(a). These measurement data exhibit a strong temperature drift – the optical path length expands during the heating phase, and shrinks again while the fiber is cooling down. However, the difference,

$$\hat{z}_{\mathrm{comp}} = \hat{z} - \hat{z}_{\mathrm{cal}}, \tag{3.9}$$

(black curve) stays constant, Fig. 3.4(a). A quantitative characterization was done by a controlled heating of a 0.5 m-long section of the fiber in a water bath, Fig. 3.4(b). No heatsinks were applied outside this 0.5 m-range. Each temperature step was followed by sufficient settling time of around half an hour. Increasing the temperature while measuring a constant object height results in a relative optical path length change $(\Delta D/\Delta T)/L = (14.8 \pm 0.5)\,\mu\mathrm{m/(K\,m)}$. This in fair agreement with the value of $10.7\,\mu\mathrm{m/(K\,m)}$ that was estimated

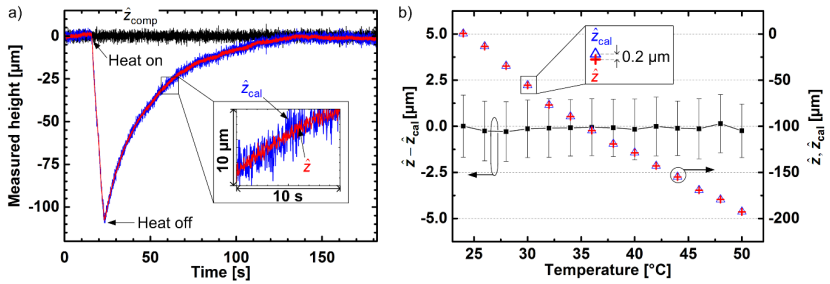

Fig. 3.4: Influence of fiber temperature drift on the measured object height, and compensation of this drift. (a) Qualitative demonstration. A section of fiber CPL3-D in Fig. 3.1 is rapidly heated for a few seconds with a heat gun. The measured object height $\hat{z}$ decreases during the heating period due to expansion of the fiber and approaches its true value $z = 0$ while cooling down (solid red, $\lambda = 1550\,\text{nm}$). The measured calibration height $\hat{z}_{cal}$ follows this curve closely (solid blue, $\lambda = 1300\,\text{nm}$), but exhibits more noise because of the lower optical comb power, see inset. The difference $\hat{z}_{comp} = \hat{z} - \hat{z}_{cal}$, which measures the true temperature-compensated object height (black) z with reference to z_{cal}, remains unaffected. (b) Quantitative demonstration. A 0.5 m long section of the optical fiber path CPL3-D is immersed in a water bath which is heated in 2 K steps. At each temperature step, the distances $\hat{z}$ and $\hat{z}_{cal}$ to fixed targets at z and z_{cal}, respectively, are measured 500 times. Blue triangles and red crosses denote the measured averages $\langle \hat{z} \rangle$ and $\langle \hat{z}_{cal} \rangle$, respectively (vertical axis on the right). The black squares represent the averages of the differences $\langle \hat{z}_{comp} \rangle$ (vertical axis left), and the error bars indicate ±1 standard deviation $\sigma_{\hat{z},comp}$. The optical fields traverse the heated fiber section twice so that the relevant geometrical path length is $L_h = 2{\times}0.5\,\text{m}$. While the true height z remains constant, the measured object and calibration heights $\hat{z}$ and $\hat{z}_{cal}$ change because the optical path length D_h of the heated fiber section for 1550 nm and 1300 nm changes with a linear coefficient of $(2\Delta\hat{z}/\Delta T)/L_h = (\Delta D_h/\Delta T)/L_h = (14.8 \pm 0.5)\,\mu\text{m}/(\text{K m})$ according to Eq. (3.4), (3.5), while $\hat{z}_{comp}$ remains constant.

from published data of other groups, Eq.(3.5). The discrepancy is attributed to heat conduction along the fiber, which increases the effective heated length. The temperature-compensated height $\hat{z}_{comp} = \hat{z} - \hat{z}_{cal}$ stays constant within the measurement accuracy over the whole temperature range, demonstrating the effectiveness of the compensation scheme.

3.2.3.2 Stochastic time-dependent system uncertainties due to path length fluctuations

During extended measurement times, the optical path length varies due to random refractive index fluctuations of the air in the free-space path, and

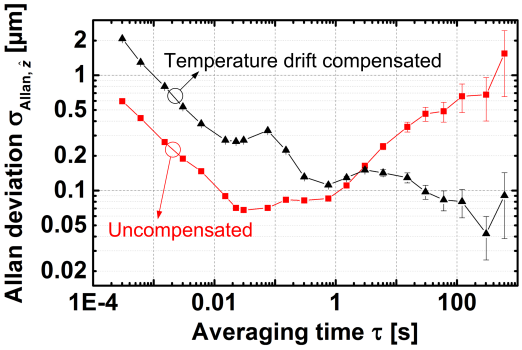

Fig. 3.5: Allan deviations calculated from repeated measurements to a mirror at a fixed distance. Result for uncompensated measurement shown in red, result for temperature-drift-compensated measurement shown in black.

because of the remaining uncompensated optical fiber path length fluctuation due to the wavelength dependency of n and $\mathrm{d}n/\mathrm{d}T$, see Eq. (3.7) and associated text. For quantifying the stability of the system, we record a number of values $\hat{z}$ at time intervals Δt and subdivide the total measurement time into subperiods of duration $\tau = N\Delta t$, which are subscripted by n. Each subperiod n therefore comprises $\nu = 1, 2, \ldots, N$ data points $\hat{z}_{n,\nu}$. As a measure for the long-term stability we use the Allan variance,

$$\sigma^2_{\mathrm{Allan},\hat{z}}(\tau) = \frac{1}{2}\left\langle \left(\langle \hat{z}_{n+1}\rangle_\tau - \langle \hat{z}_n\rangle_\tau\right)^2 \right\rangle_n, \quad \langle \hat{z}_n\rangle_\tau = \frac{1}{N}\sum_{\nu=1}^{N} \hat{z}_{n,\nu}, \quad \tau = N\Delta t, \tag{3.10}$$

where the brackets $\langle\rangle$ denote the average of the respective quantity. For repeated uncompensated measurements $\hat{z}_{n,\nu}$ under nominally stable environmental conditions, the resulting Allan deviation $\sigma_{\mathrm{Allan},\hat{z}}$ is plotted in Fig. 3.5. For short averaging times τ, random fluctuations lead to a relatively large $\sigma_{\mathrm{Allan},\hat{z}}$, which decreases as the averaging time τ increases. However, the averaging does not help for long-term drifts, e.g., on a time scale of 1s or more, where the Allan deviation of the uncompensated measurements starts increasing again. This can be overcome by the dual-wavelength drift compensation scheme. In a second experiment, we record the Allan deviation for the compensated measurement value $\hat{z}_{\mathrm{comp}} = \hat{z} - \hat{z}_{\mathrm{cal}}$ as defined in Eq. (3.9). Note that, for small

averaging times, the resulting Allan deviation $\sigma_{\mathrm{Allan},\hat{z},\mathrm{comp}}$ of the compensated measurements is larger than the Allan deviations $\sigma_{\mathrm{Allan},\hat{z}}$ of the uncompensated scheme. This is caused by smaller comb power and hence the higher noise levels of the calibration measurement in combination with the fact that the variance of a sum of the two independent random variables $\langle \hat{z}_n \rangle_\tau$ and $\left\langle \hat{z}_{\mathrm{cal},n} \right\rangle_\tau$ equals the sum of the variances $\sigma^2_{\langle \hat{z} \rangle} + \sigma^2_{\langle \hat{z},\mathrm{cal} \rangle}$. For long averaging times or for measurements over extended periods, long-term drifts dominate the Allan deviation of the uncompensated measurements, while the compensated measurement reduces the effect of such drifts significantly. Our current real-time measurement rate is $1/\Delta t = 3.3\,\mathrm{kHz}$. For typical surface scans as conducted in our proof-of-principle demonstrations, we record around 10^6 data points which takes around 300 s. The Allan deviation of the compensated measurement (black curve, Fig. 3.5) is as small as 60 nm. Without compensation (red curve, Fig. 3.5), the additional measurement uncertainty would be much larger, even in the case of a nominally stable laboratory environment. To achieve high precision with a fiber-based system in an uncontrolled workshop environment, temperature drift compensation is indispensable.

3.2.3.3 Measurement precision dependent on signal-to-noise power ratio

When temperature-related measurement errors are compensated, the measurement precision of the system is eventually limited by noise. We therefore quantify the influence of various sources of noise: Phase noise and relative intensity noise (RIN) of the comb sources, shot noise (quantum noise) to be seen in the photodiode current, noise of the transimpedance amplifiers (TIA) that amplify the photocurrent, quantization noise of the analog-to-digital converter, and stochastic crosstalk from the finite isolation of the 3 dB splitter (CPL3 in Fig. 3.1).

It turns out that for the operating conditions of interest, quantization noise is negligible. Because we employ a self-heterodyne detection scheme, phase noise of the source is not transferred to the photodetector current. The influence of the remaining noise sources on the signal-to-noise power ratio (SNR) and on the overall distance measurement accuracy is discussed in the following paragraphs.

Relative intensity noise: Although mitigated by the balanced detection scheme, relative intensity noise (RIN) of the optical carriers still leads to some fluctuations of the photocurrent amplitude and the associated voltage signal. The corresponding relations are derived in Appendix B and C. The quantity S_λ (unit A/W) is the detector sensitivity, R_{TIA} (unit Ω) denotes the transimpedance gain of the TIA unit, $\mathrm{RIN}_{\mathrm{spec},\lambda}$ is the height of the RIN spectral density of the respective laser with center wavelength λ, and Δf is the detection bandwidth. Assuming total optical comb powers $P_{\mathrm{sig},\lambda}$ and $P_{\mathrm{LO},\lambda}$, respectively, the resulting noise variance of the voltage is given as [189]

$$\sigma^2_{\mathrm{RIN}} = \sum_{\lambda} \left(S_\lambda \mathrm{R}_{\mathrm{TIA}}\right)^2 \mathrm{RIN}_{\mathrm{spec},\lambda} P_{\mathrm{LO},\lambda} P_{\mathrm{sig},\lambda} \Delta f, \tag{3.11}$$

where the sum $\sum_\lambda$ comprises the two wavelengths $\lambda_{\mathrm{obj}} = 1550\,\mathrm{nm}$ and $\lambda_{\mathrm{cal}} = 1300\,\mathrm{nm}$.

Shot noise: The shot noise (quantum noise) variance of the voltage (unit V^2) at the output of the balanced photodetectors (BD) in the receivers $\mathrm{Rx}_{\mathrm{meas}}$ and $\mathrm{Rx}_{\mathrm{ref}}$ depends on the total optical comb power $P_{\mathrm{sig},\lambda} + P_{\mathrm{LO},\lambda}$ impinging on the detector for each center wavelength $\lambda = \left\{\lambda_{\mathrm{obj}}, \lambda_{\mathrm{cal}}\right\}$,

$$\sigma^2_{\mathrm{shot}} = 2e \sum_{\lambda} S_\lambda \left(P_{\mathrm{sig},\lambda} + P_{\mathrm{LO},\lambda}\right) R^2_{\mathrm{TIA}} \Delta f. \tag{3.12}$$

Noise-equivalent power: Noise of a photodetector system is usually specified in terms of its noise-equivalent power (NEP), which includes the effects of photodetector quantum noise and electronic noise of the TIA. The resulting noise variance of the voltage is

$$\sigma^2_{\mathrm{TIA}} = \left(R_{\mathrm{TIA}} \mathrm{NEP} \cdot S_{\mathrm{NEP}}\right)^2 \Delta f. \tag{3.13}$$

The quantity S_{NEP} stands for the photodetector sensitivity at the wavelength where the NEP was measured by the manufacturer of the device. In Appendix D, we show that σ^2_{TIA} is dominated by electronic noise contributions.

These noise contributions lead to a finite signal-to-noise ratio (SNR). According to Eq. (3.32) in Appendix A, the signal amplitude $\hat{V}_{m,\lambda}$ of a sinusoidal

voltage generated by heterodyne mixing of the m-th lines of signal comb and LO comb (see Fig. 3.2) is given by

$$\hat{V}_{m,\lambda} = S_\lambda \sqrt{2P_{m,\mathrm{sig},\lambda}\, 2P_{m,\mathrm{LO},\lambda}}\; R_{\mathrm{TIA}}, \tag{3.14}$$

where $P_{m,\mathrm{sig},\lambda}$ and $P_{m,\mathrm{LO},\lambda}$ denote the comb line powers of the signal and the LO comb. Relative intensity noise of the source, photodetector shot noise, and TIA noise are independent so that their variances can be added for a total noise variance $\sigma^2_{\mathrm{tot}} = \sigma^2_{\mathrm{RIN}} + \sigma^2_{\mathrm{Shot}} + \sigma^2_{\mathrm{TIA}}$. The SNR for the m-th IF line from combs with a center wavelength λ is then

$$\mathrm{SNR}_{m,\lambda} = \frac{\frac{1}{2}\hat{V}^2_{m,\lambda}}{\sigma^2_{\mathrm{tot}}} = \frac{\frac{1}{2}S^2_\lambda R^2_{\mathrm{TIA}}\, 2P_{m,\mathrm{sig},\lambda}\, 2P_{m,\mathrm{LO},\lambda}}{\sigma^2_{\mathrm{RIN}} + \sigma^2_{\mathrm{Shot}} + \sigma^2_{\mathrm{TIA}}}. \tag{3.15}$$

From this $\mathrm{SNR}_{m,\lambda}$ the variance of the measured electrical phase can be calculated. To this end, the m-th line in the measured electrical spectrum Fig. 3.2(b) is represented by a sinusoidal with frequency $f_m = \Delta f_0 + m\Delta f_{\mathrm{mod}}$. Finite $\mathrm{SNR}_{m,\lambda}$ then leads to a fluctuation of both amplitude and phase of this sinusoidal. These fluctuations are represented by an in-phase component $x = \hat{n}\cos\psi$ and a quadrature component $y = \hat{n}\sin\psi$, where ψ is equally distributed in the interval $0 \ldots 2\pi$,

$$V_{m,\lambda} = \left(\hat{V}_{m,\lambda} + x\right)\cos(\omega_m t) - y\sin(\omega_m t), \quad x = \hat{n}\cos\psi, \quad y = \hat{n}\sin\psi. \tag{3.16}$$

The phase $\varphi_{m,\lambda}$ of signal $V_{m,\lambda}$ is determined by $\tan\varphi_{m,\lambda} = y/\left(\hat{V}_{m,\lambda} + x\right)$, which can be approximated by $\tan\varphi_{m,\lambda} \approx y/\hat{V}_{m,\lambda} \approx \varphi_{m,\lambda}$ because $x \ll \hat{V}_{m,\lambda}$ and $y \ll \hat{V}_{m,\lambda}$ for a large $\mathrm{SNR}_{m,\lambda}$. The noise components are unbiased and equal in variance, $\overline{x^2} = \overline{y^2} = \sigma^2_{\mathrm{tot}}$, therefore the phase variance becomes [190]

$$\sigma^2_{\varphi,m,\lambda} = \frac{\overline{y^2}}{\hat{V}^2_{m,\lambda}} = \frac{\frac{1}{2}\hat{n}^2}{\hat{V}^2_{m,\lambda}} = \frac{\sigma^2_{\mathrm{tot}}}{\hat{V}^2_{m,\lambda}} = \frac{1}{2\times\mathrm{SNR}_{m,\lambda}}. \tag{3.17}$$

The phase variance for the IF lines as detected by $\mathrm{Rx}_{\mathrm{meas}}$ and $\mathrm{Rx}_{\mathrm{ref}}$ are then

$$\sigma^2_{\varphi,m,\lambda,\mathrm{meas}} = \frac{1}{2\times\mathrm{SNR}_{m,\lambda,\mathrm{meas}}}, \qquad \sigma^2_{\varphi,m,\lambda,\mathrm{ref}} = \frac{1}{2\times\mathrm{SNR}_{m,\lambda,\mathrm{ref}}}. \tag{3.18}$$

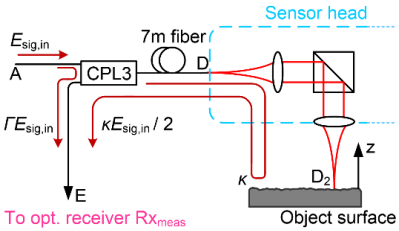

Fig. 3.6: The signal field $E_{\mathrm{sig,in}}$ at point A is coupled to the sensor head via the 3 dB coupler CPL3. The field is reflected at the object surface with an amplitude reflection coefficient κ, and the reflected field $\kappa E_{\mathrm{sig,in}}/2$is redirected to the optical receiver $\mathrm{Rx}_{\mathrm{meas}}$. A small portion $\Gamma E_{\mathrm{sig,in}}$ of the input light propagates directly to $\mathrm{Rx}_{\mathrm{meas}}$ due to the finite isolation Γ of coupler CPL3. For a precise measurement, $\kappa/2 \gg \Gamma$should hold.

The signal-to-noise power ratios $\mathrm{SNR}_{m,\lambda,\mathrm{meas}}$ and $\mathrm{SNR}_{m,\lambda,\mathrm{ref}}$ are found by substituting in Eq. (3.15) $P_{m,\mathrm{sig},\lambda}$, $P_{m,\mathrm{LO},\lambda}$ by $P_{m,\mathrm{sig},\lambda,\mathrm{meas}}$, $P_{m,\mathrm{LO},\lambda,\mathrm{meas}}$, and $P_{m,\mathrm{sig},\lambda,\mathrm{ref}}$, $P_{m,\mathrm{LO},\lambda,\mathrm{ref}}$, respectively.

3.2.3.4 Impact of stochastic crosstalk

For low backscattered power levels, the measurement precision is limited by crosstalk via the finite isolation of the 3 dB output coupler CPL3 in Fig. 3.1, which is used to couple the light to and from the sensor head, see Fig. 3.6. For the coupler used in our experiments, the crosstalk amounts to $\Gamma = E_{\mathrm{sig,cross}}/E_{\mathrm{sig,in}}$, $\Gamma_{\mathrm{dB}} = 20\lg\Gamma = -57$ dB. The input component of the electric field is denoted by $E_{\mathrm{sig,in}}$, and the crosstalk component by $E_{\mathrm{sig,cross}} = \Gamma E_{\mathrm{sig,in}}$. The actual signal component $E_{\mathrm{sig,out}} = \kappa E_{\mathrm{sig,in}}/2$ includes the $1/\sqrt{2}$ coupling factor of the 3dB coupler in the forward and in the backward direction as well as the amplitude reflection coefficient κ associated with the sensor head and the object surface.

In the following, we denote the optical path length from CPL3 through the 7 m long fiber leading to the sensor head and back to CPL3 (path CPL3-D-CPL3 in Fig. 3.1) as $D_{2\times 7\mathrm{m}}$. The optical path length for the signal component is denoted as D_z (path A-CPL3-D-D_2-D-CPL3-E). The optical path length D_{cross} (path A-CPL3-E) for the crosstalk component can then be expressed by

$D_{\text{cross}} = D_z - D_{2\times 7\text{m}} - 2z$. The amplitude of each comb line m arriving at the detector is a superposition of the actual signal component and the crosstalk,

$$E_{m,\text{sig}}(\omega_m) = \hat{E}_{m,\text{sig,in}} \Re\left\{\frac{1}{2}\kappa \exp\left(\mathrm{j}\left(\omega_m t - D_z \frac{\omega_m}{c}\right)\right) + \Gamma \exp\left(\mathrm{j}\left(\omega_m t - D_{\text{cross}} \frac{\omega_m}{c}\right)\right)\right\}. \tag{3.19}$$

With the auxiliary relations

$$x' = \Gamma \cos\left((D_{2\times 7\text{m}} + 2z)\frac{\omega_m}{c}\right) \qquad y' = \Gamma \sin\left((D_{2\times 7\text{m}} + 2z)\frac{\omega_m}{c}\right), \tag{3.20}$$

we can simplify Eq. (3.19)and write in analogy to Eq. (3.16)

$$\frac{E_{m,\text{sig}}(\omega_m)}{\hat{E}_{m,\text{sig,in}}} = \left(\frac{1}{2}\kappa + x'\right)\cos\left(\omega_m t - D_z \frac{\omega_m}{c}\right) - y' \sin\left(\omega_m t - D_z \frac{\omega_m}{c}\right). \tag{3.21}$$

Our calibration measurement compensates any fluctuations in the optical path length D_z. The in-phase crosstalk $x' \ll \frac{1}{2}\kappa$ is a small contribution, but the quadrature crosstalk y' leads to a phase error $\tan\varphi_{m,\text{cross}} \approx y'/(\kappa/2) \approx \varphi_{m,\text{cross}}$. Without stochastic fluctuations of the path length $D_{2\times 7\text{m}}$, this systematic error is λ-periodic when changing $2z$, $\varphi_{m,\text{cross}} \approx \frac{\Gamma}{\kappa/2}\sin\left((D_{2\times 7\text{m}} + 2z)\,\omega_m/c\right)$, and is called cyclic error [191]. However, due to thermal fluctuations of the fiber path length $D_{2\times 7\text{m}}$, the phases of x' and y' in Eq. (3.20) vary randomly on the time scale of environmental thermal fluctuations. Considering the first term in Eq. (3.19) as signal and the second term as noise, we define a cross-talk related signal-to-noise power ratio

$$\text{SNR}_{\text{cross}} = \frac{\left(\frac{1}{2}\kappa\right)^2}{\frac{1}{2}\Gamma^2} = \frac{(\kappa/2)^2}{\Gamma^2}. \tag{3.22}$$

In our experiments, we measure the object distance z with a sampling rate of 3.3 kHz and evaluate the mean and the variance of this distance by averaging over 1,000 samples. This corresponds to an observation time of $1000/3.3\,\text{kHz} = 303\,\text{ms}$. The cross-talk related variance of these measurements is hence dominated by fluctuations with bandwidths bigger than $1/(2\times 303\,\text{ms}) = 3.3\,\text{kHz}/(2\times 1000) = 1.65\,\text{Hz}$ and smaller than $3.3\,\text{kHz}/2 = 1.65\,\text{kHz}$.

Typical spectra of stochastic room temperature fluctuations cover a range up to 4 Hz [183]. For frequencies from 1.65 Hz up to 4 Hz the standard deviation of the room temperature is approximately $\sigma_T = 5\,\mathrm{mK}$. The dynamic thermal response of a standard Hytrel jacketed singlemode optical fiber has a 3 dB bandwidth of roughly 10 Hz [192] and reacts much faster than the room temperature can fluctuate. With a geometrical path length $L = 2 \times 7\,\mathrm{m}$ for $D_{2\times7\mathrm{m}}$, and with the relation $\mathrm{d}D_{2\times7\mathrm{m}}/(L\mathrm{d}T) \approx 11\,\mu\mathrm{m}/(\mathrm{K\,m})$ from Eq. (3.5), the effective optical path length fluctuation during the observation time is of the order $\sigma_{D_{2\times7\mathrm{m}}} = \mathrm{d}D_{2\times7\mathrm{m}}/(L\mathrm{d}T)\, L\sigma_T = 0.8\,\mu\mathrm{m}$. For simplicity, we approximate the Gaussian probability density function (pdf) for the randomly changing optical path length $D_{2\times7\mathrm{m}}$by a rectangular pdf with a width of $2\sigma_{D_{2\times7\mathrm{m}}} = 1.6\,\mu\mathrm{m}$, centered at the expectation value $\langle D_{2\times7\mathrm{m}}\rangle$. With an object wavelength of $\lambda_m = 2\pi c/\omega_m = 1.55\,\mu\mathrm{m}$, the phase terms $2\pi D_{2\times7\mathrm{m}}/\lambda_m$ of x' and y' are equally distributed in the interval $0 \ldots 2\pi$, and we can proceed in analogy to Eq. (3.17). The phase variance due to stochastic crosstalk is therefore

$$\sigma^2_{\varphi,m,\mathrm{cross}} = \frac{1}{2 \times \mathrm{SNR}_{\mathrm{cross}}} \qquad \text{for} \quad \Gamma \ll \frac{\kappa}{2}. \tag{3.23}$$

For the calibration wavelength, the reflection coefficient κ of the calibration mirror is so large that the crosstalk influence can be neglected.

3.2.3.5 Calculation of the distance uncertainty from the phase variances

The measured distance is calculated from the slope $\mathrm{d}\Delta\varphi_m/\mathrm{d}m$ of the phase differences between measurement and reference signal, see Eq. (3.4). The phase fluctuation of the m-th IF line pair with a standard deviation $\sigma_{\Delta\varphi,m,\lambda}$ comprises contributions originating from both IF lines as seen by $\mathrm{Rx}_{\mathrm{meas}}$ and by $\mathrm{Rx}_{\mathrm{ref}}$, see Eq. (3.18), and from the crosstalk as specified in Eq. (3.23). Because these three random processes are uncorrelated, the respective variances are to be added,

$$\sigma^2_{\Delta\varphi,m,\lambda} = \sigma^2_{\varphi,m,\lambda,\mathrm{meas}} + \sigma^2_{\varphi,m,\lambda,\mathrm{ref}} + \sigma^2_{\varphi,m,\mathrm{cross}} := \sigma^2_{\Delta\varphi,\lambda}. \tag{3.24}$$

If we assume spectrally perfectly flat combs, the SNR is the same for each line m, and therefore all lines have the same variance $\sigma^2_{\Delta\varphi,\lambda}$ of the phase difference. To obtain the slope, a linear regression is used. From the analytic formula for the slope uncertainty of a linear regression [193], the variance of the measured

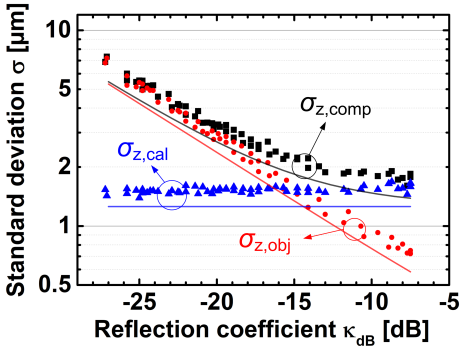

Fig. 3.7: Standard deviation of distance measurements (filled symbols) and theoretical curves (solid lines) as a function of the reflection coefficient $\kappa_{\mathrm{dB}} = 20\lg\kappa$ for the 1550 nm signal comb. The theoretical curves were obtained from calculations that are based on measured shapes of the comb spectra. For the 1550 nm signal comb, the total emitted signal comb power is –2.5 dBm at point D in Fig. 3.1. Noise and temperature fluctuations dictate the standard deviations for the distance measurements at the object wavelength (red, $\sigma_{z,\mathrm{obj}}$) and at the calibration wavelength (blue,$\sigma_{z,\mathrm{cal}}$). The standard deviation decreases with an increasing reflection coefficient when measuring at the object wavelength, while the return path for the calibration wavelength and therefore the measured standard deviation remains essentially constant. However, because there is less power available for the calibration measurement, we find that $\sigma_{z,\mathrm{cal}} > \sigma_{z,\mathrm{obj}}$ for a high reflection coefficient in the object path. The variance $\sigma^2_{z,\mathrm{comp}}$ for the compensated distance measurement results from adding the variances $\sigma^2_{z,\mathrm{obj}}$ and $\sigma^2_{z,\mathrm{cal}}$. The smallest standard deviation is $\sigma_{z,\mathrm{comp}} = 2\,\mu\mathrm{m}$ and is dominated by the standard deviation of the calibration measurement.

distance z at center wavelength λ can be calculated when using a number of N comb lines,

$$\sigma^2_{z,\lambda} = \frac{\sigma^2_{\Delta\varphi,\lambda}}{N}\,\frac{3}{\left(\omega_{\mathrm{mod,sig}}/c\right)^2\left(N^2-1\right)}. \tag{3.25}$$

The evaluation of N =7 comb lines with $f_{\mathrm{mod,sig}} = 40$ GHz corresponds to the interrogation of an optical spectrum with 240 GHz bandwidth. It is a key feature of the dual comb-based heterodyne detection that robust and inexpensive low-frequency (<200 MHz) electronic detection is sufficient for high-precision distance measurement, while exploiting optical bandwidths of hundreds or even thousands of gigahertz. To fully understand the system capabilities and limitations, we use a numerical model considering that the combs are not spectrally flat. Measurement results together with calculated data are plotted

in Fig. 3.7. The standard deviations of both individual measurements $\sigma_{z,\mathrm{obj}}$ and $\sigma_{z,\mathrm{cal}}$ as well as the standard deviation of the temperature-compensated measurement $\sigma_{z,\mathrm{comp}}$ are plotted as a function of reflection coefficient $\kappa_{\mathrm{dB}} = 20\lg\kappa$ for the 1550 nm signal comb (total power –2.5 dBm at point D in Fig. 3.1). The standard deviation $\sigma_{z,\mathrm{obj}}$ of the distance measurement to the object surface decreases with an increasing reflection coefficient κ, while the standard deviation $\sigma_{z,\mathrm{cal}}$ of the measured distance to the calibration mirror remains essentially constant. The results of the compensated distance measurements (red circles) confirm the theoretical prediction (solid line) according to Sect 3.3. The parameters used for the calculations are listed in Appendix E. For large reflection coefficients of the object surface, the precision of the compensated measurement is limited by the uncertainty of the calibration measurement. The high uncertainty of the calibration measurement results from the fact that the comb generators see a higher modulator insertion loss at 1300 nm. For small reflection coefficients, the object measurement dominates the uncertainty of the compensated measurement. A detailed analysis of the effect of the distribution of optical power between object and calibration measurement is offered in Appendix F. Nevertheless, the reflection coefficient has a dynamic range of 20 dB for a standard deviation of distance measurements below 8 µm. Therefore the distance to a large variety of surfaces can be measured accurately. For characterization independent of speckle-induced phase noise, which depends on the specific surface roughness, a mirror was used as a measurement target for the measurements presented in Fig. 3.7. Measurements to optically rough surfaces include an additional error due to speckle-induced phase noise with a magnitude depending on the surface characteristics [133, 194, 195].

3.2.3.6 Performance comparison with the state of the art

In addition to measurement accuracy the time needed for one measurement is an important parameter, especially if motion blur should be avoided when scanning an object by moving a measurement spot over its surface, or if fast and dense sample digitization is required.

A compilation of standard deviations σ and measurement times τ for published comb-based distance measurement systems is plotted in Fig. 3.8. The dashed line represents the relation $\sigma = p\ \tau^{-1/2}$ for averaging statistically independent noisy samples. The proportionality factor p is determined by

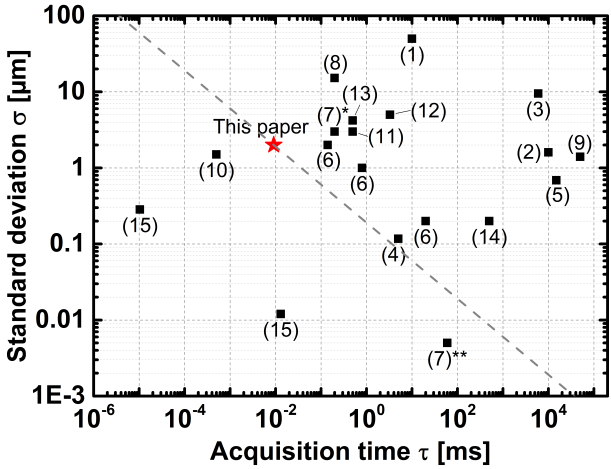

Fig. 3.8: Standard deviation σ of distance measurement and acquisition time τ in a double-logarithmic display for published comb-based distance measurement systems exploiting synthetic-wavelength interferometry. The assignment of the labels (numbers in round brackets) to the associated literature reference is documented in Table 3.1. The dashed line represents the relation $\sigma = p\ \tau^{-1/2}$ for averaging statistically independent noisy samples. The proportionality factor $p = 2\,\mu\text{m}\sqrt{9.1\,\mu\text{s}} = 6 \times 10^{-9}\,\text{m}\ \text{s}^{1/2}$ is determined by our experimental data (label ★, $\sigma = 2\,\mu\text{m}$, $\tau = 9.1\,\mu\text{s}$). Demonstrations with smaller p are found below the dashed line and have a smaller standard deviation for a given measurement time. Demonstration (7)** stands out due to a standard deviation of 5 nm at 60 ms acquisition time, which was achieved by combining SWI with classical optical interferometry at a single comb tone. Considering the SWI part only, the standard deviation of demonstration (7) amounts to 3 µm at 0.2 ms acquisition time, indicated by data point (7)*. Considering pure SWI measurements only, our experiment outperforms all previous demonstrations except for (10) and (15), both of which relied on broadband parametric combs with associated complex setups.

Table 3.1: Labels used in Fig. 3.8, denoting the published performance parameters of comb-based distance measurement systems, and the associated literature reference

Label	Literature reference
(1)	[35] K. Minoshima et al., Appl. Opt. **39**(30), 5512–5517 (2000)
(2)	[127] K. Minoshima et al., 13th Int. Conf. on Ultrafast Phenomena (OSA, 2002), TuB3
(3)	[121] N. R. Doloca et al, Meas. Sci. Technol. **21**(11), 115302–115309 (2010)
(4)	[126] J. Lee et al., Nature Photonics **4**(10), 716–720 (2010)
(5)	[124] S. Yokoyama et al., Opt. Express **17**(20), 17324–17337 (2009)
(6)	[37] T.-A. Liu et al., Opt. Express **19**(19), 18501–18509 (2011)
(7)	[34] I. Coddington et al., Nature Photonics **3**(6), 351–356 (2009)
(8)	[118] J. Lee et al., Meas. Sci. Technol. **24**(4), 45201–45209 (2013)
(9)	[125] X. Wang et al., Precis. Eng. **37**(3), 635–639 (2013)
(10)	[116] V. Ataie et al., in Opt. Fiber Comm. Conf. (OSA, 2013), OTh3D2
(11)	[133] E. Baumann et al., Opt. Express **22**(21), 24914–24928 (2014)
(12)	[J4] C. Weimann et al., Appl. Opt. **54**(20), 6334–6344 (2015)
(13)	[128] H. Zhang et al., IEEE Photonics J. **7**(3), 1–8 (2015)
(14)	[129] M.-G. Suh et al., Science **359**, 884–887 (2018)
(15)	[J8] P. Trocha et al., Science **359**, 887–891 (2018)

our experimental data denoted by the label ★. Measurement systems with smaller p lie below the dashed line and have a smaller standard deviation for a given measurement time. System (7) (ref. [34]) excels in terms of precision, but at the cost of an elaborate setup: Two MLL frequency combs are used, which are phase-locked to achieve linewidths of a few Hertz, and the accuracy of the synthetic-wavelength interferometry is improved by an additional interferometric measurement, which is only possible for mirror-like flat object surfaces.

System (10) (ref. [116]) achieves an impressively small measurement time, again at the cost of setup complexity: The system comprises two paramet-

ric comb generators, each with one phase modulator, two injection-locked laser diodes, wavelength-division multiplexing splitters and combiners, two high-power fiber amplifiers, and multiple nonlinear and linear fiber sections. Recently, in system (15) (ref. [J8]), two broadband Kerr combs and high-frequency detection electronics are utilized to achieve an impressive combination of small measurement time and high precision. However, the generation of two Kerr comb involves complicated setups with high power optical amplifiers and the utilized high-frequency detection electronics are prohibitively expensive for many industrial applications. In contrast to that, our demonstration relies on a comparatively simple concept that only comprises electro-optic modulators and the associated drive circuitry, enabling detection and data processing with relatively low-frequency electronics, and is amenable to photonic integration [J5, J10, J11].

3.2.4 Experimental demonstration

3.2.4.1 Outlier removal

The slope $\mathrm{d}\Delta\varphi_m/\mathrm{d}m$ for determining the distance is calculated from a linear regression model. This allows the implementation of a robust distance outlier removal: The two parameters of a linear regression model are determined by minimizing the squared differences between measured phase values $\Delta\varphi_m$ and the model values $\Delta\Phi_m$. The quality of the fit is quantified with the coefficient of determination $r^2 = 1 - SS_{\mathrm{res}}/SS_{\mathrm{tot}}$, which is specified by the sum of the squared errors $SS_{\mathrm{res}} = \sum_m (\Delta\varphi_m - \Delta\Phi_m)^2$ between measurements and model, and by the sum of the squared deviations $SS_{\mathrm{tot}} = \sum_m \left(\Delta\varphi_m - \overline{\Delta\varphi_m}\right)^2$ of the measurements from the mean $\overline{\Delta\varphi_m}$. Setting a suitable threshold to r^2 allows the removal of outliers, which may, e.g., be caused by particularly noisy phase measurements in case of a small object reflection κ, or by phase unwrapping errors.

We demonstrate the viability of the outlier removal technique for an extreme case with large reflected power variations. To this end, we use an ordinary printed-circuit board as depicted in Fig. 3.9(a) as a test sample and scan its surface topography along a line indicated as *x*. The sensor is moved with the help of a CMM and is kept at a constant height. The variety of surface

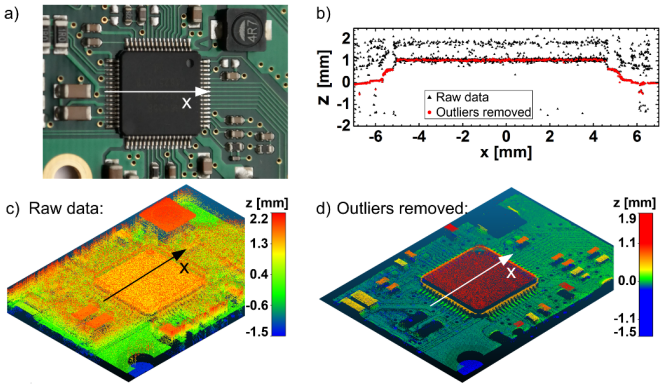

Fig. 3.9: Demonstration of outlier removal. (a) Photograph of a printed-circuit board (PCB), comprising a variety of surfaces including an integrated circuit (IC) with a black polymer package. (b) Height profile of the sample along a line in x-direction, across the black package of the IC, see Subfigure (a). Black: Raw data. Red: Data after outlier removal. (c) Color-coded surface profile with 1.5 million measurement points resulting from a measurement scan without outlier removal. (d) Color-coded surface profile after outlier removal, comprising $0.8{\times}10^6$ measurement points with an r^2 better than the threshold 0.99.

types, the surface height variations, and the limited depth of field (300 µm) of our objective lens lead to large variations of the reflected optical power and therefore to uncertainties in the measured height profile. Moreover, the measured distances cover almost the whole of the unambiguity range of 3.7 mm, making unwrapping errors of the noisy phases more likely at the edges of the unambiguity range. This leads to a significant number of outliers as can be seen in Fig. 3.9(b), which shows the raw data (black filled circles) of the height profile along an x-directed scan in Fig. 3.9(a). However, if we consider only the subset of data points which leads to a coefficient of determination $r^2 \geq 0.99$, a clean height profile can be extracted, see red dots in Fig. 3.9(b). This is also to be seen when comparing the fussy display of the raw data in Fig. 3.9(c) with the crisp display in Fig. 3.9(d) where almost 50 % of the data points were removed as outliers. In practice, the number of outliers is not as extreme, because the CMM adaptively adjusts the sensor height with respect to the surface according to the measured distance, thereby avoiding disadvantageous defocusing and measurements at the edge of the unambiguity range. Lateral scanning is stopped during height adjustments and continued

after the height has been adjusted to within a chosen range intervall above the surface. This procedure avoids the record of range data with additional potential errors caused by simultaneous movement in z-direction and range data acquisition. By operating close to the focal length of the objective lens, the amount of collected back-scattered light is maximized, which increases the obtained SNR, thus improving the measurement precision, as analyzed in Sections 3.2.3.3 – 3.2.3.5.

3.2.4.2 Verification by tactile measurements

To confirm the accuracy of our distance measurement scheme, we compare optical profile measurements of steps in milled aluminum blocks with tactile reference measurements. Also here, we used the outlier removal technique described in the previous section. For scanning we use again a CMM (Carl Zeiss O-Inspect 442 with VAST XXT probe) with a maximum scanning speed of 300 mm/s in x- and y-direction and 100 mm/s in z-direction. For tactile height measurements, the system has a maximum permissible probing error $\mathrm{MPE}_P = 1.9\,\mu\mathrm{m}$, [196, 197]. Five samples were prepared with typical surface treatments encountered in industrial applications to provide exemplary results for a variety of surfaces, see Fig. 3.10(a). The surface profile is measured along a line (x-axis) across the first five steps #1,#2, . . . , #5, taking 60 measurements with the tactile probe and 40,000 measurements with the optical sensor, see Fig. 3.10(b). The differences between the averaged optical sensor values $\overline{z}_{\mathrm{opt}}$ and the averaged mechanically measured values $\overline{z}_{\mathrm{tact}}$ are plotted in Fig. 3.10(d) for each step surface. For all samples, these differences are in the range of a few micrometers only. A full 3D point cloud from optical measurements is shown in Fig. 3.10(c), showing clearly the topography of the “KIT IPQ” engraving.

3.2.4.3 Application examples

In this section we give two more examples for surface profile measurements. In Fig. 3.11, a photograph and the measured height profile of the backside of a 20 Euro-cent coin are shown. The waist radius 8.7 µm of our measurement beam together with the high mechanical resolution of the CMM allows to resolve fine details that are not accessible with a conventional tactile measure-

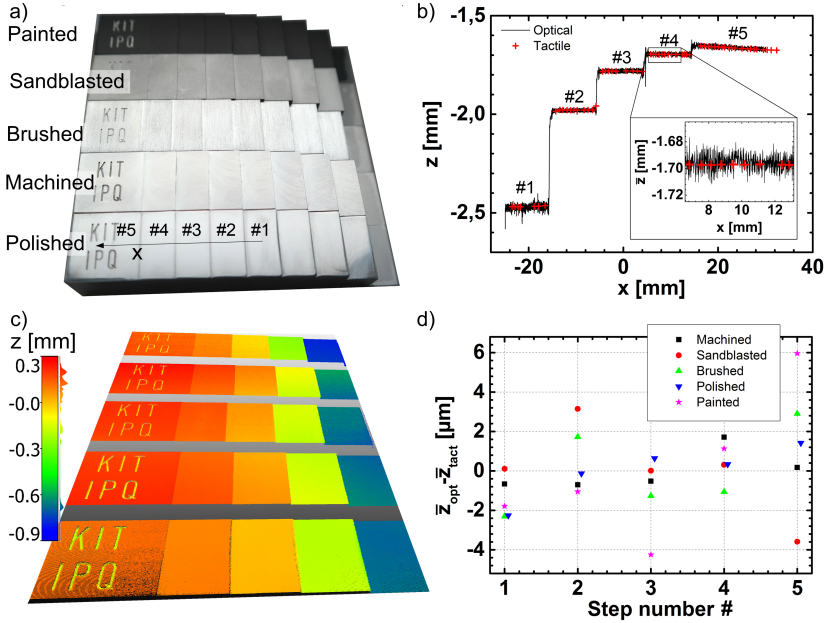

Fig. 3.10: Comparison of optical measurements to tactile reference measurements. (a) Photograph of steps milled in an aluminum block and prepared with different surface treatments. (b) Scan along the line marked by the arrow on the polished sample. Optical measurements (black) and tactile measurements (red) agree well. Tactile measurements were performed with an industrial coordinate measuring machine (CMM). (c) Color-coded surface profiles of the samples shown in (a), $5.1{\times}10^6$ points in total. The measurements show clearly the topography of the "KIT IPQ" engraving (d) Differences of mean values of optical ($\overline{z}_{\mathrm{opt}}$) and of tactile measurements ($\overline{z}_{\mathrm{tact}}$) for each step. For all samples, these differences are in the range of a few micrometers.

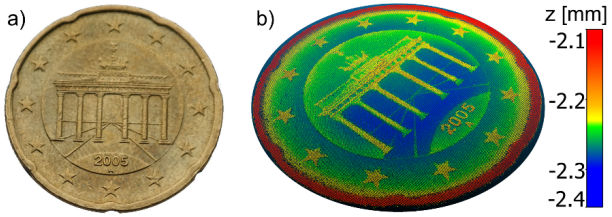

Fig. 3.11: Surface topography measurements of a 20 Euro-cent coin. (a) Photograph of the coin. (b) Color-coded surface profile with 0.7×10^6 points resulting from a scanning optical topography measurement.

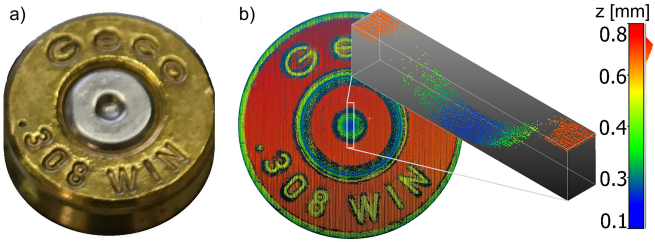

Fig. 3.12: Surface topography measurements. (a) Photograph of the backside of a used bullet casing. (b) Color-coded surface profile with 0.6×10^6 points resulting from a scanning optical topography measurement. Inset: Zoomed view of a volume, detailing a cross section through the indention caused by the firing pin.

ment system. Another example is shown in Fig. 3.12, where the photograph of a used bullet casing together with the height profile scan is depicted. The dent made by the firing pin can be seen clearly. Imperfections of the firing pin geometry leave characteristic marks on the bullet casing which may be used in forensic studies to identify the gun that was used to fire the bullet [198–200]. The inset in Fig. 3.12 provides a zoomed view of a volume, detailing a cross section through the indention. Our outlier removal technique described in Section 3.2.4.1 leads to less densely sampled regions, where a high angle of incidence together with the specular surface characteristics of the specific sample are the cause of low returned power levels. Only reliable measurement points are recorded. The high accuracy of the measured height profile paves the road for an application in other fields such as in forensics.

3.2.5 Summary and conclusion

We have demonstrated a robust, technically straightforward, and yet precise comb-based distance measurement concept based on dual-color modulator-generated frequency combs. The technique can maintain its precision even under realistic industrial boundary conditions. An acquisition time of 9.1 µs per point avoids motion blur. We have further introduced a compensation scheme that eliminates temperature-induced drift of the fiber optic components and thus permits placement of critical optical and electronic components many meters remote from the sensor head. This scheme enables operation of the sensor on a coordinate measuring machine and is key to deploying the technique in a harsh industrial environment. To the best of our knowledge, our experiments represent the first demonstration of dead-zone-free drift compensation for comb-based distance measurements through optical fibers. In the current implementation, measured distances are output at a rate of 3.3 kHz, which allows a rapid recording of a large numbers of points while continuously scanning the sensor head. We demonstrate the viability of the concept by height profile measurements on a wide range of samples, where we achieve precisions in the single-digit micrometer regime.

Appendix A: Multi-heterodyne detection

In the following section, we give a rigorous mathematical description of the measurement scheme, which relies on quadratic detection of detuned frequency combs (FC) by the measurement and reference detector. Analytical signals $\underline{E}(\mathrm{t})$ are used to describe the time-domain electric fields, with the real part of the analytical signal representing the physically relevant field, $E(\mathrm{t}) = \Re\left\{\underline{E}(\mathrm{t})\right\}$. The optical power is then given by $P = Z_0^{-1}\left\langle E^2(t)\right\rangle$, where $\langle -\rangle$ denotes the average over a few cycles of the optical carrier and $Z_0 = 376.7\,\Omega$ represents the wave impedance of free space. For simplicity, we describe here only one set of frequency combs at a single center wavelength λ_{cal} or λ_{obj}. In a first step we consider the measurement detector ($\mathrm{Rx}_{\mathrm{meas}}$) only. In accordance to the system detailed in Fig. 3.1, we consider the complex optical amplitudes $\underline{E}_{\mathrm{sig,meas}}$ for

the signal comb arriving at the measurement detector. Each signal comb line l has an (angular) optical frequency $\omega_{l,\mathrm{sig}}$,

$$\omega_{l,\mathrm{sig}} = \omega_{0,\mathrm{sig}} + l\omega_{\mathrm{mod,sig}}. \tag{3.26}$$

The amplitudes of the signal comb lines are denoted as $\hat{E}_{l,\mathrm{sig,meas}}$, and the associated optical path length to the detector amounts to $2z + D_{\mathrm{sig,meas}}$, where $D_{\mathrm{sig,meas}}$ denotes the optical path length through the measurement setup to and from the origin $z = 0$ of the measurement coordinate system, see Fig. 3.1. Similarly, the complex optical amplitudes of the LO comb at the measurement detector are denoted as $\underline{E}_{\mathrm{LO,meas}}$, and each comb line m has an (angular) optical frequency $\omega_{m,\mathrm{LO}}$,

$$\omega_{m,\mathrm{LO}} = \omega_{0,\mathrm{LO}} + m\omega_{\mathrm{mod,LO}} = \left(\omega_{0,\mathrm{sig}} + \Delta\omega_0\right) + m\left(\omega_{\mathrm{mod,sig}} + \Delta\omega_{\mathrm{mod}}\right), \tag{3.27}$$

with a center frequency detuning $\Delta\omega_0$, a detuning of the line spacing of $\Delta\omega_{\mathrm{mod}}$, and an amplitude $\hat{E}_{m,\mathrm{LO,meas}}$. The LO comb arrives at the measurement detector after propagation over the optical path length $D_{\mathrm{LO,meas}}$, which is entirely located within the measurement setup. The complex amplitudes of the two FC at the measurement detector are then given as

$$\begin{aligned}
\underline{E}_{\mathrm{sig,meas}}(t) &= \sum_l \hat{E}_{l,\mathrm{sig,meas}} \exp\left(\mathrm{j}\omega_{l,\mathrm{sig}}t\right) \exp\left(-\mathrm{j}\left(2z + D_{\mathrm{sig,meas}}\right)\omega_{l,\mathrm{sig}}/c\right) \\
\underline{E}_{\mathrm{LO,meas}}(t) &= \sum_m \hat{E}_{m,\mathrm{LO,meas}} \exp\left(\mathrm{j}\omega_{m,\mathrm{LO}}t\right) \exp\left(-\mathrm{j}D_{\mathrm{LO,meas}}\omega_{m,\mathrm{LO}}/c\right).
\end{aligned} \tag{3.28}$$

The superposition of the signal and LO comb on perfectly balanced photodetectors (BD) with sensitivity S leads to a photocurrent containing multiple IF tones. The photocurrent i_{meas} of the measurement detector is given by

$$\begin{aligned}
i_{\mathrm{meas}}(t) &= Z_0^{-1} S \cdot \Re\left\{\underline{E}_{\mathrm{sig,meas}}(t)^* \, \underline{E}_{\mathrm{LO,meas}}(t)\right\} \\
&= Z_0^{-1} S \cdot \Re\left\{\begin{array}{l}
\displaystyle\sum_l \sum_m \hat{E}_{l,\mathrm{sig,meas}} \hat{E}_{m,\mathrm{LO,meas}} \\
\cdot \exp\left(\mathrm{j}\left(\Delta\omega_0 + (m-l)\,\omega_{\mathrm{mod,sig}} + m\Delta\omega_{\mathrm{mod}}\right)t\right) \\
\cdot \exp\left(\mathrm{j}\left(\left(2z + D_{\mathrm{sig,meas}}\right)\omega_{l,\mathrm{sig}} - D_{\mathrm{LO,meas}}\omega_{m,\mathrm{LO}}\right)/c\right)
\end{array}\right\}.
\end{aligned} \tag{3.29}$$

The photocurrent i_{ref} of the reference detector can be derived in an analogous way by replacing "meas" by "ref" in the subscripts,

$$\begin{aligned} i_{\mathrm{ref}}(t) &= Z_0^{-1} S \cdot \Re\left\{ \underline{E}_{\mathrm{sig,ref}}(t)^* \, \underline{E}_{\mathrm{LO,ref}}(t) \right\} \\ &= Z_0^{-1} S \cdot \Re\left\{ \begin{array}{l} \sum_l \sum_m \hat{E}_{l,\mathrm{sig,ref}} \hat{E}_{m,\mathrm{LO,ref}} \\ \cdot \exp\left(\mathrm{j}\left(\Delta\omega_0 + (m-l)\,\omega_{\mathrm{mod,sig}} + m\Delta\omega_{\mathrm{mod}}\right) t\right) \\ \cdot \exp\left(\mathrm{j}\left(D_{\mathrm{sig,ref}}\omega_{l,\mathrm{sig}} - D_{\mathrm{LO,ref}}\omega_{m,\mathrm{LO}}\right)/c\right) \end{array} \right\}. \end{aligned} \tag{3.30}$$

In this relation, the quantities $D_{\mathrm{sig,ref}}$ and $D_{\mathrm{LO,ref}}$ denote the optical path lengths between the respective comb source and the reference detector.

The frequency detunings $\Delta f_0 = \Delta\omega_0/(2\pi)$ and $\Delta f_{\mathrm{mod}} = \Delta\omega_{\mathrm{mod}}/(2\pi)$ amount to tens of megahertz and are small compared to the line spacing $\omega_{\mathrm{mod,sig}}$ of roughly 40 GHz. In theory, the photocurrent spectrum shows beat signals at distinct intermediate frequencies $f_{m,l}$,

$$f_{m,l} = \left|\Delta f_0 + (m-l)\, f_{\mathrm{mod,sig}} + m\,\Delta f_{\mathrm{mod}}\right|. \tag{3.31}$$

However, only a subset of these lines can actually be acquired by the photodetector and the subsequent A/D converter. For the FC deployed in our experiments, the analog bandwidth B of the used photodetectors amounts to 350 MHz and is much smaller than the ~ 40 GHz line spacing of the frequency combs, $B \ll f_{\mathrm{mod,sig}} \approx f_{\mathrm{mod,LO}}$. Moreover, the number of comb lines is limited such that $m\,\Delta f_{\mathrm{mod,LO}} \ll f_{\mathrm{mod,sig}} \approx f_{\mathrm{mod,LO}}$ for all comb line indices m.

As a consequence, for a given LO comb line m, only the beat note with the corresponding signal comb of same index $m = l$ is visible in the photocurrent. IF lines are hence found at distinct frequencies $f_{\mathrm{IF},m} = |\Delta f_0 + m\,\Delta f_{\mathrm{mod}}|$. These signals are amplified by a transimpedance amplifier with a transimpedance of R_{TIA}. The resulting voltage signal $V_{\mathrm{meas}}(t)$ at the measurement detector is then given as

$$\begin{aligned} V_{\mathrm{meas}}(t) &= \sum_m \hat{V}_{m,\mathrm{meas}} \cos\left(\left(\Delta\omega_0 + m\Delta\omega_{\mathrm{mod}}\right) t + \varphi_{m,\mathrm{meas}}\right), \\ \hat{V}_{m,\mathrm{meas}} &= S R_{\mathrm{TIA}} \sqrt{2P_{m,\mathrm{sig,meas}} 2P_{m,\mathrm{LO,meas}}}. \end{aligned} \tag{3.32}$$

The corresponding phases $\varphi_{m,\mathrm{meas}}$ of the IF lines at the measurement detector can be derived from Eq. (3.29),

$$\begin{aligned}
&\varphi_{m,\mathrm{meas}}\left(2z + D_{\mathrm{sig,meas}}, D_{\mathrm{LO,meas}}\right) \\
&\quad = \left(\left(2z + D_{\mathrm{sig,meas}}\right)\omega_{m,\mathrm{sig}} - D_{\mathrm{LO,meas}}\omega_{m,\mathrm{LO}}\right)/c \\
&\quad = \left(\left(2z + D_{\mathrm{sig,meas}}\right) - D_{\mathrm{LO,meas}}\right)\left(\omega_{0,\mathrm{sig}} + m\omega_{\mathrm{mod,sig}}\right)/c \\
&\qquad - D_{\mathrm{LO,meas}}\left(\Delta\omega_0 + m\Delta\omega_{\mathrm{mod}}\right)/c \\
&\quad = 2\pi\left(\left(2z + D_{\mathrm{sig,meas}}\right) - D_{\mathrm{LO,meas}}\right)\Lambda_m^{-1} \\
&\qquad + 2\pi\left(\left(2z + D_{\mathrm{sig,meas}}\right) - D_{\mathrm{LO,meas}}\right)\lambda_{0,\mathrm{sig}}^{-1} \\
&\qquad - D_{\mathrm{LO,meas}}\left(\Delta\omega_0 + m\Delta\omega_{\mathrm{mod}}\right)/c.
\end{aligned} \tag{3.33}$$

The last part of Eq. (3.33) contains the so-called synthetic wavelength

$$\Lambda_m = c\left(m f_{\mathrm{mod,sig}}\right)^{-1} \tag{3.34}$$

and shows the relation to classical interferometry with a single optical wavelength λ, where the phase shift φexperienced by an optical signal after propagation over the optical path length D is determined by $\varphi = 2\pi D\lambda^{-1}$.

The beat signals at the reference detector have the exactly same frequencies as the beat signals at the measurement detector and serve as phase references. Their phases are determined analogously to Eq. (3.33) and are given as

$$\varphi_{m,\mathrm{ref}}\left(D_{\mathrm{sig,ref}}, D_{\mathrm{LO,ref}}\right) = \left(D_{\mathrm{sig,ref}}\omega_{m,\mathrm{sig}} - D_{\mathrm{LO,ref}}\omega_{m,\mathrm{LO}}\right)/c. \tag{3.35}$$

The phase differences of the various beat signals are given by:

$$\begin{aligned}
\Delta\varphi_m(z) =& \varphi_{m,\mathrm{meas}}\left(2z + D_{\mathrm{sig,meas}}, D_{\mathrm{LO,meas}}\right) - \varphi_{m,\mathrm{ref}}\left(D_{\mathrm{sig,ref}}, D_{\mathrm{LO,ref}}\right) \\
&= \left(2z + D_{\mathrm{sig,meas}} - D_{\mathrm{LO,meas}} - \left(D_{\mathrm{sig,ref}} - D_{\mathrm{LO,ref}}\right)\right) m\omega_{\mathrm{mod,sig}}/c \\
&\quad + \left(2z + D_{\mathrm{sig,meas}} - D_{\mathrm{LO,meas}} - \left(D_{\mathrm{sig,ref}} - D_{\mathrm{LO,ref}}\right)\right)\omega_{0,\mathrm{sig}}/c \\
&\quad - \left(D_{\mathrm{LO,meas}} - D_{\mathrm{LO,ref}}\right)\Delta\omega_0/c \\
&\quad - \left(D_{\mathrm{LO,meas}} - D_{\mathrm{LO,ref}}\right) m\Delta\omega_{\mathrm{mod}}/c.
\end{aligned} \tag{3.36}$$

The distance information is extracted from evaluating the slope of the unwrapped phase differences $\Delta\varphi_m(z)$ as a function of the comb line index m. This slope is given by

$$\begin{aligned}\frac{\mathrm{d}\Delta\varphi_m(z)}{\mathrm{d}m} =& \frac{\omega_{\mathrm{mod,sig}}}{c}\left(2z + D_{\mathrm{sig,meas}} - D_{\mathrm{LO,meas}} - D_{\mathrm{sig,ref}} + D_{\mathrm{LO,ref}}\right) \\ &- \frac{\Delta\omega_{\mathrm{mod}}}{c}\left(D_{\mathrm{LO,meas}} - D_{\mathrm{LO,ref}}\right).\end{aligned} \tag{3.37}$$

If the optical path lengths inside the fiber was constant, all terms containing $D_{\mathrm{sig,meas}}$, $D_{\mathrm{LO,meas}}$, $D_{\mathrm{sig,ref}}$ and $D_{\mathrm{LO,ref}}$ in Eq. (3.37) could be eliminated by a simple calibration to an arbitrary zero point z_0 by subtracting a constant offset such that $\mathrm{d}\Delta\varphi_m(z_0 = 0)/\mathrm{d}m = 0$. For any other distance, the quantity z - z_0 could then be determined accurately from the measured slope as $\omega_{\mathrm{mod,sig}}$ and c are precisely known. However, due to temperature fluctuations of the effective optical path length fluctuation setup and the optical fibers, the various optical path lengths change by $\Delta D_{\mathrm{sig,meas}}$, $\Delta D_{\mathrm{LO,meas}}$, $\Delta D_{\mathrm{sig,ref}}$ and $\Delta D_{\mathrm{LO,ref}}$ within a time of $t - t_0$, see Eq. (3.1). The difference of the slope with respect to $z_0 = 0$, $t_0 = 0$ is then given by

$$\begin{aligned}&\frac{\mathrm{d}\Delta\varphi_m(z,t)}{\mathrm{d}m} - \frac{\mathrm{d}\Delta\varphi_m(z_0 = 0, t_0 = 0)}{\mathrm{d}m} \\ =& \frac{\omega_{\mathrm{mod,sig}}}{c}\left(2z + \Delta D_{\mathrm{sig,meas}} - \Delta D_{\mathrm{LO,meas}} - \left(\Delta D_{\mathrm{sig,ref}} - \Delta D_{\mathrm{LO,ref}}\right)\right) \\ &- \frac{\Delta\omega_{\mathrm{mod}}}{c}\left(\Delta D_{\mathrm{LO,meas}} - \Delta D_{\mathrm{LO,ref}}\right). \\ \cong& \frac{\omega_{\mathrm{mod,sig}}}{c}\left(2z + \Delta D_{\mathrm{sig,meas}} - \Delta D_{\mathrm{LO,meas}} - \left(\Delta D_{\mathrm{sig,ref}} - \Delta D_{\mathrm{LO,ref}}\right)\right).\end{aligned} \tag{3.38}$$

The third line in Eq. (3.38) can be neglected, as $\Delta\omega_{\mathrm{mod}} \ll \omega_{\mathrm{mod,sig}}$ holds, and because for a typical fiber installation $\left|\Delta D_{\mathrm{LO,meas}} - \Delta D_{\mathrm{LO,ref}}\right| \ll \left|\Delta D_{\mathrm{sig,meas}} - \Delta D_{\mathrm{LO,meas}} - \left(\Delta D_{\mathrm{sig,ref}} - \Delta D_{\mathrm{LO,ref}}\right)\right|$ is true.

Appendix B: Balanced detection in the presence of noise

In the following section, we analyze the influence of relative intensity noise (RIN) in the balanced reception scheme. Using a signal representation as in

Eq. (3.16), the RIN is treated as a complex noise component $\underline{N}(t) = x''(t) + \mathrm{j}y''(t)$ with a real in-phase noise component $x''(t)$ and a real quadrature noise component $y''(t)$. The noise is Gaussian, unbiased, $\langle x''(t)\rangle = 0$, $\langle y''(t)\rangle = 0$, and the corresponding variances are $\sigma^2_{x''} = \sigma^2_{y''} = \widehat{w}_{o,\mathrm{RIN}}\Delta f$, where we assume flat optical spectral noise power density of $\widehat{w}_{o,\mathrm{RIN}}$ within the detection bandwidth Δf.

Like the shot noise in Eq. (3.12), the RIN is determined by the total optical comb powers $P_{\mathrm{sig},\lambda}$ and $\mathrm{P}_{\mathrm{LO},\lambda}$ [201]. The detection process is thus treated as heterodyne reception of a monochromatic signal with a monochromatic LO, each with an optical power equal to the corresponding total optical comb power. Signal and LO field are derived from the same source, but are decorrelated with respect to the RIN(f)-bandwidth of $B = 1\,\mathrm{GHz}$ by a spatial separation larger than $c/(nB) = 0.67\mathrm{m}$ inside fibers with a refractive index of $n = 1.5$. As a consequence, both contributions are statistically independent. Furthermore, the contributions of both lasers (wavelengths λ_{obj} and λ_{cal}) are statistically independent. For a simpler description, we first consider only a single laser source. The variances of the voltage fluctuations caused by both lasers are then added, see Eq. (3.11).

The real electric fields of signal and LO, $E_{\mathrm{sig}}(t)$ and $E_{\mathrm{LO}}(t)$, with amplitudes $\hat{E}_{\mathrm{sig,LO}}$ and frequencies $f_{\mathrm{sig,LO}} = \omega_{\mathrm{sig,LO}}/(2\pi)$ are perturbed by the in-phase and quadrature RIN components, $x''_{\mathrm{sig,LO}}(t)$ and $y''_{\mathrm{sig,LO}}(t)$:

$$\begin{aligned} E_{\mathrm{sig}}(t) &= \left[\hat{E}_{\mathrm{sig}} + x''_{\mathrm{sig}}(t)\right]\cos\left(\omega_{\mathrm{sig}}t\right) - y''_{\mathrm{sig}}(t)\sin\left(\omega_{\mathrm{sig}}t\right) \\ E_{\mathrm{LO}}(t) &= \left[\hat{E}_{\mathrm{LO}} + x''_{\mathrm{LO}}(t)\right]\cos\left(\omega_{\mathrm{LO}}t\right) - y''_{\mathrm{LO}}(t)\sin\left(\omega_{\mathrm{LO}}t\right). \end{aligned} \tag{3.39}$$

The fields in Eq. (3.39) are incident on the two ports of a 3 dB coupler in front of a balanced receiver. Assuming an ideal 3 dB coupler with perfect splitting ratio, the fields $E_{1,2}(t)$ incident on each photodiode 1 and 2 are given as:

$$E_1(t) = \frac{1}{\sqrt{2}}\left(E_{\mathrm{sig}}(t) - E_{\mathrm{LO}}(t)\right) \qquad E_2(t) = \frac{1}{\sqrt{2}}\left(E_{\mathrm{sig}}(t) + E_{\mathrm{LO}}(t)\right). \tag{3.40}$$

The photocurrents $i_1(t)$ and $i_2(t)$ of each photodiode with a sensitivity S are calculated as

$$i_1(t) = Z_0^{-1} S\left\langle E_1^2(t)\right\rangle \qquad i_2(t) = Z_0^{-1} S\left\langle E_2^2(t)\right\rangle. \tag{3.41}$$

Evaluating Eq. (3.41) by forming the square, averaging over an optical period and neglecting all terms containing only as small noise contributions, the difference of the photocurrents $i_{-}(t) = i_2(t) - i_1(t)$ is given as

$$\begin{aligned} i_{-}(t) =& i_2(t) - i_1(t) \\ =& Z_0^{-1} S \left[\hat{E}_{\mathrm{sig}} \hat{E}_{\mathrm{LO}} \cos\left(\left(\omega_{\mathrm{sig}} - \omega_{\mathrm{LO}} \right) t \right) \right. \\ &+ \hat{E}_{\mathrm{sig}} \left(x''_{\mathrm{LO}}(t) \cos\left(\left(\omega_{\mathrm{sig}} - \omega_{\mathrm{LO}} \right) t \right) + y''_{\mathrm{LO}}(t) \sin\left(\left(\omega_{\mathrm{sig}} - \omega_{\mathrm{LO}} \right) t \right) \right) \\ &\left. + \hat{E}_{\mathrm{LO}} \left(x''_{\mathrm{sig}}(t) \cos\left(\left(\omega_{\mathrm{sig}} - \omega_{\mathrm{LO}} \right) t \right) - y''_{\mathrm{sig}}(t) \sin\left(\left(\omega_{\mathrm{sig}} - \omega_{\mathrm{LO}} \right) t \right) \right) \right]. \end{aligned} \tag{3.42}$$

The first term in Eq. (3.42) is the noise-free intermediate frequency term (IF), the second term corresponds to noise of the LO laser down-converted by the signal, and the third term corresponds to noise of the signal laser down-converted by the LO. RIN leads to a random fluctuation of the photocurrent amplitude at the intermediate frequency (IF) $\omega_{\mathrm{sig}} - \omega_{\mathrm{LO}}$, which is given by the sum of the variances of the statistically independent noise terms in Eq. (3.42),

$$\begin{aligned} \left\langle i^2_{\mathrm{RIN,tot}} \right\rangle =& \left\langle \left| i_{\mathrm{RIN,sig}} \right|^2 \right\rangle + \left\langle \left| i_{\mathrm{RIN,LO}} \right|^2 \right\rangle \\ =& \frac{1}{2} Z_0^{-1} S^2 \left(\hat{E}^2_{\mathrm{sig}} \left(\sigma^2_{x'',LO} + \sigma^2_{y'',LO} \right) + \hat{E}^2_{\mathrm{LO}} \left(\sigma^2_{x'',\mathrm{sig}} + \sigma^2_{y'',\mathrm{sig}} \right) \right) \\ =& Z_0^{-1} S^2 \left(\hat{E}^2_{\mathrm{sig}} \widehat{w}_{o,\mathrm{RIN,LO}} + \hat{E}^2_{\mathrm{LO}} \widehat{w}_{o,\mathrm{RIN,sig}} \right) \Delta f \\ =& 2 S^2 \left(P_{\mathrm{sig}} \widehat{w}_{o,\mathrm{RIN,LO}} + P_{\mathrm{LO}} \widehat{w}_{o,\mathrm{RIN,sig}} \right) \Delta f, \end{aligned} \tag{3.43}$$

for optical powers $P_{\mathrm{sig,LO}} = Z_0^{-1} \left\langle E^2_{\mathrm{sig,LO}}(t) \right\rangle = \frac{1}{2} Z_0^{-1} \hat{E}^2_{\mathrm{sig,LO}}$. For given RIN power spectral densities $\widehat{w}_{o,\mathrm{RIN}}$ $\widehat{w}_{o,\mathrm{RIN,sig}}$ and $\widehat{w}_{o,\mathrm{RIN,LO}}$, the current fluctuation due to RIN can now be calculated. However, manufacturers of laser sources do not specify the fluctuation of *optical fields*, but rather the spectrum of the fluctuating *optical power* as measured by recording the spectrum of the fluctuating current with a directly detecting photodiode. The relation between these quantities is derived in Appendix C.

Appendix C: Optical field fluctuation and RIN

The height $\widehat{w}_{o,\mathrm{RIN}}$ of the constant optical RIN power spectral density (PSD) for both the signal and the LO source can be calculated from the associated electrical PSD $w_{i,\mathrm{RIN}}(f)$. Many laser manufacturers specify this value in terms of

$$\mathrm{RIN}(f) = \frac{w_{i,\mathrm{RIN}}(f)}{\langle i \rangle^2}. \tag{3.44}$$

To derive the relation between RIN(f) and $\widehat{w}_{o,\mathrm{RIN}}$, we use a signal representation as in Eq. (3.16). A harmonic electric field with real amplitude $\hat{E}$ and frequency f_0 is perturbed by complex noise $\underline{N}(t) = x'''(t) + \mathrm{j}y'''(t)$ with a real in-phase noise component $x'''(t)$ and a real quadrature noise component $y'''(t)$,

$$E(t) = \left[\hat{E} + x'''(t)\right]\cos(\omega_0 t) - y'''(t)\sin(\omega_0 t). \tag{3.45}$$

The noise is Gaussian, unbiased such that $\langle x'''(t)\rangle = 0$and $\langle y'''(t)\rangle = 0$, and the corresponding variances are $\sigma^2_{x'''} = \sigma^2_{y'''} = \widehat{w}_{o,\mathrm{RIN}}B$ assuming a flat optical PSD within an optical bandwidth B. With the photodetector sensitivity S, the photocurrent becomes

$$i(t) = Z_0^{-1}S\left\langle E^2(t)\right\rangle = \frac{1}{2}Z_0^{-1}S\left(\hat{E}^2 + \left\langle x'''^2(t)\right\rangle + \left\langle y'''^2(t)\right\rangle\right). \tag{3.46}$$

Using the Wiener-Khintchine theorem, the (two-sided) PSD $\Theta_i(f)$ can be found by calculating the covariance of the photocurrent, and by applying a Fourier transform,

$$\Theta_i(f) = \int_{-\infty}^{+\infty}\langle i(t)\,i(t-\tau)\rangle\exp(-\mathrm{j}2\pi\tau f)\,\mathrm{d}\tau. \tag{3.47}$$

With Eq. (3.46), Eq. (3.47) and when converting the two-sided spectrum $\Theta_i(f)$ to a one-sided spectrum, $w_i(f) = 2\Theta_i(f)$ for $f > 0$, $w_i(f) = 0$ for $f < 0$, the result is

$$w_i(f) = 2S^2 \begin{pmatrix} \left(\frac{1}{2}Z_0^{-1}\hat{E}^2 + \widehat{w}_{o,\mathrm{RIN}}B\right)^2 \delta(f) \\ + \widehat{w}_{o,\mathrm{RIN}}Z_0^{-1}\hat{E}^2\left[\mathrm{H}(f) - \mathrm{H}\left(f - \frac{B}{2}\right)\right] \\ + \widehat{w}_{o,\mathrm{RIN}}^2(B-f)\left[\mathrm{H}(f) - \mathrm{H}(f-B)\right] \end{pmatrix}. \tag{3.48}$$

The Heaviside function is defined by $\mathrm{H}(f) = 1$ for $f > 0$ and $\mathrm{H}(f) = 0$ for $f < 0$. If we exchange $S \to \alpha$, $\hat{E} \to P$, and compare the terms in Eq. (3.48) to [202], Eq. (4.5-11) and Eq. (4.5-13), we see that the relations are identical. The first term is disregarded, as an electrical spectrum analyzer measures spectra for frequencies $f > 0$ only such that a spectral DC component $\delta(f)$ is suppressed. The third term stems from photomixing noise with noise and is neglected here because for the given bandwidth $B \approx 1\,\mathrm{GHz}$ it is a small contribution. The second term $w_{i2}(f) = 2Z_0^{-1}S^2\widehat{w}_{o,\mathrm{RIN}}\hat{E}^2\left[\mathrm{H}(f) - \mathrm{H}(f - B/2)\right]$ represents the specified electrical $\mathrm{RIN}(f)$ for an optical power $P_o = \frac{1}{2}Z_0^{-1}\hat{E}^2$ in terms of the height $\widehat{w}_{o,\mathrm{RIN}}$ of the optical PSD,

$$\mathrm{RIN}(f) = \frac{w_{i2}(f)}{\langle i\rangle^2} = \begin{cases} \frac{2Z_0^{-1}S^2\widehat{w}_{o,\mathrm{RIN}}\hat{E}^2}{S^2P_o^2} = \frac{4\widehat{w}_{o,\mathrm{RIN}}}{P_o} & \text{for } 0 < f < \frac{B}{2}, \\ 0 & \text{else.} \end{cases} \tag{3.49}$$

For calculating the height $\widehat{w}_{o,\mathrm{RIN,sig}}$ and $\widehat{w}_{o,\mathrm{RIN,LO}}$ of the optical noise power densities of signal and LO, we need the constant height $\mathrm{RIN}_{\mathrm{spec}} = \mathrm{RIN}(f < B/2)$ of the measured $\mathrm{RIN}(f)$-spectra together with the optical powers P_{sig} and P_{LO} ,

$$\widehat{w}_{o,\mathrm{RIN,sig}} = \frac{1}{4}\mathrm{RIN}_{\mathrm{spec}}P_{\mathrm{sig}}, \qquad \widehat{w}_{o,\mathrm{RIN,LO}} = \frac{1}{4}\mathrm{RIN}_{\mathrm{spec}}P_{\mathrm{LO}}. \tag{3.50}$$

Substituting Eq. (3.50) in Eq. (3.43) yields (as also obtained in [189]),

$$\left\langle i^2_{\mathrm{RIN,tot}} \right\rangle = S^2 \mathrm{RIN}_{\mathrm{spec}} P_{\mathrm{LO}} P_{\mathrm{sig}}\ \Delta f. \tag{3.51}$$

Appendix D: Noise-equivalent power (NEP)

The NEP of a photodetector (unit: $\mathrm{W}/\sqrt{\mathrm{Hz}}$) is defined by the optical signal power P_{NEP} needed to detect the signal within a bandwidth Δf with a power SNR of one, $P_{\mathrm{NEP}} = \mathrm{NEP}\sqrt{\Delta f}$. Considering thermal electronic noise with a current variance $\left\langle i^2_{\mathrm{R}} \right\rangle$ and shot noise $\left\langle i^2_{\mathrm{shot}} \right\rangle = 2eS_{\mathrm{NEP}} P_{\mathrm{NEP}} \Delta f$, where S_{NEP} stands for the photodetector sensitivity at the wavelength where the NEP was measured by the manufacturer, the following relation has to hold:

$$\frac{(S_{\mathrm{NEP}} P_{\mathrm{NEP}})^2}{\left\langle i^2_{\mathrm{R}} \right\rangle + \left\langle i^2_{\mathrm{shot}} \right\rangle} = 1. \tag{3.52}$$

With the values for our system, $\mathrm{NEP} = 20\,\mathrm{pW}/\sqrt{\mathrm{Hz}}$, $S_{\mathrm{NEP}} = 1\,\mathrm{A/W}$ and $\Delta f = 110\,\mathrm{kHz}$ we calculate $\left\langle i^2_{\mathrm{R}} \right\rangle = 4.4\times10^{-17}\,\mathrm{A}^2$ and $\left\langle i^2_{\mathrm{shot}} \right\rangle = 2.3\times10^{-22}\,\mathrm{A}^2$, thus $\left\langle i^2_{\mathrm{R}} \right\rangle \gg \left\langle i^2_{\mathrm{shot}} \right\rangle$. The NEP thus is dominated by electronic noise.

Appendix E: Parameters used for calculation of theoretical curves

The parameters used for the calculations in Section 3.2.3.5 and Section 3.2.3.6 are summarized in Table 3.2. The values are derived from data measured during the experiments or in some cases from the specifications provided by the equipment manufacturer.

Appendix F: Distribution of optical power between object and calibration measurement

This section is based on the error analysis introduced in Sections 3.2.3.3 to 3.2.3.5. The signal-to-noise power ratio $\mathrm{SNR}_{m,\lambda}$ of the heterodyne IF line signals is proportional to the powers of the comb lines $P_{\mathrm{m,sig},\lambda}$, $P_{\mathrm{m,LO},\lambda}$ received

Table 3.2: Parameters used for the calculated predictions in Section 3.2.3.5 and Section 3.2.3.6

Parameter	Values used for calculations
Number of evaluated lines N	7
$P_{m,\mathrm{sig},\lambda_{\mathrm{obj}},\mathrm{meas}}$ for m = -3. . . 3 for κ = 1 [dBm]	{−25.6, −17.3, −17.7, −20.2, −20.1, −17.6, −24.5}
$P_{m,\mathrm{LO},\lambda_{\mathrm{obj}},\mathrm{meas}}$ for m = -3. . . 3 [dBm]	{−23.2, −16.8, −18.2, −20.9, −20.7, −17.8, −22.4}
$P_{m,\mathrm{sig},\lambda_{\mathrm{obj}},\mathrm{ref}}$ for m = -3. . . 3 [dBm]	{−26.3, −18.0, −18.4, −20.9, −20.8, −18.3, −25.2}
$P_{m,\mathrm{LO},\lambda_{\mathrm{obj}},\mathrm{ref}}$ for m = -3. . . 3 [dBm]	{−28.9, −22.5, −23.9, −26.6, −26.4, −23.5, −28.1}
$P_{m,\mathrm{sig},\lambda_{\mathrm{cal}},\mathrm{meas}}$ for m = -3. . . 3 [dBm]	{−30.5, −27.6, −31.1, −31.9, −29.6, −26.6, −33.3}
$P_{m,\mathrm{LO},\lambda_{\mathrm{cal}},\mathrm{meas}}$ for m = -3. . . 3 [dBm]	{−26.9, −24.8, −28.3, −29.4, −26.9, −23.9, −29.1}
$P_{m,\mathrm{sig},\lambda_{\mathrm{obj}},\mathrm{ref}}$ for m = -3. . . 3 [dBm]	{−30.6, −27.7, −31.2, −32.0, −29.7, −26.7, −33.4}
$P_{m,\mathrm{LO},\lambda_{\mathrm{obj}},\mathrm{ref}}$ for m = -3. . . 3 [dBm]	{−39.0, −36.9, −40.4, −41.5, −39.0, −36.0, −41.2}
$\mathrm{RIN}_{\mathrm{spec},\lambda_{\mathrm{obj}}}$ [dBc/Hz]	-138
$\mathrm{RIN}_{\mathrm{spec},\lambda_{\mathrm{cal}}}$ [dBc/Hz]	-145
$S_{\lambda_{\mathrm{obj}}}$ [A/W]	1.05
$S_{\lambda_{\mathrm{cal}}}$ [A/W]	0.95
R_{TIA} [V/A]	700
Δf [kHz]	110
NEP [pW/$\sqrt{\mathrm{Hz}}$]	20
Γ_{dB} [dB]	-57
$f_{\mathrm{mod,sig}}$ [GHz]	40

by the detectors, see Eq. (3.15). Signal and calibration combs are generated with the same modulators, which tolerate a limited input power only. This input power limitation restricts the achievable SNR and thus the achievable measurement precision. Therefore the relative optical power distribution between the object and the calibration laser has to be considered as a function of the reflection coefficient κ associated with backscattering of power from the sample surfaces. The power received at 1300 nm from the calibration mirror remains constant, so no dependency on κ is to be expected for the standard deviation $\sigma_{z,\mathrm{cal}}$ of the calibration measurement.

Fig. 3.13 illustrates the system performance for the reflections $\kappa_{\mathrm{dB}} = -9\,\mathrm{dB}$, Fig. 3.13(a) and Fig. 3.13(c), and $\kappa_{\mathrm{dB}} = -22\,\mathrm{dB}$, Fig. 3.13(b) and Fig. 3.13(d), and for different laser power levels entering the MZM comb generators. The calculated standard deviations of object and calibration measurements, Fig. 3.13(a) and Fig. 3.13(b), as well as of the compensated measurements, Fig. 3.13(c) and Fig. 3.13(d), are displayed as surface plots. The limited launch power of maximum 20 dBm into the used MZM poses an additional constraint and is marked by the red line. The standard deviation belonging to the experimental power settings are marked in each subfigure with a black dot. Comparing Fig. 3.13(a) and Fig. 3.13(b), it can be seen that for $\kappa_{\mathrm{dB}} = -9\,\mathrm{dB}$ the standard deviation $\sigma_{z,\mathrm{cal}}$ of the calibration measurement dominates, while for smaller object reflections $\kappa_{\mathrm{dB}} = -22\,\mathrm{dB}$ the standard deviation $\sigma_{z,\mathrm{obj}}$ of the object measurement is larger. This is also illustrated in Fig. 3.7.

The compensated measurement has a standard deviation which is always larger than either $\sigma_{z,\mathrm{cal}}$ or $\sigma_{z,\mathrm{obj}}$. In our experiments, standard deviations of 2 µm for $\kappa_{\mathrm{dB}} = -9\,\mathrm{dB}$ and 5 µm for $\kappa_{\mathrm{dB}} = -22\,\mathrm{dB}$, can be achieved, Fig. 3.13(c) and Fig. 3.13(d). As many technical samples lead to reflection coefficients in that range, the experimental power settings represent a well-chosen trade-off, resulting in standard deviations close to minimum values for the compensated measurement.

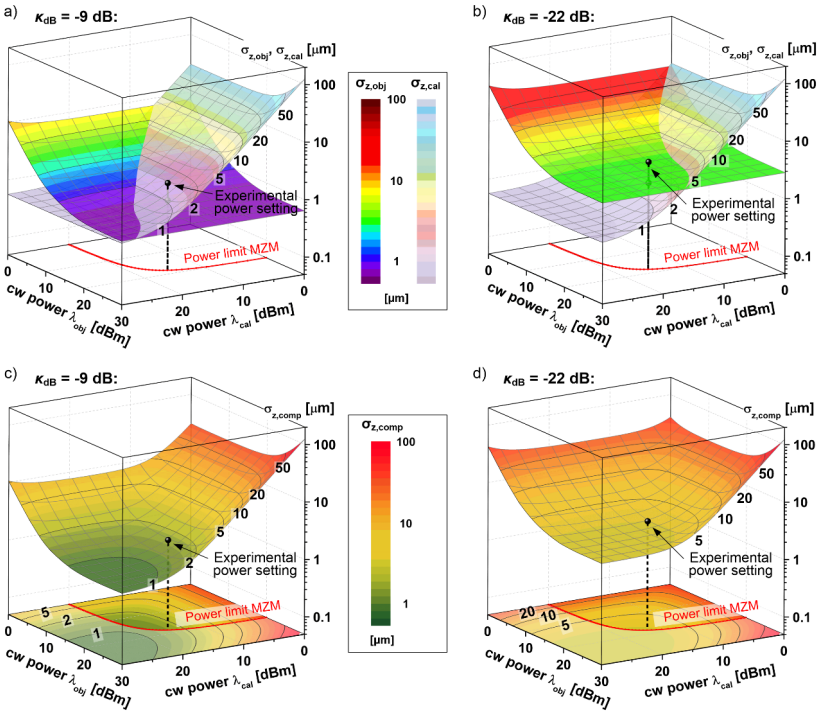

Fig. 3.13: Calculated standard deviations of the distance measurements as a function of laser input powers into the MZM comb generators for two different values of the object reflection κ_{dB}. Experimental power settings are marked by black dots (calibration laser: 15 dBm, object laser: 18 dBm). The 20 dBm input power limitation of the MZM is indicated by a red line. (a) Individual calculated standard deviations $\sigma_{z,\mathrm{obj}}$ and $\sigma_{z,\mathrm{cal}}$ for $\kappa_{\mathrm{dB}} = -9$ dB. (b) Individual calculated standard deviations $\sigma_{z,\mathrm{obj}}$ and $\sigma_{z,\mathrm{cal}}$ for $\kappa_{\mathrm{dB}} = -22$ dB. (c) Calculated standard deviation $\sigma_{z,\mathrm{comp}}$ for $\kappa_{\mathrm{dB}} = -9$ dB. (d) Calculated standard deviation $\sigma_{z,\mathrm{comp}}$ for $\kappa_{\mathrm{dB}} = -22$ dB.

[*End of paper* [J1]]

4 Silicon photonic receiver system for dual-comb distance metrology

This chapter describes the implementation and demonstration of an integrated photonic receiver circuit for dual-comb distance measurements. Section 4.1 contains an overview on the general state of the art in the field silicon photonic integration, and Section 4.2 gives an overview on silicon photonic integrated circuits for distance measurements. The principle of the silicon photonic receiver circuit for dual-comb distance metrology is finally explained in Section 4.3, and the experimental setup as well as the obtained results are discussed and analyzed.

4.1 Silicon-on-insulator photonic integrated circuits

Silicon photonics has become a mature platform for photonic integrated circuits (PIC) over the past few years, with many essential building blocks being readily available for a system-level design [203, 204]. The basic portfolio of passive building blocks of a photonic system includes waveguides, grating couplers, and splitters, while the basic active building blocks include modulators, thermo-optic phase shifters, and photodetectors. This section gives a short overview over these elements.

The device geometries and a cross sectional view of a typical silicon PIC are sketched in Fig. 4.1. Silicon PIC are currently mostly fabricated on 8-inch silicon-on-insulator (SOI) wafers that were originally developed for CMOS electronics. The device layer consisting of crystalline silicon has a typical thickness of 220 nm. It is separated from the substrate by a so-called buried oxide layer (BOX) consisting of silicon dioxide with a typical thickness of 2 µm. Depending on the foundry, 248 nm lithographic processes

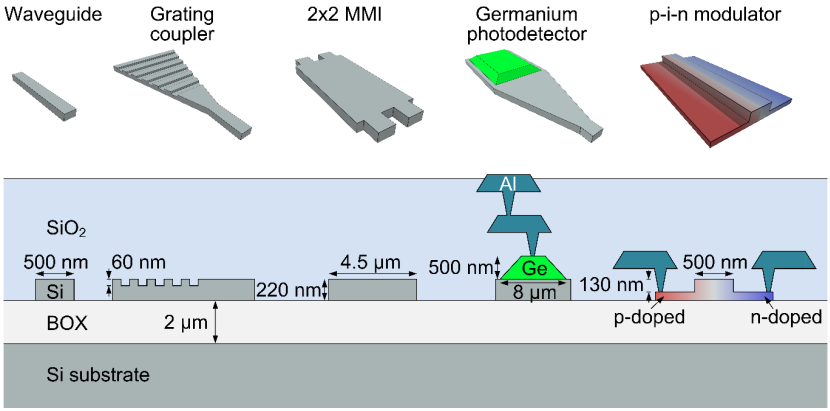

Fig. 4.1: Sketch of common passive and active elements used in silicon photonic integrated circuits (top), along with the corresponding cross sections and the associated typical dimensions (bottom). Aluminum vias and multi-layer interconnects ensure electrical connectivity of active elements. MMI: Multimode interference coupler. BOX: Buried oxide layer. Figure redrawn with adaptions from [203].

or 193 nm lithographic processes followed by anisotropic etch steps are used for structuring the waveguides. Epitaxially grown germanium is used to form photodiodes. Ion implantation is used for doping with various doping levels. After fabrication of the optical and opto-electronic elements, a metal stack with vias, interconnects and contact pads is added. Depending on the specific process flow, aluminum, copper, AlCu or tungsten is used.

Waveguides: Due to the high refractive index contrast between the silicon core (refractive index $n_{\mathrm{Si}} \approx 3.48$ at a wavelength of 1550 nm) and the silicon dioxide cladding ($n_{\mathrm{SiO_2}} \approx 1.44$), waveguides with sub-wavelength transverse dimensions and tight bend radii can be designed. A typical single-mode channel waveguide for a wavelength of 1.55 µm has a width of 500 nm with typical propagation losses of about 2-3 dB/cm [203–205]. Bend radii as small as 3 µm with excess loss of 0.009 dB can be realized [206].

Grating Couplers: Grating couplers are commonly used for coupling light between optical fibers and PIC [207–210]. The light is diffracted out of the substrate plane of the PIC by a diffraction grating formed by periodic perturbations in the etch depth, where the grating period is chosen such that light

propagating in the waveguide is efficiently diffracted into a specific direction to the top of the substrate plane. The size mismatch of mode diameters between optical fibers and silicon waveguides is taken into account by a taper section. Compared to edge coupling, grating couplers provide the advantage of being deployable at any location on the chip surface. Typical insertion losses of grating couplers range from 2 dB to 6 dB, depending on design and additional process steps [204, 211].

Multimode interference couplers (MMI): MMI are widely used in PIC as optical couplers and power dividers [212]. MMI make use of the so-called self-imaging effect first observed by Talbot [213], realized in multi-mode waveguides [214, 215]. Compared to directional couplers, MMI offer an attractive combination of small footprint, relaxed fabrication tolerances, low losses and high bandwidth [216–218]. Excess insertion losses are typically in the range of 0.5 dB [205].

Photodetectors: Photodetectors on silicon are commonly made from germanium (Ge) as an absorbing material. Germanium can be grown with high quality on Si substrates [145, 219] and is compatible with CMOS processes such that monolithic integration becomes possible [220]. Another benefit is a strong photon absorption in the telecommunication wavelength range, thereby enabling short devices. Waveguide-integrated photodetectors use evanescent coupling of light from a solicon waveguide to a germanium vertical *p-i-n* junction forming the photodiode. The photodetectors currently offered as building blocks by the foundries exhibit responsivities of 0.5–0.74 A/W and bandwidths of 20–58 GHz [203–205].

Modulators: Many modulators on SOI PIC employ the plasma dispersion effect, where the refractive index inside the waveguide is changed by a variation of the free carrier density [143, 221–225]. To this end, two basic schemes are used: Carrier injection through a forward-biased *p-i-n* structure that is integrated into the waveguide core or carrier depletion using waveguides with reversed-biased lateral *p-n* junctions. Carrier injection yields very compact devices, for which π-voltage-length products as low as $U_\pi L = 0.36\,\mathrm{V\,mm}$ have been shown [226]. However, with this approach, the bandwidth is limited by the free carrier lifetime to a few gigahertz [227]. Carrier depletion-type modulators, on the other hand, achieve higher bandwidths of several tens of gigahertz [228]. However, the typical modulation efficiency is considerably

lower with voltage-length products of $U_\pi L \approx 10\,\mathrm{V\,mm}$ [224], leading to larger devices with typical lengths of several millimeters.

Thermo-optic phase shifters making used of thermo-optic changes of the refractive index are also available, however they are relatively slow with bandwidths in the kilohertz regime and they are subject to thermal crosstalk [229, 230]. With the given trade-offs, the appropriate type of modulator can be chosen depending on the requirements of the application. A relatively new approach with less limitations concerning bandwidth and modulation efficiency is the use of silicon-organic hybrid (SOH) modulators, which is discussed separately in Section 6.1.

4.2 State of the art in silicon photonic integrated circuits for distance measurements

Photonic integration has a large potential for applications in optical metrology, allowing to realize complex optical systems within a very small footprint. The silicon photonic platform is particularly attractive, offering mature high-yield fabrication processes, which are accessible through established foundry processes and which offer the potential for co-integration of photonic and electronic circuits. These advantages can be leveraged to realize optical distance measurement systems or components thereof as PICs. So far, demonstrations of distance measurements with silicon photonic chips are either based on schemes using frequency-swept lasers [101, 105, 231] or interferometry with a single wavelength [106].

In [101], frequency-modulated continuous-wave (FMCW) ranging is demonstrated using an electronically tuned distributed Bragg reflector (DBR) laser. The frequency ramp of the laser is linearized by using a silicon photonic PIC containing a Mach-Zehnder interferometer and a photodiode, heterogeneously integrated with CMOS control electronics, whereas the optical system performing the actual distance measurement is realized with classical fiber-optical components. A root-mean-square precision of 8 µm for 5.5 µs measurement time is realized, however, this precision is limited to a depth range of ±5 cm from the range baseline, where the path length difference between signal and LO is zero. Due to phase noise induced by the frequency tuning, the preci-

sion is a function of the path length difference between signal and LO, and it degrades to 4.2 mm at the edges of the measurement window.

In [105], a frequency-swept optical signal is generated from a CW laser using a modulator and chirped driving signals. Detection is realized on a silicon photonic chip, achieving a depth resolution of 15 µm with an acquisition time of 500 µs.

In [231], a laser is swept in frequency to realize a FMCW ranging. The optical system for detection with waveguides, couplers and photodiodes is contained on a silicon photonic chip. Absolute distance errors of less than 10 mm within a measurement range of 2 m and 10 ms measurement time are demonstrated.

A different concept is realized in [106]. Here an integrated heterodyne interferometer for measurements of small relative displacements is demonstrated. The silicon photonic chip contains single-sideband modulators, which are used to generate signal and LO from a single, off-chip CW laser. Waveguides, power splitters and detectors are realized on the chip as well. Distance measurements with a standard deviation of 2 nm are demonstrated. However, due to the single-wavelength interferometric scheme, the unambiguity range is limited to 775 nm – too low for many industrial applications.

In contrast to the state of the art, the work presented Section 4.3 relies on a silicon PIC for distance measurements with electro-optically generated frequency combs. The measurement results are directly traceable to the electronically defined modulation frequency, and no linearization of a laser sweep is needed. Waveguides, power splitters and photodiodes are realized on a silicon photonic chip. The chip also contains a tunable power splitter, which allows for tuning between reference and measurement signals as an added functionality. Distance measurements with root-mean-square errors of 3.4 µm are demonstrated for measurement times of 14 µs. While the frequency combs are still generated off-chip within the framework of these experiments, electro-optic frequency comb sources can also be realized on the silicon photonic platform using the silicon-organic hybrid (SOH) approach, as demonstrated in Chapter 6.

4.3 Silicon photonic integrated circuit for fast distance measurement with frequency combs

The contents of the following section is taken from a publication in Optics Express [J11]. The structure and the layout of this document was slightly adapted to fit the format of this thesis.

[*Start of paper* [J11]]

Silicon photonic integrated circuit for fast and precise dual-comb distance metrology

Optics Express; Volume 25; Issue 24; pp. 30091-30104; November 2017
DOI: 10.1364/OE.25.030091

C. Weimann,[1,2,3] M. Lauermann,[1,2] F. Hoeller,[3] W. Freude,[1,2] and C. Koos[1,2]

[1]*Institute of Photonics and Quantum Electronics (IPQ), Karlsruhe Institute of Technology (KIT), 76131 Karlsruhe, Germany*

[2]*Institute of Microstructure Technology (IMT), KIT, 76344 Eggenstein-Leopoldshafen, Germany*

[3]*Corporate Research and Technology, Carl Zeiss AG, Oberkochen, Germany*

4.3.1 Introduction

High-precision distance sensors are of great importance for a wide range of applications such as inline inspection of mechanical parts or precise referencing of translation axes in industrial machinery. These sensors need to be compact, robust, and capable of providing absolute distance measurements with single-digit micrometer accuracy and short acquisition times. So far, miniaturization of optical sensors has mainly been achieved by emulating conventional macroscopic optical configurations using discrete micro-optical components such as micro-lenses and micro-optical benches [232, 233]. These schemes, however, require costly assembly and highly precise alignment of a multitude of components and are therefore not well suited for mass production. At the same time,

photonic integrated circuits (PIC) have gained considerable maturity. Silicon photonics emerges as a particularly attractive platform, lending itself to large-scale photonic-electronic integration on the basis of mature high-yield CMOS processes that are offered by widely available foundry services [234,235]. Photonic integration is currently mainly driven by data- and telecommunication applications such as high-speed optical interconnects, but it is indisputable that there is also large application potential for PIC in optical sensing and metrology. However, while early demonstrations of PIC for interferometric distance measurements made use of GaAs/AlGaAs and Lithium-Niobate ($LiNbO_3$) as integration platform [236–238], there are only very few examples where large-scale silicon photonic integration has been exploited for applications in optical metrology. Using the silicon-on-insulator (SOI) platform, laser Doppler vibrometers and optical frequency shifters have been demonstrated [103,239,J10] and an optical coherence tomography system has been realized [C7]. An integrated heterodyne interferometer for measurements of relative displacements with a standard deviation of 2 nm was demonstrated in [106]. However, like all optical single-wavelength interferometric schemes, this approach is limited to an unambiguity range of half the optical wavelength, i.e., approximately 775 nm, which prohibits its use for many applications in industrial metrology. A silicon PIC for absolute distance measurements with an electrically-generated laser frequency chirp was demonstrated in [105], achieving a depth resolution of 15 µm for an acquisition time of 500 µs. While this represents an important demonstration, the approach cannot yet fulfill the requirement of sub-10 µm measurement accuracy in conjunction with measurement rates well in excess of 10 kHz that are associated with many applications in industrial high-precision metrology. Measurement principles based on optical frequency combs have recently shown to deliver the sought-after combination of precision and measurement speed [37, 116, 240, J6]. However, these works employ classical macroscopic optical setups, e.g. using fiber-optical components.

In this paper, we expand on our previous work [C5] and demonstrate a silicon-on-insulator PIC for fast and precise absolute distance measurements using a pair of frequency combs (FC) as optical sources for multi-heterodyne synthetic-wavelength interferometry. The precisely known frequency spacing of the comb lines provides a number of precisely known synthetic wavelengths, the phases of which can be measured simultaneously via heterodyne detection with a detuned optical frequency comb used as a local oscillator. The combination of a dual-comb measurement scheme with photonic integration on

silicon presented in this paper results in a fast, precise and very compact optical distance sensor. We achieve standard deviations of less than 5 µm for an acquisition time of 14 µs, enabling measurement rates well beyond 50 kHz. Our system consists of a heterodyne interferometer, comprising a multitude of components such as power splitters and waveguides as well as phase shifters and photodetectors, all integrated into a single silicon PIC covering an on-chip footprint of 0.25 mm^2. An on-chip tunable power splitter (TPS) is used to distribute the available power of the local oscillator in an optimum way. The PIC relies entirely on the standard device portfolio offered by a silicon photonic foundry and does not require any customized components or fabrication steps. The FC are generated externally by modulating cw lasers with standard telecom-grade dual-drive Mach-Zehnder modulators (MZM). The MZM are driven by fixed-frequency sinusoidal electrical signals in push-push operation to generate frequency combs that typically comprise 5 – 20 equidistant lines [83, 134]. In future implementations, silicon receiver PIC may be monolithically co-integrated with high-performance frequency comb generators using the silicon-organic hybrid (SOH) approach [J5, J13]. Moreover, when combined with ultra-broadband Kerr comb generators in a hybrid multi-chip assembly, such silicon receiver PIC will pave the path towards ultra-fast high-precision distance measurements with chip-scale systems [59,60,240,J9].

4.3.2 Experimental setup with silicon photonic chip and measurement principle

A schematic of the experimental setup is depicted in Fig. 4.2(a). Light from a continuous-wave (CW) laser with a wavelength $\lambda_0 = 1550$ nm is amplified to a power of 18 dBm in an erbium-doped fiber amplifier (EDFA), then split by a fiber coupler, and fed into a pair of Mach-Zehnder modulators (MZM) for frequency comb generation (FC 1 and FC 2). The use of a central wavelength within the C band (1530 nm -– 1565 nm), which is commonly used for fiber-optic telecommunication, allows to employ commercially widely available components as well as to make use of the standard device portfolio offered by any silicon foundry. The lithium-niobate MZM are driven by sinusoidal electrical signals with frequencies of $f_{\mathrm{mod,LO}} = 40.000$ GHz for FC 1 and $f_{\mathrm{mod,sig}} = 39.957$ GHz for FC 2. The corresponding modulation depth amounts to 1.5π. The phase-modulated light exhibits a comb-like spectrum

with a line spacing precisely defined by the respective driving frequencies, Insets (I) and (II) in Fig. 4.2(a). By adjusting the bias voltage, the relative phase and the amplitudes of the driving signals between both arms of the modulator, the frequency combs are spectrally flattened [83, 134]. Both MZM are temperature-stabilized via thermoelectric coolers and their corresponding controllers, ensuring stable bias points. We did not measure the time dependency of the comb spectra, but we could not observe any short-term or long-term degradation of the flatness of the spectral envelope of the frequency combs during our experiments. FC 1 is additionally frequency-shifted by $\Delta f_0 = 55\,\mathrm{MHz}$ using an acousto-optic modulator (AOM). The FC are coupled to the PIC using a fiber array and grating couplers. FC 2 enters the PIC at the port marked by (1) in Fig. 4.2. A multimode interference coupler (MMI) is used to split the comb into two parts. One part of FC 2 is directly guided to the reference detector, the other part exits the chip again at port (2), is guided to the measurement path and emitted by a collimator towards the measurement target, here represented by a mirror. After back-and-forth propagation over the measurement distance z, this part of FC 2 is coupled back to the PIC through port (4) and fed to the measurement detector. FC 1 enters the PIC at port (3) and is distributed to both measurement and reference detector via a power splitter with tunable splitting ration (tunable power splitter, TPS). The TPS is realized by *p-i-n* phase shifters in a MZM configuration and allows for a flexible power distribution of FC 1 on both detectors. The detectors consist of vertical Germanium p-i-n junctions [203] and are realized as balanced photodetectors for optimum suppression of common-mode signal components. A microscopic image of the PIC is depicted in Fig. 4.3. The occupied on-chip area of all elements amounts to $0.25\,\mathrm{mm}^2$.

FC 1 serves as local oscillator (LO) for heterodyne detection of FC 2, which is further also called signal comb. The line spacing of FC 1 is detuned by $\Delta f_{\mathrm{mod}} = 43\,\mathrm{MHz}$ and its center frequency is detuned by $\Delta f_0 = 55\,\mathrm{MHz}$ with respect to FC 2, as illustrated in Fig. 4.2(b). The comb lines of FC 1 and FC 2 are superimposed on the balanced photodetectors and quadratic detection leads to a multitude of sinusoidal photocurrents at distinct intermediate frequencies (IF) in the baseband. With an integer m denoting the order of the comb lines, the photocurrent shows N spectral lines at frequencies $|\Delta f_0 + m\,\Delta f_{\mathrm{mod}}|$, as depicted schematically in Fig. 4.2(c). A rigorous mathematical description of the measurement scheme can be found in Appendix A.

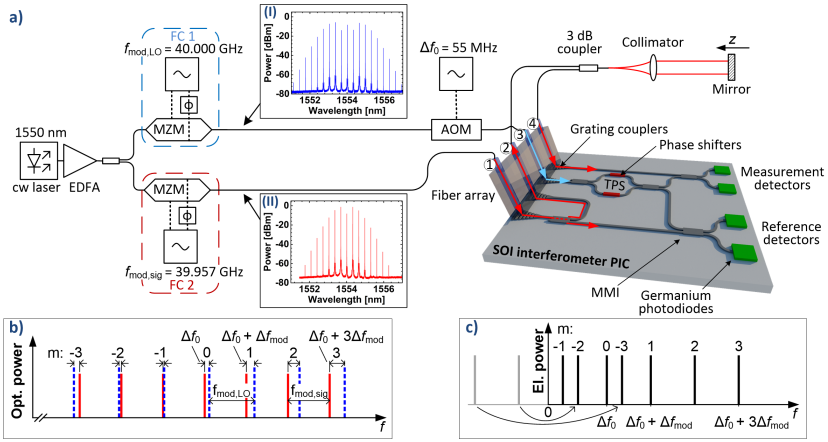

Fig. 4.2: Experimental setup and detection principle. (a) Light from a CW laser is amplified in an erbium-doped fiber amplifier (EDFA) to a power of 18 dBm, split, and directed to two MZM. Two slightly detuned frequency combs (FC 1 and FC 2, see insets I and II for optical spectra) with a line spacing of $f_{\mathrm{mod,LO}} = 40.000\,\mathrm{GHz}$ and $f_{\mathrm{mod,sig}} = 39.957\,\mathrm{GHz}$ are generated by sinusoidal phase modulation. FC 1 is additionally shifted by $\Delta f_0 = 55\,\mathrm{MHz}$ in an acousto-optical modulator (AOM). The light is coupled to the SOI interferometer PIC from above via a fiber array and grating couplers. FC 1 is coupled to the PIC through port 3, is split with a tunable power splitter (TPS),and is further distributed by a tunable power splitter (TPS) to the measurement and the reference detector, where it acts as local oscillator (LO) for multi-heterodyne detection of FC 2. FC 2 is coupled to the PIC through port 1 and split by a multimode interference coupler (MMI). One part of FC 2 is guided directly to the reference detectors, where it is superimposed with FC 1. The other part exits the PIC through port 2, is guided via single-mode fibers to a collimator and propagates over the free-space measurement path of length z. The reflected light is coupled back into the fiber, sent to the PIC through port 4, and finally superimposed with FC 1 on the measurement detectors. (b) Schematic optical power spectra of FC 1 (dashed blue lines) and FC 2 (continuous red lines). The line spacings of FC 1 and FC 2 are slightly detuned by $\Delta f_{\mathrm{mod}} = |f_{\mathrm{mod,LO}} - f_{\mathrm{mod,sig}}|$, and the center frequencies are offset by Δf_0. (c) Schematic one-sided spectrum of the photocurrent (negative frequencies grayed out). Quadratic detection of FC 1 and FC 2 by a photodiode leads to a multitude of sinusoidal IF signals with frequencies $|\Delta f_0 + m\Delta f_{\mathrm{mod}}|$ in the photocurrent (heterodyne detection). Negative frequencies of the corresponding two-sided spectrum are drawn in gray and mirrored to positive frequencies of the one-sided spectrum. The phases of the IF signals are directly linked to the phase shifts accumulated by the lines of the FC during propagation.

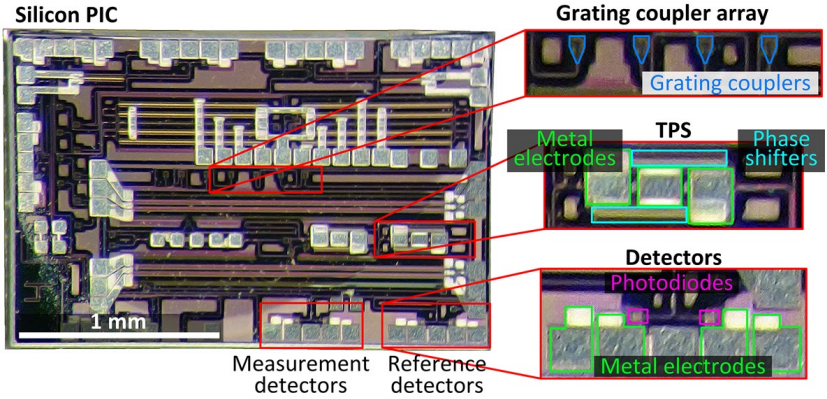

Fig. 4.3: Microscope image of the silicon PIC. The main elements used by the distance sensor system are highlighted by colored frames and depicted magnified on the right-hand side. Connecting waveguides are routed between additional optical circuits for other purposes, which are co-integrated on the same chip. The occupied on-chip area of the distance sensor system amounts to $0.25\,\mathrm{mm}^2$.

To find the distance z to the mirror, the spectrum of the photocurrent is analyzed. The phases of the IF beat notes are directly linked to the phase shifts that the FC accumulate during their propagation to the respective detectors. The measurement distance z is extracted from the IF phase differences between reference and measurement detectors [34, C4, J6]. With the exception of the measurement distance z, all other optical path lengths in the system are fixed. Their influence on the phases can be removed by a calibration measurement (for details see Appendix A). The phase differences $\Delta\varphi_m$ between reference and measurement detector are linked to the distance z by the propagators $\exp\left(-\mathrm{j}\omega_{m,\mathrm{sig}}2z/c\right)$ of the reflected signal comb lines m of FC 2 with (angular) frequency $\omega_{m,\mathrm{sig}} = 2\pi f_{m,\mathrm{sig}} = 2\pi\left(f_{0,\mathrm{sig}} + m f_{\mathrm{mod},\mathrm{sig}}\right)$, where $f_{0,\mathrm{sig}} = c/\lambda_0$ is defined by the input CW laser and c is the vacuum speed of light. As described in Eq. (4.14)) of Appendix A, the unwrapped phase differences of the IF signals with respect to a calibration at z_0 can then be expressed as

$$\delta\varphi_m(z) = \Delta\varphi_m(z) - \Delta\varphi_m(z_0) = 2(z - z_0)\, m\omega_{\mathrm{mod},\mathrm{sig}}/c + 2(z - z_0)\,\omega_{0,\mathrm{sig}}/c. \tag{4.1}$$

The last term in Eq. (4.1) corresponds to the phase evaluated in classical interferometry at an optical wavelength $\lambda_0 = 2\pi c\omega_{0,\mathrm{sig}}^{-1}$. However, due to the

2π-periodicity of the phase and the back-and-forth propagation to the mirror, this would only provide an unambiguity range of $\lambda_0/2 = 775\,\text{nm}$. Additionally, drifts of the laser wavelength would introduce errors. The first term in Eq. (4.1), however, corresponds to the phases evaluated in interferometry with so-called synthetic wavelengths $\Lambda_m = 2\pi c \left(m\omega_{\text{mod,sig}}\right)^{-1}$ [136], see Appendix A. This considerably extends the unambiguity range to $\Lambda_1/2 = 3.75\,\text{mm}$, while at the same time the measurement result is traceable to the stability of the electronically provided drive frequency $\omega_{\text{mod,sig}}$. The unambiguity range could be extended further by, e.g., subsequent measurements with different comb line spacings [34, 125], or by a combination with longer-range time-of-flight measurement schemes [J4].To extract the information contained in the $N-1$ synthetic wavelengths provided simultaneously by the use of a frequency comb, the slope with respect to m is calculated from Eq. (4.1),

$$\frac{\mathrm{d}\delta\varphi_m(z)}{\mathrm{d}m} = 2(z - z_0)\frac{\omega_{\text{mod,sig}}}{c}. \tag{4.2}$$

As $\omega_{\text{mod,sig}}$ and c are accurately know, the distance z with respect to a calibration position z_0 can be precisely determined. This approach is illustrated in Fig. 4.4. The measured IF power spectra for both measurement and reference detector are depicted in Fig. 4.4(a), showing the evaluated 7 lines with $m = -3, \ldots, 0, \ldots, 3$. The heterodyne detection scheme with a slightly detuned LO comb (FC 1) allows sampling of an optical bandwidth of $(7-1)\times 40\,\text{GHz} = 240\,\text{GHz}$ with an electrical bandwidth of less than 200 MHz. The phases of the individual beat notes are extracted by performing a discrete Fourier transform (DFT) after analog-to-digital conversion (A/D) of the IF signals with a resolution of 12 bit and sample rate of 3.6 GS/s. The DFT operates on 5×10^4 samples per channel, which corresponds to an acquisition time of 14 µs. The slope of the unwrapped phase differences is determined by a linear regression, as illustrated in Fig. 4.4(b), and is proportional to the measurement distance $z - z_0$. The signal processing steps to extract the measurement distance can be realized efficiently on an FPGA to enable real-time operation [C6].

4.3.3 Measurement results

For performance characterization, we measure the distance to a plane mirror mounted on a motorized translation stage. The stage has a feedback-controlled

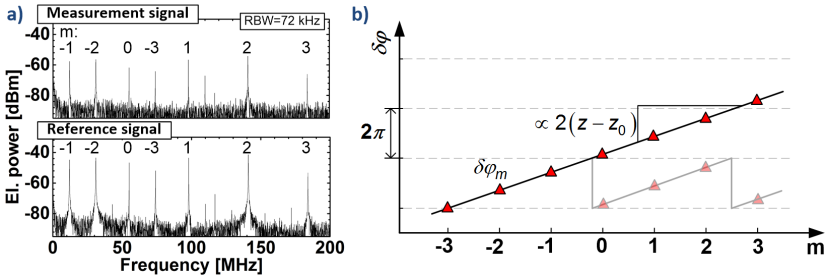

Fig. 4.4: Data processing for dual-comb synthetic-wavelength interferometry. (a) Measured one-sided spectrum of the photocurrents of measurement and reference detectors acquired at a resolution bandwidth (RBW) of 72 kHz. The IF lines are indexed by m as in Fig. 4.2. Lines with index $m < -1$ that, in the present configuration, would appear at negative frequencies in the two-sided electrical power spectrum, are mirrored to the positive frequency range in the one-sided spectrum as explained in Fig. 4.2. (b) Differences of the IF phases $\delta\varphi_m$ as measured between the reference and the measurement detectors as a function of the line index m. Phase values before unwrapping (sawtooth-like shapes) are depicted in light colors, illustrating the 2π-periodicity. The unwrapped phase values follow a linear relationship. The slope of the fitted straight line is proportional to the optical path length difference between reference and measurement paths, see Eq. (4.2).

positioning accuracy of 50 nm and serves as a reference for our distance measurements. The power emitted into free space amounts to -4.5 dBm. The distance measurement results are shown in Fig. 4.5(a). The unwrapped measured distance z is plotted as function of the distance set on the translation stage z_{set}, see blue crosses in Fig. 4.5(a). Each distance measurement corresponds to an acquisition time of 14 µs. The mean of the distance error $z - z_{\mathrm{set}}$ is calculated from 10 subsequent measurements at the same position, see black dots in Fig. 4.5(a). Error bars indicate a range of twice the standard deviation. The absolute value of the mean error stays below 4 µm, while the standard deviation stays below 5 µm for all positions. The root-mean-square position error calculated over the whole measurement range amounts to 3.4 µm. The small deviations of the mean distance error from 0 µm are partly due to thermal path length fluctuations in the optical fibers used in the current measurement setup and partly due to crosstalk caused by reflections of on-chip devices such as MMI or grating couplers. While the latter can be alleviated by using devices with low back-reflection [241], we further analyze the effect of thermal path length fluctuations. The systematic error due to thermally varying optical path length differences ΔD inside the optical fibers with a geometric length of L is

estimated in the following using published data. The group refractive index is denoted as n, the thermo-optic coefficient as $\mathrm{d}n/\mathrm{d}T$, the thermal expansion coefficient as $\alpha_L = (\mathrm{d}L/\mathrm{d}T)/L$ and the length-averaged temporal temperature difference of the optical fibers as ΔT. The optical path length $D = nL$ varies with temperature according to $\mathrm{d}D = (n\mathrm{d}(L)/\mathrm{d}T + L\mathrm{d}(n)/\mathrm{d}T)\,\mathrm{d}T$. With the previous definitions, the temperature-induced optical path length variations are given as

$$\Delta D = \left(n\alpha_L + \frac{\mathrm{d}n}{\mathrm{d}T}\right) L\Delta T. \tag{4.3}$$

With $n = 1.4679$ [184], $\alpha_L \approx 0.5\times10^{-6}\mathrm{K}^{-1}$ [182], and $\mathrm{d}n/\mathrm{d}T \approx 10\times10^{-6}\mathrm{K}^{-1}$ [182, 186], the relative optical path length change amounts to

$$(\Delta D/\Delta T)/L = 10.7\,\mu\mathrm{m}/(\mathrm{K\,m})\,. \tag{4.4}$$

Typical room temperature fluctuations during the time period of approximately 1 min needed to move the measurement target to the next position are approximately $\Delta T = 0.1$ K [183]. The dynamic thermal response of a standard Hytrel jacketed single-mode optical fiber has a 3 dB bandwidth of roughly 10 Hz [192] and thus the temperature of the fiber is expected to follow the temperature fluctuations of the room temperature on this time scale. With Eq. (4.4) and the geometric fiber length of $L = 5$ m used in our experiment, we expect systematic deviations in the order of $\Delta D \approx 5\,\mu$m, which fits well to the experimentally observed deviations of the mean values, see Fig. 4.5(a). This systematic error source can be overcome by reduced fiber lengths, by active compensation, e.g., by a simultaneous calibration measurement at a second center wavelength [C6], or by full integration of the sensor system on the chip, which, due to its low mass and volume, could potentially be temperature-stabilized without great technical effort.

A mirror was used as a measurement target for the presented characterization measurements, but in principle also optically rough surfaces could be measured, albeit at a reduced precision due to decreased signal-to-noise power ratio and because of speckle-induced phase noise [194, 195, 242]. The influence of the tunable power splitter (TPS) can be seen in Fig. 4.5(b). The measured optical powers of the LO comb FC 1 arriving at the reference detector and the measurement detector are plotted in blue as a function of the current applied to the *p-i-n* phase shifter in one arm of the TPS. The standard deviation for repeated measurements is plotted in magenta. The power split-

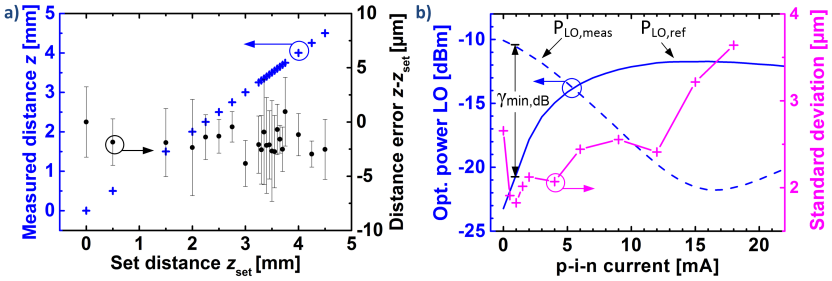

Fig. 4.5: Measurement results. (a) Unwrapped measured distances z (blue) and errors z-z_{set} (black) vs. set distance z_{set}. Error bars indicated a range of twice the standard deviation obtained from 10 subsequent measurements at the same position. Acquisition time per measurement is 14 µs. The accuracy of the positioning stage used for setting the distance z_{set} is specified to be better than 50 nm. The small deviations of the mean distance error from 0 µm are attributed to thermal path length fluctuations in the optical fibers and to crosstalk caused by reflections from on-chip devices such as MMI or grating couplers. (b) Optical power of FC 1 (LO) at measurement and reference detector ($P_{\mathrm{LO,meas}}$ and $P_{\mathrm{LO,ref}}$) along with corresponding standard deviation for the distance measurement, both plotted vs. the current of the *p-i-n* phase shifter in the TPS. The power splitting ratio resulting in minimum standard deviation is indicated by $\gamma_{\mathrm{min,dB}}$.

ting ratio γ_{dB} can be adjusted via the current through the *p-i-n* phase shifter to yield the lowest standard deviation for given power levels. The optical power of signal comb FC 2 arriving at the measurement detector $P_{\mathrm{sig,meas}}$ is subject to additional power losses $\eta = P_{\mathrm{sig,meas}}/P_{\mathrm{sig,ref}}$ compared to the power $P_{\mathrm{sig,ref}}$ arriving at the reference detector. With total grating coupler losses of 2×5 dB, free-space to fiber coupling losses of 7 dB and the 6 dB loss for twice propagating through an additional 3 dB coupler, the additional loss amounts to $\eta_{\mathrm{dB}} = 10\lg(\eta) = -23$ dB. To compensate this lower signal power arriving at the measurement detector, the TPS is set in a way that most of the power of the LO comb FC 1 is distributed to the measurement detector. The input power into the TPS is denoted P_{LO}, the power splitting ration γ. The two optical power levels $P_{\mathrm{LO,ref}} = \gamma P_{\mathrm{LO}}$ and $P_{\mathrm{LO,meas}} = (1-\gamma)P_{\mathrm{LO}}$ denote the optical powers of the LO comb FC 1 arriving at reference detector and measurement detector respectively. Experimentally, we find a value of $\gamma_{\mathrm{dB}} = 10\lg(\gamma) = -10.2$ dB to result in the minimum standard deviation and use this value for the characterization measurements. This is close to the theoretical optimum value of $\gamma_{\mathrm{dB,theo}} = -11.8$ dB, see Appendix B. For other measurement path losses, the splitting ratio can be dynamically adapted to always operate at optimum condi-

tions. It is a strong advantage of photonic integration that such functionalities can be realized at virtually no additional cost.

4.3.4 Vision for further photonic integration

Our vision of a future fully integrated distance sensor chip is illustrated in Fig. 4.6. The envisaged sensor chip consists of a multi-chip assembly where electronic and photonic wire bonds [243–245] are used to connect the individual chips. This approach allows to combine the distinct advantages of complementary photonic integration platforms: The cw carriers can be provided by III-V semiconductor lasers and FC can be generated by sinusoidal phase modulation in highly efficient silicon-organic hybrid (SOH) comb generators [J5, J13] driven by conventional RF oscillators with slightly detuned frequencies. Signal splitting and combining as well as heterodyne detection can be accomplished by the standard silicon photonic device portfolio, comprising also on-chip Germanium photodiodes. For coupling of light to and from the measurement path, chip-attached micro lenses could be used, fabricated by the same direct-write three-dimensional two-photon lithography used for photonic wire bonding [J7]. Read-out and processing of electric signals is realized with standard electronic components connected through electrical wirebonds. As a specific advantage of the hybrid integration approach, the scheme can easily be adapted for use with other chip-scale comb sources such as ultrabroadband Kerr comb generators which could further enhance the performance [240]. We see the main challenges in the minimizing the optical insertion losses, in realizing of a cost-effective packaging for hybrid integration, and in fabricating miniaturized comb sources. In general, chip-scale sensor systems stand out due to their ultra-compact footprint, which is an important asset for many applications. Moreover, the devices are mechanically robust and lend themselves to massive parallelization, e.g., by integrating a multitude of measurement channels on a single photonic chip.

4.3.5 Summary

We demonstrated an integrated silicon PIC capable of fast and accurate distance measurement with 3.75 mm unambiguity range using the concept of synthetic-

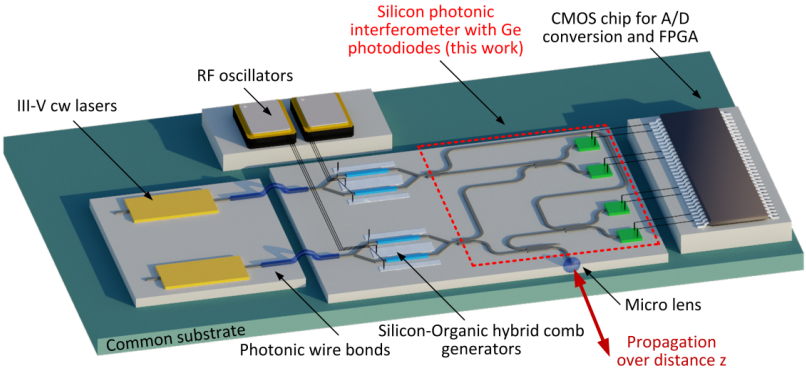

Fig. 4.6: Vision for a future chip-scale distance measurement system. The photonic elements comprise light sources (III-V CW lasers), frequency comb generators realized by silicon-organic hybrid (SOH) modulators [J5, J13], and an interferometer with photo detectors as demonstrated in this work. The electronic components comprise DC voltage supply (not depicted), RF oscillators for driving the comb generators, and readout and processing circuitry, e.g., A/D converters connected to an FPGA. The individual elements are assembled on a common submount. Electrical connections are realized by standard wire bonding techniques. Light is routed by silicon single-mode on-chip waveguides and by photonic wire bonds, the latter being fabricated by direct-write three-dimensional two-photon lithography [243–245]. Using the same fabrication technique, a tailored free-form micro lens can be printed directly to the facet of the optical chip to collimate the light radiated to and from the chip edge used to collimate the light used for distance measurement [J7].

wavelength interferometry with externally generated frequency combs. A root-mean-square error of 3.4 µm is achieved for an acquisition time of 14 µs. The PIC covers an on-chip footprint of approximately 0.25 mm^2 and relies entirely on the standard device portfolio offered by a silicon photonic foundry. There are many possibilities of further extend of the concept, such as co-integration of lasers sources, comb generators [J5] or electronics. We believe that large-scale photonic integration will enable completely new sensing and measurement systems of unprecedented scalability and functionality in the near future.

Appendix A: Mathematical description of measurement scheme

In the following section, we give a rigorous mathematical description of the measurement scheme, which relies on quadratic detection of two detuned frequency combs by the measurement and reference detector. Analytical signals $\underline{E}(\mathrm{t})$ are used to describe the time-domain electric fields, with the real part of the analytical signal representing the physically relevant field, $E(\mathrm{t}) = \Re\left\{\underline{E}(\mathrm{t})\right\}$. The optical power is then given by $P = Z_0^{-1}\left\langle E^2(t)\right\rangle$, where $\langle - \rangle$ denotes the average over a few cycles of the optical carrier and where $Z_0 = 376.7\,\Omega$ represents the wave impedance of free space. In a first step we consider the measurement detector only. In accordance to the system detailed in Fig. 4.2(a) we consider the complex optical amplitudes $\underline{E}_{\mathrm{sig,meas}}$ for the signal comb FC 2 arriving at the measurement detector. Each signal comb line l has an (angular) optical frequency $\omega_{l,\mathrm{sig}}$,

$$\omega_{l,\mathrm{sig}} = \omega_{0,\mathrm{sig}} + l\omega_{\mathrm{mod,sig}}. \tag{4.5}$$

The amplitudes of the signal comb lines are denoted as $\hat{E}_{l,\mathrm{sig,meas}}$, and the associated optical path length to the detector amounts to $2z + D_{\mathrm{sig,meas}}$, where $D_{\mathrm{sig,meas}}$ denotes the optical path length through the measurement setup to and from the origin $z = 0$ of the measurement coordinate system. Similarly, the complex optical amplitudes of the LO comb FC 1 at the measurement detector are denoted as $\underline{E}_{\mathrm{LO,meas}}$, and each comb line m has an (angular) optical frequency $\omega_{m,\mathrm{LO}}$,

$$\omega_{m,\mathrm{LO}} = \omega_{0,\mathrm{LO}} + m\omega_{\mathrm{mod,LO}} = \left(\omega_{0,\mathrm{sig}} + \Delta\omega_0\right) + m\left(\omega_{\mathrm{mod,sig}} + \Delta\omega_{\mathrm{mod}}\right), \tag{4.6}$$

with a center frequency detuning $\Delta\omega_0$ and a detuning of the line spacing of $\Delta\omega_{\mathrm{mod}}$, an amplitude $\hat{E}_{m,\mathrm{LO,meas}}$. The LO comb arrives at the measurement detector after propagation over the optical path length $D_{\mathrm{LO,meas}}$, which is

entirely located within the measurement setup. The complex amplitudes of the two FC at the measurement detector are then given as

$$\begin{aligned}\underline{E}_{\mathrm{sig,meas}}(t) &= \sum_l \hat{E}_{l,\mathrm{sig,meas}} \exp\left(\mathrm{j}\omega_{l,\mathrm{sig}} t\right) \exp\left(-\mathrm{j}\left(2z + D_{\mathrm{sig,meas}}\right)\omega_{l,\mathrm{sig}}/c\right) \\ \underline{E}_{\mathrm{LO,meas}}(t) &= \sum_m \hat{E}_{m,\mathrm{LO,meas}} \exp\left(\mathrm{j}\omega_{m,\mathrm{LO}} t\right) \exp\left(-\mathrm{j}D_{\mathrm{LO,meas}}\omega_{m,\mathrm{LO}}/c\right).\end{aligned} \tag{4.7}$$

The superposition of the signal and LO comb on the measurement detector with sensitivity S leads to a photocurrent containing multiple IF tones. The AC-part of the photocurrent $i_{\mathrm{AC,meas}}$ of the measurement detector is given by

$$\begin{aligned}i_{\mathrm{AC,meas}}(t) &= Z_0^{-1} S \cdot \Re\left\{\underline{E}_{\mathrm{sig,meas}}(t)^* \, \underline{E}_{\mathrm{LO,meas}}(t)\right\} \\ &= Z_0^{-1} S \cdot \Re\left\{\begin{array}{l}\sum_l \sum_m \hat{E}_{l,\mathrm{sig,meas}} \hat{E}_{m,\mathrm{LO,meas}} \\ \qquad \cdot \exp\left(\mathrm{j}\left(\Delta\omega_0 + (m-l)\,\omega_{\mathrm{mod,sig}} + m\Delta\omega_{\mathrm{mod}}\right)t\right) \\ \qquad \cdot \exp\left(\mathrm{j}\left((2z + D_{\mathrm{sig,meas}})\omega_{l,\mathrm{sig}} - D_{\mathrm{LO,meas}}\omega_{m,\mathrm{LO}}\right)/c\right)\end{array}\right\}.\end{aligned} \tag{4.8}$$

The AC-part of the photocurrent $i_{\mathrm{AC,ref}}$ of the reference detector can be derived in an analogous way by replacing "meas" by "ref" in the subscript,

$$\begin{aligned}i_{\mathrm{AC,ref}}(t) &= Z_0^{-1} S \cdot \Re\left\{\underline{E}_{\mathrm{sig,ref}}(t)^* \, \underline{E}_{\mathrm{LO,ref}}(t)\right\} \\ &= Z_0^{-1} S \cdot \Re\left\{\begin{array}{l}\sum_l \sum_m \hat{E}_{l,\mathrm{sig,ref}} \hat{E}_{m,\mathrm{LO,ref}} \\ \qquad \cdot \exp\left(\mathrm{j}\left(\Delta\omega_0 + (m-l)\,\omega_{\mathrm{mod,sig}} + m\Delta\omega_{\mathrm{mod}}\right)t\right) \\ \qquad \cdot \exp\left(\mathrm{j}\left(D_{\mathrm{sig,ref}}\omega_{l,\mathrm{sig}} - D_{\mathrm{LO,ref}}\omega_{m,\mathrm{LO}}\right)/c\right)\end{array}\right\}.\end{aligned} \tag{4.9}$$

In this relation, the quantities $D_{\mathrm{sig,ref}}$ and $D_{\mathrm{LO,ref}}$ denote the optical path lengths between the respective combs source and the reference detector. Note that, in contrast to Eq. (4.8) the external measurement distance 2z does not appear in the reference path length.

The frequency detunings $\Delta f_0 = \Delta\omega_0/(2\pi)$ and $\Delta f_{\mathrm{mod}} = \Delta\omega_{\mathrm{mod}}/(2\pi)$ amount to tens of megahertz and are small compared to the line spacing $f_{\mathrm{mod,sig}} = \omega_{\mathrm{mod,sig}}/(2\pi)$ of roughly 40 GHz. In theory, the photocurrent spectrum shows beat signals at distinct intermediate frequencies $f_{m,l}$,

$$f_{m,l} = \left|\Delta f_0 + (m-l)\, f_{\mathrm{mod,sig}} + m\, \Delta f_{\mathrm{mod}}\right|. \tag{4.10}$$

However, only a subset of these lines can actually be acquired by the photodetector and the subsequent A/D converter. For the FC deployed in our experiments, the analog bandwidth B of the A/D converter used to record the signals amounts to 1.3 GHz and is much smaller than the 40 GHz line spacing of the frequency combs, $B \ll f_{\mathrm{mod,sig}} \approx f_{\mathrm{mod,LO}}$. Moreover, the number of comb lines is limited such that $m\Delta f_{\mathrm{mod,LO}} \ll f_{\mathrm{mod,sig}} \approx f_{\mathrm{mod,sig}}$ for all comb line indices m. As a consequence, for a given LO comb line m, only the beat note with the corresponding signal comb of same index $m = l$ is visible in the photocurrent. IF lines are hence found at distinct frequencies $f_{\mathrm{IF},m} = |\Delta f_0 + m\,\Delta f_{\mathrm{mod}}|$. The corresponding phases $\varphi_{m,\mathrm{meas}}$ of the IF lines at the measurement detector can be derived from Eq. (4.8),

$$\begin{aligned}
&\varphi_{m,\mathrm{meas}}\left(2z + D_{\mathrm{sig,meas}}, D_{\mathrm{LO,meas}}\right)\\
&\quad= \left((2z + D_{\mathrm{sig,meas}})\omega_{m,\mathrm{sig}} - D_{\mathrm{LO,meas}}\omega_{m,\mathrm{LO}}\right)/c\\
&\quad= \left((2z + D_{\mathrm{sig,meas}}) - D_{\mathrm{LO,meas}}\right)\left(\omega_{0,\mathrm{sig}} + m\omega_{\mathrm{mod,sig}}\right)/c\\
&\qquad - D_{\mathrm{LO,meas}}\left(\Delta\omega_0 + m\Delta\omega_{\mathrm{mod}}\right)/c\\
&\quad= 2\pi\left((2z + D_{\mathrm{sig,meas}}) - D_{\mathrm{LO,meas}}\right)\Lambda_m^{-1}\\
&\qquad + 2\pi\left((2z + D_{\mathrm{sig,meas}}) - D_{\mathrm{LO,meas}}\right)\lambda_{0,\mathrm{sig}}^{-1}\\
&\qquad - D_{\mathrm{LO,meas}}\left(\Delta\omega_0 + m\Delta\omega_{\mathrm{mod}}\right)/c.
\end{aligned} \tag{4.11}$$

The last part of Eq. (4.11) contains the so-called synthetic wavelength $\Lambda_m = c\left(m f_{\mathrm{mod,sig}}\right)^{-1}$ and shows the relation to classical interferometry with a single optical wavelength λ, where the phase shift φ experienced by an optical signal after propagation over the optical path length D is determined by $\varphi = 2\pi D\lambda^{-1}$. The beat signals at the reference detector have the exactly same frequencies as the beat signals at the measurement detector and serve as phase reference. Their phases are determined analogously to Eq. (4.11) and are given as

$$\varphi_{m,\mathrm{ref}}\left(D_{\mathrm{sig,ref}}, D_{\mathrm{LO,ref}}\right) = \left(D_{\mathrm{sig,ref}}\omega_{m,\mathrm{sig}} - D_{\mathrm{LO,ref}}\omega_{m,\mathrm{LO}}\right)/c. \tag{4.12}$$

The phase difference of the beat signals is given by:

$$\begin{aligned}\Delta\varphi_m(z) =& \varphi_{m,\mathrm{meas}}\left(2z + D_{\mathrm{sig,meas}}, D_{\mathrm{LO,meas}}\right) - \varphi_{m,\mathrm{ref}}\left(D_{\mathrm{sig,ref}}, D_{\mathrm{LO,ref}}\right)\\ =& \left(2z + D_{\mathrm{sig,meas}} - D_{\mathrm{LO,meas}} - \left(D_{\mathrm{sig,ref}} - D_{\mathrm{LO,ref}}\right)\right) m\omega_{\mathrm{mod,sig}}/c\\ & \left(2z + D_{\mathrm{sig,meas}} - D_{\mathrm{LO,meas}} - \left(D_{\mathrm{sig,ref}} - D_{\mathrm{LO,ref}}\right)\right) \omega_{0,\mathrm{sig}}/c\\ & - \left(D_{\mathrm{LO,meas}} - D_{\mathrm{LO,ref}}\right) \Delta\omega_0/c\\ & - \left(D_{\mathrm{LO,meas}} - D_{\mathrm{LO,ref}}\right) m\Delta\omega_{\mathrm{mod}}/c.\end{aligned} \tag{4.13}$$

Subtracting the values $\Delta\varphi_m(z_0)$ from a calibration measurement at the position z_0, we arrive at Eq. (4.1),

$$\Delta\varphi_m(z) - \Delta\varphi_m(z_0) = 2(z - z_0)\, m\omega_{\mathrm{mod,sig}}/c + 2(z - z_0)\,\omega_{0,\mathrm{sig}}/c. \tag{4.14}$$

The distance $z - z_0$ can thus be extracted by extracting the slope of the linear relationship between $\Delta\varphi_m$ and m.

Appendix B: Optimum power splitting ratio

In the following section we derive an expression for the optimum splitting ratio of the TPS, see Fig. 4.2(a), used to distribute the power of the LO comb FC 1 onto measurement and reference photodetectors. Due to the relatively low optical powers impinging on the photodetectors, the current system is limited by thermal noise. The noise current variance is thus independent of the optical power and denoted as $\sigma^2_{I,\mathrm{noise}}$. For simplicity, we assume that both detectors feature the same noise current variance. The optical power of a comb line is given as $P_m = Z_0^{-1}\left\langle E_m^2(t)\right\rangle = Z_0^{-1}\left\langle \hat{E}_m^2 \cos(\omega_m t)\right\rangle = \frac{1}{2} Z_0^{-1}\hat{E}_m^2$, where $\langle -\rangle$ denotes the average over a few carrier periods. Using this relation and Eq. (4.8) with $m = l$, the power signal-to-noise ratio SNR_m of a single IF line with index m is given by

$$\mathrm{SNR}_m = \frac{\frac{1}{2}S^2 2P_{m,\mathrm{sig}} 2P_{m,\mathrm{LO}}}{\sigma^2_{I,\mathrm{noise}}}. \tag{4.15}$$

For distance measurement, we valuate the phase of theses IF lines. The accuracy is thus dictated by the phase variance $\sigma^2_{\varphi,m}$, which is given by [190]

$$\sigma^2_{\varphi,m} = \frac{1}{2 \times \mathrm{SNR}_m}. \tag{4.16}$$

The distance z is calculated from a linear regression of the phase differences $\Delta\varphi_m = \varphi_{m,\mathrm{meas}} - \varphi_{m,\mathrm{ref}}$ between measurement and reference detector. For simplification, we assume a number of N spectrally uniform IF lines with equal SNR and drop the index m. The noise of measurement and reference detector is statistically independent such that the phase variances can be added,

$$\sigma^2_{\Delta\varphi} = \sigma^2_{\varphi,\mathrm{meas}} + \sigma^2_{\varphi,\mathrm{ref}}. \tag{4.17}$$

Then the variance of the measured distance z is given from the analytic formula for the slope uncertainty of a linear regression [193] and is proportional to the variance of the phase difference $\sigma^2_{\Delta\varphi}$,

$$\sigma^2_z = \frac{\sigma^2_{\Delta\varphi}}{N} \frac{3}{\left(\omega_{\mathrm{mod,sig}/c}\right)^2 \left(N^2 - 1\right)}. \tag{4.18}$$

With Eq. (4.15) and Eq. (4.16), Eq. (4.17) can be written as

$$\sigma^2_{\Delta\varphi} = \frac{\sigma^2_{I,\mathrm{noise}}}{4S^2} \left(\frac{1}{P_{\mathrm{sig,meas}} P_{\mathrm{LO,meas}}} + \frac{1}{P_{\mathrm{sig,ref}} P_{\mathrm{LO,ref}}} \right). \tag{4.19}$$

We consider Fig. 4.7 to express the optical powers of the comb lines impinging on the respective detectors in Eq. (4.19) in the following way: The input power into the TPS is denoted P_{LO}. With the power splitting ratio γ, $P_{\mathrm{LO,meas}} = (1-\gamma)\, P_{\mathrm{LO}}$ and $P_{\mathrm{LO,ref}} = \gamma P_{\mathrm{LO}}$. The additional power loss of $P_{\mathrm{sig,meas}}$ compared to $P_{\mathrm{sig,ref}}$ is denoted η, $\eta = P_{\mathrm{sig,meas}}/P_{\mathrm{sig,ref}}$, as discussed in Section 4.3.3. With these relations, we can write Eq. (4.19) as

$$\sigma^2_{\Delta\varphi} = \frac{\sigma^2_{I,\mathrm{noise}}}{4S^2 P_{\mathrm{LO}} P_{\mathrm{sig,ref}}} \left(\frac{1}{\eta\,(1-\gamma)} + \frac{1}{\gamma} \right). \tag{4.20}$$

The power splitting ratio γ can easily be adapted by changing the interference conditions of the MZM forming the TPS. For a maximum measurement pre-

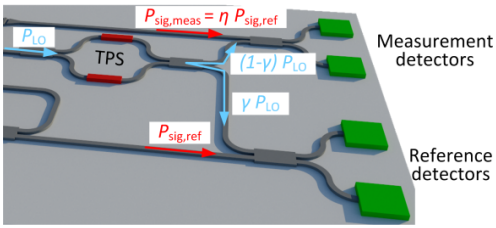

Fig. 4.7: Schematic of power distribution on measurement and reference detectors. $P_{\mathrm{sig,meas}}$ is subject to an additional loss of $\eta_{\mathrm{dB}} = 10\lg(\eta) = -23\mathrm{dB}$ when compared to $P_{\mathrm{sig,ref}}$ due to coupling losses, see Fig. 4.2 and the discussion in Section 4.3.3. The power of the LO comb FC 1 is distributed between both detectors by the TPS with a tunable power splitting ratio of γ.

cision, the goal is to minimize $\sigma^2_{\Delta\varphi}(\gamma) \propto \sigma^2_z$, Eq. (4.20). We find a minimum at

$$\gamma_{\mathrm{min}} = \frac{1}{1+\eta^{-1/2}}. \tag{4.21}$$

In our case $\eta_{\mathrm{dB}} = 10\lg(\eta) = -23\,\mathrm{dB}$. Inserting this value in Eq. (4.21), we calculate a theoretical optimum value of $\gamma_{\mathrm{min,dB,theo}} = 10\lg(\gamma_{\mathrm{min}}) = -11.8\,\mathrm{dB}$. This is close to the experimentally measured value of $\gamma_{\mathrm{min,dB}} = -10.2\,\mathrm{dB}$.

[*End of paper* [J11]]

5 Referencing of synthetic wavelengths with electro-optic frequency combs

This chapter describes a distance measurement system in which a coarse time-of-flight measurement with a wide range of unambiguity is combined with an interferometric distance measurement using synthetic wavelengths to refine the measurement accuracy. The synthetic wavelengths are generated by the frequency differences between four continuous-wave (CW) lasers. To make the use of free-running continuous-wave lasers possible, said frequency differences continuously tracked during the distance measurement by a referencing module that exploits electro-optic frequency comb generation. The background of the presented work in this chapter is summarized in Section 5.1, and an overview of the state of the art is given in Section 5.2. Section 5.3 finally introduces the measurement principle and the experimental setup and provides an analysis and a discussion of the obtained results.

5.1 Background

The results presented here were obtained in a joined effort together with the Fraunhofer Institute for Physical Measurement Techniques (IPM) in Freiburg during a project funded by the Baden-Württemberg Stiftung (project „Synthetic Lambda“).

In the framework of this cooperation, Harald Wölfelschneider contributed all elements related to the coarse time-of-flight measurement, Markus Fratz mainly contributed the elements concerning the synthetic-wavelength interferometry as such, while the author contributed all elements concerning the referencing module for calibration of the synthetic wavelengths simultaneously to the distance measurement.

5.2 State of the art in synthetic-wavelength interferometry referenced by frequency combs

This section provides a summary of the state of the art in referencing of synthetic wavelengths using frequency combs. Essentially, the regular and precise spacing of comb lines in the frequency domain is exploited as an optical frequency ruler. Depending on the employed measurement scheme, this ruler needs to provide absolute or relative information. While for interferometry with optical wavelengths knowledge of absolute frequencies is essential, measurements of relative frequency differences are sufficient for synthetic-wavelength interferometry.

In [131], synthetic-wavelength interferometry is combined with optical interferometry. To this end, an Er-doped femtosecond fiber laser, stabilized to a Rb atomic clock, is combined with four distributed feedback lasers (DFB) at different wavelengths. A rough measurement of the DFB-laser wavelengths with a wavelength meter provides an initial value. The wavelengths are then stabilized by feedback loops with respect to adjacent comb lines by detecting beat frequencies on photodetectors. Using an optical switch, measurements are conducted sequentially for one wavelength at a time. A Twyman-Green interferometer is used in conjunction with a piezoelectric transducer for a well-defined phase shift, which is needed for the underlying evaluation algorithm. The interferogram is recorded by a charge-coupled device (CCD). Due to the combination of synthetic-wavelength interferometry and conventional optical interferometry, a standard deviation of 3 nm and an unambiguity range of 50 mm is obtained. The measurement time is 400 ms, partly limited by the switching time for the subsequent measurements.

In [133], a MEMS-based external-cavity diode laser (ECDL) with a frequency sweep spanning 1 THz is used for frequency-modulated continuous-wave (FMCW) ranging. To linearize the sweep in frequency, a comb generated by a femtosecond fiber laser is used. A distance standard deviation of 2 µm with a measurement time of 0.5 ms is demonstrated for ranging to a brushed aluminum surface.

In [132], a frequency-tunable external-cavity diode laser (ECDL) is calibrated by a frequency comb generated from a femtosecond mode-locked laser with

a repetition rate of 250 MHz. To this end, a wavelength meter provides an initial rough measurement of the frequency of the ECDL. For stabilization of the ECDL emission frequency, the beat signal between the ECDL tone and the nearest comb line is detected after superposition on a photodiode. The frequency of said beat signal is then used in a feedback loop to control the frequency of the ECDL. This scheme allows for highly precise frequency tuning of the ECDL over the range of 200 GHz. Distance measurements with standard deviations of 4.6 µm are obtained by evaluation of the phase at different frequencies with heterodyne detection. No explicit measurement time is stated in the paper.

The work presented in [139] also relies on a ECDL laser referenced to a frequency comb generated from a femtosecond mode-locked laser with a line spacing of 81 MHz. After a coarse measurement with a wavelength meter, the beat frequency of the ECDL to the nearest comb line is measured, and the ECDL is locked to that frequency. Distance measurements are done with four different wavelengths, evaluating both synthetic and single wavelengths. A standard deviation of 64 nm is achieved for a measurement distance of 1 m, using a real-time compensation for the refractive index of the air by monitoring several environmental parameters.

In contrast to the state of the art, the work presented here employs simple, free-running CW lasers without any locking electronics [J4], see Section 5.3. The differences in emission frequencies, and thus the synthetic wavelengths, are not tightly controlled, but merely monitored continuously during the measurement. Relative frequency drifts of the lasers can thus be corrected when calculating the distance from the phase differences measured at the different wavelengths. No additional frequency comb sources are required – the combs are generated by electro-optic modulation from the same CW lasers that are used for the synthetic-wavelength interferometry. This approach lends itself to photonic integration, see Chapter 6, with the potential for chip-scale optical frequency referencing devices.

5.3 Synthetic-wavelength interferometry improved with frequency calibration and unambiguity range extension

The contents of the following section is taken from a publication in Applied Optics [J4]. The structure and the layout of this document was slightly adapted to fit the format of this thesis.

[*Start of paper* [J4]]

Synthetic wavelength interferometry improved with frequency calibration and unambiguity range extension

Applied Optics; Volume 54; Issue 20; pp. 6334-6343; 2015
DOI: 10.1364/AO.54.006334

C. Weimann[1,2], M. Fratz[3], H. Wölfelschneider[3], Wolfgang Freude[1,2], Heinrich Höfler[3], Christian Koos[1,2]

[1]*Institute of Photonics and Quantum Electronics (IPQ), Karlsruhe Institute of Technology (KIT), Engesserstrasse 5, 76131 Karlsruhe, Germany*

[2]*Institute of Microstructure Technology (IMT), Karlsruhe Institute of Technology (KIT), Hermann-von-Helmholtz-Platz 1,76344 Eggenstein-Leopoldshafen, Germany*

[3]*Fraunhofer Institute for Physical Measurement Techniques, Heidenhofstrasse 8, 79110 Freiburg, Germany*

5.3.1 Introduction

Precisely measuring the geometry of large technical objects is important for many applications in science and engineering such as high-precision alignment, wear inspection, as well as in-line or at-line quality control in production. Optical distance measuring methods are inherently well suited for these applications, offering, e.g., non-contact probing within large measurement volumes. For practical measurements, a number of challenges need to be addressed. As an example, objects are often made by machining metal,

thus exhibiting discontinuously stepped surfaces with considerable roughness. Insensitivity to optical surface properties and a large unambiguity range are key requirements. Moreover, to allow dense digitization of free-form surfaces in a harsh production environment, high measurement speed and robustness against environmental influences are indispensable while accuracies in the micrometer range should be maintained.

An overview of various optical measurement methods is given in [113]. Classical time-of-flight (TOF) methods using pulsed laser sources or lasers with sinusoidally modulated intensity [160, 178] offer unambiguity ranges of up to several hundred meters and measurement rates of more than 1 MHz, but the accuracy is typically limited to the millimeter region. For an increased accuracy, one can use an envelope with a higher frequency by utilizing the inter-mode beats of an optical frequency comb [35] as measured by a photodetector. Using a specific target, namely a corner retro-reflector, distance measurements with sub-micrometer standard deviations σ were already demonstrated by evaluating the phases of comb beat notes with frequencies as high as 40 GHz [115]. At these frequencies, expensive photodetectors with its associated broadband electronics are indispensable. Optical heterodyne detection schemes overcome the problem of RF analysis by using a second reference frequency comb with a slightly shifted center frequency and a different line spacing for shifting and scaling the RF beats to a lower frequency range. A sufficiently broad comb covers a high optical bandwidth leading to a good accuracy, while evaluating the beat between the closely spaced lines of measurement and reference comb requires only low-frequency electronics [34, 37]. Because the power of the reference comb (acting as a "local oscillator") can be large, the sensitivity is strongly increased. This allows to measure the distance to scattering technical surfaces with an accuracy in the micrometer range, and with microsecond acquisition times [C4]. It has recently been demonstrated that a heterodyne receiver can be efficiently integrated on a silicon photonic chip with a footprint less than a square-millimeter [C5]. Nevertheless, the practical use of dual-comb heterodyne distance metrology is still hampered by the considerable technical effort that is needed to ensure stable operation of two broadband frequency combs with fixed offsets of center frequency and line spacing.

As an alternative to TOF methods or dual-comb heterodyne schemes, multi-wavelength interferometry (MWLI) can be used. This technique relies on two or more continuous-wave (CW) lasers with different wavelengths to extend

the unambiguity range of conventional optical interferometry [135, 136]. The phases of all CW carriers can be obtained individually in a low-frequency range. While it is advantageous to employ simple CW lasers, the measurement accuracy is limited by the wavelength stability [137, 138]. To overcome this problem, lines of a stabilized frequency comb from a mode-locked laser can be used to lock the wavelengths of distributed feedback (DFB) laser diodes [131]. For measuring the optical phases, an interferogram is evaluated by a charge-coupled device (CCD) camera, employing a piezoelectric transducer for a well-defined phase shift, which is needed for an appropriate evaluation algorithm [131]. However, this scheme requires considerable technical effort for locking the DFB lasers to the femtosecond master laser. Moreover, the measurement rate in [131] is limited to only 2.5 Hz by the fact that the measurements are done subsequently for each wavelength using an optical switch.

In this thesis, we show that high-precision measurements are also possible with free-running CW lasers, for which the differences of the emission frequencies are continuously monitored. We combine the large unambiguity range of a TOF scheme with the high precision of a synthetic-wavelength interferometry (SWI) technique. The phase differences for the various light sources are evaluated simultaneously from a single frame of a CCD line camera by combining spatial and spatial-frequency multiplexing. For continuously referencing the synthetic wavelengths, we modulate the CW laser lines with a sinusoidal signal of accurately known frequency. We then detect low-frequency beat notes between higher-order sidebands that belong to adjacent lines. This allows to determine the synthetic wavelengths with highest precision and hence to trace the results back to widely available frequency standards. When measuring the displacement of a machined aluminum target in a stand-off distance of 1 m with a measurement rate of 300 Hz, we achieve standard deviations σ between 3 µm and 15 µm. The accuracy of the current system is limited by the update rate of the wavelength-referencing scheme, and an improvement to $\sigma < 1$ µm should be feasible in future implementations.

5.3.2 Measurement system

The system layout is depicted in Fig. 5.1. It consists of three main modules: A time-of-flight (TOF) module to measure the distance within a large unambiguity range, a synthetic-wavelength interferometry (SWI) module to increase the

measurement accuracy to the micrometer range, and a synthetic-wavelength reference (SWR) module to continuously monitor the synthetic wavelengths and to compensate the influence of laser frequency drifts. All three modules operate simultaneously. TOF measurements share the same beam path to the target as the SWI measurement by using a dichroic mirror to combine the associated lasers. A set of four self-injection locked laser diodes (Laser 1 ... 4; OEWaves, linewidth 300 Hz) are used for the SWI. The output power of these lasers is split evenly between the SWI module and the reference module using 3 dB fiber couplers. The operation principle and the implementations of the modules are described in the following sections.

5.3.2.1 Time-of-flight measurement

The setup for the TOF measurements is depicted in more detail in Fig. 5.2. A fiber-coupled laser diode emitting light at a wavelength of 1470 nm is intensity-modulated with a modulation frequency $f_{\mathrm{mod}} = 128\,\mathrm{MHz}$ and shines on the target. The back-scattered light is detected with an InGaAs avalanche photodiode (APD). The intensity-modulated light generates an electrical signal with a frequency of 128 MHz, which is amplified in a first amplifier. Heterodyne down-mixing with a local oscillator (LO) at 120 MHz generates an intermediate frequency (IF) signal at 8 MHz. This IF signal is sent through a logarithmic amplifier to ensure a high dynamic range. A low-pass filter (LP) suppresses sum-frequency terms and high-frequency distortions that arise from the logarithmic amplification. The baseband signal is then digitalized by a 14-bit analog-to-digital converter (ADC). To calculate the distance, the phase difference to an 8 MHz reference signal, derived from the same frequency basis as the modulation and the LO signal, is calculated with a field-programmable gate array (FPGA) using a coordinate rotation digital computer (CORDIC) algorithm [246, 247]. The 8 MHz reference signal is passed through an identical LP to compensate the influence of temperature drifts of the filter component on the phase measurement to a certain extent. The whole setup realizes a lock-in amplifier with a measurement rate of 1 MHz. With a measured phase difference $\Delta\phi$, the distance z_{TOF} then is calculated from

$$z_{\mathrm{TOF}} = \frac{c\Delta\phi}{4\pi f_{\mathrm{mod}}}, \tag{5.1}$$

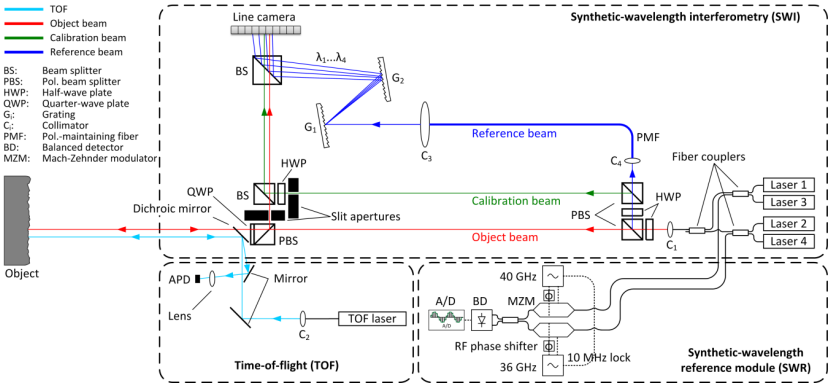

Fig. 5.1: Optical setup, combining a time-of-flight (TOF) module for a large unambiguity range, a synthetic-wavelength interferometry (SWI) module for increasing the measurement accuracy, and a synthetic-wavelength reference (SWR) module for monitoring the frequency spacings of the CW laser sources (Laser 1 ... 4). (**TOF**) The TOF module measures the coarse distance with a large unambiguity range. A laser diode is sinusoidally modulated in intensity, and the phase of the modulation signal in the reflected beam is a measure of the time of flight. (**SWI**) Four CW lasers with frequencies in a range ±375 GHz around 193.4 THz (1.55 µm) send their light to a target from where it is reflected. This object beam is superimposed with reference beams $\lambda_1 \ldots \lambda_4$ and detected by a line camera for measuring the phase differences in the SWI module. This is done by recording four interferograms of the four lasers, where each laser beam interferes with a delayed copy of itself (reference beam, blue). For each laser, the copy is inclined at a different angle with respect to the original due diffraction gratings G_1 and G_2. A line camera then records four interferograms which are distinguished by different spatial periodicities. (**SWR**) The SWR module measures the frequency differences of the lasers. Pairs of lasers are phase modulated with dual-drive MZM such that the generated comb of sidebands overlap for neighboring lasers. We then detect beat signals of closely spaced sidebands and infer the respective carrier frequency offsets from the well-known MZM drive frequencies, see Section 5.3.2.

where c is the vacuum speed of light. Considering that the phase is only defined in a $[0, 2\pi]$ range, the unambiguity range amounts to 1.17 m. The results for TOF distance measurements to a fixed target can be seen in Fig. 5.3. At the given measurement rate of 1 MHz, the distance is determined with $\sigma = 2.2$ mm, Fig. 5.3(a). The acquisition time amounts to only 1 µs whereas the SWI measurement rate is only 300 Hz, enabling averaging to improve the accuracy. For averaging over 2000 samples, the TOF standard deviation drops to 250 µm, Fig. 5.3(b). This is larger than the expected value of $2.2\,\text{mm}/\sqrt{2000} = 50\,\mu\text{m}$ due to small systematic fluctuations of the measurement result, caused by slightly different temperature dependencies of the electric low-pass filters used

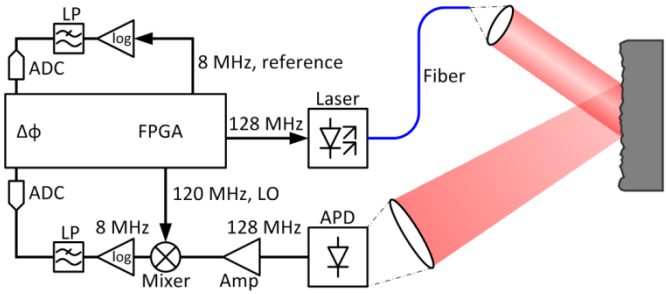

Fig. 5.2: Setup used for TOF measurements. A 1470 nm laser is intensity-modulated with 128 MHz. The backscattered signal is detected with an InGaAs avalanche photodiode (APD), amplified (Amp)) and mixed down to an 8 MHz intermediate frequency. Logarithmic amplification (log) enables a high dynamic range. After low-pass filtering (LP), the signal is analog-digital converted (ADC) and the phase difference to a reference signal is calculated on an FPGA with 1 MHz measurement rate.

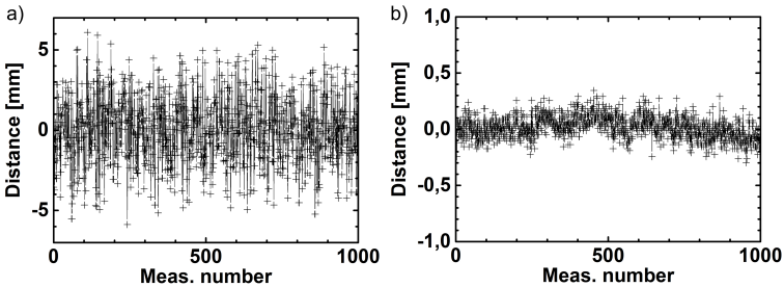

Fig. 5.3: Results of TOF measurements to a fixed target. (a) Measurements with the full TOF measurement rate of 1 MHz, exhibiting a standard deviation of $\sigma = 2.2$ mm. (b) Measurements employing averaging over 2000 values lead to a standard deviation of $\sigma = 250\,\mu$m. Due to temperature drifts of the low-pass filters, σ reduces by less than $\sqrt{2000}$.

in the measurement and the reference path, see Fig. 5.2. However, these fluctuations are unimportant, because the final accuracy will be determined by the SWI module.

5.3.2.2 Synthetic-wavelength interferometry

The fine-scale measurement is based on synthetic-wavelength interferometry [248–250] with four different wavelengths $\lambda_1 \ldots \lambda_4$. The light from each laser is split into an object beam, a reference beam, and a calibration beam. The object beam propagates to a measurement object and back to a CCD line camera, the surface of which is perpendicular to the incident beam; the two-way distance to and from the object is denoted as z. The reference beam is tilted by two subsequent gratings, so that the beams with $\lambda_1 \ldots \lambda_4$ hit the CCD camera at different angles after a propagation distance z_{ref}. Object and reference beam superimpose on the CCD camera, which records four so-called object interferograms with different spatial frequencies. The calibration beam propagates over a distance z_{cal} and hits the CCD camera at a different position than the object beam. Calibration beam and reference beam superimpose, and the CCD camera records another set of four so-called calibration interferograms, again with four different spatial frequencies, see Fig. 5.4. The phase $\varphi_{i,\mathrm{object}}$ of the resulting fringe pattern depends on the optical path length difference $z - z_{\mathrm{ref}}$ between object and reference beam:

$$\varphi_{i,\mathrm{object}} = 2\pi \frac{z - z_{\mathrm{ref}}}{\lambda_i}. \tag{5.2}$$

To compensate thermal and mechanical influences of the setup, an additional calibration measurement is taken. To this end, a part of the reference beam is tapped and forms a calibration beam. After propagation over a fixed distance z_{cal}, the calibration beam is superimposed with the reference beam on a different pixel range of the line camera. This yields a fringe pattern with the same spatial frequency as the object beam, the phase of which is given by

$$\varphi_{i,\mathrm{cal}} = 2\pi \frac{z_{\mathrm{cal}} - z_{\mathrm{ref}}}{\lambda_i}. \tag{5.3}$$

To calculate the compensated distance $z - z_{\mathrm{cal}}$, we consider the phase difference $\Delta\varphi_i = \varphi_{i,\mathrm{object}} - \varphi_{i,\mathrm{cal}}$ between object fringes and calibration fringes,

$$\Delta\varphi_i = 2\pi \frac{z - z_{\mathrm{cal}}}{\lambda_i}. \tag{5.4}$$

As the calculated phase values are 2π-periodic, the obtainable measurement unambiguity range is limited to half of the laser wavelength $\lambda_i/2$. Additionally,

the use of the phases of single wavelengths is significantly limited in the case of rough targets, where laser speckles lead to a random phase distribution [251]. To overcome this problem, rather than considering the phases of individual wavelengths, we evaluate the phase differences $\Delta\varphi_{ij} = \Delta\varphi_i - \Delta\varphi_j$ obtained from different wavelengths λ_i and λ_j,

$$\Delta\varphi_{ij} = \Delta\varphi_i - \Delta\varphi_j = 2\pi\frac{2z - z_{\text{cal}}}{\Lambda_{ij}}, \tag{5.5}$$

with the so called synthetic wavelengths Λ_{ij} [252, 253]:

$$\Lambda_{ij} = \frac{\lambda_i\lambda_j}{\left|\lambda_i - \lambda_j\right|} = \frac{c}{\Delta f_{ij}}. \tag{5.6}$$

In essence, considering the differences of the phases obtained from two CW signals at wavelengths λ_i and λ_j corresponds to an interferometric measurement at a synthetic wavelength that is associated with the frequency difference Δf_{ij} between the signals. A small frequency difference leads to a large synthetic wavelength, thus greatly increasing the unambiguity range. On the other, for given accuracy of the phase measurement, a large frequency difference and hence a small synthetic wavelength are desirable for an accurate distance measurement.

In our setup, we use four different laser wavelengths $\lambda_1 \ldots \lambda_4$, requiring 8 phase measurements for simultaneously acquiring the calibration and the object beam. These phase measurements can be obtained from a single readout of the CCD camera by using the principle of holographic phase detection. The concept is illustrated in Fig. 5.4. Both object beam (red) and calibration beam (green) are incident on the CCD line camera from surface-normal direction, whereas the reference beam (blue) impinges at a defined angle. This leads to interference fringes at a characteristic spatial frequency. For spatial multiplexing, object and calibration beam cover different pixel regions of the line camera, whereas the reference illuminates the entire line. The phases $\varphi_{i,\text{object}}$ and $\varphi_{i,\text{cal}}$ can hence be separated by simply evaluating the corresponding pixel range. Moreover, by using individual reference beam angles for each optical wavelength, the associated interference patterns exhibit characteristic spatial frequencies and can be separated by a spatial Fourier transform [135, 254, 255].

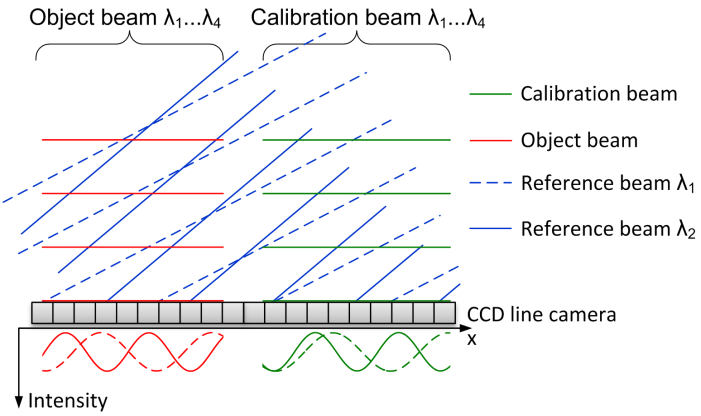

Fig. 5.4: Detection principle for the synthetic-wavelength interferometry (SWI). Both object beam (red) and calibration beam (green) are incident on the CCD line camera from surface-normal direction, whereas the reference beams (blue) impinge at different angles. For sake of simplicity, only the phase fronts of a single wavelength in object beam and calibration beam, and only λ_1 and λ_2 of the reference beam are depicted. The superposition on the line camera leads to interference fringes with different spatial frequencies for each optical wavelength; the associated interference patterns can be separated by a spatial Fourier transform. Object and calibration beam cover different pixel regions of the line camera, whereas the reference illuminates the entire line. The optical phases of the object or calibration and the reference beam are associated with the phase of the spatial interference pattern in the respective pixel range.

The complete setup of the SWI module is depicted in Fig. 5.1. Four fiber-coupled CW lasers (Laser 1 – 4) with wavelengths of 1547.11 nm, 1548.65 nm, 1550.48 nm and 1552.92 nm are coupled to the same polarization-maintaining (PM) single-mode fiber using PM fiber couplers. The fiber is connected to a collimator, where the light of all lasers is emitted into the free-space path. Polarization beam splitters are used to split the light onto the object beam (red), the calibration beam (green) and the reference beam (blue), thereby enabling control of the splitting ratios by half-wave plates (HWP). The object beam propagates to the target and the backscattered light is reflected into the direction of the CCD line scan camera. A slit aperture is used to select the pixel range which is illuminated by the object beam. The calibration beam has an optical path in close proximity to the object beam, thus cancelling effects of the environment such as temperature fluctuations. Another slit aperture is used to choose a pixel range to be illuminated by the calibration beam that is different

from that illuminated by the object beam. In addition, four reference beams, illuminating the entire line camera, are incident under distinct angles which lead to the distinct spatial frequencies of the associated interference fringes. The four reference beams are obtained by splitting the combined signal of all four wavelengths. To this end, we use a setup comprising two blazed gratings (600 lines/mm, blaze angle 28.7°), see Fig. 5.1. This optical setup produces different incident angles of the reference beams for each laser. The generated fringes on the line camera can be seen in Fig. 5.5(a). The intensity distribution is formed by the interference of the different reference beams with the object and the calibration beam, where the latter two are incident on different pixel ranges. The various interference patterns are separated by a spatial Fourier transform of the intensity distribution, Fig. 5.5(b). This leads to four distinct patterns P1, P2, P3, and P4, each corresponding to the interference fringes of the reference beam with the calibration and the object beam coming from the same laser. To obtain the individual phase information of each wavelength, each of the patterns is band-pass filtered in the spatial frequency domain. The analytical signals in the spatial domain are obtained by means of a discrete Hilbert transform, which is approximated by setting all spectral components at negative spatial frequencies to zero and using an inverse Fourier transform. This leads to complex amplitudes in the space domain, the magnitudes of which are plotted in Fig. 5.5(c). For each laser wavelength λ_i, the fringe phase difference $\Delta\varphi_i$ between object beam and calibration beam can now be determined by calculating the mean phase difference between the complex values at the corresponding pixels.

5.3.2.3 Absolute referencing of synthetic wavelengths

The accuracy of the SWI results depends on the accuracy of the phase measurement as well as on accurate knowledge of the frequency differences Δf_{ij} between the four lasers, which define the synthetic wavelengths, $\Lambda_{ij} = c/\Delta f_{ij}$. In our system we permanently monitor these frequency differences during operation, thereby enabling highly precise distance measurement and reducing requirements posed on the wavelength stability of the lasers. Moreover, the distance measurement is linked to a highly precise electronic frequency reference, ensuring direct traceability of the results to widely available frequency standards typically featuring relative accuracies of better than 10^{-12}. As a consequence, high-precision calibration objects are not required. The prin-

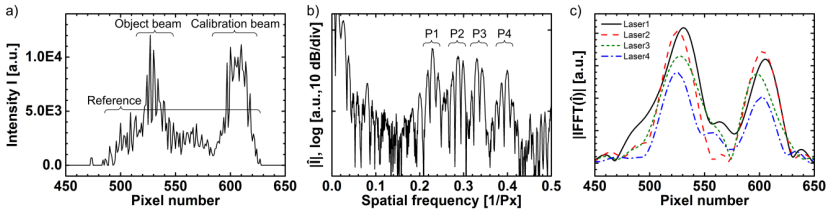

Fig. 5.5: Signals processed for the synthetic-wavelength interferometry. (a) Intensity distribution detected on the line camera. Object beam and calibration beam can be evaluated separately using different pixel ranges. (b) Fourier transform of the intensity distribution on the line camera. For each wavelength, an individual reference beam is used, impinging on the line camera at an individual angle. The interference with the object beam and the calibration beam leads to different spatial frequencies for fringes generated by each wavelength. Since the interference patterns cover only a small part of the pixel range, broadened patterns P1, P2, P3, and P4 rather than distinct peaks are visible in spatial power spectrum. (c) Magnitude of inverse Fourier transforms for bandpass-filtered patterns P1. . . P4 corresponding to lasers 1-4. The fringe phase differences between object beam and calibration beam can now be evaluated individually for each laser by calculating the mean phase difference between the complex values at the corresponding pixels.

ciple of referencing the synthetic wavelengths is illustrated in Fig. 5.6. The concept is similar to the one described in [256], with the main difference that our technique does not require a high-Q resonator to which the modulation frequency is adapted. This greatly simplifies the scheme and enables implementation in a robust metrology system. The lasers used in this work exhibit frequency differences in the order of several hundreds of gigahertz, thereby creating synthetic wavelengths that are small enough to achieve the desired measurement accuracy in the micrometer regime. Due to the large frequency spacing, direct detection of the heterodyne beat signal between neighboring laser wavelengths is impossible with state-of-the-art electronics. This can be overcome by modulating each CW carrier with precisely defined frequencies of 36 GHz and 40 GHz using standard telecommunication electro-optic modulators. The modulation leads to a multitude of equidistant sidebands, the spacing of which is precisely defined by the modulating frequency, see Fig. 5.6. Considering sidebands of up to 6^{th} order, the spacing between nearest-neighbor sidebands is relatively small and ranges from several hundred megahertz to just above 1 GHz. Upon quadratic detection on a standard photodiode, the associated beat signals can be detected using inexpensive low-frequency electronics. If the frequency differences between the lasers are roughly known a priori,

Fig. 5.6: Schematic illustration of referencing scheme for synthetic wavelengths: Standard telecommunication electro-optic modulators are used to generate multiple sidebands around each laser line, Fig. 5.1. The spacing of the laser lines is dictated by the respective modulation frequency. Direct detection on an standard photodiode leads to low-frequency beat signals $f_{\mathrm{beat},ij}$ between pairs of closely spaced side lines that have been derived from carrier i and j. Measurement of these beat frequencies allows for referencing of synthetic wavelengths. In the depicted example, the four laser lines are spaced by 294.8 GHz, 187.6 GHz, and 232.8 GHz. Lasers 1 and 3 are modulated by 36 GHz, whereas lasers 2 and 4 are modulated by 40 GHz. This leads to beat frequency differences of Δf_{12} = 1200 MHz, Δf_{23} = 400 MHz, and Δf_{34} = 800 MHz.

e.g., from measurements with an optical spectrum analyzer, the measured beat frequencies $f_{\mathrm{beat},ij}$ allow for a precise determination of the laser frequency differences Δf_{ij}. Given the order of the corresponding sidebands n_i, n_j and the RF modulation frequencies $f_{\mathrm{mod},i}$, $f_{\mathrm{mod},j}$, the spacing Δf_{ij} of the optical carriers can be calculated from

$$\Delta f_{ij} = n_i f_{\mathrm{mod},i} + n_j f_{\mathrm{mod},j} \pm f_{\mathrm{beat},ij}. \tag{5.7}$$

The sign of the beat frequency f_{beat} as well as the attribution to a certain pair of lasers is determined by a small thermal detuning of the frequency of a certain laser during the initialization procedure of the setup, which leads to a shift in frequency of the corresponding beat.

The technical implementation of the synthetic-wavelength reference module is depicted in Fig. 5.1. The lasers 1 ... 4 are connected to optical 3 dB-splitters to combine the laser outputs pairwise and to split the power between the distance measurement and the reference measurement. The optical carriers are modulated by dual-drive lithium niobate Mach-Zehnder Modulators (MZM) using sinusoidal drive signals with frequencies of 36 GHz and 40 GHz respectively. The amplitude and phase relation of the drive signals in the two arms of the MZM is optimized to generate broadband frequency combs [134]. The electrical drive signals are derived from a common 10 MHz frequency

reference and are amplified, achieving a peak-to-peak modulation depth of up to 3π which leads to higher-order sidebands with sufficient power. In our experiment, the used frequency reference comprises a common temperature-compensated quartz crystal oscillator with an estimated relative accuracy of less than 4×10^{-7}, which sufficient to ensure that the measurement accuracy is limited by the phase measurement accuracy and not by the frequency uncertainty of the reference. Nevertheless, higher referencing accuracies could easily be achieved, e.g., by using an oven-controlled crystal oscillator or by deriving the frequency reference from widely available time signals as provided by the Global Positioning System (GPS) or the DCF77 transmitter. The modulated carriers are brought to interference and the generated beats between neighboring sidebands are detected on a balanced detector (BD). The detector features a 3 dB bandwidth of 800 MHz and acts as a low-pass filter that suppresses unwanted beat signals with considerably higher frequencies. After analog-to-digital conversion (A/D) of the photocurrent at a sampling rate of 3.6 GS/s, the beat frequencies are evaluated in the digital domain using Fourier analysis and peak fitting with Lorentzian model functions. Both the sinusoidal modulator drive signals as well as the clock of the A/D converter are derived from the frequency reference, thereby enabling highly precise and traceable measurement of Δf_{ij}.

Experimental results of the frequency measurement are depicted in Fig. 5.7. The four lasers in the 1550 nm range are distributed over a spectral range of almost 6 nm, corresponding to approximately 750 GHz, Fig. 5.7(a). The generated sidebands for measurement of the frequency differences are shown in Fig. 5.7(b), covering the spectral range between the laser lines to generate beat signals with relatively low frequencies.

The electrical spectrum of the photocurrent is depicted in Fig. 5.8. Laser 4 exhibits a bigger line width than the other lasers, leading to a broadened beat signal in the electrical spectrum around Δf_{34} = 800 MHz, Fig. 5.8(a). After a first peak detection step, the peak positions are refined by fitting Lorentzian model functions to the measured spectra. This enables highly precise calculation of the frequency differences between the lasers. The lasers are not stabilized with respect to each other, and environmental influences like slight temperature changes lead to a frequency drift and hence to a temporal variation of the frequency differences, Fig. 5.8(b). If disregarded, this random change in synthetic wavelengths would significantly affect the accuracy of the

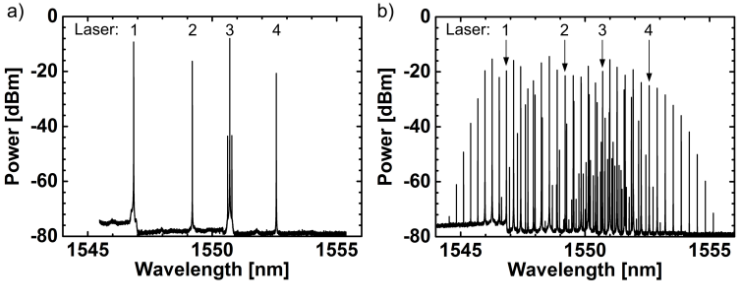

Fig. 5.7: Recorded optical spectra. (a) Spectrum of the four CW lasers without sideband generation. The optical carriers are distributed over a spectral range of almost 6 nm, corresponding to approximately 750 GHz. (b) Optical spectrum including higher-order sidebands generated by modulation. Beat signals between closely spaced pairs of sidebands can be detected with a photodiode and allow to determine the spacing of the optical carriers.

distance measurement. From an error-propagation analysis, we estimate the allowed uncertainty of the frequency differences to be of the order of 1 MHz for a measurement accuracy of better than 1 µm. Our scheme fulfills this requirement – by simultaneously measuring the mutual frequency differences of three closely spaced laser lines, we estimate the accuracy of our referencing scheme to be better than 400 kHz.

5.3.2.4 Choice of wavelengths and data fusion

By calculating the phase differences for all combinations of the four laser wavelengths, six different synthetic wavelengths between 0.41 mm and 1.56 mm can be evaluated, see Table 5.1. To maximize measurement accuracy, a synthetic wavelength as small as possible is advantageous, which means the wavelength difference of two lasers should be large. At the same time, the unambiguity range of the SWI measurement should be significantly larger than the noise of the TOF measurement to enable error-free combination of the large-scale measurements with the fine-scale ones. One way to realize a large unambiguity range would be to choose two lasers with very closely spaced wavelengths. However, this would lead to reduced accuracy: The referencing scheme described in Section 5.3.2.3 limits the maximum frequency difference between

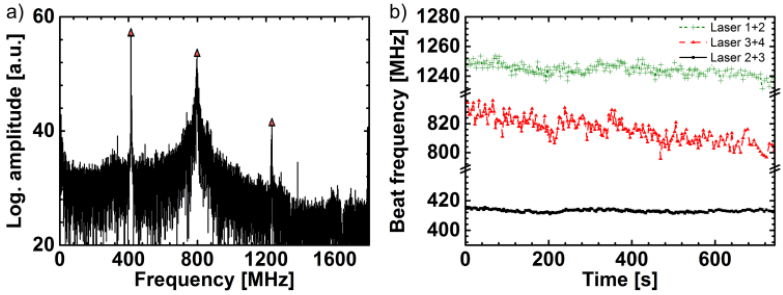

Fig. 5.8: (a) Electrical spectrum of beat signals between neighboring sidebands. Laser 4 exhibits a broader linewidth, which is mapped to the electrical domain. (b) Measured beat frequencies over time during a measurement. The lasers are not stabilized, and highly precise measurements are enabled by the ability to monitor frequency spacing simultaneously to the distance measurement.

Table 5.1: Optical, synthetic and second-order synthetic wavelengths used in the experiment.

	λ_1	λ_2	λ_3	λ_4		
Opt. wavelength [nm]	1547.11	1548.65	1550.48	1552.92		
	Λ_{12}	Λ_{13}	Λ_{14}	Λ_{23}	Λ_{24}	Λ_{34}
Synth. wavelength [mm]	1.56	0.71	0.41	1.31	0.56	0.99
	$\Lambda_{12,23}$	$\Lambda_{23,34}$	$\Lambda_{13,24}$			
2nd synth. wavelength [mm]	8.38	3.97	2.69			

two spectrally adjacent lasers. To realize one synthetic wavelength as small as possible, all wavelengths differences should hence be as large as possible to maximize the total wavelength difference between laser 1 and laser 4. This leads to a configuration with similar wavelength differences between neighboring lasers. To still maintain a large unambiguity range, second-order synthetic wavelengths $\Lambda_{ij,kl}$ can be generated from synthetic wavelengths in analogy to equation (5.6), $\Lambda_{ij,kl} = \frac{\Lambda_{ij}\Lambda_{kl}}{|\Lambda_{ij}-\Lambda_{kl}|}$. The second-order synthetic wavelength used in our experiment are listed in Table 5.1. The unambiguity range of the SWI is enhanced to more than 4 mm, which is 16 times the standard deviation of the TOF measurement.

To merge the SWI phases measured for different synthetic wavelengths and the TOF measurement results to a single distance value, we developed an approach similar to the one described in [257]. A phase value measured for a distinct synthetic wavelength Λ_{ij} permits a multitude of distances with a Λ_{ij}-periodic probability distribution, Fig. 5.9. The measurements at each wavelength have a measurement uncertainty, which dictates the variance of the probability peaks. As expected, the distance measurement uncertainty is smaller for smaller synthetic wavelengths, as the phase measurement accuracy is the same in all cases. To resolve the ambiguity, the product of the probabilities for all evaluated wavelengths is formed and the maximum is detected. The position of the maximum corresponds to the most probable distance and is used as measurement result. This method proved to be very robust in practice.

The evaluation of the phase values and the merging of the different measurement scales were realized on a graphic card (GeForce 480), achieving a total measurement rate of 300 Hz. The speed is mainly limited by the data evaluation of the SWI signals where the digital Fourier-filtering is the most time-consuming process. We believe that the measurement rate can be increased further to several kilohertz by using dedicated computer architectures such as FPGAs or more powerful graphic cards.

5.3.3 Results

The distance measurement scheme was tested on scattering technical surfaces. In a first experiment, we repeatedly measured the distance to the same spot on a rough aluminum plate, see Fig. 5.10. During the measurements the distance between the target and the measurement setup was kept constant. The SWI module was turned on and off during the measurement to study the impact on the measurement accuracy. Two effects can be seen from Fig. 5.10: First, the measurement uncertainty decreases significantly as soon as the SWI is turned on. The standard deviation from the local mean value for the pure TOF measurements is of the order of 200 µm, whereas only 8 µm of standard deviation are observed during the periods when both modules are used simultaneously. Second, a slight drift of the TOF measurement results can be observed. As stated in Section 5.3.2, this drift is caused by slightly different temperature dependences of the electrical low-pass filters. As long as

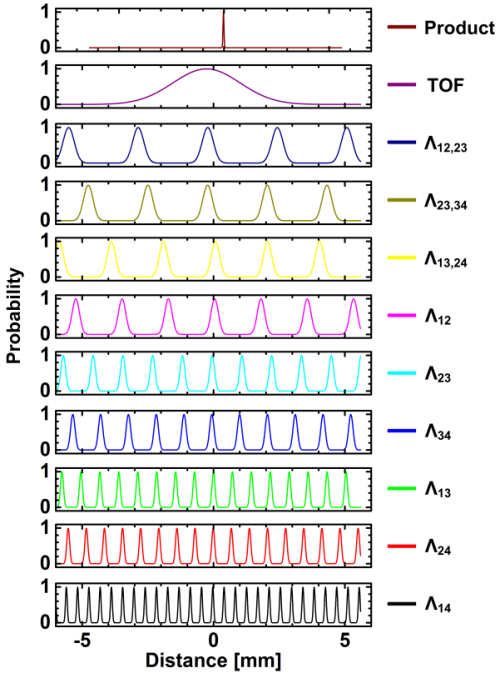

Fig. 5.9: Ambiguous probability distributions of measurements at different synthetic wavelengths for a given distance. For each wavelength, the distribution is assumed to be Gaussian, centered at the measured distance value with a variance corresponding to the measurement uncertainty. Evaluating the maximum of the product of all distributions leads to the most probable distance.

the sum of noise and drift is smaller than the 4 mm unambiguity range of the SWI module, these effects have no negative effect on the refined measurement.

In a second set of measurements, the rough aluminum target was moved stepwise from an arbitrarily chosen zero position in 5 mm-steps towards the sensor, see Fig. 5.11. The linear translation stage used to move the target has a specified absolute accuracy of 50 nm (PI M-511.HD) and serves as reference. The distance covered by the movement was 100 mm. During this stepwise movement, 6500 single measurements were performed. We consider only measurement results taken for a static target. The distances to the target are accurately measured, see Fig. 5.11(a). The standard deviation of each of the distance

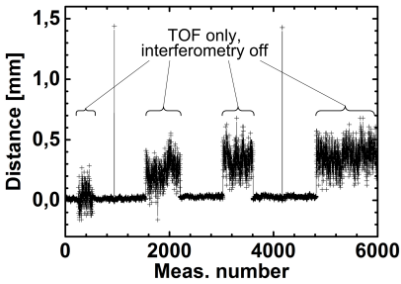

Fig. 5.10: Distance measurements to a fixed aluminum target having a scattering machined surface. The SWI considerably increases the measurement accuracy, which is shown by turning the module on and off. Some drift is seen for the TOF module, but this has no negative influence on the result as long as the drift is below the 4 mm unambiguity range of the synthetic-wavelength interferometry.

steps is plotted in Fig. 5.11(b), exhibiting values between 3 µm and 15 µm. We attribute the remaining fluctuations to fast drifts of the laser wavelength which cannot be monitored by our current reference module. In the current implementation, the update rate is limited to 1 Hz by data transfer via USB and by the interfacing with the SWI module. The frequency referencing itself is based on A/D-converted waveforms with durations of 8.3 µs. This would enable update rates of more than 10 kHz using enhanced data processing, e.g., on an FPGA.

We experimentally confirm that the measurement accuracy is indeed limited by fast frequency drifts of the laser: As seen in the electrical beat spectrum, Fig. 5.8, one of the lasers (laser 4) generates a broader RF beat signal. This is due to a stronger short-term frequency drift of this particular device. Measurements without this laser give standard deviations in the range of 0.6 µm. . . 1.8 µm, but increase the probability to select the wrong unambiguity range.

5.3.4 Summary and conclusion

We demonstrate an optical distance measurement system using a combination of TOF and holographic SWI with synthetic wavelengths referenced to highly precise frequency standards. The system is capable of measurements to scat-

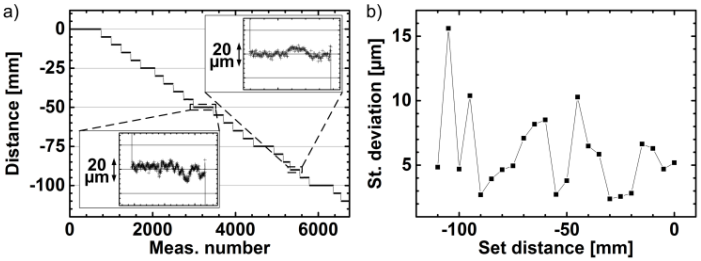

Fig. 5.11: Distance measurements on a static target moved by 5 mm steps on a translation stage. (a) Measured and actual distances. Inset: Detailed view of typical measurement values on one step. (b) Standard deviation of measurements on each distance step.

tering machined surfaces with an unambiguity range of 1.17 m and micrometer accuracy at measurement rates of 300 Hz. The synthetic wavelengths are determined simultaneously to the distance measurements, providing a referenced scale without the need for additional wavelength stabilization schemes or more complex calibration procedures.

[*End of paper* [J4]]

6 Silicon-organic hybrid (SOH) frequency comb sources

This chapter describes the first demonstration of electro-optic frequency comb generation on silicon-on-insulator using the silicon-organic hybrid (SOH) approach. To demonstrate the viability of the approach, the generated comb lines are used as carriers in wavelength division multiplexing data transmission experiments, in which terabit/s data rates are achieved. In Section 6.1, the SOH approach is introduced and an overview of the properties of the organic materials and the associated modulator structures which are utilized is given. The state of the art in chip-scale frequency comb generators is summarized in Section 6.2. Section 6.3 finally gives an explanation of the used comb generation principle and the experimental setup and discusses the obtained results.

6.1 Silicon-organic hybrid (SOH) modulators

All-silicon modulators based on the plasma dispersion effect have a very limited applicability for electro-optic generation of broadband frequency combs. Either they have a limited bandwidth, or their $U_\pi L$-product is too large to achieve the high modulation depth needed for frequency comb generation with available high-frequency electrical amplifiers, see Section 4.1. The silicon-organic hybrid (SOH) approach overcomes these limitations by combining silicon slot waveguides with highly efficient organic electro-optic materials [150–153], which are tailored to exhibit high electro-optic coefficients [89,154–156]. SOH electro-optic modulators exhibit high bandwidth and ultra-low $U_\pi L$-products, thereby enabling devices with small footprints [86–88, 90, 91, 157, 158]. This allows for efficient electro-optic frequency comb generation, which is demonstrated in Section 6.3 and employed in a WDM data transmission experiment. A condensed overview of the SOH approach is given in the following subsections.

6.1.1 Organic electro-optic materials formed by chromophores

This brief summary of organic electro-optic materials is based on the overview given in [154]. The second-order nonlinear organic materials discussed here contain so-called chromophores. These molecules are nonlinear and optically active due to a delocalized electron density stretched over an extended π-conjugated bridge between an acceptor group and a donor group, see Fig. 6.1(a) for the DLD164 chromophore used in this work [156]. Thus the molecule is easily polarized in response to an external electric field. The microscopic dipole moment of a single molecule containing higher-order nonlinear terms can be described as

$$p_i = p_{0,i} + \sum_j \alpha_{ij} E_j + \sum_{jk} \beta_{ijk} E_j E_k + \sum_{jkl} \gamma_{ijkl} E_j E_k E_l + \ldots, \tag{6.1}$$

with $p_{0,i}$ as element of the permanent electric dipole moment, α_{ij} as element of the linear polarizability tensor, β_{ijk} and γ_{ijkl} as elements of the second-order polarizability tensor and third-order polarizability tensor, respectively. The magnitude of the Pockels effect is governed by β_{ijk}.

To find the relation of the microscopic parameters to the macroscopic material properties, additional considerations are necessary. The indices $i, j, k \in \{x, y, z\}$ denote the orthogonal axes of the coordinate system of the molecule. In typical chromophores, the molecular coordinate system can be chosen such that only one component along the dipole axis z, β_{zzz}, contributes significant terms. However, to achieve a macroscopic nonlinear susceptibility $\chi^{(2)}_{33}$, the molecules forming the bulk material need to be aligned in a noncentrosymmetric anisotropic manner in a dedicated poling step. To account for the alignment of the molecules, the average molecular acentric order parameter $\langle \cos^3 \theta \rangle$ is introduced. With θ being the angle between axis z of an individual chromophore and the desired poling direction along laboratory axis 3, along which optical and electrical field vectors are assumed to be oriented, $\langle \cos^3 \theta \rangle$ denotes the average orientation of the chromophores. Together with the number density of active molecules N and the Lorentz-Onsager local field factor g correcting for partial screening effects, the macroscopic $\chi^{(2)}_{33}$ is given by [258]

$$\chi^{(2)}_{33} = N \beta_{zzz} \langle \cos^3 \theta \rangle g. \tag{6.2}$$

Inserting Eq. (6.2) in Eq. (2.32) yields a macroscopic linear electro-optic coefficient r_{33} given by

$$r_{33} = -2N\beta_{zzz} \left\langle \cos^3 \theta \right\rangle g \frac{1}{n^4}. \tag{6.3}$$

As shown in Section 2.4.2, a high magnitude of the modulation depth is necessary to generate broadband optical frequency combs by electro-optic modulation. Inserting Eq. (6.3) in Eq. (2.34), the modulation depth $A_{\mathrm{SOH}} = \pi \hat{U}_{\mathrm{mod}}/U_\pi$ of a modulator using the SOH approach reads

$$A_{\mathrm{SOH}} = -\frac{\hat{U}_{\mathrm{mod}}}{d} N\beta_{zzz} \left\langle \cos^3 \theta \right\rangle g \frac{1}{n} k_0 L. \tag{6.4}$$

Within some practical limitations, the quantities in Eq. (6.4) are chosen to maximize A_{SOH}. The voltage amplitude $\hat{U}_{\mathrm{mod}}$ is limited either by the maximum available output voltage of high-frequency amplifiers or by the breakdown voltage of the organic electro-optic material. The number density N is determined by the density of the neat material used in this work, which cannot be increased arbitrarily, as otherwise the material would crystallize in a centrosymmetric head-to-tail orientation. The second-order polarizability β_{zzz} is determined by the molecular properties of the chromophores, and the length L of the modulator is limited by microwave propagation loss and bandwidth considerations due to RC cut-off. The average molecular acentric order parameter $\left\langle \cos^3 \theta \right\rangle$ is maximized by aligning the chromophores with respect to the external field. This is done in a so-called poling procedure.

The poling procedure is illustrated in Fig. 6.1(b). In the initial unpoled material, the orientation of the chromophores is random, and the electro-optic coefficient is zero. For poling, the material is heated above its glass-transition temperature T_g to allow free motion of the molecules. An electric field is applied, exerting a force upon the dipolar chromophores and thus aligning them. With the field still being applied, the material is cooled back to room temperature, conserving the obtained acentric alignment of the chromophores even after the field is switched off. With this procedure, a material with a macroscopic electro-optic coefficient is obtained.

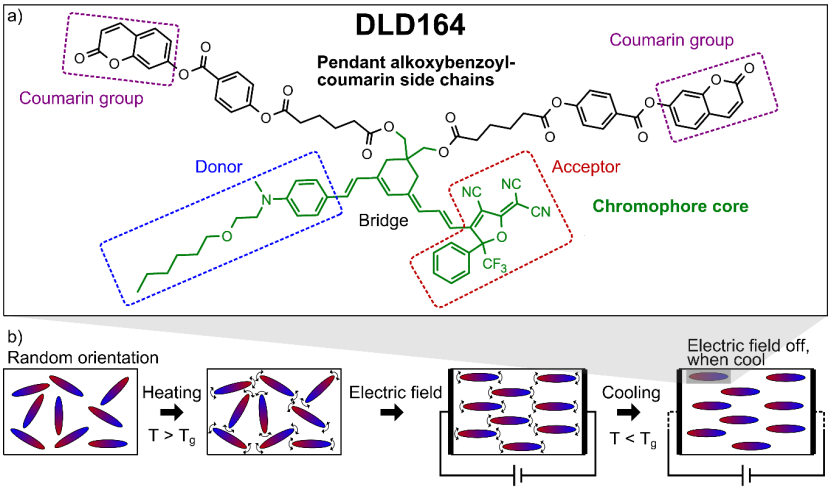

Fig. 6.1: Chemical structure and poling process. (a) Structure of the DLD164 chromophore used in this work [156]. The electro-optically active chromophore core (green) comprises a donor group (blue), connected to an acceptor group (red) via a pi-conjugated bridge. Pendant side chains (black) with coumarin groups (violet) inhibit partial crystallization of the material and enhance the acentric order upon poling due to intermolecular electrostatic interactions. (b) Poling procedure: The dipolar chromophores (blue-red ellipses) are initially randomly oriented. The material is heated above its glass-transition temperature T_g to allow free motion of the molecules. An electric field is applied to align the molecules. While the field is still applied, the material is cooled back to room temperature to conserve the acentric alignment of the chromophores. Afterwards, the poling field is switched off.

6.1.2 DLD164 – The chromophore material used in this work

As discussed in Section 2.4.2, a high modulation depth is necessary to generate broadband frequency combs via electro-optic modulation. To achieve this, the π-voltage-length product,

$$U_\pi L = \frac{2\pi d}{n^3 r_{33} k_0}, \tag{6.5}$$

needs to be as small as possible. This calls for materials with high electro-optic coefficients r_{33}. This works builds on a material comparison of three different state-of-the-art electro-optic materials, reporting electro-optic coefficients of

Table 6.1: Adapted from [259]. Summary of electro-optic parameters achieved with different materials.

Material	n	r_{33} in-device [pm/V]	$n^3 r_{33}$ in-device [pm/V]	$U_\pi L$ [Vmm]	Ref.
DLD164	1.83	190	1164	0.48	[87, 156]
YLD124 (25 wt.%), PSLD41	1.73	230	1130	0.52	[260]
PSLD41	1.72	97	494	1.23	[154]
YLD124 (25 wt.%), PMMA	1.7	29	142	4.10	[87,156,261]

more than 200 pm/V [87, 259]. The findings are summarized in Table 6.1. Comparing the values of $U_\pi L$, DLD164 is clearly the material of choice for use in electro-optic frequency comb generators. In comparison to a conventional electro-optic material such as $LiNbO_3$ with $n^3 r_{33} \approx 400\,\mathrm{pm/V}$, the advantage of organic chromophore materials becomes evident.

DLD164: As material of choice in this thesis, a short summary of its properties is given here. DLD164 was developed by the group of Larry R. Dalton at the University of Washington, Seattle. Its synthesis is described in [156], and the chemical structure of the molecule is depicted in Fig. 6.1(a). The electro-optically active chromophore core (green) comprises a donor group (marked in blue), connected to an acceptor group (marked in red) via a π-conjugated bridge. Pendant side chains (black) with coumarin groups (marked in violet) inhibit partial crystallization of the material due to intermolecular electrostatic interactions. Thus the neat material can be used without embedding it in a polymer matrix, increasing the number density N [155,156,262]. Furthermore, the side chains reduce the number of rotational degrees of freedom of the molecule, enhancing the acentric order upon poling. [155, 262].

DLD164 has a relatively low glass-transition temperature of $T_g = 66\,^\circ\mathrm{C}$. Due to thermally induced motion of the chromophore molecules, at room temperature the acentric order after poling is lost within a time period in the order of weeks, after which the material has to be poled again. However, in future

work the thermal stability is likely to be improved by further modifications to the molecule, introducing cross-linking groups to the polymers to reduce the thermal reorientation subsequent to poling [263, 264]. As an example, SOH modulators with more stable organic electro-optical materials have been demonstrated to operate at 80 °C [153] and to withstand high-temperature storage at 85 °C for more than 2000 h [152].

The deposition of DLD164 onto the silicon chip is done via spin coating from a solution of 1,1,2-trichloroethane. Prior to poling, the material is dried by heating it under vacuum. More details about the preparation can be found in [87, 166].

6.1.3 Silicon-organic hybrid modulator structure

A modulator design combining the excellent electro-optic properties of organic chromophore materials with the silicon photonic platform has been developed over the recent years [86, 87, 152, 153, 157, 158, 265, 266]. SOH optical modulators [J13] have been demonstrated to exhibit ultra-high electro-optic coefficients of more than 300 pm/V [89] and have been widely used for optical communications. Transmission demonstrations cover conventional Mach-Zehnder modulators for technically simple intensity modulation and direct detection schemes [90, 91] as well as I/Q modulators for coherent transmission at symbol rates of up to 100 GBd [267–269]. SOH modulators stand out due to their ultra-low π-voltages [89], enabling operation of the devices directly from the binary output ports of standard CMOS circuits, without the need for additional drive amplifiers [270].

The structure of a typical SOH phase modulator is sketched in Fig. 6.2. A silicon slot waveguide is covered and filled by the electro-optic organic cladding material, which is spin-coated or dispensed onto the chip. The slot is defined by 220 nm-high two rails which are electrically connected to metal electrodes via 60 nm thick n-doped silicon strips. A voltage applied to the electrodes thus drops across the 100 nm wide slot, leading to high electric field strengths for relatively low voltages. The initial poling process also makes use of these electrodes. A simulated optical mode profile showing the magnitude of the electrical optical field for a quasi TE-mode is shown in Fig. 6.4. Most of the guided light is concentrated inside the slot, leading to a high

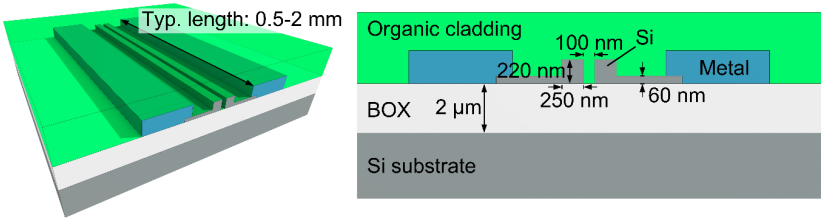

Fig. 6.2: Dimensions of a SOH phase modulator. Typical device lengths are 0.5–2 mm. A 100 nm wide slot waveguide is covered by electro-optic organic cladding (DLD164). The waveguide is connected to two metal electrodes via two n-doped, 60 nm thick silicon strips.

overlap between electro-optic cladding, modulating electrical field and optical field. This yields highly efficient phase modulation quantified by ultra-small $U_\pi L$-products, and high modulation depths can be achieved for electro-optic generation of frequency combs.

6.2 State of the art in highly integrated optical frequency comb sources

There are several approaches for optical frequency comb generation with chip-scale devices. This section gives an overview of the state of the art in this field. The principles used for comb generation are divided into four categories: Generation via parametric nonlinear processes in highly nonlinear, non-resonant waveguides, generation via nonlinear processes in microring resonators, generation with integrated mode-locked laser diodes and electro-optic generation in integrated modulators.

6.2.1 Generation in highly nonlinear integrated waveguides

Broadband frequency combs can be generated by exploiting third-order nonlinear effects. Starting from a high-power "seed" frequency comb, new frequencies are generated via parametric processes such as four-wave mixing,

self-phase modulation, and cross-phase modulation [55, 56]. The viability of the approach has first been demonstrated in glass fibers [39,62,63,271,272] and has later been extended to photonic integrated circuits [65–68]. In this context, integrated waveguides with high index contrast and nanometer dimensions are advantageous, as high optical intensities can be achieved inside the waveguides with relatively moderate pump powers. However, careful dispersion engineering is key for high efficiency of the nonlinear processes. Furthermore, the lines of the seed comb need to be phase coherent with one another, meaning that they need to share a common, deterministic phase evolution in order to achieve a phase-coherent comb spectrum [61]. In [65], a frequency comb with a 30 dB bandwidth spanning from 1500 nm to 3300 nm is generated from a silicon-on-insulator waveguide. To achieve this, an optical parametric oscillator pumped by a Ti-Sapphire mode-locked laser is coupled to the waveguide. While very broadband combs can be generated with this approach, so far the high-powered seed sources needed for such schemes have been realized off-chip, as they are not easily realized as chip-scale devices.

6.2.2 Microresonator Kerr combs

Another approach using parametric nonlinear processes to generate frequency combs are the so-called Kerr frequency combs. A strong CW pump laser is coupled into a highly nonlinear microresonator with a high Q-factor. Parametric third-order nonlinearities in the resonator cavity give rise to broadband frequency combs [57]. The microresonators can be monolithically integrated in the form of whispering-gallery mode resonators [58, 273–276] in various material systems, or as integrated ring-resonators typically made of silicon nitride [277–279] or alternative material systems such as aluminum gallium arsenide [280]. A detailed summary is given in [281]. Very broadband frequency combs have been realized with this approach. A comb spanning two-thirds of an octave from 1.33 µm to 2 µm is reported in [59], and octave spanning combs suitable for self-referencing are reported in [282]. The viability of these comb sources for practical applications such as WDM data transmission has been demonstrated [J3,J12], achieving data transmission with up to 50 Tbit/s on 179 optical carriers using microresonator-based frequency combs as sources [60]. However, early experiments resulted in the formation of detrimental multiplet lines instead of single comb lines [283]. Advanced pumping schemes are nec-

essary to generate dense combs with smooth spectral envelopes. Formation of multiplet lines can be avoided by the generation of solitons inside the resonator, which requires careful dispersion engineering [284, 285] and spectral detuning of the pump laser with respect to the pumped resonance [286]. While the most beneficial property of Kerr combs is the large bandwidth generated from just a CW laser and a microresonator, their disadvantages are the need for relatively high pump powers, a fixed line spacing dictated by the free spectral range of the cavity, and less freedom concerning the choice of the center wavelength.

6.2.3 Mode-locked laser diodes

Semiconductor mode-locked lasers are another possible option to realize integrated frequency comb sources. Demonstrations include single-section semiconductor mode-locked lasers based on III-V quantum dots or quantum dashes [287–292], semiconductor lasers achieving mode-locking with saturable absorber section inside the laser cavity [293–295], and pulsed lasers based on gain-switching [296, 297]. The laser sources can be fabricated monolithically using standardized III-V fabrication processes [298], or can be heterogeneously integrated on silicon PICs [299–302]. While very compact and power-efficient comb sources can be realized with mode-locked laser diodes, the line spacing is typically determined by the cavity length and therefore fixed. Furthermore, in the context of quantum-dot mode-locked lasers, phase noise of the comb lines is reported to be an issue, making phase noise compensation schemes [303, 304, C8] or injection locking [38, 296, J2] necessary for practical demonstrations of WDM data transmission.

6.2.4 Integrated electro-optic modulators

Frequency combs can be generated via sinusoidal phase modulation of CW laser light in arrangements of phase modulators. This approach is used in this work and explained in more detail in Section 2.4. In terms of bandwidth, combs generated via electro-optic modulation can typically not compete with parametric nonlinear combs. Additionally, high-frequency driving signals are necessary, requiring dedicated RF electronics. However, electro-optically generated combs are very well controllable, stable and easy to use. They provide

an exceptionally high degree of flexibility in terms of line spacing and center wavelength, the former being determined by the modulation frequency and the latter by the choice of laser wavelength. The linewidth of the comb lines is determined by the linewidth of the CW laser, enabling comb lines to be used as high-quality carriers for WDM systems. Based on modulators, the approach is particularly well suited for dense photonic integration. So far, demonstrations of densely integrated comb generators making use of this scheme have been shown on the InP material platform [305–308], while realization on the silicon photonic platform was hampered by the lack of high speed modulators with low π-voltage. In the work presented here, the silicon-organic hybrid (SOH) approach is leveraged to realize electro-optic comb generators densely integrated on silicon photonic chips. The viability of the comb sources is demonstrated by realizing WDM data transmission at terabit/s data rates and over distances of up to 300 km [J5], see Section 6.3.

6.3 WDM data transmission at terabit/s data rates

Wavelength division multiplexing (WDM) is a multiplexing technique used to increase the aggregate data rate transmitted by an optical fiber link. Laser tones with different wavelengths are used as individual carriers, on which data is encoded via modulation. The modulated carriers are then multiplexed into an optical fiber and transmitted. At the receiver side, the carriers are demultiplexed and detected. Multiplexing and demultiplexing can be realized with passive optical filters, e.g., arrayed waveguide gratings, add/drop filters realized from ring resonators, or cascaded Mach-Zehnder interferometers acting as interleavers.

To realize high-capacity WDM systems, three main parameters can be maximized: The symbol rate, the number of transmitted bits per symbol, and the number of parallel channels. The symbol rate is limited by the bandwidth of available electronic and electro-optic components. The number of the bits per symbol is limited by the achievable signal-to-noise ratio, as the signal quality needs to be good enough to be able to separate distinct signal levels. This leaves the number of parallel channels as available parameter. As the transmission window of optical fibers is huge, with a usable wavelength

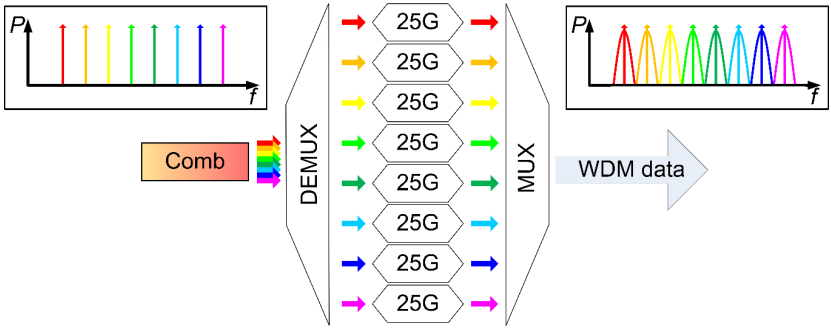

Fig. 6.3: Schematic of an optical transmitter based on frequency combs. The carriers generated by the comb source are demultiplexed (DEMUX), modulated with independent data and then recombined in a multiplexer (MUX). Matching the comb line spacing to the occupied channel bandwidth allows spectrally efficient data transmission.

range from ~1300 nm to 1700 nm [309], the challenge lies in the efficient realization of multi-channel WDM transceivers. Such a transceiver requires a large number of densely spaced carriers with precisely defined frequencies. This is called dense wavelength division multiplexing (DWDM). In fixed-grid DWDM as defined in ITU standard G.694.1, channels are spaced by intervals of 12.5 GHz, 25 GHz, 50 GHz or 100 GHz, centered at 193.1 THz. The dense channel spacing imposes relatively tight wavelength tolerances on the utilized light sources, which are typically temperature-stabilized distributed feedback (DFB) lasers. Within the additional definition of a flexible DWDM grid in the standard, the minimum channel width is also determined as 12.5 GHz, but the center frequency can be chosen with a finer granularity of 6.25 GHz, even increasing the demands on the laser wavelength tolerances.

In contrast to using a dedicated laser for each channel, frequency combs are promising candidates to generate a multitude of carriers with precisely defined frequencies. In such a scheme only a single center frequency and the line spacing need to be controlled in order to match the defined grid. The schematic of an optical transmitter based on frequency combs is shown in Fig. 6.3. A multitude of carriers is generated by the comb source. The carriers are then demultiplexed using a passive optical filter. Independent data are modulated onto each carrier, in this example with a symbol rate of 25 GBd. After modulation, the channels are multiplexed into an optical fiber for transmission.

As discussed in Section 6.2, electro-optic frequency combs offer a very flexible choice of line spacing and center wavelength, easily adaptable to different frequency grids. By leveraging the high bandwidth and low $U_\pi L$-product offered by the SOH approach, electro-optic comb generators integrated on an SOI substrate are demonstrated in this work. The comb sources are used for WDM data transmission experiments with Tbit/s data rates. All other elements can be realized efficiently on the silicon photonic platform [87,144,310], paving the path towards Tbit/s transceiver modules integrated onto a single silicon PIC.

6.3.1 Silicon-organic hybrid (SOH) frequency comb sources for terabit/s data transmission

The contents of the following section is taken from a publication in Optics Express [J5]. The structure and the layout of this document was slightly adapted to fit the format of this thesis.

[*Start of paper* [J5]]

Silicon-organic hybrid (SOH) frequency comb sources for terabit/s data transmission

Optics Express; Volume 22; Issue 3; pp. 3629-3637; February 2014
DOI: 10.1364/OE.22.003629

C. Weimann,[1,*] P. C. Schindler,[1] R. Palmer,[1] S. Wolf,[1] D. Bekele,[1] D. Korn,[1] J. Pfeifle,[1] S. Koeber,[1] R. Schmogrow,[1] L. Alloatti,[1] D. Elder,[2] H. Yu,[3] W. Bogaerts,[3] L. R. Dalton,[2]
W. Freude,[1] J. Leuthold,[1,4] and C. Koos[1,5]

[1]*Karlsruhe Institute of Technology (KIT), Institute of Photonics and Quantumelectronics (IPQ) and Institute of Microstructure Technology (IMT), 76131 Karlsruhe, Germany*

[2]*University of Washington, Department of Chemistry, Seattle, WA 98195-1700, USA*

[3]*Ghent University – IMEC, Photonics Research Group, Gent, Belgium*

[4]*Electromagnetic Fields & Microwave Electronics Laboratory (IFH), ETH-Zurich, Zurich, Switzerland*

6.3.1.1 Introduction

Optical frequency combs are key elements for a multitude of applications such as optical metrology [34], arbitrary-waveform generation [20], and terabit/s communications [311]. In many cases, narrow optical linewidth and the ability to freely choose center wavelength and line spacing are essential. Moreover, dense integration of comb sources along with other devices is important to realize miniaturized systems with high degrees of complexity. This applies especially to high-speed data transmission, where line spacings of tens of gigahertz are needed for spectrally efficient super-channel transmission with terabit/s data rates [312]. A particularly suitable and versatile approach for integrated frequency comb generation is based on periodic modulation of a continuous-wave (CW) laser with electro-optic phase shifters in an appropriate arrangement [80, 82, 134, 313]. In such schemes, the optical linewidth is determined by the CW laser, the line spacing can be adjusted via the modulation frequency, and the number of comb lines depends on the modulation depth and the number of cascaded devices [78, 81, 84]. In cases where modulation depth is limited, the bandwidth of the comb spectrum can be increased by inserting the phase modulator in an amplifying feedback loop [76, 305, 314]. However, this leads to a restriction of the line spacing due to the round-trip time of the loop, where a resonance condition must be fulfilled. Previous demonstrations of modulator-based frequency combs have mainly focused on using conventional lithium niobate devices [80, 81, 83, 84] along with discrete fiber-optic components. Integrated comb sources have been realized on the InP platform by inserting a phase modulator into an amplifying ring resonator [305]. This arrangement enables generation of 6 lines with a spacing of around 10 GHz and a spectral flatness of 5 dB. However, for many applications, it would be highly desirable to realize miniaturized frequency comb sources on the silicon photonic platform, thereby complementing the already rich portfolio of available devices [93]. One of the main obstacles towards silicon-based comb sources is the limitation associated with currently available phase modulators: Fast modulation is possible with depletion-type pn-junction phase shifters, but these devices feature relatively large voltage-length products $U_\pi L$ of typically more than 10 V mm [143, 222, 224]. Injection-type phase shifters, on the other hand, have smaller $U_\pi L$, but modulation bandwidths are limited by the carrier lifetime [226].

In this section we demonstrate the first modulator-based comb source on a silicon-on-insulator (SOI) substrate. We use the concept of silicon-organic hybrid (SOH) integration [86, 88, 150, 265, 315] which combines nanophotonic SOI waveguides with organic cladding materials to realize highly efficient broadband phase shifters [266]. The devices exhibit voltage-length products as small as $U_\pi L = 2$ V mm at DC. Using a dual-drive Mach-Zehnder modulator (MZM), we demonstrate generation of a flat-top frequency comb comprising 7 lines with a spacing of 40 GHz and a spectral flatness of 2 dB [C2]. We demonstrate the viability of SOH comb sources in a series of data transmission experiments, where we explore different line spacings, symbol rates, pulse shapes, and modulation formats. A total line rate of 1.152 Tbit/s and a net spectral efficiency of 4.9 bit/s/Hz are achieved by using a comb with 25 GHz line spacing. In this experiment, 9 carriers are modulated with Nyquist pulses at a symbol rate of 18 GBd using 16-state quadrature amplitude modulation (16QAM) and quadrature phase shift keying (QPSK). In a similar experiment, we reduce the complexity by using QPSK on 7 channels only, thereby enabling transmission over a distance of up to 300 km. For a comb with 40 GHz line spacing and conventional non-return-to-zero (NRZ) QPSK signals, we use a symbol rate of 28 GBd on 9 channels to transmit an aggregate line rate of 1.008 Tbit/s over up to 300 km.

6.3.1.2 SOH modulators for frequency comb generation

The SOH phase shifter [158, 266] consists of an optical slot waveguide [316] electrically connected to copper slotlines through 60 nm thick doped silicon strips. A schematic cross section and simulated mode profile of the optical slot waveguide are depicted in Fig. 6.4(a). The modulation voltage applied to the electrodes drops across the narrow slot, resulting in a high electric field that strongly overlaps with the optical mode. This leads to highly efficient electro-optic interaction and hence to a low voltage-length product $U_\pi L$. The silicon waveguides are fabricated on a SOI wafer with a 2 µm thick buried oxide and a 220 nm thick device layer using 193 nm deep-UV lithography. After processing, the SOI waveguides are covered with the electro-optic chromophore DLD164 [317], which entirely fills the slot. The electro-optic cladding is applied by spin coating and poled at elevated temperatures with a DC voltage applied across the slotline electrodes. More details about the phase shifter can be found in [158]. Our comb generators consist of two phase shifters in a

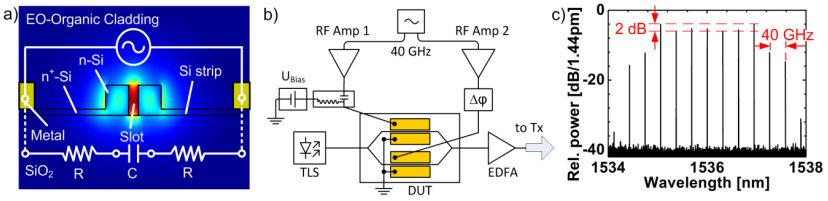

Fig. 6.4: Dual-drive frequency comb generator and spectrum. (a) Schematic cross-section and simulated optical mode of a silicon-organic hybrid (SOH) phase modulator. The two rails of a silicon slot waveguide are electrically connected to metal electrodes by 60 nm high n-doped silicon strips. The waveguide is covered by an electro-optic cladding material (DLD164), which entirely fills the slot. (b) Integrated dual-drive frequency comb generator: A tunable laser source (TLS) is coupled to a dual-drive SOH Mach-Zehnder modulator (MZM) via grating couplers. The arms are driven by two sinusoidal 40 GHz signals. Flat combs are obtained by carefully adjusting the signal powers and phases along with the bias voltage U_{Bias}. Fiber-chip coupling losses are compensated by an erbium-doped fiber amplifier (EDFA). (c) Flat-top spectrum obtained for electrical drive powers of 28 dBm and 23 dBm measured at the output of the amplifiers, showing 7 lines within 2 dB flatness. The lines are spaced by 40 GHz.

Mach-Zehnder interferometer. These phase shifters are either driven independently in a dual-drive configuration, or in push-pull mode using a single drive signal that induces opposite phase shifts in the two arms. We investigate two MZM types: A 2 mm long dual-drive modulator, and a 1 mm long single-drive device.

The experimental setup with a dual-drive MZM is shown in Fig. 6.4(b). A tunable laser source (TLS) is coupled to the chip via grating couplers [318], and the electrodes for the sinusoidal drive signals are contacted with RF probes. The generated frequency comb has a flexible line spacing determined by the modulation frequency. Using sinusoidal drive signals with carefully adjusted amplitude and phase [134], a spectrally flat frequency comb can be generated. The voltage-length product of each phase modulator was measured at DC to be $U_\pi L = 2\,\mathrm{V\,mm}$. This allows an efficient generation of higher-order optical sidebands with electrical drive powers of approximately 28 dBm and 23 dBm in the respective arms. The resulting optical spectrum is shown in Fig. 6.4(c). We achieve a spectral flatness of 7 lines within 2 dB. The line spacing amounts to 40 GHz. By comparing the measured optical spectrum to simulations, we estimate the peak-to-peak modulation depth in the two MZM arms to be 3.6π and 2.7π, respectively. The phase difference of about π matches nicely to theoretical predictions for an optimally flat comb [134].

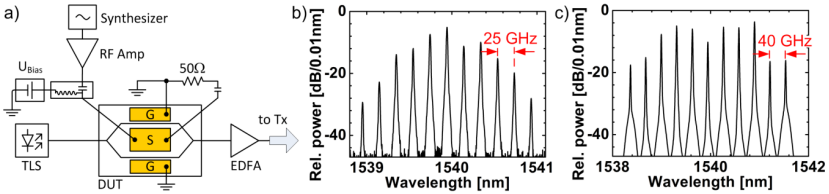

Fig. 6.5: Single-drive frequency comb generator and spectra. (a) Schematic of the single-drive push-pull frequency comb generator: A tunable laser source (TLS) is coupled to the SOH MZM via grating couplers. The device is driven by sinusoidal signals of different frequencies, thereby defining the line spacing of the generated comb. The operation point can be chosen with the bias voltage U_{Bias}. The electrodes are terminated with 50 Ω. Fiber-chip coupling losses are compensated by an erbium-doped fiber amplifier (EDFA). (b) Resulting optical spectrum using an electrical drive signal of 25 GHz and a RF power of 23 dBm, yielding 7 lines with a spectral flatness of 10 dB. (c) Resulting optical spectrum using an electrical drive signal of 40 GHz and a RF power of 29 dBm, yielding 7 lines with a spectral flatness of 7 dB.

Spectrally flat frequency combs are advantageous for WDM transmission, since low-power lines are avoided and all WDM channels have the same signal quality. However, the use of a single-drive MZM simplifies the experimental setup considerably, because only one electrical amplifier is needed. A single-drive device is demonstrated using the setup depicted in Fig. 6.5(a). For the push-pull device, the voltage-length product of each individual phase modulator amounts to $U_\pi L = 2\,\mathrm{V\,mm}$. Fig. 6.5(b) shows the comb spectrum generated by an electrical drive signal with a frequency of 25 GHz and a power of 23 dBm measured at the output of the amplifier. The spectrum has 7 lines within a power range of 10 dB. Fig. 6.5(c) shows the optical spectrum generated with a 40 GHz drive signal. Here, a slightly higher amplifier output power of 29 dBm is used to overcome the frequency-dependent increase of electrode losses and to enable larger optical bandwidth. We obtain a comb featuring 7 lines with a flatness of 7 dB. In contrast to the dual-drive comb generator, the spectral flatness cannot be optimized by adjusting the drive parameters, and an external optical filter is required to obtain flat-top comb spectra, see Section 6.3.1.3. As the dual-drive MZM chip broke during preliminary data transmission experiments, we continued the experiments with single-drive devices.

All generated combs feature excellent wavelength stability of ± 2.5 pm and linewidths in the order of 100 kHz, solely governed by the CW laser. The line spacing is determined to an accuracy of better than 10^{-9} by the synthesizer

that is used to drive the modulators. The stability of the power per line is mainly given by the ability to maintain constant driving conditions. Since the modulators were operated without thermal stabilization at relatively high optical and electrical power levels, it was necessary to manually adjust the bias voltage in intervals of several minutes to compensate thermal drift and to preserve the spectral envelope of the comb. Bias point drift can be overcome by temperature stabilization of the device or by electronic feedback control.

6.3.1.3 Terabit/s data transmission using SOH frequency comb sources

To demonstrate the viability and the flexibility of SOH frequency comb sources, we perform a series of data transmission experiments using different symbol rates, pulse shapes, and modulation formats. For maximum spectral efficiency, dense line spacing of 25 GHz is used in combination with Nyquist pulse shaping. This allows generation of a data stream with an aggregate line rate of 1.152 Tbit/s and a spectral efficiency of 4.9 bit/s/Hz. The experiment was performed with a single-drive push-pull device, resulting in comb lines with noticeable power differences. A homogeneous power distribution among the optical channels can be achieved by using a programmable optical filter for spectral flattening. In combination with more robust QPSK modulation, this enables transmission of a 504 Gbit/s data stream over a distance of up to 300 km. In simpler transmission schemes where spectral efficiency is not of prime importance, conventional NRZ pulses may be used in combination with larger channel spacing. We generate a line spacing of 40 GHz by simply increasing the modulation frequency of our comb source, allowing transmission of 28 GBd NRZ-QPSK signals without undue cross talk between neighboring channels. Using this scheme, we demonstrate transmission with an aggregate line rate of 1.008 Tbit/s over up to 300 km.

Generation of terabit/s data streams using dense combs and Nyquist pulse shaping

To generate a data stream with high spectral efficiency, we use the experimental setup shown in Fig. 6.6. The frequency comb is obtained from a single-drive push-pull MZM driven by a 25 GHz sinusoidal signal, see Fig. 6.5(b) for the raw comb spectrum prior to data modulation. A programmable optical

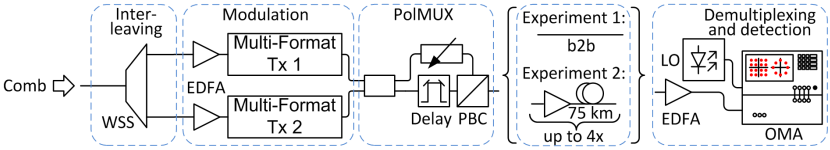

Fig. 6.6: Data transmission setup. A wavelength-selective switch (WSS) splits the comb into even and odd carriers which are modulated independently in a multi-format transmitter. The two sets of channels are recombined, and polarization multiplexing (PolMUX) is emulated by creating time-shifted copies of the data stream and merging them on orthogonal polarizations. Experiment 1: In a first experiment, the data is fed directly into the receiver (back-to-back, b2b). Experiment 2: Up to 4 spans of 75 km SMF are used for transmission over up to 300 km. At the receiver, the signal is amplified and the channels are demultiplexed and detected by an optical modulation analyzer (OMA). A free-running external cavity laser acts as a local oscillator (LO) for coherent reception.

filter (Finisar WaveShaper, wavelength selective switch, WSS) is then used to separate even and odd carriers, which are modulated with independent pseudo-random bit sequences (PRBS) of length $2^9 - 1$. Modulation is done by multi-format transmitters, generating Nyquist pulses [319] at a symbol rate of 18 GBd and enabling a wide variety of different modulation formats [320]. Polarization-division multiplexing (PDM) is emulated by splitting the data stream, delaying one part with respect to the other, and merging them in a polarization beam combiner on orthogonal polarization states. The signal is received and characterized by an optical modulation analyzer (OMA, Agilent N4391A) with a free-running external cavity laser as local oscillator (LO). Digital signal processing is performed for polarization demultiplexing and equalization. We record the constellation diagrams and extract the error vector magnitude (EVM) as a measure for signal quality for each channel and each polarization.

The results are depicted in Fig. 6.7. The strongest carriers 2. . . 8 were suitable for PDM-16QAM modulation, whereas the two weakest carriers 1 and 9 supported PDM-QPSK signals only. All channels show measured bit error ratios (BER) better than 4.3×10^{-3}, which is below the hard-decision forward-error correction (FEC) threshold of 4.5×10^{-3} [321]. The aggregate line rate is 1.152 Tbit/s. Taking into account a 6.7% overhead for the hard-decision FEC, we obtain a net spectral efficiency of 4.9 bit/s/Hz. In the current experiment, we chose a line spacing of 25 GHz, which is in accordance with standards recommended by the International Telecommunication Union [322]. In principle,

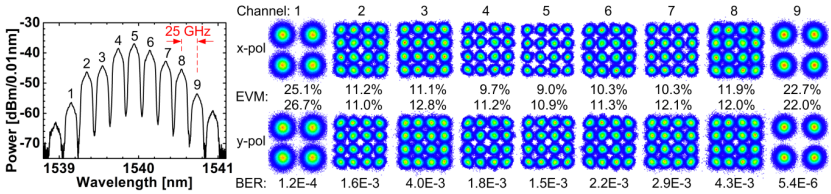

Fig. 6.7: Results of back-to-back data transmission. A total of 9 carriers spaced by 25 GHz were generated by an integrated SOH comb source. Optical spectrum of the modulated carriers (left) and constellation diagrams (right) for all channels and both polarizations are depicted along with measured EVM values. The 7 strongest carriers were modulated with Nyquist pulse-shaped 16QAM signals, whereas QPSK was used for weaker carriers 1 and 9. The symbol rate is 18 GBd. We obtain BER values below the hard-decision threshold for all channels, yielding an aggregate line rate of 1.152 Tbit/s.

this would enable a symbol rate of 25 GBd per channel, since no spectral guard band is needed for Nyquist-WDM [39]. However, the actual symbol rate was limited to 18 GBd by our current transmitter hardware. As a consequence, parts of the spectrum had to remain unused, thus offering potential for further increasing spectral efficiency in future experiments. Transmission of the signal over large distances was not possible due to insufficient BER margin, which was mainly caused by the rather high on-chip insertion loss of the modulator amounting to approximately 21 dB. We attribute this loss to an imperfect fabrication of the multi-mode interference couplers used in the MZM. With improved fabrication steps we would expect an on-chip loss of around 6 dB.

Transmission of a Nyquist-WDM signal with spectrally flattened comb

To improve the signal quality of the data transmission, the experiment was repeated using QPSK and the 7 strongest lines, which were in addition spectrally flattened with the WSS for a more homogeneous channel performance. For this experiment, we use a different comb generator with a voltage-length product of $U_\pi L = 3.2$ V mm at DC, which is slightly larger than the value for the devices used in the previous section. All carriers were modulated with sinc-shaped Nyquist pulses at a symbol rate of 18 GBd using PDM-QPSK signals. The resulting spectrum consists of 7 channels with similar optical power, Fig. 6.8(a). In Fig. 6.8(b), the average error vector magnitudes (EVM) of both polarizations are shown for all channels and all transmission distances (0 km, 75 km,

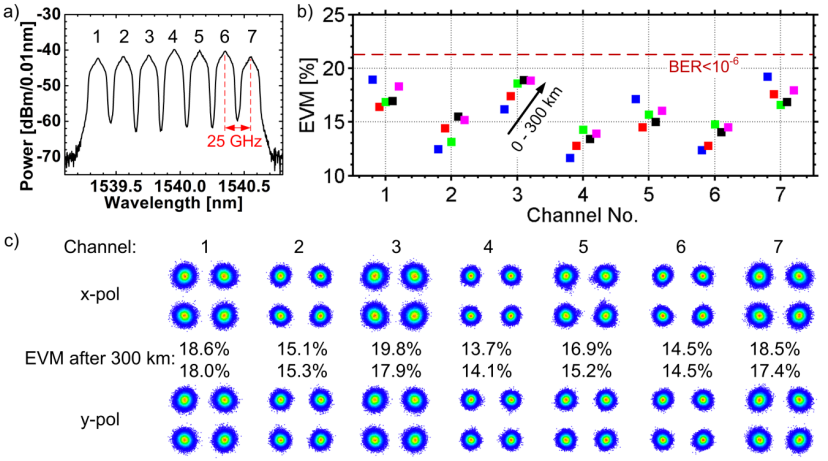

Fig. 6.8: Results for data transmission of QPSK signals: (a) Optical spectrum of the modulated carriers. The 7 strongest carriers are spectrally flattened by the WSS. (b) The average EVM of both polarizations over channel number are shown color-coded (and slightly offset for clarity of presentation) for each length of fiber span (0 km, 75 km, 150 km, 225 km, 300 km). Drift of the operation point of the integrated comb source leads to some deviations from equal optical power for each channel, but BER below 10^{-6} are achieved for all channels nonetheless. (c) Constellation diagrams of all 7 channels and both polarizations after 300 km transmission.

150 km, 225 km, 300 km). The EVM of all channels are smaller than 21.2 %, which corresponds to a BER of 10^{-6} and is indicated by a dashed red line in Fig. 6.8(b) [323]. Fig. 6.8(c) shows the constellation diagrams of all channels and both polarizations after transmission over 300 km. The demonstrated line rate amounts to 504 Gbit/s. The operation point of the comb generator was not stabilized, leading to some residual drift. This drift caused variations in channel performance during the measurements. A bias stabilization scheme could avoid this impairment in future experiments.

Terabit/s WDM transmission using NRZ-QPSK

To demonstrate data transmission with conventional NRZ pulses and symbol rates of 28 GBd, we increase the line spacing of our comb to 40 GHz. The comb spectrum comprises 9 lines that are usable for data transmission, see

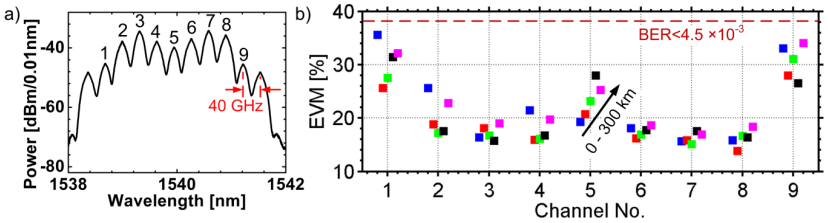

Fig. 6.9: Results for data transmission of NRZ QPSK signals: (a) Optical spectrum of the modulated carriers for 40 GHz spacing and 29 dBm of RF power measured at the output of the drive amplifier. (b) Average EVM of both polarizations over channel number. The results obtained for different fiber spans (0 km, 75 km, 150 km, 225 km, 300 km) are color-coded and slightly offset for clarity of presentation. Drift of the operating point of the comb source leads to variations of the BER obtained for different transmission distances. Nonetheless, BER values below the hard-decision threshold of 4.5 × 10-3 are achieved for all channels, yielding a gross line rate of 1.008 Tbit/s.

Fig. 6.5(c). The optical spectrum of the modulated carriers can be seen in Fig. 6.9(a). Fig. 6.9(b) depicts the average EVM of both polarizations for all channels and various transmission distances (0 km, 75 km, 150 km, 225 km, 300 km). The EVM of all channels is below the threshold for hard-decision FEC, which corresponds to a BER of 4.5×10^{-3} and is represented by the red dashed line in Fig. 6.9(b) [323]. The total line rate amounts to 1.008 Tbit/s. As before, slight variations in channel performance during the measurements are caused by drift of the operating point and can be mitigated by using electronic bias point stabilization in future experiments.

6.3.1.4 Future research directions

A key aspect of SOH devices is the long-term stability of the poling-induced molecular order. The material used for the current experiments consists of a rather loose arrangement of DLD164 electro-optic chromophores and hence has a relatively low glass transition temperature of only 66°C. This limits the on-chip power dissipation. In our experiments, the devices were operated at lasers powers of up 18 dBm, measured in the input fiber, which corresponds to 12 dBm of on-chip laser power, taking into account typical fiber-chip coupling losses of 6 dB. At the same time, up to 28 dBm of RF power was continuously coupled to the chip. Still, even at these power levels, the material was stable

enough to enable the presented experiments under ambient atmosphere in a normal lab environment.

We expect that stability of the electro-optic material can be significantly improved by synthetically modified DLD164 chromophores that bear specific crosslinking agents for post-poling lattice hardening. The viability of this approach has already been demonstrated for similar classes of electro-optic compounds, yielding materials being stable for temperatures of up to 250 °C [223,324]. It has also been demonstrated experimentally that these techniques can be applied to realize temperature-stable all-polymeric MZM [325]. For DLD164, the addition of crosslinking agents to the side groups can be realized without affecting the electro-optic activity of the chromophore or the interaction of the side chains. This is subject to ongoing research.

Moreover, the insertion loss of the device is currently limiting its practical applicability. In addition to approximately 6 dB of fiber-chip coupling loss per interface, the device features an on-chip loss of approximately 21 dB. Moreover, modulation distributes the incoming power over many spectral lines, resulting in typical output powers between -27 dBm and -17 dBm per comb line, measured in the fiber immediately after the modulator. We expect that the overall insertion losses can be reduced dramatically by systematic optimization of fiber-chip coupling [326], and by improving device design and fabrication.

6.3.1.5 Summary and conclusion

We demonstrate modulator-based frequency comb generators fabricated on the silicon-organic hybrid (SOH) platform. Using a dual-drive MZM, we generate flat-top frequency combs featuring 7 lines with a spacing of 40 GHz and a spectral flatness of 2 dB. This performance can well compete with integrated InP-based comb generators, where a phase modulator inside an amplifying ring was used to demonstrate 6 lines with a spacing of around 10 GHz and a spectral flatness of 5 dB. The viability of the SOH comb generators is confirmed in a series of data transmission experiments, where we demonstrate line rates of more than 1 Tbit/s and transmission distances of up to 300 km. Spectral efficiencies of up to 4.9 bit/s/Hz are achieved by using 16QAM signals along with a line spacing of 25 GHz and Nyquist pulse shaping at a symbol rate of

18 GBd. We believe that SOH comb sources can become essential elements within the already rich silicon photonic device portfolio.

[*End of paper* [J5]]

7 Summary and outlook

7.1 Summary

This chapter summarizes the demonstrated concepts in the fields of electro-optic frequency combs and photonic integration and their applications in optical distance metrology and optical communication.

Electro-optic comb generation has been shown to be a particularly attractive option for offering flexible control over line spacing and central wavelength. The line spacing is determined by the frequency of the electrical driving signal, while the central wavelengths are given by the lasers coupled to the comb generator. This versatility has been employed to overcome several application-specific challenges. In Chapter 3, a pair of electro-optic FC are used for distance measurements to technical surfaces. To acquire surface profiles, a fiber-coupled remote measurement head is mounted on a coordinate measuring machine. A temperature compensation scheme making use of a second pair of electro-optic FC at a different central wavelength has been implemented to mitigate the thermal drift occurring in the fiber-optical setup, which otherwise would have severely limited the measurement accuracy. Fast measurements with an acquisition time of 9.1 µs and accuracy in the single-digit micrometer regime under challenging operating conditions are demonstrated [J1]. In Chapter 5, the electro-optic comb generators have been used to calibrate the relative frequency differences between four lasers used for synthetic-wavelength interferometry. The possibility to choose the comb line spacing as well as the capability of the comb generators to accommodate different central wavelengths have been key aspects of the success of the experiment. The implemented frequency referencing scheme allows for highly precise measurements with free-running lasers without the need for additional wavelength stabilization or more complex calibration procedures, thus greatly simplifying the technical effort typically associated with synthetic-wavelength interferometry [J4].

Electro-optic comb generation lends itself to photonic integration, and silicon photonics represents a particularly attractive platform, allowing cost-efficient high-yield mass production of highly compact optical systems with unprecedented functionality. However, it is challenging to realize silicon-based phase modulators with the required combination of bandwidth and phase modulation efficiency for broadband frequency comb generation. In this work it has been shown for the first time, that with the so-called silicon-organic hybrid (SOH) approach [86–91, 157, 158, 267–270], electro-optic comb generators on silicon can be realized, see Chapter 6. The generation of spectrally flat frequency combs with 7 lines within 2 dB and comb line spacings of 25 GHz and 40 GHz has been demonstrated [J5], and the practical viability of these combs has been demonstrated in a series of data transmission experiments, where the individual comb lines serve as carriers in a wavelength division multiplexing system. Transmission at data rates of more than 1 Tbit/s over distances of up to 300 km have been achieved. Again, the flexibility of electro-optic combs has been proven to be advantageous, allowing to maximize the spectral efficiency by appropriate tuning of the line spacing.

Drastic footprint reduction compared to a conventional setup using fiber-optical components has been demonstrated by integrating an optical receiver for comb-based distance measurement on a silicon photonic chip, see Chapter 4. The system comprises a heterodyne receiver structure including tunable power splitters and on-chip photodetectors, with an on-chip footprint of well below $1\,\mathrm{mm}^2$. The performance characteristics are comparable to a macroscopic fiber-based setup. Distance measurements with root-mean-square errors of $3.4\,\mu\mathrm{m}$ have been demonstrated for measurement times of $14\,\mu\mathrm{s}$ [J11]. While the frequency combs have been generated off-chip for these experiments, the feasibility of electro-optic frequency comb sources on the silicon photonics platform has been demonstrated in Chapter 6, making use of the silicon-organic hybrid (SOH) approach. This paves the way towards mass-producible, miniaturized sensor chips, which could be tightly integrated into industrial machinery.

7.2 Outlook

Looking beyond the scope of the presented work, a number of avenues for further research are evident. The performance characteristics of approaches using frequency combs are in large parts determined by the properties of the employed frequency comb sources, in particular by the provided bandwidth and the line spacing. Advances in the field of frequency comb generation are thus a relatively straightforward way to improve upon important system parameters. A very promising type of integrated frequency comb source relies on Kerr-nonlinear microring resonators, which can produce ultra-broadband frequency combs with large line spacings and smooth spectral envelopes. The viability of such devices for applications in WDM telecommunication has been shown in several papers [60, 327, J3]. Recently, the same class of comb sources has been employed to ultrafast laser ranging [240,J9], making use of the measurement principle introduced in Chapter 3 and Chapter 4. The high optical bandwidth enabled distance measurements with an Allan deviation of 12 nm at an averaging time of 14 µs. Further improvements could be possible by the use of self-referenced comb sources [59], potentially increasing the precision by additionally considering optical interferometry at single wavelengths. It is also to be expected that the experimental effort currently involved when working with Kerr combs will decrease significantly – recently even a battery-operated device has been demonstrated [71]. This growth in maturity is needed to support potential applications of frequency combs outside of optics labs, e.g., within industrial environments. Specifically for the SOH comb generators based on electro-optic modulation (introduced in Chapter 6), further innovation is likely to come from the development of advanced electro-optic organic materials. Research towards improved thermal stability of the acentric order achieved by the poling procedure will likely result in materials being able to meet demanding industrial standards such as Telcordia, thus enabling reliable long-term employment [152, 153, 155, 262]. Another research direction in this field aims towards higher electro-optic coefficients [89, 155, 156, 262]. This has the potential to result in higher optical comb bandwidths for a given drive voltage, as more comb lines are generated when the modulation depth is increased.

In order to realize the full potential of highly miniaturized systems that photonic integration promises, more components need to be integrated into a single

package. Further investigation could focus on the realization of photonic packages, combining integrated frequency comb sources with application-specific photonic integrated circuits. As optical frequency combs are an incredibly versatile tool in the field of optics and photonics, a range of applications will likely benefit from progress in this area.

A Mathematical definitions

A.1 Fourier transformation

The Fourier transform of a function $g(t)$ with respect to the variable t is denoted as $\mathcal{F}\{g(t)\}$,

$$\tilde{g}(\omega) = \mathcal{F}\{g(t)\} = \int_{-\infty}^{\infty} g(t)\, \mathrm{e}^{-\mathrm{j}\omega t}\, \mathrm{d}t \tag{A.1}$$

$$g(t) = \mathcal{F}^{-1}\{\tilde{g}(\omega)\} = \frac{1}{2\pi} \int_{-\infty}^{\infty} \tilde{g}(\omega)\, \mathrm{e}^{\mathrm{j}\omega t}\, \mathrm{d}\omega \tag{A.2}$$

B Optical data transmission

B.1 Mach-Zehnder modulator

A Mach-Zehnder modulator (MZM) is used to modulate the amplitude of light by making use of interference. An MZM comprises phase modulators arranged in a Mach-Zehnder interferometer structure, see Fig. B.1. The input light is split into two paths. At least one of the paths contains a phase modulator. This allows control of the phase difference between the optical signals propagating via the two paths by applying electrical driving signals. At the output of the MZM, the light from both paths is superimposed. Depending on the acquired phase difference, constructive or destructive interference or in-between states can be achieved. This is can be seen in the optical field transfer function, which reads (e.g. [328]):

$$\begin{aligned}\frac{E_{\text{out}}(t)}{E_{\text{in}}(t)} &= \frac{1}{2}\left(e^{\mathrm{j}\Delta\varphi_1(t)} + e^{\mathrm{j}\Delta\varphi_2(t)}\right) \\ &= e^{\mathrm{j}(\Delta\varphi_1(t)+\Delta\varphi_2(t))/2}\cos\left[\frac{(\Delta\varphi_1(t)-\Delta\varphi_2(t))}{2}\right].\end{aligned} \tag{B.1}$$

So-called push-pull operation is obtained for $\Delta\varphi_2(t) = -\Delta\varphi_1(t)$. With this driving condition, Eq. (B.1) becomes

$$\frac{E_{\text{out}}(t)}{E_{\text{in}}(t)} = \cos\left(\Delta\varphi_1(t)\right), \tag{B.2}$$

resulting in chirp-free amplitude modulation. It is possible to use multiple amplitude levels to encode information. An example of such a modulation format, which can be generated by a MZM in push-pull operation, is 2ASK-2PSK (amplitude-shift keying, phase shift keying). The constellation diagram is shown in Fig. B.1. Two amplitude levels and two phase states (0, π) are utilized to encode 2 bits/symbol.

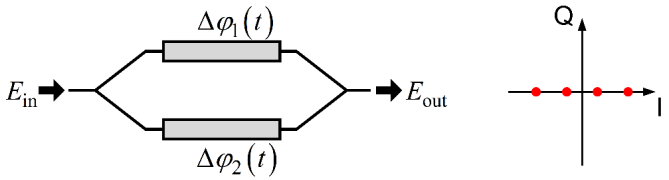

Fig. B.1: Mach-Zehnder modulator (MZM) and constellation diagram of 2ASK-2PSK (amplitude-shift keying, phase shift keying) modulation.

B.2 IQ modulator and complex modulation formats

The electrical field of an optical signal can be measured in both amplitude and phase with coherent reception schemes. This allows encoding of information on both the amplitude and the phase or, equivalently, on the real and the imaginary part of the complex wave amplitude, thereby increasing the number of bits per symbol. The quadrature axis can be used by employing IQ modulators. The schematic of an IQ modulator is sketched in Fig. B.2. It comprises two MZM nested in a "parent" Mach-Zehnder interferometer. The optical path along one of the arms of the parent MZM contains an additional phase shift of $\pi/2$ relative to the other arm. In this way, the real part or the in-phase (I) component and the imaginary part or the quadrature (Q) component can be addressed independently by applying driving signals to MZM 1 and MZM 2. This allows the generation of complex modulation formats. As an example, the constellation diagram of 16QAM (16-state quadrature amplitude modulation) is shown, carrying an information content of 4 bits/symbol.

B.3 Nyquist wavelength division multiplexing

To maximize the capacity of data transmission systems, the available bandwidth has to be used as efficiently as possible. This is quantified by the spectral efficiency, which is the amount of transmitted data divided by the utilized bandwidth. Theoretically, a bandwidth-limited signal can be fully encoded within its Nyquist bandwidth $1/T$. Other frequency components outside the

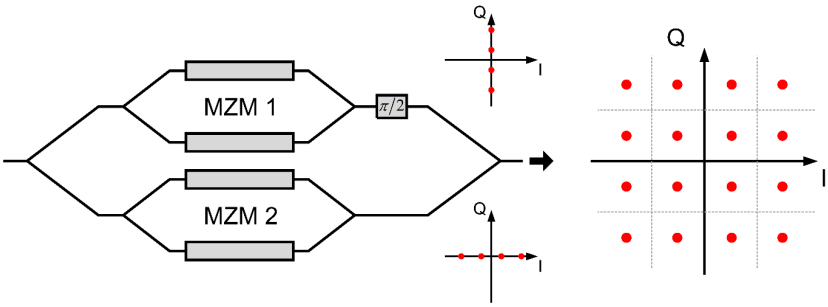

Fig. B.2: IQ modulator comprising two nested MZM in a parent MZM and constellation diagram of 16QAM (16-state quadrature amplitude modulation).

Nyquist bandwidth can potentially be suppressed by accordingly designed filters. This allows a reduction of the required bandwidth to a rectangular spectrum within the Nyquist bandwidth. An example is given in Fig. B.3: The non-return-to-zero (NRZ) waveform exhibits a sinc^2-shaped spectrum with side lobes. As a consequence when multiplexing the unfiltered NRZ signals on several carriers, they have to be spaced far enough apart in order to minimize inter-channel interference. With appropriate filtering, the spectrum can be minimized to a rectangular flat spectrum with a bandwidth of $1/T$. This allows a much tighter channel spacing and thus an increased spectral efficiency of the so-called Nyquist WDM. The shape of the spectrum implies a sinc-shaped time-domain waveform with overlapping pulses. Several ways to implement such a filter efficiently are discussed in [319].

B.4 Error vector magnitude

The ratio of wrongly received bits to totally transmitted bits for a data transmission depends on the signal quality and is called the bit-error ratio (BER). A certain level of BER can be tolerated as it can be compensated by forward error-correction (FEC) algorithms together with some redundancy in the transmitted data. To determine the quality of a data transmission system, the BER can be measured directly just by counting the wrongly transmitted bits of a known bit sequence. However, this becomes impractical for high quality

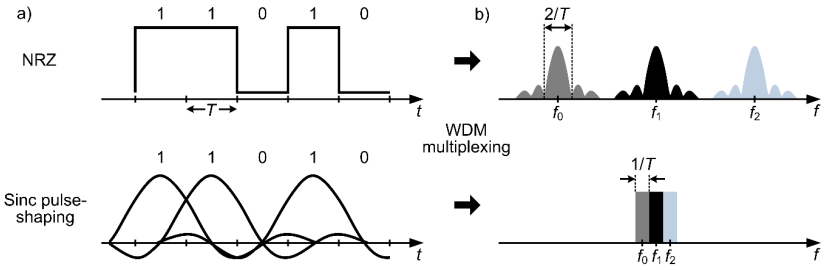

Fig. B.3: Effect of pulse shaping on the spectral efficiency of a WDM data transmission. (a) Waveform of a sequence of bits for non-return-to-zero (NRZ) and pulse shaping with a sinc-function. (b) Corresponding optical spectra for WDM of the signals on three carriers f_0 to f_2. The unfiltered power spectrum of the NRZ waveform is sinc^2-shaped, requiring a wider carrier spacing and guard bands to prevent inter-channel interference. The power spectrum of the sinc-shaped pulses is rectangular with a spectral width corresponding to the Nyquist bandwidth $1/T$. This allows tight spectral spacing of the carriers without guard bands.

signals, where the low error occurrence would require transmission of very large amounts of data. In such a case other metrics related to the BER can be used. For the complex modulation formats used in this work, the error vector magnitude (EVM) is used as a quality metric [323]. To determine the EVM, the error vector $\underline{E}_{\mathrm{err},i}$ of a received symbol i is given as the difference between the received complex electric field $\underline{E}_{\mathrm{rec},i}$ and the transmitted complex electric field $\underline{E}_{\mathrm{trans},i}$ in the complex plane,

$$\underline{E}_{\mathrm{err},i} = \underline{E}_{\mathrm{rec},i} - \underline{E}_{\mathrm{trans},i}. \tag{B.3}$$

The EVM is then given as the root-mean-square of $\left|\underline{E}_{\mathrm{err},i}\right|$ for all N symbols, normalized to the largest field vector magnitude in the constellation $\left|\underline{E}_{\mathrm{trans,m}}\right|$,

$$\mathrm{EVM_m} = \frac{\sqrt{\frac{1}{N}\sum_{i=1}^{N}\left|\underline{E}_{\mathrm{err},i}\right|^2}}{\left|\underline{E}_{\mathrm{trans,m}}\right|}. \tag{B.4}$$

The subscript "m" denotes the normalization to the largest field vector magnitude, which was used throughout this work. For additive white Gaussian

noise, quadratic constellations and data-aided reception, the EVM is related to the BER according to [323]:

$$\mathrm{BER} \approx \frac{\left(1 - M^{-1/2}\right)}{\frac{1}{2}\log_2 M} \mathrm{erfc}\left[\sqrt{\frac{3}{2\,(M-1)}\,\frac{1}{(k\mathrm{EVM_m})^2}}\right], \tag{B.5}$$

where M represents the constellation size, i.e., the number of possible constellation points of the modulation format, and where the factor k with $k = 1$ for QPSK and $k = 9/5$ for 16QAM accounts for different maximum and average field amplitudes of the modulation formats.

C Parameters of different types of frequency comb sources

This appendix contains a tabular listing of data from literature used to compile Fig. 1.3.

Table C.1: Center wavelength, bandwidth and line spacing for frequency combs generated by solid-state lasers from literature.

Center wavelength [nm]	Bandwith [THz]	Bandwidth after nonlin. broad. [THz]	Line spacing [GHz]	Ref.
800	351	-	0.065	[329]
1030	1.4	214	1	[330]
1560	1.7	157	0.075	[331]
890	9.1	327	0.093	[332]
1558	1.9	150	0.075	[53]
780	12	350	10	[333]
1535	0.33	-	101	[54]
1534	0.03	-	10	[334]
1534	0.3	-	40	[335]

Table C.2: Center wavelength, bandwidth and line spacing for frequency combs generated by fiber lasers from literature.

Center wavelength [nm]	Bandwith [THz]	Bandwidth after non-lin. broad. [THz]	Line spacing [GHz]	Ref.
1560	4.9	-	0.038	[336]
1040	11.1	-	0.05	[337]
1567	1.25	156	0.2	[48]
1560	3	143	0.1	[338]
1050	3.4	518	0.09	[339]
1530	5	-	0.03	[340]
1530	2.5	150	0.05	[341]
1560	3.1	166	0.086	[342]
1040	n.a.	300	0.25	[343]
1020	n.a.	269	0.5	[344]
1025	1.6	-	3	[51]
1573	2.1	-	1	[52]

Table C.3: Center wavelength, bandwidth and line spacing for frequency combs generated by semiconductor lasers from literature.

Center wavelength [nm]	Bandwith [THz]	Bandwidth after non-lin. broad. [THz]	Line spacing [GHz]	Ref.
1550	1.2	-	10	[345]
9000	1.9	-	11	[346]
1038	1.5	228	1.75	[347]
995	0.8	-	1	[348]
995	1.5	-	2.8 – 7.9	[349]
1550	0.75	-	10	[350]
1037	0.98	-	175	[351]

Table C.4: Center wavelength, bandwidth and line spacing for frequency combs generated by direct electro-optic modulation without cavity enhancement from literature.

Center wavelength [nm]	Bandwith [THz]	Bandwidth after non-lin. broad. [THz]	Line spacing [GHz]	Ref.
1550	0.15	12.5 with 125 cw lasers	12.5	[77]
1542	0.5 – 1	-	6 – 18	[81]
1550	0.2 – 0.4	-	8.5 – 19	[79]
1512	0.09	-	10	[80]
1533	0.2	-	14	[174]
1550	0.07	-	10	[170]
1535	0.03	-	3	[82]
1550	0.23	-	10	[83]
1550	0.31	-	12	[352]
1546	0.5	-	42.6	[78]
1550	0.4	-	10	[84]
1545	0.2	1	10	[353]
1550	0.17	-	10	[354]
1580	1.5	-	25	[355]
1550	0.23	3.6	10	[356]
1550	0.5	18	10	[357]
1560	0.22	1	10	[358]
1550	2.6	-	25	[359]

Table C.5: Center wavelength, bandwidth and line spacing for frequency combs generated by cavity-enhanced electro-optic modulation from literature.

Center wavelength [nm]	Bandwith [THz]	Bandwidth after non-lin. broad. [THz]	Line spacing [GHz]	Ref.
1550	0.05 – 0.08	-	9 – 14	[305]
1550	4	-	5.8	[256]
1555	0.18	-	26.8	[360]
1550	0.4	-	10	[75]
1550	4.5	-	26	[314]

Table C.6: Center wavelength, bandwidth and line spacing for frequency combs generated by microring resonators from literature.

Center wavelength [nm]	Bandwith [THz]	Bandwidth after non-lin. broad. [THz]	Line spacing [GHz]	Ref.
1550	30	-	25	[361]
1555	34.8	-	400	[277]
1555	24.9	-	1170	[277]
1550	37	-	6400	[362]
1556	10	-	143	[363]
1560	165	-	850	[282]
1560	23.5	-	172	[364]
1550	70	-	875	[57]
1550	50.2	-	375	[57]
1550	35	-	99	[365]
1550	35	-	225	[365]
1560	24	-	20	[366]
1560	24	-	40	[366]
1560	24	-	80	[366]
1000	55	-	230	[366]

Table C.7: Center wavelength, bandwidth and line spacing for frequency combs generated by highly nonlinear fibers (HNLF) from literature.

Center wavelength [nm]	Bandwidth [THz]	Bandwidth after nonlin. broad. [THz]	Line spacing [GHz]	Ref.
1550	12	-	100	[271]
1550	18.8	-	125	[63]
1550	17.5	-	417	[62]
1550	25	-	200	[61]
1550	25	-	400	[61]
1550	20	-	200	[272]

Glossary

List of symbols

Greek symbols

α_L	Thermal expansion coefficient
$\Gamma,\ \Gamma_{\mathrm{dB}}$	Isolation of coupler
$\gamma,\ \gamma_{\mathrm{dB}}$	Power splitting ratio
$\Delta\varphi_m,\ \Delta\Phi_m$	Phase difference of mth comb line, measured / model value
δ	Delta function
δ_{ij}	Kronecker delta
η	Power losses
η_m	Power conversion efficiency
η_{ij}	Element of impermeability tensor
Θ_i	Two-sided power spectral density of electrical current
θ	Variable
κ	Amplitude reflection coefficient
$\Lambda,\ \Lambda_{ij}$	Synthetic wavelength
$\Lambda_{ij,kl}$	Second-order synthetic wavelength
λ	Wavelength
σ	Standard deviation

σ_{Allan}	Allan deviation
τ	Measurement time
φ_m	Phase of mth comb line
$\chi^{(2)}_{hk}$	Tensor element of second-order susceptibility
ω	Angular frequency
ω_{mod}	Angular modulation frequency

Latin symbols

A	Modulation depth
a	Variable
B	Bandwidth
c, c_0	Speed of light in vacuum
$\underline{\hat{D}}$	Complex amplitude of electric displacement
D	Optical path length inside fibers
$d_{i,j}$	Distance from retroreflector position i to module j
d	Spacing of capacitor plates
E	Electric field
$\underline{E}$	Analytical signal of electric field
$\underline{\hat{E}}$	Complex electric field amplitude
E_{mod}	External electric field applied to modulators
e	Elementary charge
f	Frequency
f_{mod}	MZM driving frequency / comb line spacing

Δf_0	Detuning of center frequencies
Δf_{mod}	Detuning of MZM driving frequencies
Δf_{ij}	Difference frequency between lasers i and j
Δf	Detection bandwidth
H	Heaviside function
i	Electrical current
$\mathrm{J}_m\,(a)$	Bessel functions of the first kind
k_0	Wavenumber $k_0 = \frac{2\pi}{\lambda}$
L	Geometric path length inside fibers
$m,\ l$	Order of comb line
N	Number of comb lines
$n,\ n_0$	Refractive index
P	Power
p	Proportionality factor
R_{TIA}	Transimpedance
r^2	Coefficient of determination
r_{33}	Linear electro-optic coefficient along axis 3
S	Detector sensitivity
SS_{res}	Sum of squared errors
SS_{tot}	Sum of squared deviations from mean
T	Temperature
t	Time
U_π	Voltage for a phase difference of π between MZM arms
U_{bias}	Bias voltage

U_{mod}, $\hat{U}_{\mathrm{mod}}$	Modulator driving voltage / voltage amplitude
U_{π}	Voltage needed for a phase shift ofπ
$\hat{V}$	Voltage amplitude
$\widehat{w}_{\mathrm{o,RIN}}$	Optical power spectral density of RIN
$w_{i,\mathrm{RIN}}$	Associated electrical power spectral density of RIN
z, z_{cal}, z_{ref}	Optical path lengths for object / calibration / reference path
$\hat{z}$, $\hat{z}_{\mathrm{cal}}$	Measured optical path lengths
Δz_{ua}	Unambiguity range
z_{comp}, $\hat{z}_{\mathrm{comp}}$	Temperature compensated real and measured optical path length

Acronyms

16QAM	16-state quadrature amplitude modulation
3D	Three-dimensional
4Q	Four-quadrant photodiode
A/D	Analog-to-digital
AC	Alternating current
ADC	Analog-to-digital converter
AOM	Acousto-optical modulator
APD	Avalanche photodiode
ASE	Amplified spontaneous emission
BD	Balanced photodetector
BER	Bit-error ratio
BP	Band pass

BS	Beam splitter
CCD	Charge-coupled device
CMM	Coordinate measuring machine
CPL	Optical coupler
CW	Continuous-wave
DC	Direct current
DFB	Distributed feedback
DFT	Discrete Fourier transform
EDFA	Erbium-doped fiber amplifier
EVM	Error vector magnitude
FC	Frequency comb
FEC	Forward-error correction
FMCW	Frequency-modulated continuous wave
FPGA	Field-programmable gate array
GPS	Global positioning system
HWP	Half-wave plate
IF	Intermediate frequency
LO	Local oscillator
MLL	Mode-locked laser
MMI	Multimode interference coupler
MWLI	Multi-wavelength interferometry
MZM	Mach-Zehnder modulator
NEP	Noise-equivalent power
NRZ	Non-return-to-zero

OMA	Optical modulation analyzer
PC	Personal computer
PCB	Printed-circuit board
PD	Photodiode
PDF	Probability density function
PDFA	Praseodymium-doped fiber amplifier
PDM	Polarization-division multiplexing
PIC	Photonic integrated circuit
PM	Polarization-maintaining
PRBS	Pseudo-random bit sequences
QPSK	Quadrature phase shift keying
RBW	Resolution bandwidth
RF	Radio frequency
RIN	Relative intensity noise
Rx	Receiver
SMF	Single-mode fiber
SNR	Signal-to-noise power ratio
SOH	Silicon-organic hybrid
SOI	Silicon-on-insulator
SWI	Synthetic-wavelength interferometry
SWR	Synthetic wavelength reference
TIA	Transimpedance amplifier
TLS	Tunable laser source
TOF	Time-of-flight

TPS Tunable power splitter

WSS Wavelength-selective switch

Bibliography

[1] C. Weimann, C. Koos, M. Fratz, and H. Woelfelschneider, "System und Verfahren zur Distanzmessung," DE Patent DE 10 2014 004 697 B4, March 29, 2018.

[2] J. Ye and S. T. Cundiff, *Femtosecond optical frequency comb*. Springer, 2005.

[3] S. A. Diddams, "The evolving optical frequency comb," *Journal of the Optical Society of America B*, vol. 27, no. 11, p. B51, 2010.

[4] D. J. Jones, "Carrier-envelope phase control of femtosecond mode-locked lasers and direct optical frequency synthesis," *Science*, vol. 288, no. 5466, pp. 635–639, 2000.

[5] Holzwarth, Udem, Hansch, Knight, Wadsworth, and Russell, "Optical frequency synthesizer for precision spectroscopy," *Physical Review Letters*, vol. 85, no. 11, pp. 2264–2267, 2000.

[6] N. R. Newbury, "Searching for applications with a fine-tooth comb," *Nature Photonics*, vol. 5, no. 4, pp. 186–188, 2011.

[7] S. Boudreau and J. Genest, "Referenced passive spectroscopy using dual frequency combs," *Optics Express*, vol. 20, no. 7, pp. 7375–7387, 2012.

[8] F. Adler, P. Masłowski, A. Foltynowicz, K. C. Cossel, T. C. Briles, I. Hartl, and J. Ye, "Mid-infrared Fourier transform spectroscopy with a broadband frequency comb," *Optics Express*, vol. 18, no. 21, p. 21861, 2010.

[9] I. Coddington, W. Swann, and N. Newbury, "Coherent dual-comb spectroscopy at high signal-to-noise ratio," *Physical Review A*, vol. 82, no. 4, 2010.

[10] S. Schiller, "Spectrometry with frequency combs," *Optics Letters*, vol. 27, no. 9, p. 766, 2002.

[11] A. Schliesser, M. Brehm, F. Keilmann, and D. W. van der Weide, "Frequency-comb infrared spectrometer for rapid, remote chemical sensing," *Optics Express*, vol. 13, no. 22, p. 9029, 2005.

[12] C. Gohle, B. Stein, A. Schliesser, T. Udem, and T. Hänsch, "Frequency comb vernier spectroscopy for broadband, high-resolution, high-sensitivity absorption and dispersion spectra," *Physical Review Letters*, vol. 99, no. 26, 2007.

[13] P. Giaccari, J.-D. Deschênes, P. Saucier, J. Genest, and P. Tremblay, "Active Fourier-transform spectroscopy combining the direct RF beating of two fiber-based mode-locked lasers with a novel referencing method," *Optics Express*, vol. 16, no. 6, p. 4347, 2008.

[14] T. Udem, "Spectroscopy: Frequency comb benefits," *Nature Photonics*, vol. 3, no. 2, pp. 82–84, 2009.

[15] J. Mandon, G. Guelachvili, and N. Picqué, "Fourier transform spectroscopy with a laser frequency comb," *Nature Photonics*, vol. 3, no. 2, pp. 99–102, 2009.

[16] B. Bernhardt, A. Ozawa, P. Jacquet, M. Jacquey, Y. Kobayashi, T. Udem, R. Holzwarth, G. Guelachvili, T. W. Hänsch, and N. Picqué, "Cavity-enhanced dual-comb spectroscopy," *Nature Photonics*, vol. 4, no. 1, pp. 55–57, 2009.

[17] T. R. Schibli, I. Hartl, D. C. Yost, M. J. Martin, A. Marcinkevicius, M. E. Fermann, and J. Ye, "Optical frequency comb with submillihertz linewidth and more than 10 W average power," *Nature Photonics*, vol. 2, no. 6, pp. 355–359, 2008.

[18] I. Coddington, W. C. Swann, L. Lorini, J. C. Bergquist, Y. Le Coq, C. W. Oates, Q. Quraishi, K. S. Feder, J. W. Nicholson, P. S. Westbrook, S. A. Diddams, and N. R. Newbury, "Coherent optical link over hundreds of metres and hundreds of terahertz with subfemtosecond timing jitter," *Nature Photonics*, vol. 1, no. 5, pp. 283–287, 2007.

[19] L.-S. Ma, Z. Bi, A. Bartels, L. Robertsson, M. Zucco, R. S. Windeler, G. Wilpers, C. Oates, L. Hollberg, and S. A. Diddams, "Optical frequency synthesis and comparison with uncertainty at the 10(-19) level," *Science (New York, N.Y.)*, vol. 303, no. 5665, pp. 1843–1845, 2004.

[20] S. T. Cundiff and A. M. Weiner, "Optical arbitrary waveform generation," *Nature Photonics*, vol. 4, no. 11, pp. 760–766, 2010.

[21] V. Torres-Company and A. M. Weiner, "Optical frequency comb technology for ultra-broadband radio-frequency photonics," *Laser & Photonics Reviews*, vol. 8, no. 3, pp. 368–393, 2014.

[22] S. Kray, F. Spöler, M. Först, and H. Kurz, "Dual femtosecond laser multiheterodyne optical coherence tomography," *Optics Letters*, vol. 33, no. 18, p. 2092, 2008.

[23] T. Bajraszewski, M. Wojtkowski, M. Szkulmowski, A. Szkulmowska, R. Huber, and A. Kowalczyk, "Improved spectral optical coherence tomography using optical frequency comb," *Optics Express*, vol. 16, no. 6, pp. 4163–4176, 2008.

[24] T. Yasui, M. Fujio, S. Yokoyama, and T. Araki, "Phase-slope and phase measurements of tunable CW-THz radiation with terahertz comb for wide-dynamic-range, high-resolution, distance measurement of optically rough object," *Optics Express*, vol. 22, no. 14, pp. 17349–17359, 2014.

[25] S. Yokoyama, R. Nakamura, M. Nose, T. Araki, and T. Yasui, "Terahertz spectrum analyzer based on a terahertz frequency comb," *Optics Express*, vol. 16, no. 17, p. 13052, 2008.

[26] D. Burghoff, T.-Y. Kao, N. Han, C. W. I. Chan, X. Cai, Y. Yang, D. J. Hayton, J.-R. Gao, J. L. Reno, and Q. Hu, "Terahertz laser frequency combs," *Nature Photonics*, vol. 8, no. 6, pp. 462–467, 2014.

[27] M. Hase, M. Katsuragawa, A. M. Constantinescu, and H. Petek, "Frequency comb generation at terahertz frequencies by coherent phonon excitation in silicon," *Nature Photonics*, vol. 6, no. 4, pp. 243–247, 2012.

[28] P. Delfyett, S. Gee, Myoung-Taek Choi, H. Izadpanah, Wangkuen Lee, S. Ozharar, F. Quinlan, and T. Yilmaz, "Optical frequency combs from semiconductor lasers and applications in ultrawideband signal processing and communications," *Journal of Lightwave Technology*, vol. 24, no. 7, pp. 2701–2719, 2006.

[29] X. Xie, Y. Dai, K. Xu, J. Niu, R. Wang, L. Yan, and J. Lin, "Broadband photonic RF channelization based on coherent optical frequency combs and I/Q demodulators," *IEEE Photonics Journal*, vol. 4, no. 4, pp. 1196–1202, 2012.

[30] R. Wu, M. Song, D. E. Leaird, and A. M. Weiner, "Comb-based radio-frequency photonic filtering with 20 ns bandwidth reconfiguration," *Optics Letters*, vol. 38, no. 15, pp. 2735–2738, 2013.

[31] T. Udem, R. Holzwarth, and T. W. Hänsch, "Optical frequency metrology," *Nature*, vol. 416, no. 6877, pp. 233–237, 2002.

[32] J. Reichert, R. Holzwarth, T. Udem, and T. W. Hänsch, "Measuring the frequency of light with mode-locked lasers," *Optics Communications*, vol. 172, no. 1–6, pp. 59–68, 1999.

[33] M. Kourogi, B. Widiyatmoko, and M. Ohtsu, "3.17-THz frequency-difference measurement between lasers using two optical frequency combs," *IEEE Photonics Technology Letters*, vol. 8, no. 4, pp. 560–562, 1996.

[34] I. Coddington, W. C. Swann, L. Nenadovic, and N. R. Newbury, "Rapid and precise absolute distance measurements at long range," *Nature Photonics*, vol. 3, no. 6, pp. 351–356, 2009.

[35] K. Minoshima and H. Matsumoto, "High-accuracy measurement of 240-m distance in an optical tunnel by use of a compact femtosecond laser," *Applied Optics*, vol. 39, no. 30, pp. 5512–5517, 2000.

[36] M. Cui, M. G. Zeitouny, N. Bhattacharya, S. A. van den Berg, H. P. Urbach, and J. J. M. Braat, "High-accuracy long-distance measurements in air with a frequency comb laser," *Optics Letters*, vol. 34, no. 13, p. 1982, 2009.

[37] T.-A. Liu, N. R. Newbury, and I. Coddington, "Sub-micron absolute distance measurements in sub-millisecond times with dual free-running femtosecond Er fiber-lasers," *Optics Express*, vol. 19, no. 19, pp. 18501–18509, 2011.

[38] J. N. Kemal, J. Pfeifle, P. Marin-Palomo, M. D. G. Pascual, S. Wolf, F. Smyth, W. Freude, and C. Koos, "Multi-wavelength coherent transmission using an optical frequency comb as a local oscillator," *Optics Express*, vol. 24, no. 22, pp. 25432–25445, 2016.

[39] D. Hillerkuss, R. Schmogrow, M. Meyer, S. Wolf, M. Jordan, P. Kleinow, N. Lindenmann, P. C. Schindler, A. Melikyan, X. Yang, S. Ben-Ezra, B. Nebendahl, M. Dreschmann, J. Meyer, F. Parmigiani, P. Petropoulos, B. Resan, A. Oehler, K. Weingarten, L. Altenhain, T. Ellermeyer, M. Moeller, M. Huebner, J. Becker, C. Koos, W. Freude, and J. Leuthold, "Single-laser 32.5 Tbit/s Nyquist WDM transmission," *Journal of Optical Communications and Networking*, vol. 4, no. 10, pp. 715–723, 2012.

[40] Prestage, Tjoelker, and Maleki, "Atomic clocks and variations of the fine structure constant," *Physical Review Letters*, vol. 74, no. 18, pp. 3511–3514, 1995.

[41] E. Peik, "Fundamental constants and units and the search for temporal variations," *Nuclear Physics B - Proceedings Supplements*, vol. 203-204, pp. 18–32, 2010.

[42] L. E. Hargrove, R. L. Fork, and M. A. Pollack, "Locking of He–Ne laser modes induced by synchronous intracavity modulation," *Applied Physics Letters*, vol. 5, no. 1, pp. 4–5, 1964.

[43] J. N. Eckstein, A. I. Ferguson, and T. W. Hänsch, "High-resolution two-photon spectroscopy with picosecond light pulses," *Physical Review Letters*, vol. 40, no. 13, pp. 847–850, 1978.

[44] R. Teets, J. Eckstein, and T. W. Hänsch, "Coherent two-photon excitation by multiple light pulses," *Physical Review Letters*, vol. 38, no. 14, pp. 760–764, 1977.

[45] Y. Baklanov and V. Chebotayev, "Narrow resonances of two-photon absorption of super-narrow pulses in a gas," *Applied Physics*, vol. 12, no. 1, pp. 97–99, 1977.

[46] H. Telle, G. Steinmeyer, A. Dunlop, J. Stenger, D. Sutter, and U. Keller, "Carrier-envelope offset phase control: A novel concept for absolute optical frequency measurement and ultrashort pulse generation," *Applied Physics B*, vol. 69, no. 4, pp. 327–332, 1999.

[47] P. Maddaloni, P. Cancio, and P. de Natale, "Optical comb generators for laser frequency measurement," *Measurement Science and Technology*, vol. 20, no. 5, p. 52001, 2009.

[48] L. C. Sinclair, I. Coddington, W. C. Swann, G. B. Rieker, A. Hati, K. Iwakuni, and N. R. Newbury, "Operation of an optically coherent frequency comb outside the metrology lab," *Optics Express*, vol. 22, no. 6, pp. 6996–7006, 2014.

[49] B. Walton, H. Margolis, V. Tsatourian, and P. Gill, "Transportable optical frequency comb based on a mode-locked fibre laser," *IET Optoelectronics*, vol. 2, no. 5, p. 182, 2008.

[50] E. Baumann, F. R. Giorgetta, J. W. Nicholson, W. C. Swann, I. Coddington, and N. R. Newbury, "High-performance, vibration-immune, fiber-laser frequency comb," *Optics Letters*, vol. 34, no. 5, p. 638, 2009.

[51] H.-W. Chen, G. Chang, S. Xu, Z. Yang, and F. X. Kärtner, "3 GHz, fundamentally mode-locked, femtosecond Yb-fiber laser," *Optics Letters*, vol. 37, no. 17, pp. 3522–3524, 2012.

[52] H. Byun, M. Y. Sander, A. Motamedi, H. Shen, G. S. Petrich, L. A. Kolodziejski, E. P. Ippen, and F. X. Kärtner, "Compact, stable 1 GHz femtosecond Er-doped fiber lasers," *Applied Optics*, vol. 49, no. 29, pp. 5577–5582, 2010.

[53] S. Schilt, N. Bucalovic, V. Dolgovskiy, C. Schori, M. C. Stumpf, G. Di Domenico, S. Pekarek, Andreas E. H. Oehler, T. Südmeyer, U. Keller, and P. Thomann, "Fully stabilized optical frequency comb with subradian CEO phase noise from a SESAM-modelocked 1.5-μm solid-state laser," *Optics Express*, vol. 19, no. 24, pp. 24171–24181, 2011.

[54] A. E. Oehler, T. Südmeyer, K. J. Weingarten, and U. Keller, "100 GHz passively mode-locked Er:Yb:glass laser at 1.5-µm with 1.6-ps pulses," *Optics Express*, vol. 16, no. 26, pp. 21930–21935, 2008.

[55] G. P. Agrawal, *Nonlinear fiber optics*. Amsterdam u.a.: Elsevier Acad. Press, 5. ed., 2013.

[56] R. W. Boyd, *Nonlinear optics*. Amsterdam u.a.: Elsevier, 3. ed., 2008.

[57] P. Del'Haye, A. Schliesser, O. Arcizet, T. Wilken, R. Holzwarth, and T. J. Kippenberg, "Optical frequency comb generation from a monolithic microresonator," *Nature*, vol. 450, no. 7173, pp. 1214–1217, 2007.

[58] R. Henriet, G. Lin, A. Coillet, M. Jacquot, L. Furfaro, L. Larger, and Y. K. Chembo, "Kerr optical frequency comb generation in strontium fluoride whispering-gallery mode resonators with billion quality factor," *Optics Letters*, vol. 40, no. 7, pp. 1567–1570, 2015.

[59] V. Brasch, E. Lucas, J. D. Jost, M. Geiselmann, and T. J. Kippenberg, "Self-referenced photonic chip soliton Kerr frequency comb," *Light: Science & Applications*, vol. 6, no. 1, p. e16202, 2016.

[60] P. Marin-Palomo, J. N. Kemal, M. Karpov, A. Kordts, J. Pfeifle, M. H. P. Pfeiffer, P. Trocha, S. Wolf, V. Brasch, M. H. Anderson, R. Rosenberger, K. Vijayan, W. Freude, T. J. Kippenberg, and C. Koos, "Microresonator-based solitons for massively parallel coherent optical communications," *Nature*, vol. 546, no. 7657, pp. 274–279, 2017.

[61] Z. Tong, A. O. J. Wiberg, E. Myslivets, B. P. P. Kuo, N. Alic, and S. Radic, "Spectral linewidth preservation in parametric frequency combs seeded by dual pumps," *Optics Express*, vol. 20, no. 16, pp. 17610–17619, 2012.

[62] B. Kuo, E. Myslivets, N. Alic, and S. Radic, "Wavelength multicasting via frequency comb generation in a bandwidth-enhanced fiber optical parametric mixer," *Journal of Lightwave Technology*, vol. 29, no. 23, pp. 3515–3522, 2011.

[63] E. Myslivets, B. P. Kuo, N. Alic, and S. Radic, "Generation of wideband frequency combs by continuous-wave seeding of multistage mixers with

synthesized dispersion," *Optics Express*, vol. 20, no. 3, pp. 3331–3344, 2012.

[64] V. Ataie, E. Myslivets, B. P.-P. Kuo, N. Alic, and S. Radic, "Spectrally equalized frequency comb generation in multistage parametric mixer with nonlinear pulse shaping," *Journal of Lightwave Technology*, vol. 32, no. 4, pp. 840–846, 2014.

[65] B. Kuyken, T. Ideguchi, S. Holzner, M. Yan, T. W. Hänsch, J. van Campenhout, P. Verheyen, S. Coen, F. Leo, R. Baets, G. Roelkens, and N. Picqué, "An octave-spanning mid-infrared frequency comb generated in a silicon nanophotonic wire waveguide," *Nature Communications*, vol. 6, p. 6310, 2015.

[66] A. R. Johnson, A. S. Mayer, A. Klenner, K. Luke, E. S. Lamb, M. R. E. Lamont, C. Joshi, Y. Okawachi, F. W. Wise, M. Lipson, U. Keller, and A. L. Gaeta, "Octave-spanning coherent supercontinuum generation in a silicon nitride waveguide," *Optics Letters*, vol. 40, no. 21, pp. 5117–5120, 2015.

[67] M. A. G. Porcel, F. Schepers, J. P. Epping, T. Hellwig, M. Hoekman, R. G. Heideman, P. J. M. van der Slot, C. J. Lee, R. Schmidt, R. Bratschitsch, C. Fallnich, and K.-J. Boller, "Two-octave spanning supercontinuum generation in stoichiometric silicon nitride waveguides pumped at telecom wavelengths," *Optics Express*, vol. 25, no. 2, pp. 1542–1554, 2017.

[68] H. Zhao, B. Kuyken, S. Clemmen, F. Leo, A. Subramanian, A. Dhakal, P. Helin, S. Severi, E. Brainis, G. Roelkens, and R. Baets, "Visible-to-near-infrared octave spanning supercontinuum generation in a silicon nitride waveguide," *Optics Letters*, vol. 40, no. 10, pp. 2177–2180, 2015.

[69] J. Liu, A. S. Raja, M. Karpov, B. Ghadiani, M. H. P. Pfeiffer, B. Du, N. J. Engelsen, H. Guo, M. Zervas, and T. J. Kippenberg, "Ultralow-power chip-based soliton microcombs for photonic integration," *Optica*, vol. 5, no. 10, pp. 1347–1353, 2018.

[70] M.-G. Suh, C. Y. Wang, C. Johnson, and K. J. Vahala, "Directly pumped 10 GHz microcomb modules from low-power diode lasers," *Optics Letters*, vol. 44, no. 7, pp. 1841–1843, 2019.

[71] B. Stern, X. Ji, Y. Okawachi, A. L. Gaeta, and M. Lipson, "Battery-operated integrated frequency comb generator," *Nature*, vol. 562, no. 7727, pp. 401–405, 2018.

[72] J. Gaertner, P. Trocha, R. Mandel, C. Koos, T. Jahnke, and W. Reichel, "Bandwidth and conversion efficiency analysis of dissipative kerr soliton frequency combs based on bifurcation theory," *Physical Review A*, vol. 100, p. 033819, 2019.

[73] T. Kobayashi, T. Sueta, Y. Cho, and Y. Matsuo, "High–repetition–rate optical pulse generator using a Fabry–Perot electro–optic modulator," *Applied Physics Letters*, vol. 21, no. 8, pp. 341–343, 1972.

[74] M. Kourogi, K. Nakagawa, and M. Ohtsu, "Wide-span optical frequency comb generator for accurate optical frequency difference measurement," *IEEE Journal of Quantum Electronics*, vol. 29, no. 10, pp. 2693–2701, 1993.

[75] S. Xiao, L. Hollberg, N. R. Newbury, and S. A. Diddams, "Toward a low-jitter 10 GHz pulsed source with an optical frequency comb generator," *Optics Express*, vol. 16, no. 12, p. 8498, 2008.

[76] K.-P. Ho and J. Kahn, "Optical frequency comb generator using phase modulation in amplified circulating loop," *IEEE Photonics Technology Letters*, vol. 5, no. 6, pp. 721–725, 1993.

[77] M. Fujiwara, M. Teshima, J. Kani, H. Suzuki, N. Takachio, and K. Iwatsuki, "Optical carrier supply module using flattened optical multicarrier generation based on sinusoidal amplitude and phase hybrid modulation," *Journal of Lightwave Technology*, vol. 21, no. 11, pp. 2705–2714, 2003.

[78] T. Healy, F. C. G. Gunning, A. D. Ellis, and J. D. Bull, "Multi-wavelength source using low drive-voltage amplitude modulators for optical communications," *Optics Express*, vol. 15, no. 6, pp. 2981–2986, 2007.

[79] W. Xie, Q. Zhou, C. Zhang, Z. Xia, H. Shi, Y. Dong, L. Yi, and W. Hu, "Coherent comb generation with continuous sweep of repetition rate over one-octave," *IEEE Photonics Technology Letters*, p. 1, 2013.

[80] l.L Gheorma and G. Gopalakrishnan, "Flat frequency comb generation with an integrated dual-parallel modulator," *IEEE Photonics Technology Letters*, vol. 19, no. 13, pp. 1011–1013, 2007.

[81] A. Metcalf, V. Torres-Company, D. Leaird, and A. Weiner, "High-power broadly tunable electrooptic frequency comb generator," *IEEE Journal of Selected Topics in Quantum Electronics*, vol. 19, no. 6, p. 3500306, 2013.

[82] S. Ozharar, F. Quinlan, I. Ozdur, S. Gee, and P. Delfyett, "Ultraflat optical comb generation by phase-only modulation of continuous-wave light," *IEEE Photonics Technology Letters*, vol. 20, no. 1, pp. 36–38, 2008.

[83] T. Sakamoto, T. Kawanishi, and M. Izutsu, "Widely wavelength-tunable ultra-flat frequency comb generation using conventional dual-drive Mach-Zehnder modulator," *Electronics Letters*, vol. 43, no. 19, pp. 1039–1040, 2007.

[84] R. Wu, V. R. Supradeepa, C. M. Long, D. E. Leaird, and A. M. Weiner, "Generation of very flat optical frequency combs from continuous-wave lasers using cascaded intensity and phase modulators driven by tailored radio frequency waveforms," *Optics Letters*, vol. 35, no. 19, p. 3234, 2010.

[85] A. K. Mishra, R. Schmogrow, I. Tomkos, D. Hillerkuss, C. Koos, W. Freude, and J. Leuthold, "Flexible RF-based comb generator," *IEEE Photonics Technology Letters*, vol. 25, no. 7, pp. 701–704, 2013.

[86] M. Hochberg, T. Baehr-Jones, G. Wang, J. Huang, P. Sullivan, L. Dalton, and A. Scherer, "Towards a millivolt optical modulator with nano-slot waveguides," *Optics Express*, vol. 15, no. 13, pp. 8401–8410, 2007.

[87] S. Koeber, R. Palmer, M. Lauermann, W. Heni, D. L. Elder, D. Korn, M. Woessner, L. Alloatti, S. Koenig, P. C. Schindler, H. Yu, W. Bogaerts, L. R. Dalton, W. Freude, J. Leuthold, and C. Koos, "Femtojoule electro-

optic modulation using a silicon–organic hybrid device," *Light: Science & Applications*, vol. 4, no. 2, p. e255, 2015.

[88] J.-M. Brosi, C. Koos, L. C. Andreani, M. Waldow, J. Leuthold, and W. Freude, "High-speed low-voltage electro-optic modulator with a polymer-infiltrated silicon photonic crystal waveguide," *Optics Express*, vol. 16, no. 6, pp. 4177–4191, 2008.

[89] C. Kieninger, Y. Kutuvantavida, D. L. Elder, S. Wolf, H. Zwickel, M. Blaicher, J. N. Kemal, M. Lauermann, S. Randel, W. Freude, L. R. Dalton, and C. Koos, "Ultra-high electro-optic activity demonstrated in a silicon-organic hybrid modulator," *Optica*, vol. 5, no. 6, pp. 739–748, 2018.

[90] S. Wolf, H. Zwickel, W. Hartmann, M. Lauermann, Y. Kutuvantavida, C. Kieninger, L. Altenhain, R. Schmid, J. Luo, A. K.-Y. Jen, S. Randel, W. Freude, and C. Koos, "Silicon-organic hybrid (SOH) Mach-Zehnder modulators for 100 Gbit/s on-off keying," *Scientific Reports*, vol. 8, no. 2598, 2018.

[91] H. Zwickel, S. Wolf, C. Kieninger, Y. Kutuvantavida, M. Lauermann, T. de Keulenaer, A. Vyncke, R. Vaernewyck, J. Luo, A. K.-Y. Jen, W. Freude, J. Bauwelinck, S. Randel, and C. Koos, "Silicon-organic hybrid (SOH) modulators for intensity-modulation / direct-detection links with line rates of up to 120 Gbit/s," *Optics Express*, vol. 25, no. 20, pp. 23784–23800, 2017.

[92] W. Bogaerts, M. Fiers, and P. Dumon, "Design challenges in silicon photonics," *IEEE Journal of Selected Topics in Quantum Electronics*, vol. 20, no. 4, pp. 1–8, 2014.

[93] Aleksandr Biberman and Keren Bergman, "Optical interconnection networks for high-performance computing systems," *Reports on Progress in Physics*, vol. 75, no. 4, p. 46402, 2012.

[94] W. N. Ye and Y. Xiong, "Review of silicon photonics: History and recent advances," *Journal of Modern Optics*, vol. 60, no. 16, pp. 1299–1320, 2013.

[95] T. Baehr-Jones, T. Pinguet, P. Lo Guo-Qiang, S. Danziger, D. Prather, and M. Hochberg, "Myths and rumours of silicon photonics," *Nature Photonics*, vol. 6, no. 4, pp. 206–208, 2012.

[96] R. Soref, "The past, present, and future of silicon photonics," *IEEE Journal of Selected Topics in Quantum Electronics*, vol. 12, no. 6, pp. 1678–1687, 2006.

[97] L. Eldada and L. W. Shacklette, "Advances in polymer integrated optics," *IEEE Journal of Selected Topics in Quantum Electronics*, vol. 6, no. 1, pp. 54–68, 2000.

[98] G. C. Righini and A. Chiappini, "Glass optical waveguides: a review of fabrication techniques," *Optical Engineering*, vol. 53, no. 7, pp. 1 – 15, 2014.

[99] M. Smit, X. Leijtens, H. Ambrosius, E. Bente, J. van der Tol, B. Smalbrugge, T. de Vries, E.-J. Geluk, J. Bolk, R. van Veldhoven, L. Augustin, P. Thijs, D. D'Agostino, H. Rabbani, K. Lawniczuk, S. Stopinski, S. Tahvili, A. Corradi, E. Kleijn, D. Dzibrou, M. Felicetti, E. Bitincka, V. Moskalenko, J. Zhao, R. Santos, G. Gilardi, W. Yao, K. Williams, P. Stabile, P. Kuindersma, J. Pello, S. Bhat, Y. Jiao, D. Heiss, G. Roelkens, M. Wale, P. Firth, F. Soares, N. Grote, M. Schell, H. Debregeas, M. Achouche, J.-L. Gentner, A. Bakker, T. Korthorst, D. Gallagher, A. Dabbs, A. Melloni, F. Morichetti, D. Melati, A. Wonfor, R. Penty, R. Broeke, B. Musk, and D. Robbins, "An introduction to InP-based generic integration technology," *Semiconductor Science and Technology*, vol. 29, no. 8, p. 083001, 2014.

[100] C. P. Dietrich, A. Fiore, M. G. Thompson, M. Kamp, and S. Höfling, "GaAs integrated quantum photonics: Towards compact and multi-functional quantum photonic integrated circuits," *Laser & Photonics Reviews*, vol. 10, no. 6, pp. 870–894, 2016.

[101] B. Behroozpour, P. A. M. Sandborn, N. Quack, T.-J. Seok, Y. Matsui, M. C. Wu, and B. E. Boser, "Electronic-photonic integrated circuit for 3D microimaging," *IEEE Journal of Solid-State Circuits*, pp. 1–12, 2016.

[102] M. H. Idjadi and F. Aflatouni, "Integrated Pound-Drever-Hall laser stabilization system in silicon," *Nature Communications*, vol. 8, no. 1209, 2017.

[103] Y. Li, S. Verstuyft, G. Yurtsever, S. Keyvaninia, G. Roelkens, D. V. Thourhout, and R. Baets, "Heterodyne laser Doppler vibrometers integrated on silicon-on-insulator based on serrodyne thermo-optic frequency shifters," *Applied Optics*, vol. 52, no. 10, pp. 2145–2152, 2013.

[104] E. Ryckeboer, A. Gassenq, N. Hattasan, L. Cerutti, B. Kuyken, J.-B. Rodriguez, E. Tournie, R. Baets, and G. Roelkens, "Silicon-on-Insulator spectrometers with integrated GaInAsSb photodiode array for wideband operation from 1500 to 2300 nm," in *CLEO: 2013*, p. JW2A.69, Optical Society of America, 2013.

[105] F. Aflatouni, B. Abiri, A. Rekhi, and A. Hajimiri, "Nanophotonic coherent imager," *Optics Express*, vol. 23, no. 4, pp. 5117–5125, 2015.

[106] D. B. Cole, C. Sorace-Agaskar, M. Moresco, G. Leake, D. Coolbaugh, and M. R. Watts, "Integrated heterodyne interferometer with on-chip modulators and detectors," *Optics Letters*, vol. 40, no. 13, p. 3097, 2015.

[107] Z. Wang, B. Potsaid, L. Chen, C. Doerr, H.-C. Lee, T. Nielson, V. Jayaraman, A. E. Cable, E. Swanson, and J. G. Fujimoto, "Cubic meter volume optical coherence tomography," *Optica*, vol. 3, no. 12, pp. 1496–1503, 2016.

[108] J. Sun, E. Timurdogan, A. Yaacobi, E. S. Hosseini, and M. R. Watts, "Large-scale nanophotonic phased array," *Nature*, vol. 493, no. 7431, pp. 195–199, 2013.

[109] H. Schwenke, U. Neuschaefer-Rube, T. Pfeifer, and H. Kunzmann, "Optical methods for dimensional metrology in production engineering," *CIRP Annals - Manufacturing Technology*, vol. 51, no. 2, pp. 685–699, 2002.

[110] J.-M. Linares, J. Chaves-Jacob, H. Schwenke, A. Longstaff, S. Fletcher, J. Flore, E. Uhlmann, and J. Wintering, "Impact of measurement procedure when error mapping and compensating a small CNC machine using

a multilateration laser interferometer," *Precision Engineering*, vol. 38, no. 3, pp. 578–588, 2014.

[111] S. Ibaraki, K. Takeuchi, T. Yano, T. Takatsuji, S. Osawa, and O. Sato, "Estimation of three-dimensional volumetric errors of numerically controlled machine tools by a tracking interferometer," *Journal of Mechanics Engineering & Automation*, vol. 2011, no. Vol. 1, Issue 4, p. 313, 2011.

[112] K. Umetsu, R. Furutnani, S. Osawa, T. Takatsuji, and T. Kurosawa, "Geometric calibration of a coordinate measuring machine using a laser tracking system," *Measurement Science and Technology*, vol. 16, no. 12, pp. 2466–2472, 2005.

[113] G. Berkovic and E. Shafir, "Optical methods for distance and displacement measurements," *Advances in Optics and Photonics*, vol. 4, no. 4, pp. 441–471, 2012.

[114] P. Balling, P. Křen, P. Mašika, and S. A. van den Berg, "Femtosecond frequency comb based distance measurement in air," *Optics Express*, vol. 17, no. 11, p. 9300, 2009.

[115] K. Minoshima and H. Inaba, "Precision length metrology using fiber-based frequency combs," in *Optical Sensors*, p. STuB1, Optical Society of America, 2010.

[116] V. Ataie, P. P. Kuo, A. Wiberg, Z. Tong, C. Huynh, N. Alic, and S. Radic, "Ultrafast absolute ranging by coherent parametric comb," in *Optical Fiber Communication Conference*, p. OTh3D2, Optical Society of America, 2013.

[117] M. Cui, M. G. Zeitouny, N. Bhattacharya, S. A. van den Berg, and H. P. Urbach, "Long distance measurement with femtosecond pulses using a dispersive interferometer," *Optics Express*, vol. 19, no. 7, pp. 6549–6562, 2011.

[118] J. Lee, S. Han, K. Lee, E. Bae, S. Kim, S. Lee, S.-W. Kim, and Y.-J. Kim, "Absolute distance measurement by dual-comb interferometry with adjustable synthetic wavelength," *Measurement Science and Technology*, vol. 24, no. 4, pp. 45201–45209, 2013.

[119] S. van den Berg, S. Persijn, G. Kok, M. Zeitouny, and N. Bhattacharya, "Many-wavelength interferometry with thousands of lasers for absolute distance measurement," *Physical Review Letters*, vol. 108, no. 18, pp. 183901–183906, 2012.

[120] K.-N. Joo and S.-W. Kim, "Absolute distance measurement by dispersive interferometry using a femtosecond pulse laser," *Optics Express*, vol. 14, no. 13, pp. 5954–5960, 2006.

[121] N. R. Doloca, K. Meiners-Hagen, M. Wedde, F. Pollinger, and A. Abou-Zeid, "Absolute distance measurement system using a femtosecond laser as a modulator," *Measurement Science and Technology*, vol. 21, no. 11, pp. 115302–115309, 2010.

[122] M. U. Piracha, D. Nguyen, I. Ozdur, and P. J. Delfyett, "Simultaneous ranging and velocimetry of fast moving targets using oppositely chirped pulses from a mode-locked laser," *Optics Express*, vol. 19, no. 12, pp. 11213–11219, 2011.

[123] Q. D. Pham and Y. Hayasaki, "Optical frequency comb interference profilometry using compressive sensing," *Optics Express*, vol. 21, no. 16, pp. 19003–19011, 2013.

[124] S. Yokoyama, T. Yokoyama, Y. Hagihara, T. Araki, and T. Yasui, "A distance meter using a terahertz intermode beat in an optical frequency comb," *Optics Express*, vol. 17, no. 20, pp. 17324–17337, 2009.

[125] X. Wang, S. Takahashi, K. Takamasu, and H. Matsumoto, "Spatial positioning measurements up to 150 m using temporal coherence of optical frequency comb," *Precision Engineering*, vol. 37, no. 3, pp. 635–639, 2013.

[126] J. Lee, Y.-J. Kim, K. Lee, S. Lee, and S.-W. Kim, "Time-of-flight measurement with femtosecond light pulses," *Nature Photonics*, vol. 4, no. 10, pp. 716–720, 2010.

[127] K. Minoshima, T. Tomita, H. Nakayama, Y. Yamaoka, and H. Matsumoto, "Ultrahigh-resolution distance meter using a frequency comb of a femtosecond mode-locked laser," in *The Thirteenth International Conference on Ultrafast Phenomena*, p. TuB3, OSA, 2002.

[128] H. Zhang, X. Wu, H. Wei, and Y. Li, "Compact dual-comb absolute distance ranging with an electric reference," *IEEE Photonics Journal*, vol. 7, no. 3, pp. 1–8, 2015.

[129] M.-G. Suh and K. J. Vahala, "Soliton microcomb range measurement," *Science (New York, N.Y.)*, vol. 359, no. 6378, pp. 884–887, 2018.

[130] Y. Salvadé, N. Schuhler, S. Lévêque, and S. Le Floch, "High-accuracy absolute distance measurement using frequency comb referenced multiwavelength source," *Applied Optics*, vol. 47, no. 14, pp. 2715–2721, 2008.

[131] S. Hyun, M. Choi, B. J. Chun, S. Kim, S.-W. Kim, and Y.-J. Kim, "Frequency-comb-referenced multi-wavelength profilometry for largely stepped surfaces," *Optics Express*, vol. 21, no. 8, pp. 9780–9791, 2013.

[132] X. Wu, H. Wei, H. Zhang, L. Ren, Y. Li, and J. Zhang, "Absolute distance measurement using frequency-sweeping heterodyne interferometer calibrated by an optical frequency comb," *Applied Optics*, vol. 52, no. 10, pp. 2042–2048, 2013.

[133] E. Baumann, F. R. Giorgetta, J.- D. Deschênes, W. C. Swann, I. Coddington, and N. R. Newbury, "Comb-calibrated laser ranging for three-dimensional surface profiling with micrometer-level precision at a distance," *Optics Express*, vol. 22, no. 21, pp. 24914–24928, 2014.

[134] T. Sakamoto, T. Kawanishi, and M. Izutsu, "Asymptotic formalism for ultraflat optical frequency comb generation using a Mach-Zehnder modulator," *Optics Letters*, vol. 32, no. 11, pp. 1515–1517, 2007.

[135] C. J. Mann, P. R. Bingham, V. C. Paquit, and K. W. Tobin, "Quantitative phase imaging by three-wavelength digital holography," *Optics Express*, vol. 16, no. 13, pp. 9753–9764, 2008.

[136] G. Margheri, C. Giunti, S. Zatti, S. Manhart, and R. Maurer, "Double-wavelength superheterodyne interferometer for absolute ranging with submillimeter resolution: results obtained with a demonstration model by use of rough and reflective targets," *Applied Optics*, vol. 36, no. 25, p. 6211, 1997.

[137] P. de Groot and S. Kishner, "Synthetic wavelength stabilization for two-color laser-diode interferometry," *Applied Optics*, vol. 30, no. 28, pp. 4026–4033, 1991.

[138] C. J. Walsh, "Limit to multiwavelength interferometry imposed by frequency instability of the source," *Applied Optics*, vol. 26, no. 1, p. 29, 1987.

[139] S. Hyun, Y.-J. Kim, Y. Kim, and S.-W. Kim, "Absolute distance measurement using the frequency comb of a femtosecond laser," *CIRP Annals*, vol. 59, no. 1, pp. 555 – 558, 2010.

[140] Cisco, "Cisco global cloud index: Forecast and methodology, 2016-2021," https://www.cisco.com/c/en/us/solutions/collateral/service-provider/global-cloud-index-gci/white-paper-c11-738085.html, accessed Feb 12, 2020.

[141] M. Mitchell, J. McNicol, V. Dangui, H. Sun, K.-T. Wu, Z. Pan, M. van Leeuwen, J. Rahn, S. Grubb, R. Nagarajan, and D. Welch, "Optical integration and multi-carrier solutions for 100G and beyond," *Optical Fiber Technology*, vol. 17, no. 5, pp. 412–420, 2011.

[142] G. Bennett, K.-T. Wu, A. Malik, S. Roy, and A. Awadalla, "A review of high-speed coherent transmission technologies for long-haul DWDM transmission at 100G and beyond," *IEEE Communications Magazine*, vol. 52, no. 10, pp. 102–110, 2014.

[143] D. Thomson, F. Gardes, J.-M. Fedeli, S. Zlatanovic, Youfang Hu, B. P.-P. Kuo, E. Myslivets, N. Alic, S. Radic, G. Mashanovich, and G. Reed, "50-Gb/s silicon optical modulator," *IEEE Photonics Technology Letters*, vol. 24, no. 4, pp. 234–236, 2012.

[144] S. Cheung, T. Su, K. Okamoto, and S. J. B. Yoo, "Ultra-compact silicon photonic 512 × 512 25 GHz arrayed waveguide grating router," *IEEE Journal of Selected Topics in Quantum Electronics*, vol. 20, no. 4, pp. 310–316, 2014.

[145] J. Michel, J. Liu, and L. C. Kimerling, "High-performance Ge-on-Si photodetectors," *Nature Photonics*, vol. 4, no. 8, pp. 527–534, 2010.

[146] L. Vivien, A. Polzer, D. Marris-Morini, J. Osmond, J. M. Hartmann, P. Crozat, E. Cassan, C. Kopp, H. Zimmermann, and J. M. Fedeli, "Zero-bias 40Gbit/s germanium waveguide photodetector on silicon," *Optics Express*, vol. 20, no. 2, pp. 1096–1101, 2012.

[147] Y. de Koninck, G. Roelkens, and R. Baets, "Electrically pumped 1550 nm single mode III-V-on-silicon laser with resonant grating cavity mirrors," *Laser & Photonics Reviews*, vol. 9, no. 2, pp. L6–L10, 2015.

[148] S. Keyvaninia, G. Roelkens, D. V. Thourhout, C. Jany, M. Lamponi, A. L. Liepvre, F. Lelarge, D. Make, G.-H. Duan, D. Bordel, and J.-M. Fedeli, "Demonstration of a heterogeneously integrated III-V/SOI single wavelength tunable laser," *Optics Express*, vol. 21, no. 3, pp. 3784–3792, 2013.

[149] Z. Fang, Q. Y. Chen, and C. Z. Zhao, "A review of recent progress in lasers on silicon," *Optics & Laser Technology*, vol. 46, no. 0, pp. 103–110, 2013.

[150] T. W. Baehr-Jones and M. J. Hochberg, "Polymer silicon hybrid systems: A platform for practical nonlinear optics," *Journal of Physical Chemistry C*, vol. 112, no. 21, pp. 8085–8090, 2008.

[151] J. Leuthold, W. Freude, J.-M. Brosi, R. Baets, P. Dumon, I. Biaggio, M. L. Scimeca, F. Diederich, B. Frank, and C. Koos, "Silicon organic hybrid technology–A platform for practical nonlinear optics," *Proceedings of the IEEE*, vol. 97, no. 7, pp. 1304–1316, 2009.

[152] C. Kieninger, Y. Kutuvantavida, H. Miura, J. N. Kemal, H. Zwickel, F. Qiu, M. Lauermann, W. Freude, S. Randel, S. Yokoyama, and C. Koos, "Demonstration of long-term thermally stable silicon-organic hybrid modulators at 85 °C," *Optics Express*, vol. 26, no. 21, pp. 27955–27964, 2018.

[153] M. Lauermann, S. Wolf, W. Hartmann, R. Palmer, Y. Kutuvantavida, H. Zwickel, A. Bielik, L. Altenhain, J. Lutz, R. Schmid, T. Wahlbrink, J. Bolten, A. L. Giesecke, W. Freude, and C. Koos, "Generation of 64 GBd 4ASK signals using a silicon-organic hybrid modulator at 80 °C," *Optics Express*, vol. 24, no. 9, pp. 9389–9396, 2016.

[154] L. R. Dalton, P. A. Sullivan, and D. H. Bale, "Electric field poled organic electro-optic materials: State of the art and future prospects," *Chemical Reviews*, vol. 110, no. 1, pp. 25–55, 2010.

[155] L. R. Dalton, D. Lao, B. C. Olbricht, S. Benight, D. H. Bale, J. A. Davies, T. Ewy, S. R. Hammond, and P. A. Sullivan, "Theory-inspired development of new nonlinear optical materials and their integration into silicon photonic circuits and devices," *Optical Materials*, vol. 32, no. 6, pp. 658–668, 2010.

[156] D. L. Elder, S. J. Benight, J. Song, B. H. Robinson, and L. R. Dalton, "Matrix-assisted poling of monolithic bridge-disubstituted organic NLO chromophores," *Chemistry of Materials*, vol. 26, no. 2, pp. 872–874, 2014.

[157] T. Baehr-Jones, B. Penkov, J. Huang, P. Sullivan, J. Davies, J. Takayesu, J. Luo, T.-D. Kim, L. Dalton, A. Jen, M. Hochberg, and A. Scherer, "Nonlinear polymer-clad silicon slot waveguide modulator with a half wave voltage of 0.25V," *Applied Physics Letters*, vol. 92, no. 16, p. 163303, 2008.

[158] R. Palmer, L. Alloatti, D. Korn, P. Schindler, M. Baier, J. Bolten, T. Wahlbrink, M. Waldow, R. Dinu, W. Freude, C. Koos, and J. Leuthold, "Low power Mach-Zehnder modulator in silicon-organic hybrid technology," *IEEE Photonics Technology Letters*, vol. 25, no. 13, pp. 1226–1229, 2013.

[159] D. Meschede, *Gerthsen Physik*. Berlin: Springer Spektrum, 25. ed., 2015.

[160] M.-C. Amann, T. Bosch, M. Lescure, R. Myllyla, and M. Rioux, "Laser ranging: A critical review of usual techniques for distance measurement," *Optical Engineering*, vol. 40, no. 1, pp. 10–19, 2001.

[161] Renishaw PLC, "Xl-80 laser system, product description," http://www.renishaw.com/en/xl-80-laser-system–8268, accessed June 18, 2017.

[162] K. Meiners-Hagen, R. Schödel, F. Pollinger, and A. Abou-Zeid, "Multi-wavelength interferometry for length measurements using diode lasers," *Measurement Science Review*, vol. 9, no. 1, pp. 16–26, 2009.

[163] C. Polhemus, "Two-wavelength interferometry," *Applied Optics*, vol. 12, no. 9, p. 2071, 1973.

[164] D. Malacara and B. J. Thompson, *Handbook of optical engineering*. CRC Press, 1 ed., 2001.

[165] J. F. Nye, *Physical properties of crystals: Their representation by tensors and matrices*. Oxford: Clarendon Press, 1985.

[166] R. Palmer, "Silicon photonic modulators for low-power applications."

[167] P. Steglich, C. Mai, C. Villringer, and A. Mai, "Direct observation and simultaneous use of linear and quadratic electro-optical effects," *Journal of Physics D: Applied Physics*, vol. 53, no. 12, p. 125106, 2020.

[168] A. Cuyt, *Handbook of continued fractions for special functions*. [Dordrecht, Netherlands]: Springer, 2008.

[169] M. Abramowitz and I. Stegun, eds., *Handbook of mathematical functions: With formulas, graphs, and mathematical tables*. Dover books on advanced mathematics, New York NY: Dover Publ, 10. ed., 1972.

[170] C. O'Riordan, S. Fabbri, and A. Ellis, "Variable optical frequency comb source using a dual parallel Mach-Zehnder modulator," in *Transparent Optical Networks (ICTON), 2011 13th International Conference on*, pp. 1–4, 2011.

[171] Q. Wang, L. Huo, Y. Xing, and B. Zhou, "Ultra-flat optical frequency comb generator using a single-driven dual-parallel Mach-Zehnder modulator," *Optics Letters*, vol. 39, no. 10, pp. 3050–3053, 2014.

[172] Y. Dou, H. Zhang, and M. Yao, "Generation of flat optical-frequency comb using cascaded intensity and phase modulators," *IEEE Photonics Technology Letters*, vol. 24, no. 9, pp. 727–729, 2012.

[173] S. Fabbri, S. Sygletos, and A. Ellis, "Multi-harmonic optical comb generation," in *European Conference and Exhibition on Optical Communication*, OSA technical digest (online), (Washington, DC), p. Mo.2.A.2, OSA The Optical Society, 2012.

[174] S. Le Floch, M. Llera, and Y. Salvade, "Sub ppm absolute distance measurements using an optical frequency comb generated by a conventional

dual-drive Mach-Zehnder modulator," in *Optical measurement systems for industrial inspection VII, Proc. of SPIE Vol. 8082, 80823S*, SPIE, 2011.

[175] M. Godbout, J.-D. Deschênes, and J. Genest, "Spectrally resolved laser ranging with frequency combs," *Optics Express*, vol. 18, no. 15, p. 15981, 2010.

[176] R. Yang, F. Pollinger, K. Meiners-Hagen, J. Tan, and H. Bosse, "Heterodyne multi-wavelength absolute interferometry based on a cavity-enhanced electro-optic frequency comb pair," *Optics Letters*, vol. 39, no. 20, pp. 5834–5837, 2014.

[177] H. Wu, T. Zhao, Z. Wang, K. Zhang, B. Xue, J. Li, M. He, and X. Qu, "Long distance measurement up to 1.2km by electro-optic dual-comb interferometry," *Applied Physics Letters*, vol. 111, no. 25, p. 251901, 2017.

[178] H. Hofler, C. Baulig, A. Blug, M. Dambacher, N. Dimopoulos, H. Wolfelschneider, W. Osten, C. Gorecki, and E. L. Novak, "Optical high-speed 3D metrology in harsh environments: Recording structural data of railway lines," in *Proceedings Volume 5856, Optical Measurement Systems for Industrial Inspection IV*, vol. 5856, pp. 296–306, SPIE, 2005.

[179] R. Noe, H. Rodler, A. Ebberg, G. Gaukel, B. Noll, J. Wittmann, and F. Auracher, "Comparison of polarization handling methods in coherent optical systems," *Journal of Lightwave Technology*, vol. 9, no. 10, pp. 1353–1366, 1991.

[180] C. E. Towers, D. P. Towers, D. T. Reid, W. N. MacPherson, R. R. J. Maier, and J. D. C. Jones, "Fiber interferometer for simultaneous multiwavelength phase measurementwith a broadband femtosecond laser," *Optics Letters*, vol. 29, no. 23, pp. 2722–2724, 2004.

[181] S. Chang, C.-C. Hsu, T.-H. Huang, W.-C. Chuang, Y.-S. Tsai, J.-Y. Shieh, C.-Y. Leung, *et al.*, "Heterodyne interferometric measurement of the thermo-optic coefficient of single mode fiber," *Chinese Journal of Physics*, vol. 38, pp. 437–442, 2000.

[182] R. E. Bartolo, A. B. Tveten, and A. Dandridge, "Thermal phase noise measurements in optical fiber interferometers," *IEEE Journal of Quantum Electronics*, vol. 48, no. 5, pp. 720–727, 2012.

[183] A.K. Melikov, U. Krüger, G. Zhou, T.L. Madsen, and G. Langkilde, "Air temperature fluctuations in rooms," *Building and Environment*, vol. 32, no. 2, pp. 101–114, 1997.

[184] Corning, "SMF-28e+ Optical Fiber, product information," http://www.corning.com/WorkArea/showcontent.aspx?id=63939, 2014, accessed March 12, 2015.

[185] C. E. Lee, J. J. Alcoz, Y. Yeh, W. N. Gibler, R. A. Atkins, and H. F. Taylor, "Optical fiber Fabry-Perot sensors for smart structures," *Smart Materials and Structures*, vol. 1, no. 2, pp. 123–127, 1992.

[186] P.-E. Dupouy, M. Büchner, P. Paquier, G. Trénec, and J. Vigué, "Interferometric measurement of the temperature dependence of an index of refraction: application to fused silica," *Applied Optics*, vol. 49, no. 4, pp. 678–682, 2010.

[187] D. B. Leviton and B. J. Frey, "Temperature-dependent absolute refractive index measurements of synthetic fused silica," *ArXiv e-prints*, no. 0805.0091, p. 0805.0091, 2008.

[188] C. Koos, C. Weimann, and J. Leuthold, "Multiscale distance measurement with frequency combs," U.S. Patent 9 976 843 (B2), May 2, 2018.

[189] S. Yun, G. Tearney, J. de Boer, N. Iftimia, and B. Bouma, "High-speed optical frequency-domain imaging," *Optics Express*, vol. 11, no. 22, pp. 2953–2963, 2003.

[190] J. Ronnau, S. Haimov, and S. P. Gogineni, "The effect of signal–to–noise ratio on phase measurements with polarimetric radars," *Remote Sensing Reviews*, vol. 9, no. 1-2, pp. 27–37, 1994.

[191] T. G. McRae, M. T. L. Hsu, C. H. Freund, D. A. Shaddock, J. Herrmann, and M. B. Gray, "Linearization and minimization of cyclic error with heterodyne laser interferometry," *Optics Letters*, vol. 37, no. 13, pp. 2448–2450, 2012.

[192] L. S. Schuetz, J. H. Cole, J. Jarzynski, N. Lagakos, and J. A. Bucaro, "Dynamic thermal response of single-mode optical fiber for interferometric sensors," *Applied Optics*, vol. 22, no. 3, pp. 478–483, 1983.

[193] P. R. Bevington and D. K. Robinson, *Data reduction and error analysis for the physical sciences*. Boston: McGraw-Hill, 3 ed., ©2003.

[194] U. Vry, "Absolute statistical error in two-wavelength rough-surface interferometry (ROSI)," *Optica Acta: International Journal of Optics*, vol. 33, no. 10, pp. 1221–1225, 1986.

[195] P. Pavliček and J. Soubusta, "Theoretical measurement uncertainty of white-light interferometry on rough surfaces," *Applied Optics*, vol. 42, no. 10, pp. 1809–1813, 2003.

[196] Carl Zeiss Industrielle Messtechnik GmbH, "O-INSPECT: Multisensor-Messgeräte, product description," http://www.zeiss.de/industrial-metrology/de_de/produkte/brochures.html?catalog=O-INSPECT_322, 2013, accessed March 12, 2015.

[197] *KMG angewendet für Längenmessungen: (ISO 10360-2:2009)*, vol. 2. Berlin: Beuth, 2010.

[198] N. Senin, R. Groppetti, L. Garofano, P. Fratini, and M. Pierni, "Three-dimensional surface topography acquisition and analysis for firearm identification," *Journal of Forensic Sciences*, vol. 51, no. 2, pp. 282–295, 2006.

[199] U. Sakarya, U. M. Leloğlu, and E. Tunalı, "Three-dimensional surface reconstruction for cartridge cases using photometric stereo," *Forensic Science International*, vol. 175, no. 2–3, pp. 209–217, 2008.

[200] Z. J. Geradts, J. Bijhold, R. Hermsen, and F. Murtagh, "Image matching algorithms for breech face marks and firing pins in a database of spent cartridge cases of firearms," *Forensic Science International*, vol. 119, no. 1, pp. 97–106, 2001.

[201] N. R. Newbury, I. Coddington, and W. Swann, "Sensitivity of coherent dual-comb spectroscopy," *Optics Express*, vol. 18, no. 8, pp. 7929–7945, 2010.

[202] S. O. Rice, "Mathematical analysis of random noise," *Bell System Technical Journal*, vol. 23, no. 3, pp. 282–332, 1944.

[203] T. Baehr-Jones, R. Ding, A. Ayazi, T. Pinguet, M. Streshinsky, N. Harris, J. Li, L. He, M. Gould, and Y. Zhang, "A 25 Gb/s silicon photonics platform," *arXiv preprint arXiv:1203.0767*, 2012.

[204] A. Novack, M. Streshinsky, R. Ding, Y. Liu, A. E.-J. Lim, G.-Q. Lo, T. Baehr-Jones, and M. Hochberg, "Progress in silicon platforms for integrated optics," *Nanophotonics*, vol. 3, no. 4-5, 2014.

[205] EuroPractice IC service, "imec-ePIXfab SiPhotonics ISIPP50G, PDK description," http://www.europractice-ic.com/SiPhotonics_technology_imec_ISIPP50G.php, accessed May 30, 2017.

[206] W. Bogaerts and S. K. Selvaraja, "Compact single-mode silicon hybrid rib/strip waveguide with adiabatic bends," *IEEE Photonics Journal*, vol. 3, no. 3, pp. 422–432, 2011.

[207] Y. Li, D. Vermeulen, Y. de Koninck, G. Yurtsever, G. Roelkens, and R. Baets, "Compact grating couplers on silicon-on-insulator with reduced backreflection," *Optics Letters*, vol. 37, no. 21, pp. 4356–4358, 2012.

[208] G. Roelkens, D. van Thourhout, and R. Baets, "High efficiency Silicon-on-Insulator grating coupler based on a poly-Silicon overlay," *Optics Express*, vol. 14, no. 24, p. 11622, 2006.

[209] F. van Laere, T. Claes, J. Schrauwen, S. Scheerlinck, W. Bogaerts, D. Taillaert, L. O'Faolain, D. van Thourhout, and R. Baets, "Compact focusing grating couplers for Silicon-on-Insulator integrated circuits," *IEEE Photonics Technology Letters*, vol. 19, no. 23, pp. 1919–1921, 2007.

[210] K. Yvind and J. M. Hvam, "High-efficiency, large-bandwidth silicon-on-insulator grating coupler based on a fully-etched photonic crystal structure," *Applied Physics Letters*, vol. 96, no. 5, p. 051126, 2010.

[211] EuroPractice IC service, "imec-ePIXfab SiPhotonics ISIPP25G, PDK description," http://www.europractice-

ic.com/SiPhotonics_technology_imec_ISIPP25G.php, accessed May 31, 2017.

[212] J. Leuthold and C. H. Joyner, "Multimode interference couplers with tunable power splitting ratios," *Journal of Lightwave Technology*, vol. 19, no. 5, p. 700, 2001.

[213] H. F. Talbot, "LXXVI. Facts relating to optical science. No. IV," *Philosophical Magazine Series 3*, vol. 9, no. 56, pp. 401–407, 1836.

[214] O. Bryngdahl, "Image formation using self-imaging techniques*," *Journal of the Optical Society of America*, vol. 63, no. 4, p. 416, 1973.

[215] R. Ulrich, "Image formation by phase coincidences in optical waveguides," *Optics Communications*, vol. 13, no. 3, pp. 259–264, 1975.

[216] L. B. Soldano and E. Pennings, "Optical multi-mode interference devices based on self-imaging: Principles and applications," *Journal of Lightwave Technology*, vol. 13, no. 4, pp. 615–627, 1995.

[217] M. Rajarajan, B. Rahman, and K. Grattan, "A rigorous comparison of the performance of directional couplers with multimode interference devices," *Journal of Lightwave Technology*, vol. 17, no. 2, pp. 243–248, 1999.

[218] M. Bachmann, P. A. Besse, and H. Melchior, "General self-imaging properties in N x N multimode interference couplers including phase relations," *Applied Optics*, vol. 33, no. 18, pp. 3905–3911, 1994.

[219] Y. Kang, H.-D. Liu, M. Morse, M. J. Paniccia, M. Zadka, S. Litski, G. Sarid, A. Pauchard, Y.-H. Kuo, H.-W. Chen, W. S. Zaoui, J. E. Bowers, A. Beling, D. C. McIntosh, X. Zheng, and J. C. Campbell, "Monolithic germanium/silicon avalanche photodiodes with 340 GHz gain–bandwidth product," *Nature Photonics*, vol. 3, no. 1, pp. 59–63, 2008.

[220] X. Sun, J. Liu, L. C. Kimerling, and J. Michel, "Room-temperature direct bandgap electroluminesence from Ge-on-Si light-emitting diodes," *Optics Letters*, vol. 34, no. 8, p. 1198, 2009.

[221] G. T. Reed, G. Mashanovich, F. Y. Gardes, and D. J. Thomson, "Silicon optical modulators," *Nature Photonics*, vol. 4, no. 8, pp. 518–526, 2010.

[222] L. Liao, A. Liu, J. Basak, H. Nguyen, M. Paniccia, D. Rubin, Y. Chetrit, R. Cohen, and N. Izhaky, "40 Gbit/s silicon optical modulator for high-speed applications," *Electronics Letters*, vol. 43, no. 22, pp. –, 2007.

[223] P. Dong, S. Liao, D. Feng, H. Liang, D. Zheng, R. Shafiiha, C.-C. Kung, W. Qian, G. Li, X. Zheng, A. V. Krishnamoorthy, and M. Asghari, "Low Vpp, ultralow-energy, compact, high-speed silicon electro-optic modulator," *Optics Express*, vol. 17, no. 25, pp. 22484–22490, 2009.

[224] M. Watts, W. Zortman, D. Trotter, R. Young, and A. Lentine, "Low-voltage, compact, depletion-mode, silicon Mach-Zehnder modulator," *IEEE Journal of Selected Topics in Quantum Electronics*, vol. 16, no. 1, pp. 159–164, 2010.

[225] R. Soref and B. Bennett, "Electrooptical effects in silicon," *IEEE Journal of Quantum Electronics*, vol. 23, no. 1, pp. 123–129, 1987.

[226] W. M. Green, M. J. Rooks, L. Sekaric, and Y. A. Vlasov, "Ultra-compact, low RF power, 10 Gb/s silicon Mach-Zehnder modulator," *Optics Express*, vol. 15, no. 25, pp. 17106–17113, 2007.

[227] G.-R. Zhou, M. W. Geis, S. J. Spector, F. Gan, M. E. Grein, R. T. Schulein, J. S. Orcutt, J. U. Yoon, D. M. Lennon, T. M. Lyszczarz, E. P. Ippen, and F. X. Kärtner, "Effect of carrier lifetime on forward-biased silicon Mach-Zehnder modulators," *Optics Express*, vol. 16, no. 8, p. 5218, 2008.

[228] P. Dong, C. Xie, L. L. Buhl, Y.-K. Chen, J. H. Sinsky, and G. Raybon, "Silicon in-phase/quadrature modulator with on-chip optical equalizer," *Journal of Lightwave Technology*, vol. 33, no. 6, pp. 1191–1196, 2015.

[229] T. Chu, H. Yamada, S. Ishida, and Y. Arakawa, "Compact $1 \times N$ thermo-optic switches based on silicon photonic wire waveguides," *Optics Express*, vol. 13, no. 25, p. 10109, 2005.

[230] N. C. Harris, Y. Ma, J. Mower, T. Baehr-Jones, D. Englund, M. Hochberg, and C. Galland, "Efficient, compact and low loss thermo-optic phase shifter in silicon," *Optics Express*, vol. 22, no. 9, pp. 10487–10493, 2014.

[231] C. V. Poulton, D. B. Cole, A. Yaacobi, and M. R. Watts, "Frequency-modulated continuous-wave LIDAR module in silicon photonics," in *2016 Optical Fiber Communications Conference and Exhibition (OFC)*, (Piscataway, NJ), p. W4E.3, IEEE, 2016.

[232] G. Ulbers, "A sensor for dimensional metrology with an interferometer using integrated optics technology," *Measurement*, vol. 9, no. 1, pp. 13–16, 1991.

[233] T. Oka, H. Nakajima, M. Tsugai, U. Hollenbach, U. Wallrabe, and J. Mohr, "Development of a micro-optical distance sensor," *Sensors and Actuators A: Physical*, no. 3, pp. 261–267, 2003.

[234] M. Hochberg and T. Baehr-Jones, "Towards fabless silicon photonics," *Nature Photonics*, vol. 4, no. 8, pp. 492–494, 2010.

[235] M. Hochberg, N. C. Harris, Ran Ding, Yi Zhang, A. Novack, Zhe Xuan, and T. Baehr-Jones, "Silicon photonics: The next fabless semiconductor industry," *IEEE Solid-State Circuits Magazine*, vol. 5, no. 1, pp. 48–58, 2013.

[236] D. Hofstetter, H. P. Zappe, and R. Dandliker, "Optical displacement measurement with GaAs/AlGaAs-based monolithically integrated Michelson interferometers," *Journal of Lightwave Technology*, vol. 15, no. 4, pp. 663–670, 1997.

[237] A. Rubiyanto, H. Herrmann, R. Ricken, F. Tian, and W. Sohler, "Integrated optical heterodyne interferometer in lithium niobate," *Journal of Nonlinear Optical Physics & Materials*, vol. 10, no. 02, pp. 163–168, 2001.

[238] H. Toda, M. Haruna, and H. Nishihara, "Integrated-optic heterodyne interferometer for displacement measurement," *Journal of Lightwave Technology*, vol. 9, no. 5, pp. 683–687, 1991.

[239] Y. Li and R. Baets, "Homodyne laser Doppler vibrometer on silicon-on-insulator with integrated 90 degree optical hybrids," *Optics Express*, vol. 21, no. 11, pp. 13342–13350, 2013.

[240] D. Ganin, P. Trocha, M. Pfeiffer, M. Karpov, A. Kordts, J. Krockenberger, P. Marin-Palomo, S. Wolf, S. Randel, W. Freude, T. J. Kip-

penberg, and C. Koos, "Ultrafast dual-comb distance metrology using dissipative kerr solitons," in *CLEO: Applications and Technology*, OSA technical digest (online), (Washington, D.C., USA), p. STh4L.6, OSA - The Optical Society, 2017.

[241] D. Vermeulen, Y. D. Koninck, Y. Li, E. Lambert, W. Bogaerts, R. Baets, and G. Roelkens, "Reflectionless grating couplers for Silicon-on-Insulator photonic integrated circuits," *Optics Express*, vol. 20, no. 20, pp. 22278–22283, 2012.

[242] E. Baumann, J.-D. Deschênes, F. R. Giorgetta, W. C. Swann, I. Coddington, and N. R. Newbury, "Speckle phase noise in coherent laser ranging: fundamental precision limitations," *Optics Letters*, vol. 39, no. 16, pp. 4776–4779, 2014.

[243] N. Lindenmann, G. Balthasar, D. Hillerkuss, R. Schmogrow, M. Jordan, J. Leuthold, W. Freude, and C. Koos, "Photonic wire bonding: A novel concept for chip-scale interconnects," *Optics Express*, vol. 20, no. 16, pp. 17667–17677, 2012.

[244] M. R. Billah, T. Hoose, T. Onanuga, N. Lindenmann, P. Dietrich, T. Wingert, M. L. Goedecke, A. Hofmann, U. Troppenz, A. Sigmund, M. Möhrle, W. Freude, and C. Koos, "Multi-chip integration of lasers and silicon photonics by photonic wire bonding," in *CLEO: 2015*, p. STu2F.2, Optical Society of America, 2015.

[245] N. Lindenmann, S. Dottermusch, M. L. Goedecke, T. Hoose, M. R. Billah, T. P. Onanuga, A. Hofmann, W. Freude, and C. Koos, "Connecting silicon photonic circuits to multicore fibers by photonic wire bonding," *Journal of Lightwave Technology*, vol. 33, no. 4, pp. 755–760, 2015.

[246] J. Valls, M. Kuhlmann, and K. Parhi, "Evaluation of CORDIC Algorithms for FPGA Design," *Journal of VLSI signal processing systems for signal, image and video technology*, vol. 32, no. 3, pp. 207–222, 2002.

[247] J. E. Volder, "The CORDIC trigonometric computing technique," *IEEE Transactions on Electronic Computers*, vol. 8, no. 3, pp. 330–334, 1959.

[248] E. Cuche, P. Marquet, and C. Depeursinge, "Simultaneous amplitude-contrast and quantitative phase-contrast microscopy by numerical re-

construction of Fresnel off-axis holograms," *Applied Optics*, vol. 38, no. 34, pp. 6994–7001, 1999.

[249] M. Schnell, P. S. Carney, and R. Hillenbrand, "Synthetic optical holography for rapid nanoimaging," *Nature Communications*, vol. 5, 2014.

[250] A. Wada, M. Kato, and Y. Ishii, "Large step-height measurements using multiple-wavelength holographic interferometry with tunable laser diodes," *Journal of the Optical Society of America A*, vol. 25, no. 12, pp. 3013–3020, 2008.

[251] J. Goodman, "Statistical properties of laser speckle patterns," in *Laser Speckle and Related Phenomena*, vol. 9 of *Topics in Applied Physics*, pp. 9–75, Springer Berlin Heidelberg, 1975.

[252] A. F. Fercher, H. Z. Hu, and U. Vry, "Rough surface interferometry with a two-wavelength heterodyne speckle interferometer," *Applied Optics*, vol. 24, no. 14, pp. 2181–2188, 1985.

[253] U. Vry, "Calculation of complex correlation coefficients of two speckle fields of different wavelengths and their application to two-wavelength-measurement techniques," *Journal of the Optical Society of America A*, vol. 5, no. 1, pp. 114–125, 1988.

[254] J. Kühn, T. Colomb, F. Montfort, F. Charrière, Y. Emery, E. Cuche, P. Marquet, and C. Depeursinge, "Real-time dual-wavelength digital holographic microscopy with a single hologram acquisition," *Optics Express*, vol. 15, no. 12, pp. 7231–7242, 2007.

[255] D. Carl, M. Fratz, M. Pfeifer, D. M. Giel, and H. Höfler, "Multi-wavelength digital holography with autocalibration of phase shifts and artificial wavelengths," *Applied Optics*, vol. 48, no. 34, pp. H1–H8, 2009.

[256] M. Kourogi, K. Nakagawa, and M. Ohtsu, "Wide-span optical frequency comb generator for accurate optical frequency difference measurement," *IEEE Journal of Quantum Electronics*, vol. 29, no. 10, pp. 2693–2701, 1993.

[257] H. E. Mats G. Lofdahl, "Algorithm for resolving 2pi ambiguities in interferometric measurements by use of multiple wavelengths," *Optical Engineering*, vol. 40, no. 6, pp. 984 – 990 – 7, 2001.

[258] L. R. Dalton, P. Günter, M. Jazbinsek, O.-P. Kwon, and P. A. Sullivan, *Organic electro-optics and photonics: Molecules, polymers, and crystals*. Cambridge: Cambridge University Press, 2015.

[259] R. Palmer, S. Koeber, M. Woessner, D. L. Elder, W. Heni, D. Korn, H. Yu, M. Lauermann, W. Bogaerts, L. R. Dalton, W. Freude, J. Leuthold, and C. Koos, "High-speed silicon-organic hybrid (SOH) modulators with 230 pm/V electro-optic coefficient using advanced materials," in *Optical Fiber Communication Conference*, OSA technical digest (online), (Washington, DC), p. M3G.4, OSA The Optical Society, 2014.

[260] Y. V. Pereverzev, K. N. Gunnerson, O. V. Prezhdo, P. A. Sullivan, Y. Liao, B. C. Olbricht, A. J. P. Akelaitis, A. K.-Y. Jen, and L. R. Dalton, "Guest-host cooperativity in organic materials greatly enhances the nonlinear optical response," *The Journal of Physical Chemistry C*, vol. 112, no. 11, pp. 4355–4363, 2008.

[261] P. A. Sullivan and L. R. Dalton, "Theory-inspired development of organic electro-optic materials," *Accounts of chemical research*, vol. 43, no. 1, pp. 10–18, 2010.

[262] S. J. Benight, L. E. Johnson, R. Barnes, B. C. Olbricht, D. H. Bale, P. J. Reid, B. E. Eichinger, L. R. Dalton, P. A. Sullivan, and B. H. Robinson, "Reduced dimensionality in organic electro-optic materials: Theory and defined order," *The journal of physical chemistry. B*, vol. 114, no. 37, pp. 11949–11956, 2010.

[263] J. Luo, M. Haller, H. Li, T.-D. Kim, and A.-Y. Jen, "Highly efficient and thermally stable electro-optic polymer from a smartly controlled crosslinking process," *Advanced Materials*, vol. 15, no. 19, pp. 1635–1638, 2003.

[264] M. Haller, J. Luo, H. Li, T.-D. Kim, Y. Liao, B. H. Robinson, L. R. Dalton, and A. K.-Y. Jen, "A novel lattice-hardening process

to achieve highly efficient and thermally stable nonlinear optical polymers," *Macromolecules*, vol. 37, no. 3, pp. 688–690, 2004.

[265] J. H. Wülbern, S. Prorok, J. Hampe, A. Petrov, M. Eich, J. Luo, A. K.-Y. Jen, M. Jenett, and A. Jacob, "40 GHz electro-optic modulation in hybrid silicon–organic slotted photonic crystal waveguides," *Optics Letters*, vol. 35, no. 16, pp. 2753–2755, 2010.

[266] L. Alloatti, D. Korn, R. Palmer, D. Hillerkuss, J. Li, A. Barklund, R. Dinu, J. Wieland, M. Fournier, J. Fedeli, H. Yu, W. Bogaerts, P. Dumon, R. Baets, C. Koos, W. Freude, and J. Leuthold, "42.7 Gbit/s electro-optic modulator in silicon technology," *Optics Express*, vol. 19, no. 12, p. 11841, 2011.

[267] S. Wolf, H. Zwickel, C. Kieninger, M. Lauermann, W. Hartmann, Y. Kutuvantavida, W. Freude, S. Randel, and C. Koos, "Coherent modulation up to 100 GBd 16QAM using silicon-organic hybrid (SOH) devices," *Optics Express*, vol. 26, no. 1, pp. 220–232, 2018.

[268] M. Lauermann, S. Wolf, P. C. Schindler, R. Palmer, S. Koeber, D. Korn, L. Alloatti, T. Wahlbrink, J. Bolten, M. Waldow, M. Koenigsmann, M. Kohler, D. Malsam, D. L. Elder, P. V. Johnston, N. Phillips-Sylvain, P. A. Sullivan, L. R. Dalton, J. Leuthold, W. Freude, and C. Koos, "40 GBd 16QAM signaling at 160 Gb/s in a Silicon-Organic Hybrid modulator," *Journal of Lightwave Technology*, vol. 33, no. 6, pp. 1210–1216, 2015.

[269] M. Lauermann, R. Palmer, S. Koeber, P. C. Schindler, D. Korn, T. Wahlbrink, J. Bolten, M. Waldow, D. L. Elder, L. R. Dalton, J. Leuthold, W. Freude, and C. Koos, "Low-power silicon-organic hybrid (SOH) modulators for advanced modulation formats," *Optics Express*, vol. 22, no. 24, pp. 29927–29936, 2014.

[270] S. Wolf, M. Lauermann, P. Schindler, G. Ronniger, K. Geistert, R. Palmer, S. Köber, W. Bogaerts, J. Leuthold, W. Freude, and C. Koos, "DAC-less amplifier-less generation and transmission of QAM signals using sub-volt Silicon-Organic Hybrid modulators," *Journal of Lightwave Technology*, vol. 33, no. 7, pp. 1425–1432, 2015.

[271] B. P.-P. Kuo, E. Myslivets, V. Ataie, E. G. Temprana, N. Alic, and S. Radic, "Wideband parametric frequency comb as coherent optical carrier," *Journal of Lightwave Technology*, vol. 31, no. 21, pp. 3414–3419, 2013.

[272] Z. Tong, A. O. J. Wiberg, E. Myslivets, B. P. P. Kuo, N. Alic, and S. Radic, "Broadband parametric multicasting via four-mode phase-sensitive interaction," *Optics Express*, vol. 20, no. 17, pp. 19363–19373, 2012.

[273] W. Liang, D. Eliyahu, V. S. Ilchenko, A. A. Savchenkov, A. B. Matsko, D. Seidel, and L. Maleki, "High spectral purity Kerr frequency comb radio frequency photonic oscillator," *Nature Communications*, vol. 6, p. 7957, 2015.

[274] I. S. Grudinin, N. Yu, and L. Maleki, "Generation of optical frequency combs with a CaF_2 resonator," *Optics Letters*, vol. 34, no. 7, p. 878, 2009.

[275] W. Liang, A. A. Savchenkov, A. B. Matsko, V. S. Ilchenko, D. Seidel, and L. Maleki, "Generation of near-infrared frequency combs from a MgF_2 whispering gallery mode resonator," *Optics Letters*, vol. 36, no. 12, pp. 2290–2292, 2011.

[276] B. J. M. Hausmann, I. Bulu, V. Venkataraman, P. Deotare, and M. Lončar, "Diamond nonlinear photonics," *Nature Photonics*, vol. 8, no. 5, pp. 369–374, 2014.

[277] J. S. Levy, A. Gondarenko, M. A. Foster, A. C. Turner-Foster, A. L. Gaeta, and M. Lipson, "CMOS-compatible multiple-wavelength oscillator for on-chip optical interconnects," *Nature Photonics*, vol. 4, no. 1, pp. 37–40, 2009.

[278] F. Ferdous, H. Miao, D. E. Leaird, K. Srinivasan, J. Wang, L. Chen, L. T. Varghese, and A. M. Weiner, "Spectral line-by-line pulse shaping of on-chip microresonator frequency combs," *Nature Photonics*, vol. 5, no. 12, pp. 770–776, 2011.

[279] D. J. Moss, R. Morandotti, A. L. Gaeta, and M. Lipson, "New CMOS-compatible platforms based on silicon nitride and Hydex for nonlinear optics," *Nature Photonics*, vol. 7, no. 8, pp. 597–607, 2013.

[280] M. Pu, L. Ottaviano, E. Semenova, and K. Yvind, "Efficient frequency comb generation in AlGaAs-on-insulator," *Optica*, vol. 3, no. 8, pp. 823–826, 2016.

[281] Y. K. Chembo, "Kerr optical frequency combs: Theory, applications and perspectives," *Nanophotonics*, vol. 5, no. 2, 2016.

[282] P. Del'Haye, T. Herr, E. Gavartin, M. L. Gorodetsky, R. Holzwarth, and T. J. Kippenberg, "Octave spanning tunable frequency comb from a microresonator," *Physical Review Letters*, vol. 107, no. 6, p. 63901, 2011.

[283] T. Herr, K. Hartinger, J. Riemensberger, C. Y. Wang, E. Gavartin, R. Holzwarth, M. L. Gorodetsky, and T. J. Kippenberg, "Universal formation dynamics and noise of Kerr-frequency combs in microresonators," *Nature Photonics*, vol. 6, no. 7, pp. 480–487, 2012.

[284] T. Herr, V. Brasch, J. D. Jost, I. Mirgorodskiy, G. Lihachev, M. L. Gorodetsky, and T. J. Kippenberg, "Mode spectrum and temporal soliton formation in optical microresonators," *Physical Review Letters*, vol. 113, no. 12, p. 123901, 2014.

[285] A. Kordts, M. H. P. Pfeiffer, H. Guo, V. Brasch, and T. J. Kippenberg, "Higher order mode suppression in high-Q anomalous dispersion SiN microresonators for temporal dissipative Kerr soliton formation," *Optics Letters*, vol. 41, no. 3, pp. 452–455, 2016.

[286] T. Herr, V. Brasch, J. D. Jost, C. Y. Wang, N. M. Kondratiev, M. L. Gorodetsky, and T. J. Kippenberg, "Temporal solitons in optical microresonators," *Nature Photonics*, vol. 8, no. 2, pp. 145–152, 2013.

[287] R. Rosales, K. Merghem, A. Martinez, A. Akrout, J.-P. Tourrenc, A. Accard, F. Lelarge, and A. Ramdane, "InAs/InP quantum-dot passively mode-locked lasers for 1.55 – μm applications," *IEEE Journal of Selected Topics in Quantum Electronics*, vol. 17, no. 5, pp. 1292–1301, 2011.

[288] R. Rosales, S. G. Murdoch, R. T. Watts, K. Merghem, A. Martinez, F. Lelarge, A. Accard, L. P. Barry, and A. Ramdane, "High performance mode locking characteristics of single section quantum dash lasers," *Optics Express*, vol. 20, no. 8, pp. 8649–8657, 2012.

[289] F. Lelarge, B. Dagens, J. Renaudier, R. Brenot, A. Accard, F. van Dijk, D. Make, O. Le Gouezigou, J.-G. Provost, F. Poingt, J. Landreau, O. Drisse, E. Derouin, B. Rousseau, F. Pommereau, and G.-H. Duan, "Recent advances on InAs/InP quantum dash based semiconductor lasers and optical amplifiers operating at 1.55 μm," *IEEE Journal of Selected Topics in Quantum Electronics*, vol. 13, no. 1, pp. 111–124, 2007.

[290] S. Joshi, C. Calò, N. Chimot, M. Radziunas, R. Arkhipov, S. Barbet, A. Accard, A. Ramdane, and F. Lelarge, "Quantum dash based single section mode locked lasers for photonic integrated circuits," *Optics Express*, vol. 22, no. 9, pp. 11254–11266, 2014.

[291] J. Mueller, J. Hauck, B. Shen, S. Romero-Garcia, E. Islamova, S. S. Azadeh, S. Joshi, N. Chimot, A. Moscoso-Martir, F. Merget, F. Lelarge, and J. Witzens, "Silicon photonics WDM transmitter with single section semiconductor mode-locked laser," *Advanced Optical Technologies*, vol. 4, no. 2, 2015.

[292] V. Vujicic, C. Calo, R. Watts, F. Lelarge, C. Browning, K. Merghem, A. Martinez, A. Ramdane, and L. P. Barry, "Quantum dash mode-locked lasers for data centre applications," *IEEE Journal of Selected Topics in Quantum Electronics*, vol. 21, no. 6, pp. 53–60, 2015.

[293] S. Uvin, S. Keyvaninia, F. Lelarge, G.-H. Duan, B. Kuyken, and G. Roelkens, "Narrow line width frequency comb source based on an injection-locked III-V-on-silicon mode-locked laser," *Optics Express*, vol. 24, no. 5, p. 5277, 2016.

[294] A. Gubenko, I. Krestnikov, D. Livshtis, S. Mikhrin, A. Kovsh, L. West, C. Bornholdt, N. Grote, and A. Zhukov, "Error-free 10 Gbit/s transmission using individual Fabry-Perot modes of low-noise quantum-dot laser," *Electronics Letters*, vol. 43, no. 25, p. 1430, 2007.

[295] M. J. Strain, P. M. Stolarz, and M. Sorel, "Passively mode-locked lasers with integrated chirped bragg grating reflectors," *IEEE Journal of Quantum Electronics*, vol. 47, no. 4, pp. 492–499, 2011.

[296] P. M. Anandarajah, R. Maher, Y. Q. Xu, S. Latkowski, J. O'Carroll, S. G. Murdoch, R. Phelan, J. O'Gorman, and L. P. Barry, "Generation

of coherent multicarrier signals by gain switching of discrete mode lasers," *IEEE Photonics Journal*, vol. 3, no. 1, pp. 112–122, 2011.

[297] R. Zhou, S. Latkowski, J. O'Carroll, R. Phelan, L. P. Barry, and P. Anandarajah, "40nm wavelength tunable gain-switched optical comb source," *Optics Express*, vol. 19, no. 26, pp. B415–B420, 2011.

[298] C. Gordón, R. Guzmán, X. Leijtens, and G. Carpintero, "On-chip mode-locked laser diode structure using multimode interference reflectors," *Photonics Research*, vol. 3, no. 1, p. 15, 2015.

[299] Y. Cheng, X. Luo, J. Song, T.-Y. Liow, G.-Q. Lo, Y. Cao, X. Hu, X. Li, P. H. Lim, and Q. J. Wang, "Passively mode-locked III-V/silicon laser with continuous-wave optical injection," *Optics Express*, vol. 23, no. 5, pp. 6392–6399, 2015.

[300] H. Yang, D. Zhao, S. Chuwongin, J.-H. Seo, W. Yang, Y. Shuai, J. Berggren, M. Hammar, Z. Ma, and W. Zhou, "Transfer-printed stacked nanomembrane lasers on silicon," *Nature Photonics*, vol. 6, no. 9, pp. 617–622, 2012.

[301] H. Liu, T. Wang, Q. Jiang, R. Hogg, F. Tutu, F. Pozzi, and A. Seeds, "Long-wavelength InAs/GaAs quantum-dot laser diode monolithically grown on Ge substrate," *Nature Photonics*, vol. 5, no. 7, pp. 416–419, 2011.

[302] B. R. Koch, A. W. Fang, O. Cohen, and J. E. Bowers, "Mode-locked silicon evanescent lasers," *Optics Express*, vol. 15, no. 18, p. 11225, 2007.

[303] J. Pfeifle, R. Watts, I. Shkarban, S. Wolf, V. Vujicic, P. Landais, N. Chimot, S. Joshi, K. Merghem, C. Cal, M. Weber, A. Ramdane, F. Lelarge, L. P. Barry, W. Freude, and C. Koos, "Simultaneous phase noise reduction of 30 comb lines from a quantum-dash mode-locked laser diode enabling coherent Tbit/s data transmission," in *Optical Fiber Communications Conference and Exhibition (OFC), 2015*, (Piscataway, NJ), p. Tu3I.5, IEEE, 2015.

[304] P. Marin-Palomo, J. N. Kemal, P. Trocha, S. Wolf, K. Merghem, F. Lelarge, A. Ramdane, W. Freude, S. Randel, and C. Koos, "Comb-based WDM transmission at 10 Tbit/s using a DC-driven quantum-dash

mode-locked laser diode," *Optics Express*, vol. 27, no. 22, pp. 31110–31129, 2019.

[305] N. Dupuis, C. R. Doerr, L. Zhang, L. Chen, N. J. Sauer, P. Dong, L. L. Buhl, and D. Ahn, "InP-based comb generator for optical OFDM," *Journal of Lightwave Technology*, vol. 30, no. 4, pp. 466–472, 2012.

[306] T. Yamamoto, K. Hitomi, W. Kobayashi, and H. Yasaka, "Optical frequency comb block generation by using semiconductor Mach–Zehnder modulator," *IEEE Photonics Technology Letters*, vol. 25, no. 1, pp. 40–42, 2013.

[307] R. Slavik, S. G. Farwell, M. J. Wale, and D. J. Richardson, "Compact optical comb generator using InP tunable laser and push-pull modulator," *IEEE Photonics Technology Letters*, vol. 27, no. 2, pp. 217–220, 2015.

[308] N. Yokota and H. Yasaka, "Operation strategy of InP Mach–Zehnder modulators for flat optical frequency comb generation," *IEEE Journal of Quantum Electronics*, vol. 52, no. 8, pp. 1–7, 2016.

[309] R.-J. Essiambre, G. Kramer, P. J. Winzer, G. J. Foschini, and B. Goebel, "Capacity limits of optical fiber networks," *Journal of Lightwave Technology*, vol. 28, no. 4, pp. 662–701, 2010.

[310] Q. Fang, T.-Y. Liow, J. F. Song, K. W. Ang, M. B. Yu, G. Q. Lo, and D.-L. Kwong, "WDM multi-channel silicon photonic receiver with 320 Gbps data transmission capability," *Optics Express*, vol. 18, no. 5, pp. 5106–5113, 2010.

[311] D. Hillerkuss, R. Schmogrow, T. Schellinger, M. Jordan, M. Winter, G. Huber, T. Vallaitis, R. Bonk, P. Kleinow, F. Frey, M. Roeger, S. Koenig, A. Ludwig, A. Marculescu, J. Li, M. Hoh, M. Dreschmann, J. Meyer, S. Ben Ezra, N. Narkiss, B. Nebendahl, F. Parmigiani, P. Petropoulos, B. Resan, A. Oehler, K. Weingarten, T. Ellermeyer, J. Lutz, M. Moeller, M. Huebner, J. Becker, C. Koos, W. Freude, and J. Leuthold, "26 Tbit s^{-1} line-rate super-channel transmission utilizing all-optical fast Fourier transform processing," *Nature Photonics*, vol. 5, no. 6, pp. 364–371, 2011.

[312] Y.-K. Huang, E. Ip, Z. Wang, M.-F. Huang, Y. Shao, and T. Wang, "Transmission of spectral efficient super-channels using all-optical OFDM and digital coherent receiver technologies," *Journal of Lightwave Technology*, vol. 29, no. 24, pp. 3838–3844, 2011.

[313] J. Veselka and S. Korotky, "A multiwavelength source having precise channel spacing for WDM systems," *IEEE Photonics Technology Letters*, vol. 10, no. 7, pp. 958–960, 1998.

[314] J. Zhang, J. Yu, Z. Dong, Y. Shao, and N. Chi, "Generation of full C-band coherent and frequency-lock multi-carriers by using recirculating frequency shifter loops based on phase modulator with external injection," *Optics Express*, vol. 19, no. 27, pp. 26370–26381, 2011.

[315] R. Ding, T. Baehr-Jones, W.-J. Kim, A. Spott, M. Fournier, J.-M. Fedeli, S. Huang, J. Luo, A. K.-Y. Jen, L. Dalton, and M. Hochberg, "Sub-volt silicon-organic electro-optic modulator with 500 MHz bandwidth," *Journal of Lightwave Technology*, vol. 29, no. 8, pp. 1112–1117, 2011.

[316] V. R. Almeida, Q. Xu, C. A. Barrios, and M. Lipson, "Guiding and confining light in void nanostructure," *Optics Letters*, vol. 29, no. 11, pp. 1209–1211, 2004.

[317] R. Palmer, S. Koeber, W. Heni, D. Elder, D. Korn, H. Yu, L. Alloatti, S. Koenig, P. Schindler, W. Bogaerts, M. Pantouvaki, G. Lepage, P. Verheyen, J. van Campenhout, P. Absil, R. Baets, L. Dalton, W. Freude, J. Leuthold, and C. Koos, "High-speed silicon-organic hybrid (SOH) modulator with 1.6 fJ/bit and 180 pm/V in-device nonlinearity," in *ECOC'13*, p. paper We.3.B.3.

[318] D. Taillaert, F. van Laere, M. Ayre, W. Bogaerts, D. van Thourhout, P. Bienstman, and R. Baets, "Grating couplers for coupling between optical fibers and nanophotonic waveguides," *Japanese Journal of Applied Physics*, vol. 45, no. 8A, pp. 6071–6077, 2006.

[319] R. Schmogrow, M. Winter, M. Meyer, D. Hillerkuss, S. Wolf, B. Baeuerle, A. Ludwig, B. Nebendahl, S. Ben-Ezra, J. Meyer, M. Dreschmann, M. Huebner, J. Becker, C. Koos, W. Freude, and J. Leuthold, "Real-time Nyquist pulse generation beyond 100 Gbit/s and

its relation to OFDM," *Optics Express*, vol. 20, no. 1, pp. 317–337, 2012.

[320] R. Schmogrow, D. Hillerkuss, M. Dreschmann, M. Huebner, M. Winter, J. Meyer, B. Nebendahl, C. Koos, J. Becker, W. Freude, and J. Leuthold, "Real-time software-defined multiformat transmitter generating 64QAM at 28 GBd," *IEEE Photonics Technology Letters*, vol. 22, no. 21, pp. 1601–1603, 2010.

[321] F. Chang, K. Onohara, and T. Mizuochi, "Forward error correction for 100 G transport networks," *IEEE Communications Magazine*, vol. 48, no. 3, pp. S48–S55, 2010.

[322] ITU-T, "ITU-T Rec. G.694.1 (02/2012) Spectral grids for WDM applications: DWDM frequency grid."

[323] R. Schmogrow, B. Nebendahl, M. Winter, A. Josten, D. Hillerkuss, S. Koenig, J. Meyer, M. Dreschmann, M. Huebner, C. Koos, J. Becker, W. Freude, and J. Leuthold, "Error vector magnitude as a performance measure for advanced modulation formats," *IEEE Photonics Technology Letters*, vol. 24, no. 1, pp. 61–63, 2012. Explanation: OSNR means the signal-to-noise power ratio measured in the optical signal bandwidth, not in a reference bandwidth of 1 nm (12.5 GHz at $\lambda = 1.55$ µm). Erratum: In Eq. (4), replace sqrt(2) by 1. Corrections in: *IEEE Photonics Technology Letters*, vol. 24, no. 23, p. 2198, 2012.

[324] J. Luo, S. Huang, Z. Shi, B. M. Polishak, X.-H. Zhou, and A. K.-Y. Jen, "Tailored organic electro-optic materials and their hybrid systems for device applications †," *Chemistry of Materials*, vol. 23, no. 3, pp. 544–553, 2011.

[325] Y. Enami, C. T. Derose, D. Mathine, C. Loychik, C. Greenlee, R. A. Norwood, T. D. Kim, J. Luo, Y. Tian, A. K.-Y. Jen, and N. Peyghambarian, "Hybrid polymer/sol–gel waveguide modulators with exceptionally large electro–optic coefficients," *Nature Photonics*, vol. 1, no. 3, pp. 180–185, 2007.

[326] W. S. Zaoui, A. Kunze, W. Vogel, M. Berroth, J. Butschke, F. Letzkus, and J. Burghartz, "Bridging the gap between optical fibers and silicon

photonic integrated circuits," *Optics Express*, vol. 22, no. 2, pp. 1277–1286, 2014.

[327] P. Marin-Palomo, J. Kemal, T. Kippenberg, W. Freude, S. Randel, and C. Koos, "Performance of chip-scale optical frequency comb generators in coherent WDM communications," *Optics Express*, in press, 2020.

[328] P. J. Winzer and R.-J. Essiambre, "Advanced optical modulation formats," *Proceedings of the IEEE*, vol. 94, no. 5, pp. 952–985, 2006.

[329] R. Ell, U. Morgner, F. X. KÃÂrtner, J. G. Fujimoto, E. P. Ippen, V. Scheuer, G. Angelow, T. Tschudi, M. J. Lederer, A. Boiko, and B. Luther-Davies, "Generation of 5-fs pulses and octave-spanning spectra directly from a Ti:sapphire laser," *Optics Letters*, vol. 26, no. 6, pp. 373–375, 2001.

[330] S. Pekarek, T. Südmeyer, S. Lecomte, S. Kundermann, J. M. Dudley, and U. Keller, "Self-referenceable frequency comb from a gigahertz diode-pumped solid-state laser," *Optics Express*, vol. 19, no. 17, pp. 16491–16497, 2011.

[331] M. C. Stumpf, S. Pekarek, A. E. H. Oehler, T. Südmeyer, J. M. Dudley, and U. Keller, "Self-referencable frequency comb from a 170-fs, 1.5-µm solid-state laser oscillator," *Applied Physics B*, vol. 99, no. 3, pp. 401–408, 2010.

[332] R. Holzwarth, M. Zimmermann, Th. Udem, T. W. Hánsch, P. Russbüldt, K. Gäbel, R. Poprawe, J. C. Knight, W.J. Wadsworth, and P. St. J. Russell, "White-light frequency comb generation with a diode-pumped Cr:LiSAF laser," *Optics Letters*, vol. 26, no. 17, pp. 1376–1378, 2001.

[333] A. Bartels, D. Heinecke, and S. A. Diddams, "10-GHz self-referenced optical frequency comb," *Science*, vol. 326, no. 5953, p. 681, 2009.

[334] L. Krainer, R. Paschotta, G. Spuhler, I. Klimov, C. Teisset, K. Weingarten, and U. Keller, "Tunable picosecond pulse-generating laser with repetition rate exceeding 10 GHz," *Electronics Letters*, vol. 38, no. 5, pp. 225–227, 2002.

[335] S. Zeller, L. Krainer, G. Spühler, K. Weingarten, U. Keller, and R. Paschotta, "Passively mode-locked 40-GHz Er:Yb:glass laser," *Applied Physics B: Lasers and Optics*, vol. 76, no. 7, pp. 787–788, 2003.

[336] D. Deng, L. Zhan, Z. Gu, Y. Gu, and Y. Xia, "55-fs pulse generation without wave-breaking from an all-fiber Erbium-doped ring laser," *Optics Express*, vol. 17, no. 6, pp. 4284–4288, 2009.

[337] F. Ilday, J. Buckley, L. Kuznetsova, and F. Wise, "Generation of 36-femtosecond pulses from a ytterbium fiber laser," *Optics Express*, vol. 11, no. 26, pp. 3550–3554, 2003.

[338] J.-L. Peng, H. Ahn, R.-H. Shu, H.-C. Chui, and J. Nicholson, "Highly stable, frequency-controlled mode-locked erbium fiber laser comb," *Applied Physics B*, vol. 86, no. 1, pp. 49–53, 2007.

[339] P. Pal, W. H. Knox, I. Hartl, and M. E. Fermann, "Self referenced Yb-fiber-laser frequency comb using a dispersion micromanaged tapered holey fiber," *Optics Express*, vol. 15, no. 19, pp. 12161–12166, 2007.

[340] J. Rauschenberger, T. Fortier, D. Jones, J. Ye, and S. Cundiff, "Control of the frequency comb from a modelocked Erbium-doped fiber laser," *Optics Express*, vol. 10, no. 24, pp. 1404–1410, 2002.

[341] B. R. Washburn, S. A. Diddams, N. R. Newbury, J. W. Nicholson, M. F. Yan, and C. G. Jrgensen, "Phase-locked, erbium-fiber-laser-based frequency comb in the near infrared," *Optics Letters*, vol. 29, no. 3, pp. 250–252, 2004.

[342] T. R. Schibli, K. Minoshima, F.-L. Hong, H. Inaba, A. Onae, H. Matsumoto, I. Hartl, and M. E. Fermann, "Frequency metrology with a turnkey all-fiber system," *Optics Letters*, vol. 29, no. 21, pp. 2467–2469, 2004.

[343] G. Ycas, S. Osterman, and S. A. Diddams, "Generation of a 660–2100 nm laser frequency comb based on an erbium fiber laser," *Optics Letters*, vol. 37, no. 12, pp. 2199–2201, 2012.

[344] G. Wang, F. Meng, C. Li, T. Jiang, A. Wang, Z. Fang, and Z. Zhang, "500 MHz spaced Yb:fiber laser frequency comb without amplifiers," *Optics Letters*, vol. 39, no. 9, pp. 2534–2536, 2014.

[345] A. Akrout, K. Merghem, J. Tourrenc, A. Martinez, A. Shen, F. Lelarge, G.-H. Duan, and A. Ramdane, "Generation of 10 GHz optical pulses with very low timing jitter using one section passively mode locked quantum dash based lasers operating at 1.55μm," in *Optical Fiber Communication. OFC 2009. Conference on*, pp. 1–3, 2009.

[346] Q. Y. Lu, M. Razeghi, S. Slivken, N. Bandyopadhyay, Y. Bai, W. J. Zhou, M. Chen, D. Heydari, A. Haddadi, R. McClintock, M. Amanti, and C. Sirtori, "High power frequency comb based on mid-infrared quantum cascade laser at $\lambda \sim 9\,\mu$m," *Applied Physics Letters*, vol. 106, no. 5, pp. –, 2015.

[347] C. A. Zaugg, A. Klenner, M. Mangold, A. S. Mayer, S. M. Link, F. Emaury, M. Golling, E. Gini, C. J. Saraceno, B. W. Tilma, and U. Keller, "Gigahertz self-referenceable frequency comb from a semiconductor disk laser," *Optics Express*, vol. 22, no. 13, pp. 16445–16455, 2014.

[348] K. G. Wilcox, A. H. Quarterman, H. E. Beere, D. A. Ritchie, and A. C. Tropper, "Variable repetition frequency femtosecond-pulse surface emitting semiconductor laser," *Applied Physics Letters*, vol. 99, no. 13, pp. –, 2011.

[349] K. G. Wilcox, A. H. Quarterman, H. E. Beere, D. A. Ritchie, and A. C. Tropper, "Repetition-frequency-tunable mode-locked surface emitting semiconductor laser between 2.78 and 7.87 GHz," *Optics Express*, vol. 19, no. 23, pp. 23453–23459, 2011.

[350] J. Davila-Rodriguez, K. Bagnell, and P. J. Delfyett, "Frequency stability of a 10 GHz optical frequency comb from a semiconductor-based mode-locked laser with an intracavity 10,000 finesse etalon," *Optics Letters*, vol. 38, no. 18, pp. 3665–3668, 2013.

[351] K. G. Wilcox, A. H. Quarterman, V. Apostolopoulos, H. E. Beere, I. Farrer, D. A. Ritchie, and A. C. Tropper, "175 GHz, 400-fs-pulse harmonically mode-locked surface emitting semiconductor laser," *Optics Express*, vol. 20, no. 7, pp. 7040–7045, 2012.

[352] S. Choi, M. Yamamoto, D. Moteki, T. Shioda, Y. Tanaka, and T. Kurokawa, "Frequency-comb-based interferometer for profilometry and tomography," *Optics Letters*, vol. 31, no. 13, pp. 1976–1978, 2006.

[353] Y. Liu, A. J. Metcalf, V. T. Company, R. Wu, L. Fan, L. T. Varghese, M. Qi, and A. M. Weiner, "Bandwidth scaling of a phase-modulated continuous-wave comb through four-wave mixing in a silicon nano-waveguide," *Optics Letters*, vol. 39, no. 22, pp. 6478–6481, 2014.

[354] Y. Dou, H. Zhang, and M. Yao, "Improvement of flatness of optical frequency comb based on nonlinear effect of intensity modulator," *Optics Letters*, vol. 36, no. 14, pp. 2749–2751, 2011.

[355] T. Yamamoto, T. Komukai, K. Suzuki, and A. Takada, "Multicarrier light source with flattened spectrum using phase modulators and dispersion medium," *Journal of Lightwave Technology*, vol. 27, no. 19, pp. 4297–4305, 2009.

[356] R. Wu, V. Torres-Company, D. E. Leaird, and A. M. Weiner, "Supercontinuum-based 10-GHz flat-topped optical frequency comb generation," *Optics Express*, vol. 21, no. 5, pp. 6045–6052, 2013.

[357] V. Ataie, B. P.-P. Kuo, E. Myslivets, and S. Radic, "Generation of 1500-tone, 120nm-wide ultraflat frequency comb by single CW source," in *Optical Fiber Communication Conference/National Fiber Optic Engineers Conference 2013*, p. PDP5C.1, Optical Society of America, 2013.

[358] V. R. Supradeepa and Andrew M. Weiner, "Bandwidth scaling and spectral flatness enhancement of optical frequency combs from phase-modulated continuous-wave lasers using cascaded four-wave mixing," *Optics Letters*, vol. 37, no. 15, pp. 3066–3068, 2012.

[359] A. Ishizawa, T. Nishikawa, A. Mizutori, H. Takara, S. Aozasa, A. Mori, H. Nakano, A. Takada, and M. Koga, "Octave-spanning frequency comb generated by 250 fs pulse train emitted from 25 GHz externally phase-modulated laser diode for carrier-envelope-offset-locking," *Electronics Letters*, vol. 46, no. 19, p. 1343, 2010.

[360] W. Li and J. Yao, "Optical frequency comb generation based on repeated frequency shifting using two Mach-Zehnder modulators and an asym-

metric Mach-Zehnder interferometer," *Optics Express*, vol. 17, no. 26, p. 23712, 2009.

[361] A. A. Savchenkov, A. B. Matsko, V. S. Ilchenko, I. Solomatine, D. Seidel, and L. Maleki, "Tunable optical frequency comb with a crystalline whispering gallery mode resonator," *Physical Review Letters*, vol. 101, no. 9, p. 93902, 2008.

[362] L. Razzari, D. Duchesne, M. Ferrera, R. Morandotti, S. Chu, B. E. Little, and D. J. Moss, "CMOS-compatible integrated optical hyper-parametric oscillator," *Nature Photonics*, vol. 4, no. 1, pp. 41–45, 2009.

[363] P. Del'Haye, S. B. Papp, and S. A. Diddams, "Hybrid electro-optically modulated microcombs," *Physical Review Letters*, vol. 109, no. 26, p. 263901, 2012.

[364] I. S. Grudinin, L. Baumgartel, and N. Yu, "Frequency comb from a microresonator with engineered spectrum," *Optics Express*, vol. 20, no. 6, pp. 6604–6609, 2012.

[365] K. Saha, Y. Okawachi, B. Shim, J. S. Levy, R. Salem, A. R. Johnson, M. A. Foster, M. R. E. Lamont, M. Lipson, and A. L. Gaeta, "Modelocking and femtosecond pulse generation in chip-based frequency combs," *Optics Express*, vol. 21, no. 1, pp. 1335–1343, 2013.

[366] A. R. Johnson, Y. Okawachi, J. S. Levy, J. Cardenas, K. Saha, M. Lipson, and A. L. Gaeta, "Chip-based frequency combs with sub-100 GHz repetition rates," *Optics Letters*, vol. 37, no. 5, pp. 875–877, 2012.

[367] M. Born and E. Wolf, *Principles of optics: Electromagnetic theory of propagation, interference and diffraction of light*. Oxford and New York: Pergamon Press, 6 ed., 1980.

[368] A. A. Savchenkov, A. B. Matsko, W. Liang, V. S. Ilchenko, D. Seidel, and L. Maleki, "Kerr combs with selectable central frequency," *Nature Photonics*, vol. 5, no. 5, pp. 293–296, 2011.

[369] E. L. Teleanu, V. Durán, and V. Torres-Company, "Electro-optic dual-comb interferometer for high-speed vibrometry," *Optics Express*, vol. 25, no. 14, pp. 16427–16436, 2017.

Acknowledgements (German)

Die vorliegende Dissertation entstand während meiner Tätigkeit am Institut für Photonik und Quantenelektronik (IPQ) am Karlsruher Institut für Technologie (KIT). Die Ergebnisse wurden erarbeitet im Rahmen einer Forschungskooperation mit der Carl Zeiss AG, sowie im Rahmen des geförderten Projekts Synthetic Lambda der Baden-Württemberg Stiftung. Die Arbeit war zudem eingebunden in die Karlsruhe School of Optics & Photonics (KSOP), die Karlsruhe Nano-Micro Facility (KNMF), das Center for Functional Nanostructures (CFN), die Helmholtz International Research School for Teratronics (HIRST), sowie in die von der europäischen Union (EU) geförderten Projekte EnTeraPIC (ERC Starting Grant, Nummer 280145), SOFI (Nummer 248609), PHOXTROT (Nummer 318240) und OTONES (EU-FP7 PianoPlus Projekt). Sie wurde außerdem unterstützt durch die Alfried Krupp von Bohlen und Halbach-Stiftung.

An dieser Stelle möchte ich mich herzlich bei allen Personen bedanken, welche zum Gelingen dieser Arbeit beigetragen haben.

An erster Stelle danke ich Prof. Christian Koos für die Betreuung. Die gemeinsamen fachlichen Diskussionen und das entgegen gebrachte Vertrauen waren immer sehr inspirierend, und sein Enthusiasmus ein Vorbild und motivierender Antrieb für die eigene Arbeit. Prof. Wolfgang Freude bin ich sehr dankbar für zahlreiche fruchtbare Diskussionen und wertvolle Hinweise, insbesondere bei der Ausarbeitung von wissenschaftlichen Schriften und Vorträgen. Seine Erklärungen waren immer sehr hilfreich und haben die Qualität der Beiträge wesentlich gesteigert. Prof. Andreas Heinrich danke ich herzlich für seine Bereitschaft als Korreferent zu wirken, sowie für die gute Einbindung in die damalige Messtechnikgruppe während meiner Aufenthalte bei Zeiss. Danke auch an Prof. Jürg Leuthold, welcher während meiner ersten Jahre als Doktorand die Institutsleitung innehatte, für die gute gruppenübergreifende Zusammenarbeit.

Dr. Frank Höller gebührt besonderer Dank für die Betreuung und Unterstützung meiner Forschungsarbeiten und die vielen guten Ratschläge, welche mir obendrein beim Berufseinstieg sehr geholfen haben. Insbesondere die offene und unkomplizierte Einbindung in Themen auch jenseits der Promotion habe ich stets sehr genossen. Ich danke Prof. Larry Dalton und Dr. Delwin Elder für das Bereitstellen des elektro-optischen Materials, welches wesentlich zum Erfolg der integriert-optischen Frequenzkammerzeugung beigetragen hat. Dr. Markus Fratz und Harald Wölfelschneider danke ich für die gute Zusammenarbeit und die erfolgreichen gemeinsamen Messungen in Synthetic Lambda.

Ein herzliches Dankeschön für die großartige Unterstützung aus Sekretariat, IT und Werkstatt gebührt dem Institutsteam, Tatiana Gassmann, Andrea Riemensperger, Bernadette Lehmann, Angelika Olbrich, Oswald Speck, Martin Winkeler, David Guder, Manfred Hirsch, Hans Bürger, Marco Hummel und Florian Rupp. Ohne euch wäre die Arbeit am Institut um ein Vielfaches schwieriger.

Viel Spaß hat außerdem die Zusammenarbeit mit meinen Studenten gemacht. Herzlichen Dank an Andreas Messner, Bruno Ziegner, Dagmawi Bekele, Dominik Meier, Heiner Zwickel, Jan Baumann, Juned Nassir Kemal, Stefan Wolf, Thomas Fehrenbach und Tobias Baumgartner für eure Beiträge im Rahmen eurer Abschlussarbeiten. Sehr gefreut hat mich auch, dass einige von euch zu Kollegen geworden sind.

Ganz besonders möchte ich mich bei allen ehemaligen Kollegen für die fruchtbare Zusammenarbeit, die gute Atmosphäre und den außerordentlichen Zusammenhalt im Team bedanken. Dr. Simon Schneider und Aleksandar Nesic danke ich für das freundschaftliche Miteinander und die positive Stimmung in unserem Büro. Besonders dankbar bin ich Aleksandar für das großzügige Angebot, einige Zeit in seiner Wohnung unterzukommen. Dr. Sebastian Köber, Dr. Dietmar Korn, Dr. Luca Alloatti und Dr. Robert Palmer gebührt Dank für die Weiterentwicklung der Modulatoren sowie für das Testen vieler verschiedener elektro-optischer Materialien. Diese Arbeiten waren wesentliche Voraussetzungen für die erfolgreiche Demonstration von integrierten elektro-optischen Frequenzkammquellen. Für die langjährige Freundschaft seit Beginn des Studiums und die vielen schönen gemeinsamen Erlebnisse bin ich Robert besonders dankbar. Vielen Dank auch an Dr. Matthias Lauermann für seine Tätigkeit als PIC-Layouter - es war sicher nicht immer einfach

die vielen Wünsche aller Kollegen auf einem Chip unterzubringen. Für die technische Unterstützung bei den Datenübertragungsexperimenten und für die gemeinsamen Messungen bedanke ich mich herzlich bei Dr. Stefan Wolf, Dr. Philipp Schindler, Dr. René Schmogrow und Dr. Jörg Pfeifle - es hat wirklich Spaß gemacht gemeinsam die magische Terabit/s Grenze zu knacken. Allen bisher genannten sowie meinen weiteren ehemaligen Kollegen Dr. Nicole Lindenmann, Dr. Alexandra Ludwig, Dr. Argishti Melikyan, Dr. Swen König, Dr. Moritz Röger, Dr. René Bonk, Dr. David Hillerkuss, Dr. Jingshi Li, Wladislaw Hartmann, Juned Nassir Kemal, Dr. Heiner Zwickel, Philipp Trocha, Denis Ganin, Dr. Tobias Harter, Tobias Hoose, Matthias Blaicher, Sascha Mühlbrandt, Clemens Kieninger, Pablo Marin-Palomo, Sandeep Ummethala, Djorn Karnick, Kira Köhnle, Muhammad Rodlin Billah, Philipp-Immanuel Dietrich und Dr. Yasar Kutuvantavida danke ich für viele gemeinsame Kaffee- oder Kickerpausen, Grillabende auf dem Dach und gemeinsame Ausflüge - besonders gerne denke ich an die Roadtrips an der Westküste und die Hüttenwochenenden im Schnee zurück.

Ich danke außerdem Caroline Schröder für so manches Feierabendbier und viele gute Gespräche, sowie die Möglichkeit, einige Zeit unterzukommen. Für die Beantwortung so mancher Frage zur Programmierung mit C++ und die nahezu lebenslange Freundschaft danke ich Dr. Mathias Nachtmann.

Zu guter Letzt danke ich meiner Familie, meinen Eltern Maria und Hansjürgen, meiner Schwester Franziska, meiner Frau Annemarie sowie meinen Töchtern, Edna und Noemi. Ohne euren Zuspruch, euren Rückhalt und eure jahrelange Unterstützung wäre diese Arbeit nicht möglich gewesen.

List of Publications

Journal Publications

[J1] **C. Weimann**, A. Messner, T. Baumgartner, S. Wolf, F. Hoeller, W. Freude, and C. Koos, "Fast high-precision distance metrology using a pair of modulator-generated dual-color frequency combs," *Optics Express*, vol. 26, pp. 34305–34335, Dec 2018.

[J2] J. Pfeifle, V. Vujicic, R. T. Watts, P. C. Schindler, **C. Weimann**, R. Zhou, W. Freude, L. P. Barry, and C. Koos, "Flexible terabit/s Nyquist-WDM super-channels using a gain-switched comb source," *Optics Express*, vol. 23, no. 2, pp. 724–738, 2015.

[J3] J. Pfeifle, V. Brasch, M. Lauermann, Y. Yu, D. Wegner, T. Herr, K. Hartinger, P. Schindler, J. Li, D. Hillerkuss, R. Schmogrow, **C. Weimann**, R. Holzwarth, W. Freude, J. Leuthold, T. J. Kippenberg, and C. Koos, "Coherent terabit communications with microresonator Kerr frequency combs," *Nature Photonics*, vol. 8, no. 5, pp. 375–380, 2014.

[J4] **C. Weimann**, M. Fratz, H. Wölfelschneider, W. Freude, H. Höfler, and C. Koos, "Synthetic-wavelength interferometry improved with frequency calibration and unambiguity range extension," *Applied Optics*, vol. 54, no. 20, pp. 6334–6344, 2015.

[J5] **C. Weimann**, P. C. Schindler, R. Palmer, S. Wolf, D. Bekele, D. Korn, J. Pfeifle, S. Koeber, R. Schmogrow, L. Alloatti, D. Elder, H. Yu, W. Bogaerts, L. R. Dalton, W. Freude, J. Leuthold, and C. Koos, "Silicon-organic hybrid (SOH) frequency comb sources for terabit/s data transmission," *Optics Express*, vol. 22, no. 3, pp. 3629–3637, 2014.

[J6] **C. Weimann**, F. Hoeller, Y. Schleitzer, C. A. Diez, B. Spruck, W. Freude, Y. Boeck, and C. Koos, "Measurement of length and position with frequency combs," *Journal of Physics: Conference Series*, vol. 605, no. 1, p. 12030, 2015.

[J7] S. Schneider, M. Lauermann, P.-I. Dietrich, **C. Weimann**, W. Freude, and C. Koos, "Optical coherence tomography system mass-producible on a silicon photonic chip," *Optics Express*, vol. 24, no. 2, pp. 1573–1586, 2016.

[J8] P. Trocha, M. Karpov, D. Ganin, M. H. P. Pfeiffer, A. Kordts, S. Wolf, J. Krockenberger, P. Marin-Palomo, **C. Weimann**, S. Randel, W. Freude, T. J. Kippenberg, and C. Koos, "Ultrafast optical ranging using microresonator soliton frequency combs," *Science*, vol. 359, no. 6378, pp. 887–891, 2018.

[J9] P. Trocha, D. Ganin, M. Karpov, M. H. P. Pfeiffer, A. Kordts, J. Krockenberger, S. Wolf, P. Marin-Palomo, **C. Weimann**, S. Randel, W. Freude, T. J. Kippenberg, and C. Koos, "Ultrafast optical ranging using microresonator soliton frequency combs," *ArXiv e-prints*, arXiv:1707.05969, 2017.

[J10] M. Lauermann, **C. Weimann**, A. Knopf, W. Heni, R. Palmer, S. Koeber, D. L. Elder, W. Bogaerts, J. Leuthold, L. R. Dalton, C. Rembe, W. Freude, and C. Koos, "Integrated optical frequency shifter in silicon-organic hybrid (SOH) technology," *Optics Express*, vol. 24, no. 11, pp. 11694–11707, 2016.

[J11] **C. Weimann**, M. Lauermann, F. Hoeller, W. Freude, and C. Koos, "Silicon photonic integrated circuit for fast and precise dual-comb distance metrology," *Optics Express*, vol. 25, no. 24, pp. 30091–30104, 2017.

[J12] J. Pfeifle, A. Coillet, R. Henriet, K. Saleh, P. Schindler, **C. Weimann**, W. Freude, I. V. Balakireva, L. Larger, C. Koos, and Y. K. Chembo, "Optimally coherent Kerr combs generated with crystalline whispering gallery mode resonators for ultrahigh capacity fiber communications," *Physical Review Letters*, vol. 114, no. 9, p. 093902, 2015.

[J13] C. Koos, J. Leuthold, W. Freude, M. Kohl, L. Dalton, W. Bogaerts, A. L. Giesecke, M. Lauermann, A. Melikyan, S. Koeber, S. Wolf, **C. Weimann**, S. Muehlbrandt, K. Koehnle, J. Pfeifle, W. Hartmann, Y. Kutuvantavida, S. Ummethala, R. Palmer, D. Korn, L. Alloatti, P. C. Schindler, D. L. Elder, T. Wahlbrink, and J. Bolten, "Silicon-organic hybrid (SOH) and Plasmonic-organic hybrid (POH) integration," *Journal of Lightwave Technology*, vol. 34, pp. 256–268, Jan 2016.

[J14] D. Hillerkuss, T. Schellinger, M. Jordan, **C. Weimann**, F. Parmigiani, B. Resan, K. Weingarten, S. Ben-Ezra, B. Nebendahl, C. Koos, W. Freude, and J. Leuthold, "High-quality optical frequency comb by spectral slicing of spectra broadened by SPM," *IEEE Photonics Journal*, vol. 5, pp. 7201011–7201011, Oct 2013.

[J15] L. Alloatti, D. Korn, **C. Weimann**, C. Koos, W. Freude, and J. Leuthold, "Second-order nonlinear silicon-organic hybrid waveguides," *Optics Express*, vol. 20, pp. 20506–20515, Aug 2012.

Conference Publications

[C1] M. Fratz, **C. Weimann**, H. Wölfelschneider, C. Koos, and H. Höfler, "Absolutely referenced distance measurement by combination of time-of-flight and digital holographic methods," *Proc. SPIE*, vol. 8992, 2014.

[C2] **C. Weimann**, S. Wolf, D. Korn, R. Palmer, S. Koeber, R. Schmogrow, P. C. Schindler, L. Alloatti, A. Ludwig, W. Heni, D. Bekele, D. L. Elder, H. Yu, W. Bogaerts, L. R. Dalton, W. Freude, J. Leuthold, and C. Koos, "Silicon-organic hybrid (SOH) frequency comb source for data transmission at 784 Gbit/s," in *39th European Conference and Exhibition on Optical Communication (ECOC 2013)*, p. Th.2.B.1, Sep. 2013.

[C3] **C. Weimann**, P. C. Schindler, D. Bekele, R. Palmer, D. Korn, J. Pfeifle, S. Koeber, R. Schmogrow, L. Alloatti, D. L. Elder, H. Yu, W. Bogaerts, L. R. Dalton, W. Freude, J. Leuthold, and C. Koos, "Data transmission at terabit/s data rates using silicon-organic hybrid (SOH) frequency combs," in *Optical Fiber Communications Conference and Exhibition (OFC), 2014*, pp. 1–3, March 2014.

[C4] **C. Weimann**, D. Meier, S. Wolf, Y. Schleitzer, M. Totzeck, A. Heinrich, F. Hoeller, J. Leuthold, W. Freude, and C. Koos, "Fast high-precision distance measurements on scattering technical surfaces using frequency combs," in *CLEO: 2013*, p. CTu2I.3, Optical Society of America, 2013.

[C5] **C. Weimann**, M. Lauermann, T. Fehrenbach, R. Palmer, F. Hoeller, W. Freude, and C. Koos, "Silicon photonic integrated circuit for fast distance measurement with frequency combs," in *CLEO: 2014*, p. STh4O.3, Optical Society of America, 2014.

[C6] **C. Weimann**, F. Hoeller, and C. Koos, "High-precision laser ranging for industrial metrology with dual-color electro-optic frequency combs," in *116th Annual DGaO Conference (DGaO'15), 26-29 May, Brno, Czech Republic*, p. talk A4, 2015.

[C7] S. Schneider, M. Lauermann, **C. Weimann**, W. Freude, and C. Koos, "Silicon photonic optical coherence tomography system," in *CLEO: 2014*, p. ATu2P.4, Optical Society of America, 2014.

[C8] J. Pfeifle, I. Shkarban, S. Wolf, J. N. Kemal, **C. Weimann**, W. Hartmann, N. Chimot, S. Joshi, K. Merghem, A. Martinez, M. Weber, A. Ramdane, F. Lelarge, W. Freude, and C. Koos, "Coherent terabit communications using a quantum-dash mode-locked laser and self-homodyne detection," in *Optical Fiber Communications Conference and Exhibition (OFC), 2015*, p. W2A.19, IEEE, March 2015.

[C9] C. Koos, W. Freude, A. E. Guber, H. Hoelscher, A. Schimmel, M. Lauermann, S. Schneider, **C. Weimann**, S. Muehlbrandt, T. Harter, S. F. Wondimu, T. Wienhold, S. von der Ecken, P.-I. Dietrich, and G. Goering, "Photonic integration for metrology and sensing," in *Advanced Photonics 2017 (IPR, NOMA, Sensors, Networks, SPPCom, PS)*, p. ITh1A.1, Optical Society of America, 2017.

[C10] C. Koos, T. J. Kippenberg, L. P. Barry, A. Ramdane, F. Lelarge, W. Freude, P. Marin, J. N. Kemal, **C. Weimann**, S. Wolf, P. Trocha, J. Pfeifle, M. Karpov, A. Kordts, V. Brasch, R. T. Watts, V. Vujicic, A. Martinez, V. Panapakkam, and N. Chimot, "Chip-scale frequency comb generators for high-speed communications and optical metrology," in *Laser Resonators, Microresonators, and Beam Control XIX*, vol. 10090, SPIE, 2017.

[C11] C. Koos, W. Freude, L. Dalton, T. J. Kippenberg, L. P. Barry, A. Ramdane, F. Lelarge, S. Wolf, H. Zwickel, M. Lauermann, **C. Weimann**, W. Hartmann, J. N. Kemal, P. Marin, P. Trocha, J. Pfeifle, T. Herr, V. Brasch, R. T. Watts, D. Elder, A. Martinez, V. Panapakkam, and N. Chimot, "Silicon-organic hybrid (SOH) devices and their use in comb-based communication systems," in *2016 IEEE 13th International Conference on Group IV Photonics (GFP)*, pp. 56–57, Aug 2016.

[C12] C. Koos, T. J. Kippenberg, L. P. Barry, L. Dalton, A. Ramdane, F. Lelarge, W. Freude, J. N. Kemal, P. Marin, S. Wolf, P. Trocha, J. Pfeifle, **C. Weimann**, M. Lauermann, T. Herr, V. Brasch, R. T. Watts, D. Elder, A. Martinez, V. Panapakkam, and N. Chimot, "Multi-terabit/s transmission using chip-scale frequency comb sources," in *2016 18th International Conference on Transparent Optical Networks (ICTON)*, pp. 1–2, July 2016.

[C13] W. Freude, S. Schneider, M. Lauermann, P. . Dietrich, **C. Weimann**, and C. Koos, "Silicon photonic integrated circuits for optical coherence tomography," in *2016 18th International Conference on Transparent Optical Networks (ICTON)*, pp. 1–4, July 2016.

[C14] C. Koos, W. Freude, J. Leuthold, L. R. Dalton, S. Wolf, H. Zwickel, T. Hoose, M. R. Billah, M. Lauermann, **C. Weimann**, W. Hartmann, A. Melikyan, N. Lindenmann, S. Koeber, R. Palmer, D. Korn, L. Alloatti, A. . Giesecke, and T. Wahlbrink, "Silicon-organic hybrid (SOH) integration and photonic multi-chip systems: Technologies for high-speed optical interconnects," in *2016 IEEE Optical Interconnects Conference (OI)*, pp. 86–87, May 2016.

[C15] C. Koos, W. Freude, J. Leuthold, M. Kohl, L. R. Dalton, W. Bogaerts, M. Lauermann, S. Wolf, **C. Weimann**, A. Melikyan, N. Lindenmann, M. R. Billah, S. Muehlbrandt, S. Koeber, R. Palmer, K. Koehnle, L. Alloatti, D. L. Elder, A. . Giesecke, and T. Wahlbrink, "Silicon-organic hybrid (SOH) integration and photonic multi-chip systems: Extending the capabilities of the silicon photonic platform," in *2015 IEEE Photonics Conference (IPC)*, pp. 480–481, Oct 2015.

[C16] C. Koos, T. J. Kippenberg, L. P. Barry, L. Dalton, A. Ramdane, F. Lelarge, J. Leuthold, W. Freude, J. Pfeifle, **C. Weimann**, J. N. Kemal, M. Lauermann, S. Wolf, I. Shkarban, S. Koeber, T. Herr, V. Brasch,

R. T. Watts, and D. Elder, "Coherent terabit communications using chip-scale frequency comb sources," in *Nonlinear Optics*, p. NTh2A.1, Optical Society of America, 2015.

[C17] C. Koos, W. Freude, J. Leuthold, M. Kohl, L. R. Dalton, W. Bogaerts, M. Lauermann, S. Wolf, R. Palmer, S. Koeber, A. Melikyan, **C. Weimann**, G. Ronniger, K. Geistert, P. C. Schindler, D. L. Elder, T. Wahlbrink, J. Bolten, A. L. Giesecke, M. Koenigsmann, M. Kohler, and D. Malsam, "Silicon-organic hybrid (SOH) integration for low-power and high-speed signal generation," in *2015 17th International Conference on Transparent Optical Networks (ICTON)*, pp. 1–2, July 2015.

[C18] C. Koos, W. Freude, J. Leuthold, M. Kohl, L. R. Dalton, W. Bogaerts, M. Lauermann, A. Melikyan, S. Wolf, **C. Weimann**, S. Muehlbrandt, J. Pfeifle, S. Koeber, R. Palmer, P. C. Schindler, and D. L. Elder, "Silicon-organic (SOH) and plasmonic-organic (poh) hybrid integration: Extending the capabilities of silicon photonics and plasmonics," in *2015 Opto-Electronics and Communications Conference (OECC)*, pp. 1–2, June 2015.

[C19] C. Koos, T. J. Kippenberg, L. P. Barry, L. Dalton, W. Freude, J. Leuthold, J. Pfeifle, **C. Weimann**, M. Lauermann, J. N. Kemal, R. Palmer, S. Koeber, P. C. Schindler, T. Herr, V. Brasch, R. T. Watts, and D. Elder, "Terabit/s communications using chip-scale frequency comb sources," 2015.

[C20] C. Koos, W. Freude, T. J. Kippenberg, J. Leuthold, L. R. Dalton, J. Pfeifle, **C. Weimann**, M. Lauermann, R. Palmer, S. Koeber, S. Wolf, P. Schindler, V. Brasch, and D. Elder, "Terabit/s optical transmission using chip-scale frequency comb sources," in *2014 The European Conference on Optical Communication (ECOC)*, pp. 1–3, Sep. 2014.

[C21] R. Palmer, S. Koeber, M. Woessner, W. Heni, D. L. Elder, D. Korn, **C. Weimann**, P. C. Schindler, D. Bekele, L. Alloatti, W. Bogaerts, L. R. Dalton, J. Leuthold, W. Freude, and C. Koos, "Progress in silicon-organic hybrid (SOH) integration," in *11th International Conference on Group IV Photonics (GFP)*, pp. 110–111, Aug 2014.

[C22] C. Koos, J. Leuthold, W. Freude, L. R. Dalton, S. Koeber, R. Palmer, **C. Weimann**, D. L. Elder, W. Heni, D. Korn, J. Pfeifle, S. Wolf, D. Bekele, M. Woessner, L. Alloatti, P. C. Schindler, and S. Koenig, "Femtojoule modulation and frequency comb generation in silicon-organic hybrid (SOH) devices," in *2014 16th International Conference on Transparent Optical Networks (ICTON)*, pp. 1–4, July 2014.

[C23] M. Lauermann, C. Weimann, R. Palmer, P. C. Schindler, S. Koeber, C. Rembe, W. Freude, and C. Koos, "Integrated nanophotonic frequency shifter on the silicon-organic hybrid (SOH) platform for laser vibrometry," *AIP Conference Proceedings*, vol. 1600, no. 1, pp. 426–430, 2014.

[C24] V. Vujicic, J. Pfeifle, R. T. Watts, P. C. Schindler, **C. Weimann**, R. Zhou, W. Freude, C. Koos, and L. P. Barry, "Flexible Terabit/s Nyquist-WDM Superchannels with net $SE > 7\,\mathrm{bit/s/Hz}$ using a Gain-Switched Comb Source," in *CLEO: 2014*, p. SW1J.3, Optical Society of America, 2014.

[C25] J. Pfeifle, Y. Yu, P. Schindler, V. Brasch, T. Herr, **C. Weimann**, K. Hartinger, R. Holzwarth, W. Freude, T. J. Kippenberg, and C. Koos, "Transmission of a 1.44 Tbit/s Data Stream using a Feedback-Stabilized SiN Kerr Frequency Comb Source," in *Optical Fiber Communication Conference*, p. Th1A.6, Optical Society of America, 2014.

[C26] M. Lauermann, **C. Weimann**, A. Knopf, D. L. Elder, W. Heni, R. Palmer, D. Korn, P. C. Schindler, S. Koeber, L. Alloatti, H. Yu, W. Bogaerts, L. R. Dalton, C. Rembe, J. Leuthold, W. Freude, and C. Koos, "Integrated Silicon-Organic Hybrid (SOH) Frequency Shifter," in *Optical Fiber Communication Conference*, p. Tu2A.1, Optical Society of America, 2014.

[C27] W. Freude, L. Alloatti, D. Korn, M. Lauermann, A. Melikyan, R. Palmer, J. Pfeifle, P. C. Schindler, **C. Weimann**, R. Dinu, J. Bolten, T. Wahlbrink, M. Waldow, S. Walheim, P. M. Leufke, S. Ulrich, J. Ye, P. Vincze, H. Hahn, H. Yu, W. Bogaerts, V. Brasch, T. Herr, R. Holzwarth, K. Hartinger, C. Stamatiadis, M. F. O'Keefe, L. Stampoulidis, L. Zimmermann, R. Baets, T. Schimmel, I. Tomkos, K. Petermann, T. J. Kippenberg, C. Koos, and J. Leuthold, "Nonlinear Nano-Photonics," in *Frontiers in Optics 2013*, p. FTu4C.6, Optical Society of America, 2013.

[C28] J. Pfeifle, **C. Weimann**, F. Bach, J. Riemensberger, K. Hartinger, D. Hillerkuss, M. Jordan, R. Holtzwarth, T. J. Kippenberg, J. Leuthold, W. Freude, and C. Koos, "Microresonator-Based Optical Frequency Combs for High-Bitrate WDM Data Transmission," in *Optical Fiber Communication Conference*, p. OW1C.4, Optical Society of America, 2012.

[C29] W. Freude, S. Schneider, **C. Weimann**, F. Hoeller, M. Lauermann, P.-I. Dietrich, and C. Koos, "Integrated optics for optical coherence tomography and surface topography characterization," in *Light: Science & Applications, Light Conference*, 2016.

[C30] F. Hoeller, Y. Schleitzer, C. Alvarez-Diez, B. Spruck, **C. Weimann**, C. Koos, and G. Boeck, "Measurement of Length and Position with Frequency Combs," in *23rd Congress of the International Commission for Optics*, ICO, 2014.

[C31] C. Koos, T. J. Kippenberg, L. R. Dalton, W. Freude, J. Pfeifle, T. Herr, **C. Weimann**, R. Palmer, S. Koeber, M. Lauermann, and D. L. Elder, "Chip-scale frequency comb sources for terabit communications," in *URSI General Assembly and Scientific Symposium (URSI GASS'14)*, 2014.

[C32] C. Koos, W. Freude, R. Palmer, M. Lauermann, S. Koeber, J. Pfeifle, **C. Weimann**, P. C. Schindler, N. Lindenmann, T. Hoose, and M. R. Billah, "Silicon Photonics, Hybrid Integration, and Frequency Combs: Technologies for Terabit/s Communications, Teratronics, and Optical Metrology," in *115th Annual DGaO Conference*, p. talk H1, DGaO, 2014.

[C33] J. Pfeifle, V. Brasch, P. C. Schindler, **C. Weimann**, Y. Yu, W. Freude, T. J. Kippenberg, and C. Koos, "Kerr-Frequenzkämme und deren Stabilisierung für die Terabit-Kommunikation," in *115th Annual DGaO Conference*, p. talk A2, DGaO, 2014.

[C34] **C. Weimann**, S. Wolf, D. Meier, Y. Schleitzer, M. Totzeck, A. Heinrich, F. Hoeller, W. Freude, and C. Koos, "Fast high-precision distance measurements with electro-optic frequency combs," in *115th Annual DGaO Conference*, p. talk A1, DGaO, 2014.